

**ORGANIC COATING REMOVAL BY SINGLE
PARTICLE IMPACT**

by

Marcello Papini

**A thesis submitted in conformity with the requirements for the degree of Doctor of Philosophy
Department of Mechanical and Industrial Engineering
University of Toronto**

© Copyright by Marcello Papini 1999



**National Library
of Canada**

**Acquisitions and
Bibliographic Services**

**395 Wellington Street
Ottawa ON K1A 0N4
Canada**

**Bibliothèque nationale
du Canada**

**Acquisitions et
services bibliographiques**

**395, rue Wellington
Ottawa ON K1A 0N4
Canada**

Your file Votre référence

Our file Notre référence

The author has granted a non-exclusive licence allowing the National Library of Canada to reproduce, loan, distribute or sell copies of this thesis in microform, paper or electronic formats.

The author retains ownership of the copyright in this thesis. Neither the thesis nor substantial extracts from it may be printed or otherwise reproduced without the author's permission.

L'auteur a accordé une licence non exclusive permettant à la Bibliothèque nationale du Canada de reproduire, prêter, distribuer ou vendre des copies de cette thèse sous la forme de microfiche/film, de reproduction sur papier ou sur format électronique.

L'auteur conserve la propriété du droit d'auteur qui protège cette thèse. Ni la thèse ni des extraits substantiels de celle-ci ne doivent être imprimés ou autrement reproduits sans son autorisation.

0-612-41035-8

Abstract

ORGANIC COATING REMOVAL BY SINGLE PARTICLE IMPACT

Marcello Papini

**Doctor of Philosophy 1998
Department of Mechanical and Industrial Engineering
University of Toronto**

Organic coatings are often removed using solvents that create waste which is difficult and expensive to dispose of. For this reason, mechanical coating removal techniques such as blast cleaning are of increasing interest. The impact of single particles with two typical coating/substrate systems was examined in detail as an important first step to understanding the fundamental mechanisms which govern the removal of organic coatings by blast cleaning. A gas gun capable of launching single particles at speeds of up to 120 m/s and a high-speed photographic setup capable of measuring inbound and rebound particle velocities were constructed in order to characterise impact behaviour with respect to energy loss. The impact sites were photographed and the amount of coating removal was determined using image analysis.

Coating removal for a typical alkyd enamel on a pretreated steel substrate was found to be due to impact-induced buckling delamination of the coating. An analytical technique based on the coupling of a novel post-buckling analysis with an existing strain energy release rate analysis was developed with the purpose of predicting the amount of coating removed when a single particle was launched, at a given velocity, against a coated substrate. Predictions of delamination size using this model were obtained for a wide variety of incident velocities,

particle sizes, and coating thicknesses, and comparison with measured delamination size revealed good agreement.

A second coating system, consisting of a typical aerospace urethane coating with an epoxy primer applied to an aluminum substrate, was found to be eroded, and an existing rigid-plastic erosion theory developed for semi-infinite targets and spherical particles was modified to include elastic effects and shown to predict crater size well. A general rigid-plastic analysis was then developed in which the size of an impact crater, particle rebound velocity and energy loss could be predicted for an incident particle of any size, shape, and density, impacting at any angle of attack and in any orientation. Finally, a parametric study in the case of symmetric particles of arbitrary angularity revealed interesting trends with respect to coating removal.

Per Giorgio e Lucia

Senza di voi, non ce l'avrei fatta. Grazie di tutto mamma e papà.

Table of Contents

Abstract	ii
Table of Contents	v
List of Figures	ix
List of Tables.....	xv
Nomenclature.....	xvi
Acknowledgements.....	xxii
1.0 Introduction.....	1
1.1 Motivation.....	1
1.2 Thesis Objectives.....	2
1.3 Thesis Organisation	2
2.0 Experimental Apparatus.....	4
2.1 Background.....	4
2.2 Gas gun/high speed flash setup	5
3.0 Alkyd Coating/Steel Substrate System.....	10
3.1 Background	10
3.2 Model system.....	11
3.3 Characterisation of impact behaviour	13
3.3.1 Observations of crack path and impact site.....	14
3.3.2 Dominance of normal effects and comparison to Brach's model	16
3.3.3 Role of tangential effects.....	22
3.4 Evaluation of possible mechanisms of coating removal	24
3.4.1 Dynamic versus quasi-static effects	24

3.4.2	Analysis of incident kinematics.....	27
3.5	Delamination mechanism: Impact-Induced Buckling.....	38
3.5.1	Theory and analysis: Buckling analysis of clamped ring constrained from deflecting at an arbitrary inner radius.....	39
3.5.2	Theory and analysis: Calculation of arrest strain energy release rate and mode mix for interfacial cracks	46
3.5.3	Estimation of critical interfacial shear stress required to initiate delamination	54
3.6	Experimental verification of impact-induced buckling mechanism	55
3.6.1	Determination of indentation volume, V_o and radius at which buckling is prevented from occurring due to presence of particle, b	56
3.6.2	Calculation of reactions, arrest strain energy release rate, and phase angle at edge of delamination.....	59
3.6.3	Estimation of critical interfacial shear stress required to initiate delamination	63
3.7	Angular Particles	64
3.8	Summary.....	67
4.0	Urethane Coating/Epoxy Primer/Aluminum Substrate System.....	68
4.1	Experiments	68
4.2	Collision kinematics	75
4.3	Analysis of impacts	78
4.3.1	Rigid-plastic (fully plastic) analysis.....	78
4.3.2	Elastic-plastic analysis of impact	83
4.4	Comparison of Experimental and Analytical Results	86
4.5	Summary.....	89
5.0	Analytical Investigation of Erosion by Angular Particles	90
5.1	Background.....	90
5.2	Formulation of problem for general case.....	91
5.3	Symmetric particles	96
5.3.1	Formulation of equations of motion.....	96
5.3.2	Numerical solution of the differential equations.....	101
5.3.3	Algorithm for determining crater profile and contact area at end of each step.....	104

5.3.4	Limitations of model.....	108
5.4	Comparison with experimental data	109
5.5	Parametric study of impact of symmetric angular particles	112
5.5.1	Implementation of model.....	112
5.5.2	Dimensional analysis	112
5.5.3	Model systems	113
5.5.4	Results and Discussion	114
5.6	Summary	132
6.0	Discussion of mechanical properties and blasting parameters affecting coating removal.....	135
6.1	Coating system and particle properties	135
6.1.1	Hardness.....	135
6.1.2	Young's Modulus	137
6.1.3	Poisson's ratio.....	138
6.1.4	Yield strength.....	139
6.1.5	Interfacial strength	139
6.2	Effect of incident parameters on coating removal mechanism	140
7.0	Conclusions and Recommendations	142
7.1	Conclusions.....	142
7.1.1	Experimental setup	142
7.1.2	Alkyd paint/steel substrate model system	142
7.1.3	Urethane/epoxy/aluminum model system.....	143
7.1.4	Analytical investigation of erosion by angular particles.....	144
7.1.5	Mechanical properties affecting coating system behaviour.....	146
7.2	Contribution.....	148
7.3	Recommendations	148
Appendices		
A	Computer Program for Experimental Setup	A1
B	Approximate Elastic Stress/Strain Model (Modified Matthewson Analysis)	B1

C	Asymptotic solution of the buckling problem	C1
D	Excel and MathCad spreadsheets used to analyse data.....	D1
D.1	Sample Microsoft Excel experimental data spreadsheet	D1
D.2	Sample of implementation of analysis of Appendix B in a MathCad sheet.....	D2
D.3	Sample of implementation of plastic hole Mathewson analysis in a MathCad sheet	D7
D.4	Sample of implementation of buckling/strain energy release rate calculation in a MathCad sheet.....	D9
D.5	Sample of implementation of rigid-plastic analysis for spherical particles in a MathCad sheet.....	D15
D.6	Sample of implementation of rigid-plastic analysis for symmetric angular particles in a MathCad sheet	D24
	Numbered References.....	R1

List of Figures

Figure 2.1: Experimental setup.....	6
Figure 2.2: Gas gun velocity versus air pressure.....	7
Figure 2.3: Sample image obtained from experimental setup. The images of the 0.64 mm glass particle in flight have been digitally enhanced for clarity. Incident velocity = 53 m/s, incident angle = 57°.	8
Figure 3.1: Impact sites on 40 μm thick alkyd coating, 90° incident angle, incident velocities of: (a) 33 m/s, (b) 50 m/s, (c) 90 m/s.....	13
Figure 3.2: Steel substrate below impact site after removal of 40 μm coating using adhesive tape. 90° incident angle at incident velocities of: (a) 50 m/s, (b) 90 m/s.....	15
Figure 3.3: Variation of impulse ratio with angle of attack for 85 m/s total incident velocity collisions with 40 μm thick coating. Critical impulse ratio of Brach [19] also shown for $e=0$ and $e=1$	17
Figure 3.4: Area of coating removed vs. energy loss due to normal direction effects for coating thickness: Δ - 50 μm , \diamond - 40 μm , \square - 25 μm , \circ - 20 μm	18
Figure 3.5: Area of coating removed vs. energy loss due to tangential direction effects for coating thickness: Δ - 50 μm , \diamond - 40 μm , \square - 25 μm , \circ - 20 μm	19
Figure 3.6: Area of coating removed as a function of incident normal velocity component for coating thickness: Δ - 50 μm , \diamond - 40 μm , \square - 25 μm , \circ - 20 μm	20
Figure 3.7: Energy loss due to normal and tangential direction effects normalised by total incident kinetic energy as a function of incident angle of attack. Normal energy loss for coating thickness and total incident velocity: Δ - 50 μm thick coating, 80 m/s, $=$ - 40 μm , 85 m/s, \diamond - 40 μm , 56 m/s, \square - 25 μm , 42 m/s, \circ - 20 μm , 57 m/s. Tangential energy loss for coating thickness and total incident velocity: \blacktriangle - 50 μm , 80 m/s, $=$ - 40 μm , 85 m/s, \blacklozenge - 40 μm , 56 m/s, \blacksquare - 25 μm , 42 m/s, \bullet - 20 μm , 57 m/s.....	21
Figure 3.8: Average area of coating removed as a function of incident angle of attack for different ranges of incident total velocity and coating thickness. Data points represent averages of area removal measurements at each angle. \square - 55-62 m/s, 40 μm , \diamond - 81-90 m/s, 40 μm , Δ - 78-81 m/s, 50 μm , \circ - 102-108 m/s, 50 μm	22
Figure 3.9: Area of paint removed as a function of incident angle of attack for different ranges of incident total velocity and coating thickness. Data points represent averages of area removal measurements at each angle. \bullet - 38-44 m/s, 25 μm , \square	

- 25-27 m/s, 25 μm , Δ - 102-110 m/s, 25 μm , \circ - 54-62 m/s, 20 μm , \blacktriangle - 25-30 m/s, 20 μm .	23
Figure 3.10: Impact near a free edge for a 40 μm thick coating. Note the attached paint in the shape of the original free edge.	26
Figure 3.11: Geometry of indentation of coating (thickness h) on rigid substrate by a sphere of radius R .	28
Figure 3.12: Variation of coefficient of restitution, e , with area of coating removed for coating thickness: Δ - 50 μm , \diamond - 40 μm , \square - 25 μm , \circ - 20 μm .	32
Figure 3.13: Variation of coefficient of restitution, e , with incident kinetic energy in normal direction for coating thickness: Δ - 50 μm , \diamond - 40 μm , \square - 25 μm , \circ - 20 μm , --- - bare steel.	33
Figure 3.14: Coefficient of restitution as a function of incident normal velocity for 40 μm thick coating. \diamond -experimental data, \square - predicted using plastic analysis for incident portion and elastic analysis for rebound portion.	34
Figure 3.15: Energy loss due to normal direction effects vs. normal incident kinetic energy. Equations shown are linear regression curve fits. \diamond - 40 μm coating, \square - bare steel.	35
Figure 3.16: Area of coating removed vs. energy lost to coating for coating thickness: Δ 50 μm , \times 40 μm , \diamond 25 μm , \square 20 μm . Best linear fit lines: --- 50 μm , -- - 40 μm , --- 25 μm , --- 20 μm .	36
Figure 3.17: Possible equilibrium paths for an axially compressed flat plate.	39
Figure 3.18: Clamped-pinned annular plate configuration used in buckling analysis.	41
Figure 3.19: Configuration of impact site, (a) unbuckled, (b) buckled. Force, P , and moment, M , reactions in coating at edge of delamination ($r = a$).	50
Figure 3.20: Calculation of indentation volume, V_o , and radius, b , at which coating is prevented from buckling due to presence of indenting particle: (a) penetration of particle to coating/substrate interface. (b) penetration of particle into substrate.	57
Figure 3.21: Impact site for irregular glass particle launched at 42 m/s and normal incidence.	66
Figure 4.1: WYKO three-dimensional profile of impact site for normal incidence and 55 m/s incident velocity.	69
Figure 4.2: Rebound angle versus incident angle. Total incident velocity = 55m/s. \times - measured values, Δ - predicted values using present elastic-plastic analysis, \square - predicted values using fully-plastic model [24]. Error bars representing ± 1	

standard deviation in the five trials for each data point, are so close that they are overlaid by the data symbols, and thus are omitted here. All three symbols overlaid each other at 90° incident angle. 70

Figure 4.3: Rebound velocity versus incident angle. Total incident velocity = 55 m/s. X - measured values, Δ - predicted values using present elastic-plastic analysis, □ - predicted values using fully-plastic model [24]. Error bars represent ± 1 standard deviation in the five trials for each experimental data point. 71

Figure 4.4: Maximum length of impact crater versus incident angle. Total incident velocity = 55 m/s. X - measured values, Δ - predicted values using present elastic-plastic analysis, □ - predicted values using fully-plastic model [24]. Error bars represent ± 1 standard deviation in the five trials for each experimental data point. 72

Figure 4.5: Maximum depth of impact crater versus incident angle. Total incident velocity = 55 m/s. X - measured values, Δ - predicted values using present elastic-plastic analysis, □ - predicted values using fully-plastic model [24]. Error bars represent ± 1 standard deviation in the five trials for each experimental data point. 73

Figure 4.6: Measured crater volume versus incident angle. Error bars represent ± 1 standard deviation in the five trials for each data point. 74

Figure 4.7: Crater definition (not to scale). 75

Figure 4.8: Two-dimensional cross section of profile shown in Figure 4.1 taken at centre of impact site. Vertical bars indicate where crater length was measured. 75

Figure 4.9: Assumed (elastic-plastic), actual (elastic-plastic), and fully plastic curves of: (a) force-deflection, and (b) mean pressure-deflection. 76

Figure 4.10: Fully-plastic analysis of impacting spheres: (a) when crater is in full contact with sphere, and (b) when crater loses full contact with sphere 79

Figure 4.11: Geometry of assumed reversible rebound process. 84

Figure 5.1: Definition of Euler Angles, θ , ψ , ϕ , inertial (X,Y,Z), and body fixed (x,y,z) co-ordinates systems used in general analysis. Co-ordinate system (x',y',z') is attached to the centre of mass (CM), and remains parallel to the (X,Y,Z) axis. 92

Figure 5.2: Surface area element dA, and projected surface area element dA_p. Z = 0 represents the surface of the target. 94

Figure 5.3: Co-ordinate system definitions used for specific case of symmetric particles of side length h. 97

Figure 5.4: Previous crater profile (1,2,3...), current crater profile (1',2',3'...) and force application intervals for the next time step. 104

Figure 5.5: Points (Y_L^N, Z_L^*) , (Y_L^*, Z_L^N) , (Y_R^N, Z_R^*) , and (Y_R^*, Z_R^N) used to determine whether given nodes (Y_L^N, Z_L^N) and (Y_R^N, Z_R^N) are inside or outside of particle surface.....	107
Figure 5.6: Crater Volume vs. Incident Velocity for different initial particle orientations, θ_i (Figure 5.3). Predictions of model with angle of attack $\alpha = 30^\circ$, angularity, $A = 45^\circ$, dynamic hardness $p_d = 4$ GPa, friction coefficient, $\mu = 0$ shown as solid lines. Experimental data of Hutchings [7] for $8 \times 8 \times 1.5$ mm thick steel plates impacting steel targets for $\theta_i = 0^\circ, 10^\circ, 25^\circ$ shown as dots.....	110
Figure 5.7: Energy Loss vs. Incident Velocity for different initial particle orientations, θ_i (Figure 5.3). Predictions of model with angle of attack $\alpha = 30^\circ$, angularity $A = 45^\circ$, dynamic hardness $p_d = 4$ GPa, friction coefficient $\mu = 0$ shown as solid lines. Experimental data of Hutchings [7] for $8 \times 8 \times 1.5$ mm thick steel plates impacting steel targets for $\theta_i = 0^\circ, 10^\circ, 25^\circ$ shown as dots.....	110
Figure 5.8: Rotational Energy vs. Incident Velocity for different initial particle orientations, θ_i (Figure 5.3). Predictions of model with angle of attack $\alpha = 30^\circ$, angularity $A = 45^\circ$, dynamic hardness $p_d = 4$ GPa, friction coefficient $\mu = 0$ shown as solid lines. Experimental data of Hutchings [7] for $8 \times 8 \times 1.5$ mm thick steel plates impacting steel targets for $\theta_i = 0^\circ, 10^\circ, 25^\circ$ shown as dots.....	111
Figure 5.9: Particle trajectories at $4 \mu\text{s}$ intervals, obtained with model for $\pi_1 = 12.8$, and angularity, A , incident angle, α , initial orientation, θ_i , and particle side length, h , of: (a) $30^\circ, 15^\circ, 27^\circ, 8.6$ mm (b) $30^\circ, 45^\circ, 0^\circ, 8.6$ mm, (c) $45^\circ, 25^\circ, 37^\circ, 8.0$ mm (d) $45^\circ, 25^\circ, 20^\circ, 8.0$ mm. A solution time step of $0.2 \mu\text{s}$ was used in all cases...	115
Figure 5.10: Particle trajectories at $4 \mu\text{s}$ intervals, obtained with model for $\pi_1 = 12.8$, and angularity, A , incident angle, α , initial orientation, θ_i , and particle side length, h , of: (a) $60^\circ, 25^\circ, 55^\circ, 8.6$ mm (b) $60^\circ, 25^\circ, 20^\circ, 8.6$ mm (c) $80^\circ, 25^\circ, 75^\circ, 13.7$ mm (d) $80^\circ, 25^\circ, 9^\circ, 13.7$ mm. A solution time step of $0.2 \mu\text{s}$ was used in all cases.....	116
Figure 5.11: Crater profiles obtained with model corresponding to impacts shown in Figure 5.9.....	117
Figure 5.12: Crater profiles obtained with model corresponding to impacts shown in Figure 5.10.....	118
Figure 5.13: Dimensionless crater volume, π_2 , as a function of initial orientation, θ_i , for square particles impacting a frictionless target at angle of attack, $\alpha = 25^\circ$ and π_1 equal to: \bullet 7, \blacksquare 12.8, \blacktriangle 21.4, \circ 25, \square 51, \triangle 205.....	119
Figure 5.14: Dimensionless crater volume, π_2 , as a function of initial orientation, θ_i , for square particles impacting a frictionless target at angle of attack, $\alpha = 45^\circ$ and π_1 equal to: \bullet 7, \blacksquare 12.8, \blacktriangle 21.4, \circ 25, \square 51, \triangle 205.....	119

Figure 5.15: Dimensionless crater volume, π_2 , as a function of initial orientation, θ_i , for square particles impacting a frictionless target at angle of attack, $\alpha = 85^\circ$ and π_1 equal to: \bullet 7, \blacksquare 12.8, \blacktriangle 21.4, \circ 25, \square 51, \triangle 205.....	120
Figure 5.16: Dimensionless crater volume, π_2 , as a function of initial orientation, θ_i , for particles impacting a frictionless target at angle of attack, $\alpha = 5^\circ$ and π_1 fixed at two values: $\pi_1 = 12.8$ and A values: \blacktriangle 80° , \bullet 60° \blacksquare 45° , \blacktriangledown 30° , \bullet 10° . $\pi_1 = 21.9$, A values: \triangle 80° , \diamond 60° , \square 45° , \blacktriangledown 30° , \circ 10°	122
Figure 5.17: Dimensionless crater volume, π_2 , as a function of initial orientation, θ_i , for particles impacting a frictionless target at angle of attack, $\alpha = 25^\circ$ and π_1 fixed at two values: $\pi_1 = 12.8$ and A values: \blacktriangle 80° , \bullet 60° \blacksquare 45° , \blacktriangledown 30° , \bullet 10° . $\pi_1 = 21.9$, A values: \triangle 80° , \diamond 60° , \square 45° , \blacktriangledown 30° , \circ 10°	123
Figure 5.18: Dimensionless crater volume, π_2 , as a function of initial orientation, θ_i , for particles impacting a frictionless target at angle of attack, $\alpha = 45^\circ$ and π_1 fixed at two values: $\pi_1 = 12.8$ and A values: \blacktriangle 80° , \bullet 60° \blacksquare 45° , \blacktriangledown 30° , \bullet 10° . $\pi_1 = 21.9$, A values: \triangle 80° , \diamond 60° , \square 45° , \blacktriangledown 30° , \circ 10°	123
Figure 5.19: Dimensionless crater volume, π_2 , as a function of initial orientation, θ_i , for particles impacting a frictionless target at angle of attack, $\alpha = 65^\circ$ and π_1 fixed at two values: $\pi_1 = 12.8$ and A values: \blacktriangle 80° , \blacklozenge 60° \blacksquare 45° , \blacktriangledown 30° , \bullet 10° . $\pi_1 = 21.9$, A values: \triangle 80° , \diamond 60° , \square 45° , \blacktriangledown 30° , \circ 10°	124
Figure 5.20: Dimensionless crater volume, π_2 , as a function of initial orientation, θ_i , for particles impacting a frictionless target at angle of attack, $\alpha = 85^\circ$ and π_1 fixed at two values: $\pi_1 = 12.8$ and A values: \blacktriangle 80° , \bullet 60° \blacksquare 45° , \blacktriangledown 30° , \bullet 10° . $\pi_1 = 21.9$, A values: \triangle 80° , \diamond 60° , \square 45° , \blacktriangledown 30° , \circ 10°	124
Figure 5.21: Dimensionless crater volume, π_2 , as a function of initial orientation, θ_i , for particles impacting a target having friction coefficient, $\mu = 0.1$ at an angle of attack, $\alpha = 5^\circ$ and $\pi_1 = 12.8$. Angularity, A values: \blacktriangle 80° , \bullet 60° \blacksquare 45° , \blacktriangledown 30° , \bullet 10°	128
Figure 5.22: Dimensionless crater volume, π_2 , as a function of initial orientation, θ_i , for particles impacting a target having friction coefficient, $\mu = 0.1$ at an angle of attack, $\alpha = 45^\circ$ and $\pi_1 = 12.8$. Angularity, A values: \blacktriangle 80° , \bullet 60° \blacksquare 45° , \blacktriangledown 30° , \bullet 10°	129
Figure 5.23: Dimensionless crater volume, π_2 , as a function of initial orientation, θ_i , for particles impacting a target having friction coefficient, $\mu = 0.1$ at an angle of attack, $\alpha = 85^\circ$ and $\pi_1 = 12.8$. Angularity, A values: \blacktriangle 80° , \bullet 60° \blacksquare 45° , \blacktriangledown 30° , \bullet 10°	131
Figure B.1: Stresses acting on an element of the coating	B2

Figure C.1: Buckling parameters C_1 -●, and C_2 -■ as a function of $p = b/a$ C5
Figure C.2: Buckling parameters $C_2/2C_1$ -●, and α_B -■ as a function of $p = b/a$ C10

List of Tables

Table 3.1: Comparison of coating area removed keeping normal component of velocity constant, while varying tangential component of velocity.....	24
Table 3.2: Experimentally determined incident velocity and kinetic energy required to remove coating, and resulting dynamic hardness for different impacting particles and coating thickness.....	29
Table 3.3: Comparison of predicted and measured contact diameters for 40 μm thick coating impacted by glass sphere ($R=0.32$ mm, $m=0.364$ mg) using plastic flow model with dynamic harness, $p_d=190$ MPa	30
Table 3.4: Comparison of predicted velocity ($p_d = 190$ MPa) to cause penetration of coating to steel substrate, and measured velocity at onset of coating removal.	31
Table 3.5: Experimentally determined arrest strain energy release rates (G_c) and phase angles (ψ) for glass and steel spheres impacting alkyd coatings of varying thickness. h = coating thickness, N = number of experiments performed, V_n = normal component of incident velocity, α = incident angle of attack, Average a = average delamination radius, b = radius at which coating is prevented from deflecting due to presence of particle, V_c = critical indentation volume to cause buckling, V_o = calculated indentation volume.....	59
Table 3.6: Comparison of measured and predicted delamination radii for last eleven data points of Table 3.5.....	62
Table 3.7: Nominal interfacial shear stress at the edge of the ‘plastic hole’ using analysis explained in Section 3.5.3 and Reference [48]	63
Table 5.1: Average value of π_2 for all cases in Figure 5.16-Figure 5.20.....	127

Nomenclature

Due to the large number of variables used in this thesis, and the author's wish to comply with the standard conventions used in the literature, it was necessary to occasionally use the same variable in different contexts. To avoid confusion, the nomenclature has been divided into that used in each chapter.

Chapter 3

a.....	delamination radius (or size of buckled plate)
$A(r) - E(r)$	functions used in power expansion of displacements for Matthewson analysis
A_1, B_1, \dots	integration constants used in buckling analysis
b	inner radius to which buckling is prevented
c.....	contact radius between particle and coating
C_1, C_2	buckling parameters
D.....	flexural rigidity of coating
d	indentation depth of impacting particle
D^*	differential operator used in Matthewson and modified Matthewson analyses
e.....	coefficient of restitution
E.....	Young's modulus of coating
F	normal contact force applied to particle
$F(c)$	normal contact force in Matthewson analysis
$f(r)$	spherical indenter profile used in Matthewson analysis
$F_m(c)$	normal contact force in modified Matthewson analysis
$f_m(r)$	spherical indenter profile used in modified Matthewson analysis
g.....	Euler's constant (≈ 0.577)
G.....	strain energy release rate
G^*	shear modulus of coating
H.....	argument of integral used in potential energy calculation in buckling analysis

h thickness of coating
 $I_i(x), J_i(x), Y_i(x), K_i(x)$ Bessel functions of order i
 J_B strain energy of bending for buckling analysis
 J_E strain energy of stretching for buckling analysis
 J_L work done by force P in buckling analysis
 $K^{[1]}, K^{[2]}$ real and imaginary parts of (interfacial) complex stress intensity factor
 k_1, k_2, k_3, c_1, c_2 integration constants for buckling analysis
 $L(r), N(\gamma r), I(r)$ variables representing certain integrals used in buckling analysis
 l, L reference lengths for complex stress intensity factor
 m mass of particle
 $M(r)$ bending moment in buckled plate
 N number of experiments performed at particular impact condition
 P applied load per unit circumference for buckling analysis
 p ratio of b to a
 p^C critical buckling load
 p_d dynamic hardness or mean contact pressure
 R radius of impacting particle
 s perturbation parameter used in buckling analysis
 T_L^n normalised kinetic energy loss due to normal direction effects
 T_L^t normalised kinetic energy loss due to tangential direction effects
 $u^F(r)$ in-plane displacement in unbuckled configuration
 $u_M(r,z), v_M(r,z)$ r and z direction displacements used in Matthewson and modified Matthewson analyses
 V potential energy of buckled plate
 $v(r)$ in-plane change in displacement due to buckling
 V_C critical indentation volume to cause buckling of plate
 v_i incident velocity of particle
 V_o indentation volume
 $w(r)$ out-of-plane displacement in buckled configuration
 Z_i combination of Bessel functions of order i used in buckling analysis

α	incident angle of attack
α^*	parameter used in determination of $F(c)$
α_D, β_D	Dundur's parameters
α_m^*, β_m	parameters used in determination of $F_m(c)$
α_B	slope of buckled path
χ	parameter used in calculation of τ in plastic hole Matthewson analysis
δh	pile-up of coating adjacent to coating
$\overline{\epsilon_r}, \overline{\epsilon_\theta}, \overline{\epsilon_z}$	r, θ , and z direction average strains for Matthewson and modified Matthewson analyses
Δ	displacement induced at edge of buckling plate due to indentation volume
Δ_c	critical edge plate displacement to cause buckling
ϵ	parameter describing oscillating singularity in complex stress intensity factor
$\epsilon_r, \epsilon_\theta$	strain in radial and tangential directions in buckling analysis
γ	parameter for determining P^C
γ_{rz}	shear strain in coating (Matthewson and modified Matthewson analyses)
K_C, K_S	parameters used in calculation of Dundur's parameters
λ	the ratio of the particle radius squared to the radius of gyration of the particle squared
μ	impulse ratio
μ_c	critical impulse ratio
μ_C, μ_S	shear modulus of coating, and substrate, respectively
ν	Poisson's ratio of coating
$\overline{\sigma_r}, \overline{\sigma_\theta}, \overline{\sigma_z}$	r, θ , and z direction average stresses for Matthewson and modified Matthewson analyses
σ	compressive biaxial stress in plate
σ_{12}, σ_{22}	shear and normal stresses ahead of interfacial crack tip

σ_c	critical compressive stress to cause buckling
τ	shear stress at coating/substrate interface at contact radius for plastic hole Matthewson analysis
$\tau_1(r)$	shear stress at coating/substrate interface for Matthewson and modified Matthewson analyses
ω	angle describing elastic mismatch in phase angle calculations
ψ	mode-mix phase angle
Ψ	parameter describing γ -b relationship for buckling analysis
$\zeta(r)$	slope of buckled plate

Chapter 4

c	contact radius between particle and target
d	indentation depth of impacting particle
d_{elastic}	indentation depth to which energy can of indentation can be fully recovered
d_{final}	final relaxed indentation depth after spring back of target
d_{max}	maximum indentation depth reached (elastic and plastic)
h	thickness of coating
h^*	final coating thickness at bottom of crater used in elastic-plastic analysis
m	mass of impacting particle
P	normal contact force applied to particle
p_d	dynamic hardness or mean contact pressure
R	radius of impacting particle
v_i	incident velocity of particle
γ	angle used in fully-plastic theory of impact
μ	friction coefficient between target and particle
σ_1, σ_3	maximum and minimum elastic principal stresses at the onset of yield used in Tresca criterion

σ_y yield stress of coating

Chapter 5

A..... angularity of the particle

b_L, b_R Z intercept of left and right sides of the particle, respectively

CM..... centre of mass of the particle

dA contact surface area element

dA_p projection of contact surface area element on X, Y plane

dS surface differential element

E..... kinetic energy of the particle

$f(x,y)$ function describing particle surface in body-fixed frame of reference

F_X, F_Y, F_Z inertial X, Y, and Z components of the total contact force

$F_{Y_L}, F_{Y_R}, F_{Z_L}, F_{Z_R}$ normal forces in the Y and Z directions acting on the left and right side of the particle

$g(X,Y)$ function describing particle surface in inertial frame of reference

$G(X,Y,Z)$ alternate representation of particle surface in inertial frame of reference

h..... length of a side of the particle

I_x^P, I_y^P, I_z^P principle moments of inertia

I_x moment of inertia of symmetric particle

m..... mass of the particle

m_L, m_R slope of left and right sides of the particle, respectively

M_{X_L}, M_{X_R} moments in the X direction acting on left and right sides of the particle, respectively

M_x, M_y, M_z body-fixed x, y, and z components of the total moment on the particle

p_d dynamic hardness of target material

P_X, P_Y, P_Z inertial frame X, Y, and Z components of the normal contact force

q_i generalised co-ordinates

Q_i generalised forces

Q_θ, Q_ϕ, Q_ψ $\theta, \phi,$ and ψ components of the generalised force

\bar{t}_L, \bar{t}_R	unit vectors along the surfaces of the particle
T_X, T_Y, T_Z	inertial frame X, Y, and Z components of the friction force
$T_{Y_L}, T_{Y_R}, T_{Z_L}, T_{Z_R}$	inertial frame Y and Z components of the friction force acting on left and right portions of the contacting particle
v_i	incident velocity of particle
x, y, z	body-fixed co-ordinate system
x', y', z'	co-ordinate system fixed at centre of mass and remaining parallel to inertial co-ordinate system
X, Y, Z	inertial co-ordinate system
X_0, Y_0, Z_0	inertial co-ordinates of the centre of mass of the particle
x_f, y_f, z_f	body-fixed co-ordinates of a point of application of a load
Y^*	inertial Y-co-ordinate of projection of a node on the particle surface
Y_I, Z_I	inertial co-ordinate of left vertex of particle
Y_{II}, Z_{II}	inertial co-ordinate of middle vertex of particle
Y_{III}, Z_{III}	inertial co-ordinate of right vertex of particle
Y^N, Z^N	inertial co-ordinates of a node on the crater profile
α	incident angle of attack
θ, ψ, ϕ	Euler angles describing orientation of particle
θ_i	initial orientation angle
$\omega_x, \omega_y, \omega_z$	components of angular velocity with respect to the inertial frame of reference along instantaneous directions of body-fixed axes

Acknowledgements

I would like to thank my supervisor, Dr. Jan Spelt for his guidance, support, and generosity through my whole academic career. His balance of intelligence, friendliness and authority make him the ideal supervisor. I consider myself extremely lucky to have had such a long and fruitful relationship with Jan.

Thanks are also due to all my friends and colleagues in the lab over the years. Everyone has helped me at one time or another, and I would like to thank in particular Goran Fernlund for his clear explanations in our discussions of fracture mechanics. Thanks are also due to Jaleel Moidu who helped with the ultrasonic characterisation of the coating systems, and Vaheed Safavi-Ardebili for his insight into wave behaviour.

I would like to thank the Manufacturing Research Corporation of Ontario, the Natural Sciences and Engineering Research Council of Canada, and the University of Toronto for financial support. I would also like to thank Valspar Inc., in particular Mr. Denis Johnston, and the Canadian Department of National Defence for providing the paint samples and valuable technical advice.

Finally, I would like to thank Elsevier Science for permission to reproduce references [1], [9], and [10].

Chapter 1

Introduction

Organic coatings are often removed using solvents that create waste that is difficult and expensive to dispose of. For this reason, mechanical coating removal techniques such as blast cleaning are of increasing interest. In the blast cleaning process, a stream of particles is directed towards the coated substrate, and the coating is removed by mechanical means. Typical blasting media includes wheat starch, cornstarch, walnut shells, glass, plastic, steel, ceramic, and dry ice, in both granular and spherical form. The media is normally launched at high speed using either compressed air or blasting wheels, in which particles are accelerated by the centripetal force created by a rapidly spinning wheel. In small-scale applications, the media is blasted manually by a single operator using commercially available blasting equipment, but, in the aerospace industry where paint stripping of full-scale aircraft is necessary, robotic strippers have been developed. Besides coating removal, other applications of blast cleaning include the removal of adhesive flash and the cleaning of various types of processing equipment. In many blast cleaning situations, it is desired to remove the coating while leaving the underlying substrate unchanged.

1.1 Motivation

The use of blast cleaning to remove organic coatings involves a large number of parameters that can be varied to affect removal efficiency for a specific coating. These include: particle material, size, shape, moisture content, and orientation, incident velocity and angle of attack, standoff distance and dwell time. The fundamental mechanisms of coating removal

have not been established, and, as a result, the choice of these parameters for a specific coating/substrate system, is, for the most part, governed by trial-and-error and rules of thumb. This thesis is thus motivated by a need for a fundamental understanding of the underlying mechanisms that govern coating removal so that an optimal choice of blasting media and parameters can be made.

1.2 Thesis Objectives

Although multiparticle interactions, the spread of the particle streams, and the distribution of particle sizes and shapes will have a significant effect on coating removal during the blast cleaning process, a single particle study serves as a logical first step to understanding the fundamentals of coating removal. The aim of this thesis is to eliminate some of the guesswork involved in the choice of particle and blasting parameters by identifying and modelling the fundamental mechanisms of coating removal using blast cleaning for some typical coating/substrate systems. The specific objectives were:

- To construct an experimental apparatus capable of launching single particles at coated substrates at typical blast cleaning velocities, measuring the energy lost in the collision, and quantitatively assessing the damage done to the coating.
- To characterise the behaviour of typical coating/substrate systems with respect to energy loss when impacted by single particles of different sizes and shapes, and to correlate the energy loss with coating removal, thereby determining the blasting parameters that are most important for maximising coating removal.
- To identify the fundamental mechanisms (i.e. ploughing, cutting, fracture/delamination) of coating removal for the typical model coating/substrate systems.
- To develop analytical techniques to predict the amount of coating removed as a function of the process parameters and particle material properties so that the process can be optimised.

1.3 Thesis Organisation

The thesis is divided into seven chapters. Chapter 2 describes the apparatus constructed and used for the single-particle collision experiments.

In Chapter 3, the impact behaviour of an alkyd coating/steel substrate model system is analysed. The relevant background is discussed, the model system is described in detail, and the impact behaviour is characterised qualitatively. Alternate possible removal mechanisms are evaluated. An analysis capable of predicting the amount of coating removed for single spherical particles impacting the model system is then presented and experimentally verified.

Chapter 4 deals with the impact behaviour of another model system consisting of a urethane coating on an epoxy-primed aluminum substrate. The relevant background is discussed, and an analysis capable of predicting the size of craters left by impacts of single spherical particles is presented and experimentally verified.

In Chapter 5, a generally applicable analytical model of the impact of angular particles on eroding substrates is presented. A specific case, that of symmetric angular particles, is discussed in detail, and comparisons with experimental data in the literature are made. A parametric study of the effect of various incident parameters on crater size and shape is then undertaken, and conclusions with respect to maximising crater size are drawn.

In Chapter 6, the differences between the two major types of model systems discussed in Chapters 3 and 4 are identified, and suggestions are given for maximising removal in multiparticle applications, and, conversely, for improving coating erosion resistance.

In Chapter 7, the conclusions and recommendations are given.

Chapter 2

Experimental Apparatus

This chapter describes the experimental apparatus used in investigating the collision of single particles with various coated targets. First, a brief background in erosion rigs and particle velocity measurements is presented, and then a detailed description of the apparatus designed and constructed for the present study is given. The description of the experimental setup has already been published elsewhere [1].

2.1 Background

In order to characterise the erosion of both coatings and bare substrates, many investigators have designed various types of erosion rigs and gas guns. For example, Hutchings and Winter [2] have designed a gas gun that uses a reservoir full of either helium or nitrogen, and is triggered by the bursting of two diaphragms. The single particles are placed in polythene sabots that are stopped at the end of the barrel, yielding speeds of up to 600 m/s. The performance of this gun under different operating pressures and fluids was evaluated and compared to theory. Graham et al. [3] built an erosion test facility based on exploding aluminum foils that propel single particles in the size range 100-8000 μm at velocities ranging from 250-7000 m/s. Hutchings et al. [4] have designed a gun with a rectangular bore capable of launching 0.5 g particles at speeds of 300 m/s. The gun uses a solenoid valve to release a compressed gas into a barrel, and the rectangular bore ensures that the particles are launched without rotation. Sundararajan and Shewmon [5] have used helium as the accelerating fluid and a solenoid valve as the trigger in order to launch 4.76 mm steel spheres at speeds of up to 200

m/s. A theoretical and experimental study of the effect of valve opening times on the performance of gas guns can be found in the paper by White and Fowles [6].

To measure the speeds of the incident particles, experimenters have typically either used photodiodes and timers [5] or high speed photography [7]. The measurement of rebound velocity is particularly difficult, given the uncertainty in the rebound trajectory the particle will take. Sundararajan and Shewmon [5] have used two pieces of aluminum foil connected to timers to deduce this velocity. The aluminum foil was placed in the vicinity of the anticipated rebound trajectory, and allowed to be pierced by the rebounding particles. The holes left behind in the aluminum were used to trace the rebound trajectory.

2.2 Gas gun/high speed flash setup

Collisions between single particles and bare substrates are normally characterised in terms of energy losses and coefficients of restitution. A similar approach was utilised in this study to build an experimental database for collisions between various particles and some typical coating/substrate systems. In order to do this, a gas gun/high speed photographic setup was designed and constructed with the following design criteria:

- (a) single particles (50-2000 μm typical size) were to be launched at realistic blasting speeds (approximately 120 m/s)
- (b) the apparatus had to be capable of measuring the incident and rebound velocities (both direction and magnitude) so that the energy loss in the collision could be determined
- (c) the apparatus had to be capable of quantifying the amount of coating damage and/or removal
- (d) some level of automation had to be built in so that these measurements could be made quickly and accurately

Figure 2.1 shows the gas-gun/high-speed photographic setup designed and built for the present study [1]. A single particle was loaded into a cylindrical urethane sabot (6.3 mm diameter and 10 mm length) which was, in turn, loaded into a 6.3 mm inner diameter, 50 cm

long steel barrel via a breech. The target specimens (30 mm x 30 mm) were clamped onto the specimen holder which consisted of a 9 mm thick piece of steel. The specimen holder was pivoted in a clevice, which allowed rotation to any incident impact angle. The clevice, in turn, was clamped to a long steel rod permitting adjustments in the height of the target.

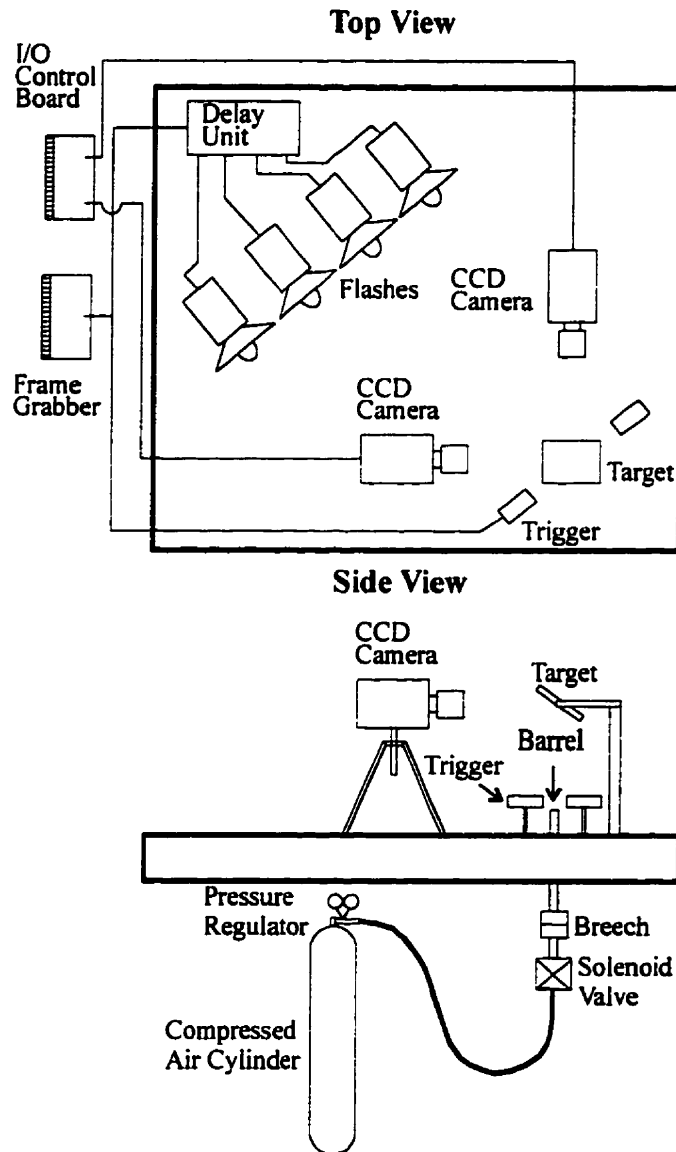


Figure 2.1: Experimental setup.

The barrel/breech was attached to a solenoid valve, which was, in turn connected to a compressed air cylinder. The fast-acting solenoid valve (Model 73216 BN2MT00, Honeywell) permitted a burst of compressed air to accelerate the urethane sabot and the blasting particle to the end of the barrel where a urethane ring stopped the sabot, but allowed the glass sphere to exit. A series of holes drilled at the top of the barrel relieved the pressure behind the sabot as it stopped, and minimised the amount of air exiting the end of the barrel with the particle.

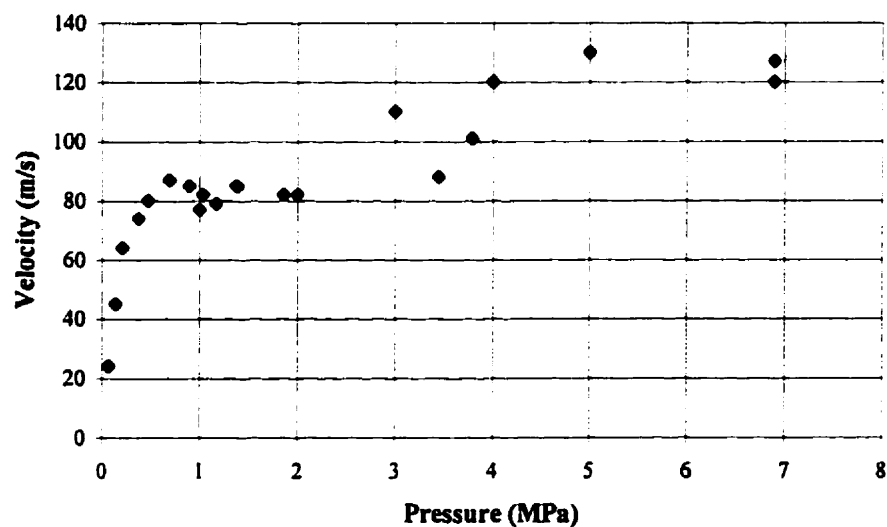


Figure 2.2: Gas gun velocity versus air pressure.

It was found that the speed of the particles exiting the barrel was independent of the size, density and shape of the particles when tested with angular and spherical glass, plastic, and steel in the diameter range 0.1 to 1 mm. This was because the mass of the particles was very small compared to that of the sabot. The pressure/velocity curve for this gas gun can be found in Figure 2.2, and, as can be seen, the velocity levels out somewhat after 1 MPa. This is probably due to the high pressure air escaping around the sabot as it is accelerated up the barrel. For a discussion of gas gun design, including the use a different gas, faster opening valve, and longer barrel to increase velocity, see Reference [8].

Two cameras (black and white CCD cameras, not special field-on-demand) were used to obtain images in perpendicular planes, thereby allowing a verification that the rebound and

incident velocity vectors were in a single plane. A true colour RGB frame grabber (Occulus TCX, Coreco Inc.) was used with the two cameras connected to two of the three channels. The frame grabber continuously grabbed frames at the rate of 60 Hz, continuously overwriting its frame buffer. Because the collisions were expected to last on the order of hundreds of microseconds, it was only necessary to have the setup determine which of the frames was the frame of interest (i.e. the frame in which the collision occurred), and then the continuous grab could be terminated with the frame of interest in the frame grabber buffer.



Figure 2.3: Sample image obtained from experimental setup. The images of the 0.64 mm glass particle in flight have been digitally enhanced for clarity. Incident velocity = 53 m/s, incident angle = 57°.

An infrared trigger mounted at the end of the barrel (VIS II, Optikon Inc.) sensed the particles as they left the barrel, and sent a signal to an I/O board (Opto 22 PB8) attached to the computer and to a delay generator. The I/O board was connected to the frame grabber and the frame grab sequence was terminated upon triggering. The trigger also caused the delay unit to generate pulses to trigger four high-speed flashes (flash duration $\cong 0.5 \mu\text{s}$) mounted near the target at adjustable delays (1 μs minimum). Because the CCD cameras are essentially light integrators, summing all the light that reaches their sensor in one frame, a trajectory of the particle (four images) appeared on the grabbed frame. The delays were timed so that two

images of the particle were just before collision, and two just after collision. A sample image obtained with this apparatus appears in Figure 2.3.

By using image analysis software (Image Pro Plus, Media Cybernetics Inc.), the precise distance between successive particle images (i.e., the distance the particle travelled between flashes) and the incident and rebound angles were measured. This distance divided by the delay between flashes gave the incident and rebound velocities of the particle. Measurements of velocity obtained in this manner are estimated (based on a worst case calculation of the error in velocity associated with a one pixel in each direction error in the determination of the position of the particle images) to be no greater than 5%. The computer program written to control and automate the frame-grabbing/flash triggering can be found in Appendix A. The data obtained from runs of this program was linked to a Microsoft Excel spreadsheet to facilitate calculations, and an example appears in Appendix D.

Chapter 3

Alkyd Coating/Steel Substrate System

This chapter will focus on the first of the two coating/substrate systems tested, the alkyd/steel system. First, a survey of the relevant literature regarding the analysis of the blast cleaning process and solid particle erosion is presented. Then, a description of the alkyd/steel system is given, followed by a description of the experiments and results. Experimental observations and arguments leading to the conclusion that the coating delaminates due to impact-induced buckling are then presented. Finally, an analytical method is presented for prediction of the amount of coating removed for glass and steel spheres impacting the model coating. Much of the material in this chapter has been previously published [1, 9, 10].

3.1 Background

Previous research related to blast cleaning is mostly of an empirical nature and very specific to particular systems [11, 12, 13]. Other useful literature can be found in the contact mechanics literature, and in the field of solid particle erosion of bare substrates. The following is a description of some of the more interesting papers that can be found.

Finnie did some of the early fundamental work on the theory of a particle cutting a substrate [14]. In Finnie's original method, the equations of motion of a particle were obtained by a simplified analysis, which considered the forces at the tip of a cutting particle to be constant. The resulting equations could be solved in closed form and estimates of crater volume and rebound parameters could then be made.

A book by Johnson provides an excellent introduction to contact mechanics, containing solutions for elastic collisions between particles and substrates [15], and for static contact

analysis of elastic layers on semi-infinite substrates [16]. Ramamurthy et. al. [17, 18] have modelled the removal of chips of paint on automobiles due to stone impacts using shock physics and finite element models of wave propagation. Brach has developed a very simple method for characterising collisions of single particles with uncoated substrates in terms of energy losses, the coefficient of restitution, and the ratio of normal to tangential impulse [19]. Matthewson [20] has developed an asymptotic solution for the static indentation of an elastic layer on a semi-infinite substrate that includes the calculation of interfacial shear stress. Rossikhin and Shitikova [21] have recently developed a wave propagation model of the impact of a rigid sphere with an elastic layer based on ray methods. Lu [22] has provided valuable observations of indentation cracks in coating/substrate systems, and has proposed a method to determine the crack paths. Diah and Williams [23] have studied the impact behaviour of paints and developed methods for the experimental determination of material properties under impact conditions.

Estimates of crater volume and rebound parameters can be obtained, in certain cases, by use of a rigid-plastic theory in which the target is assumed to be fully plastic, and the particle non-deforming. The force resisting indentation is characterised by a dynamic hardness of the target equal to the resisting force divided by the instantaneous contact area. Because the contact area is a function of time, and the resisting force was assumed perpendicular to the contact area, both the magnitude and direction of the resisting force were a function of time, and the resulting equations of motion for the particle had to be solved numerically in time steps. The groundwork for this approach was laid by Hutchings et. al. [7, 24, 25, 26] and variations of the same idea were presented by other authors [27, 28, 29, 30, 31].

An excellent review of the solid particle erosion of coatings can be found in the paper by Shipway and Hutchings [32]. The paper also outlines a method for describing coating erosion in terms of a critical dose of particles of a particular size and shape needed to remove a coating.

3.2 Model system

The first model system investigated was typical of a class of relatively soft coatings on rigid substrates, and was a test system used at the laboratories of Valspar Inc. The system

consisted of Valspar Inc. alkyd enamel of various thicknesses on Bonderite 1000 iron phosphate pretreated, polished cold-rolled steel (0.66 mm thick) obtained from ACT Laboratories. In the case of the 40 μm thick coating, the samples were obtained from Valspar Inc., whereas for the other thicknesses, the coatings were applied using a draw-down technique. The coatings were applied to the 15 x 5 cm steel plates and then cut using a shear into approximately 30 x 30 mm samples. Each of these samples was large enough for approximately 30 single impact experiments. The coating thicknesses were measured using a magnetic gage (DeFelsko Co., Positector Model 6000) having a tolerance of $\pm 2 \mu\text{m}$ and the variability in coating thickness for the samples tested was also found to be approximately $\pm 2 \mu\text{m}$.

One of the major problems encountered was the lack of any material properties for the paint. Manufacturers were unable to provide even the most basic material properties such as Young's modulus and Poisson's ratio. Because the coatings were presumably visco-elastic, and thus strain rate sensitive, this was further complicated by the fact that the material properties were needed at high rates of strain. Therefore, the Young's modulus and Poisson's ratio were determined by measuring the shear and longitudinal wave velocities using a time-of-flight ultrasonic method at 5 MHz. The wave velocities were calculated as the average of three measurements, with the maximum difference between the three measurements being approximately 2%. It was reasoned that the combination of a high measuring frequency and low strain amplitude would produce an elastic (as opposed to viscoelastic) coating response approximating that created by the very high strain rates of impact. The Young's modulus and Poisson's ratio of the coating obtained in this manner were 2.47 GPa and 0.406, respectively. The measured value of Poisson's ratio was in agreement with that obtained by Ramamurthy et al. [18] for a similar coating, and the measured Young's modulus was the same order of magnitude as those obtained for other paints by Diah and Williams using a split Hopkinson pressure bar [23].

The particles used for most of the impact experiments were glass and steel spheres. The Young's Modulus and Poisson ratio of the steel and glass spheres was 200 GPa, 0.3; and 70

GPa, 0.17, respectively. The masses of single particles of glass and steel were measured on a microbalance as the average of 50 randomly selected particles and were found to be 0.364 and 1.49 mg, respectively. The radii of the particles were also measured by taking the average of 50 measurements using a micrometer, and were found to be 0.32 mm and 0.37 mm for the glass and steel spheres, respectively with a standard deviation of approximately 0.03 mm in both cases.

3.3 Characterisation of impact behaviour

In order to investigate the effects of particle impacts on this paint, the photographic setup described in Chapter 2 was used to determine the incident and rebound velocities of single glass spheres (0.64 mm diameter) launched at various angles of attack against the coated specimens. Four paint thicknesses were used (20, 25, 40, and 50 μm) and the normal component of the incoming velocity was varied from 10 to 120 m/s. Impact experiments were also performed on the bare steel substrate for comparison purposes. In all cases, the particles remained undamaged after impact.

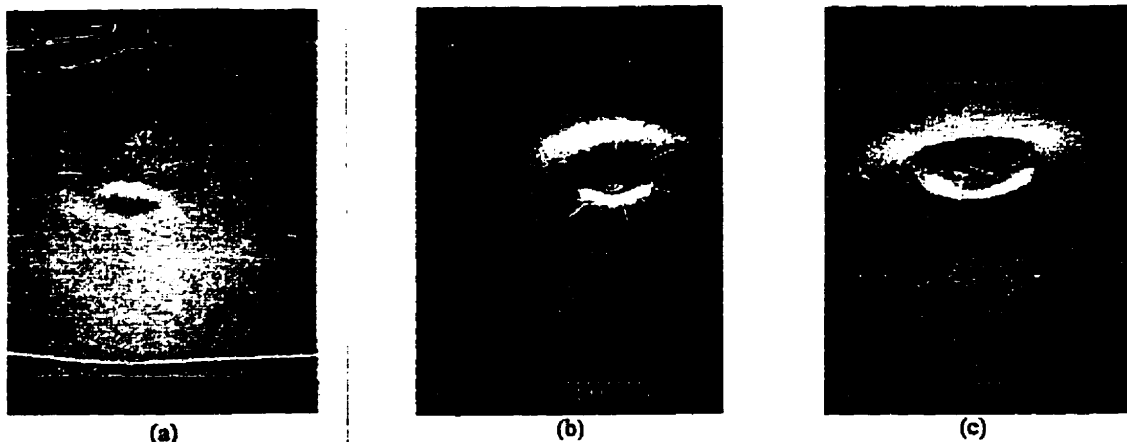


Figure 3.1: Impact sites on 40 μm thick alkyd coating, 90° incident angle, incident velocities of: (a) 33 m/s, (b) 50 m/s, (c) 90 m/s.

3.3.1 Observations of crack path and impact site

Figure 3.1(a) shows a 33 m/s velocity (at normal incidence) impact site on the paint photographed with a scanning electron microscope. The coating did not delaminate, but the impact created an indentation that was similar to the ploughing or cratering observed by Hutchings in the collisions of spheres with bare steel substrates [25].

At higher velocities, the coating delaminated approximately axisymmetrically. Figure 3.1 (b) and (c), for incident velocities of 50 m/s and 90 m/s (90° incident angle), show the blister-like nature of the impact site, with the coating delaminated below the blister. This characteristic feature may have been due to the delaminated paint chip adhering to the glass particle as it rebounded and thus being partially pulled off the substrate. Alternately, the blister may have resulted from the lateral displacement and buckling of the coating as the particle penetrated to the steel. A hole in the paint layer is visible in the centre of both Figure 3.1 (b) and (c) indicating that the glass sphere had penetrated through the paint layer. An interesting feature of the 50 m/s collision (Figure 3.1(b)) is the radial cracking pattern, which was typical only for a small range of velocities (45-55 m/s for the 40 µm coating). Impact sites for angles other than 90° showed similar features, but were slightly skewed into an oval shape for impacts at low angles of attack (with a high tangential component of incident velocity vector).

At higher velocities, it was clear that delamination had occurred; however, at lower incoming velocities, it was not so obvious. In order to determine if the coating had delaminated, special adhesive tape was applied to the impact site and pulled off in the manner described in the ASTM standard adhesion scratch test [33]. If a chip came off, it was assumed that delamination had occurred. In all cases, the tape consistently removed the paint to the bare substrate; i.e. the coating always failed by delaminating from the pretreated steel. The area removed in each collision was measured using a video camera on a microscope, a frame-grabber, and digital image analysis software.

Figure 3.2 shows the steel substrate below the impact sites of Figure 3.1 (b) and (c) after the paint chips were removed with the adhesive tape, as described above. The paint has been completely removed in both cases, and the rolling lines of the steel are visible except for a

small spot of crushed paint directly below the impact in the 50 m/s case (Figure 3.2(a)). Similar cracking patterns were observed by Lu in static indentation tests on ZnO coated Si substrates [22]. Figure 3.2(b) shows that at higher velocities (>60 m/s), the remaining dot of crushed paint on the substrate is replaced by a dimple of permanent deformation in the steel. X-ray photoelectron spectroscopy (XPS) analysis of the back surface of the removed paint chip revealed that there was no phosphate present. This, together with the fact that there was no observed paint residue left on the substrates in Figure 3.2, indicated that delamination occurred at the interface between the iron phosphate pretreatment and the paint, and not within either the paint or the iron phosphate layer.

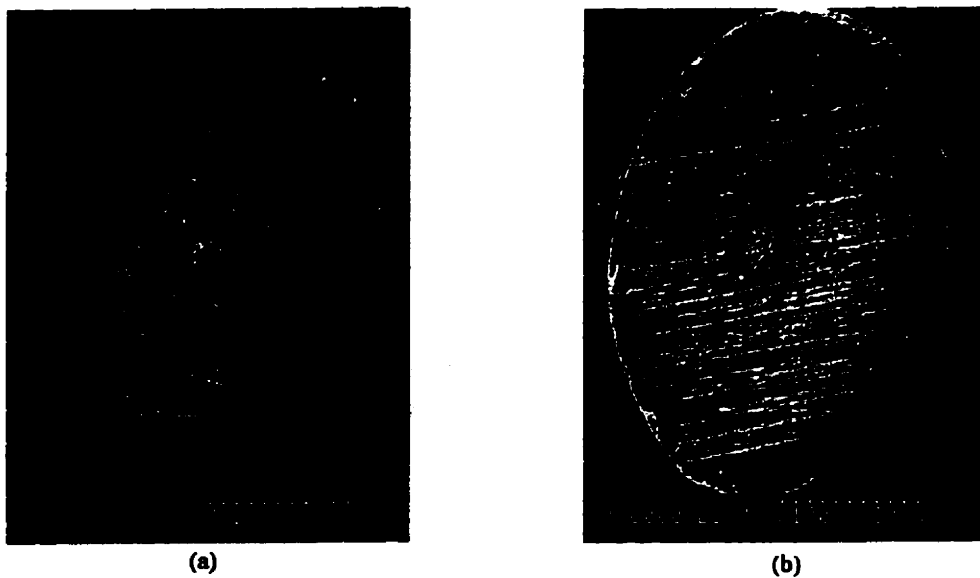


Figure 3.2: Steel substrate below impact site after removal of 40 μm coating using adhesive tape. 90° incident angle at incident velocities of: (a) 50 m/s, (b) 90 m/s.

A detailed inspection of the 50 m/s (normal incidence) impact site (Figure 3.2(a)) revealed no visible damage to the substrate, indicating that it was possible to remove paint without damaging the substrate (this will be discussed further in Section 3.3.4).

3.3.2 Dominance of normal effects and comparison to Brach's model

Brach has shown that the energy losses in a collision due to normal and tangential effects are, respectively [19],

$$T_L^n = [(1 - e^2) \sin^2 \alpha] \frac{1}{2} m v_i^2 \quad (3.1)$$

$$T_L^t = \left[\left[\frac{1}{1 + \lambda} \right] \frac{\mu}{\mu_c} \left(2 - \frac{\mu}{\mu_c} \right) \cos^2 \alpha \right] \frac{1}{2} m v_i^2 \quad (3.2)$$

where α is the angle of attack, defined as the angle between the incident velocity vector and the surface, λ is the ratio of the particle radius squared to the radius of gyration of the particle squared (5/2 for a sphere), e is the coefficient of restitution (defined as the ratio of the normal rebound velocity to the normal incident velocity), v_i is the incident velocity, and μ_c is the critical impulse ratio which defines the transition from sliding to rolling during a collision and is defined as [19],

$$\mu_c = \frac{1}{(1 + \lambda)(1 + e) \tan \alpha} \quad (3.3)$$

The impulse ratio, μ , is the ratio of tangential to normal impulse generated during the impact and is measured by taking the ratio of the change in momentum in the tangential direction to the change in momentum in the normal direction (using the appropriate components of measured incident and rebound velocities). It is important to note that the impulse ratio is equivalent to a dynamic friction coefficient only in the case where the mechanism of tangential impulse is due to friction. For a more complete discussion of impulse ratio, and the role of friction, see Reference [19]. An underlying assumption is that, regardless of the mechanism of tangential impulse, there can be no impulse ratio higher than the critical

impulse ratio, μ_c , so that if a series of impact experiments is performed at fixed incident velocity, and the measured impulse ratio is plotted versus the angle of incidence, there should be a point where the transition from sliding to rolling occurs, after which the data points lie within a band defined by equation (3.3) at $e=0$ and $e=1$ [19].

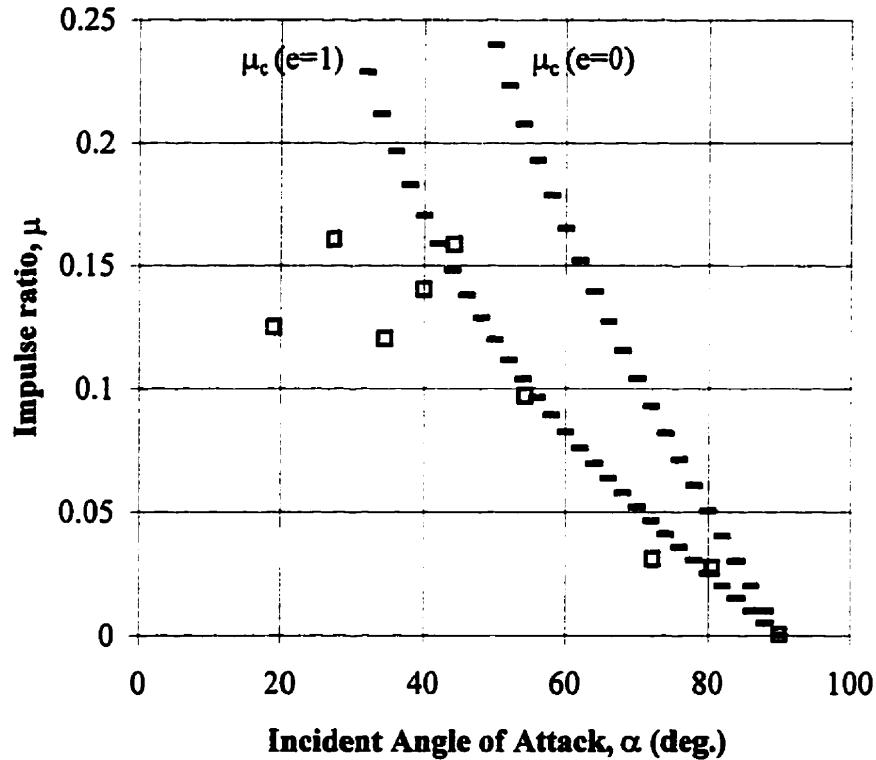


Figure 3.3: Variation of impulse ratio with angle of attack for 85 m/s total incident velocity collisions with 40 μm thick coating. Critical impulse ratio of Brach [19] also shown for $e=0$ and $e=1$.

Brach used experimental data on uncoated specimens to support his analysis, and in particular, this hypothesis of a critical impulse ratio [19]. There is, however, no reason why the analysis should not also hold for coated substrates, and Figure 3.3 shows typical data gathered in the present study. The data points are averages of multiple impacts performed at each angle of incidence. As mentioned above, the impulse ratios were calculated by taking the ratio of the change in momentum in the tangential direction to the change in momentum in the normal

direction, using the experimentally measured components of incident velocity and rebound velocity in the tangential and normal directions.

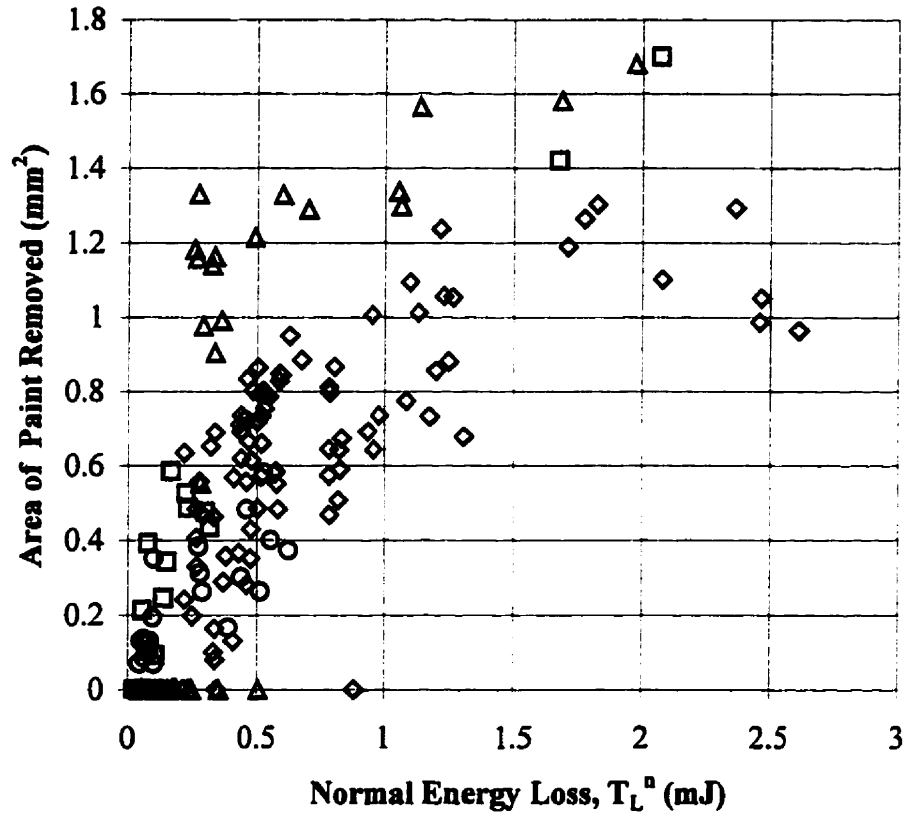


Figure 3.4: Area of coating removed vs. energy loss due to normal direction effects for coating thickness: Δ - 50 μm , \diamond - 40 μm , \square - 25 μm , \circ - 20 μm .

The transition between rolling and sliding appears to occur at a 45° angle of incidence, after which the data points roughly follow the 'envelope' defined by the theoretical critical impulse ratios at $e = 0$ and $e = 1$. The other experimental data show similar trends and all have a large amount of scatter in the impulse ratio. This relatively large scatter has been experienced by others [19, 34] and is probably due to surface irregularities and the fact that the impulse ratio is very sensitive to variations in the impact and rebound velocities.

The dependence of the paint area removed on the energy loss associated with the normal and tangential incoming velocities is shown in Figure 3.4 and Figure 3.5. The amount of paint

removed does not depend very much on energy loss due to tangential effects (Figure 3.5), but does increase with the energy loss due to normal effects (Figure 3.4).

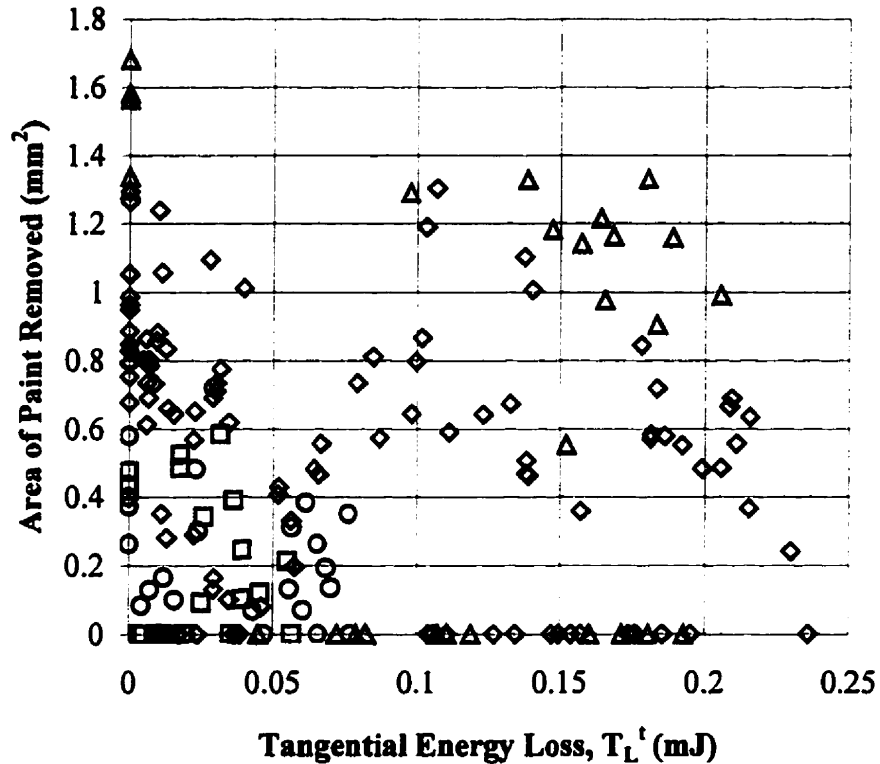


Figure 3.5: Area of coating removed vs. energy loss due to tangential direction effects for coating thickness: Δ - 50 μm , \diamond - 40 μm , \square - 25 μm , \circ - 20 μm .

This relatively strong correlation between the area loss and the energy losses due to normal effects and the relatively weak correlation between the area loss and the energy losses due to tangential effects suggests that normal effects dominate paint removal. Furthermore, a threshold value of energy loss due to normal effects exists for each coating thickness (Figure 3.4), whereas, there is no such threshold value for energy loss due to tangential effects (Figure 3.5).

Figure 3.6 is a plot of the incident normal velocity component versus the amount of coating removed for all experiments performed at angles of incidence between 18 and 90°. This illustrates that a critical amount of incident normal velocity is required, for each coating

thickness, to initiate removal of the coating, and, furthermore, that this critical value is independent of the tangential component.

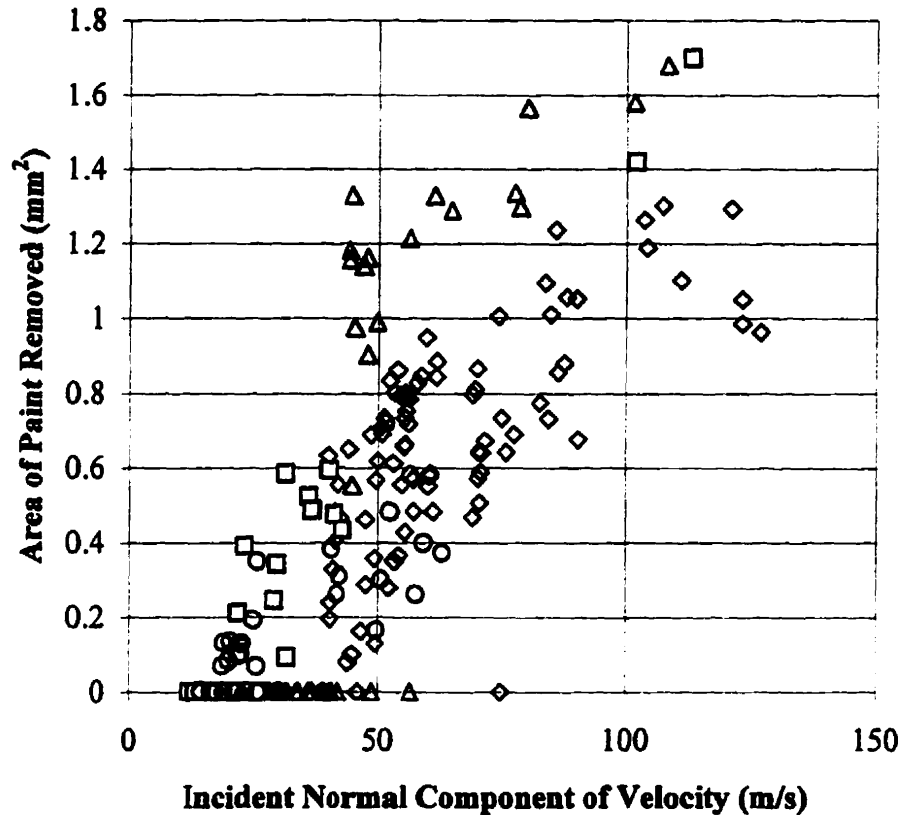


Figure 3.6: Area of coating removed as a function of incident normal velocity component for coating thickness: \triangle - 50 μm , \diamond - 40 μm , \square - 25 μm , \circ - 20 μm .

The dependence on normal effects is further illustrated by Figure 3.7, which is a plot of the energy losses normalised by the total incident kinetic energy versus angle of attack. In all cases, the energy loss in the normal direction accounts for most of the energy loss. This system exhibits, what is termed in the field of solid particle erosion, deformation or ploughing wear, as opposed to cutting wear [19, 25]. This type of deformation wear is also characterised by the dominance of normal effects, with the maximum amount of damage (energy loss and area loss) occurring at high angles of incidence ($\alpha \rightarrow 90^\circ$). This is demonstrated further in Figure 3.8 and Figure 3.9, which show the area of paint removed as a function of the incident angle of attack

for various total incident velocity ranges. The area losses are averages of multiple impacts performed at each angle. The maximum coating removal occurs at higher angles of attack, and removal does not begin until the normal component of velocity is sufficiently large.

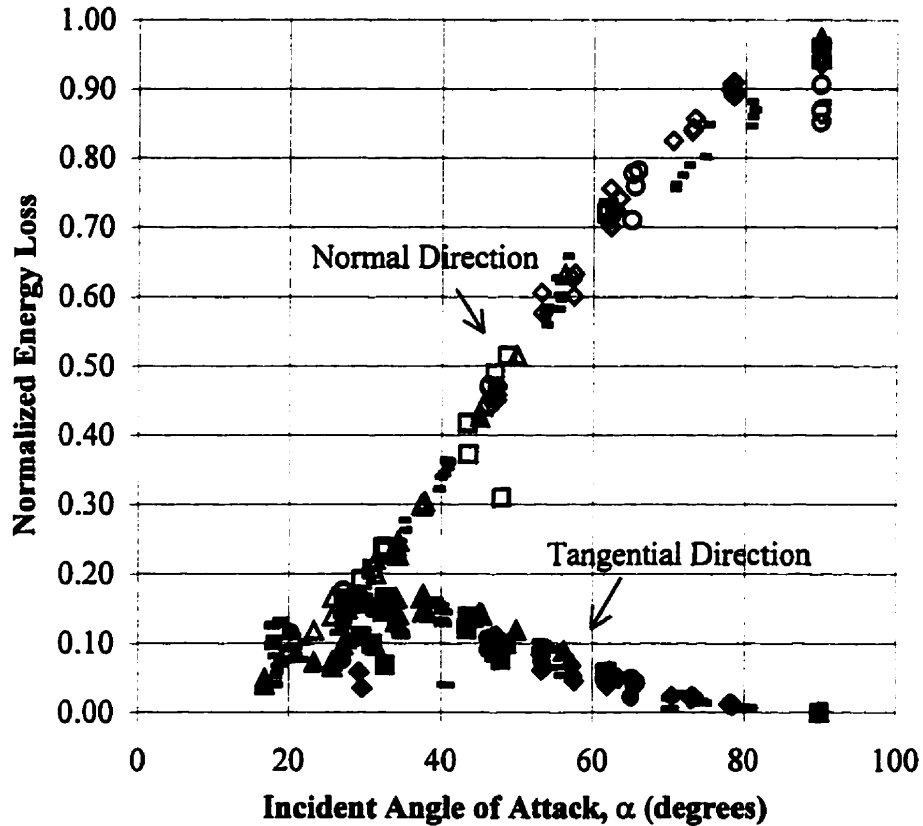


Figure 3.7: Energy loss due to normal and tangential direction effects normalised by total incident kinetic energy as a function of incident angle of attack. Normal energy loss for coating thickness and total incident velocity: Δ - 50 μm thick coating, 80 m/s, \square - 40 μm , 85 m/s, \diamond - 40 μm , 56 m/s, \square - 25 μm , 42 m/s, \circ - 20 μm , 57 m/s. Tangential energy loss for coating thickness and total incident velocity: \blacktriangle - 50 μm , 80 m/s, \blacksquare - 40 μm , 85 m/s, \blacklozenge - 40 μm , 56 m/s, \blacksquare - 25 μm , 42 m/s, \bullet - 20 μm , 57 m/s.

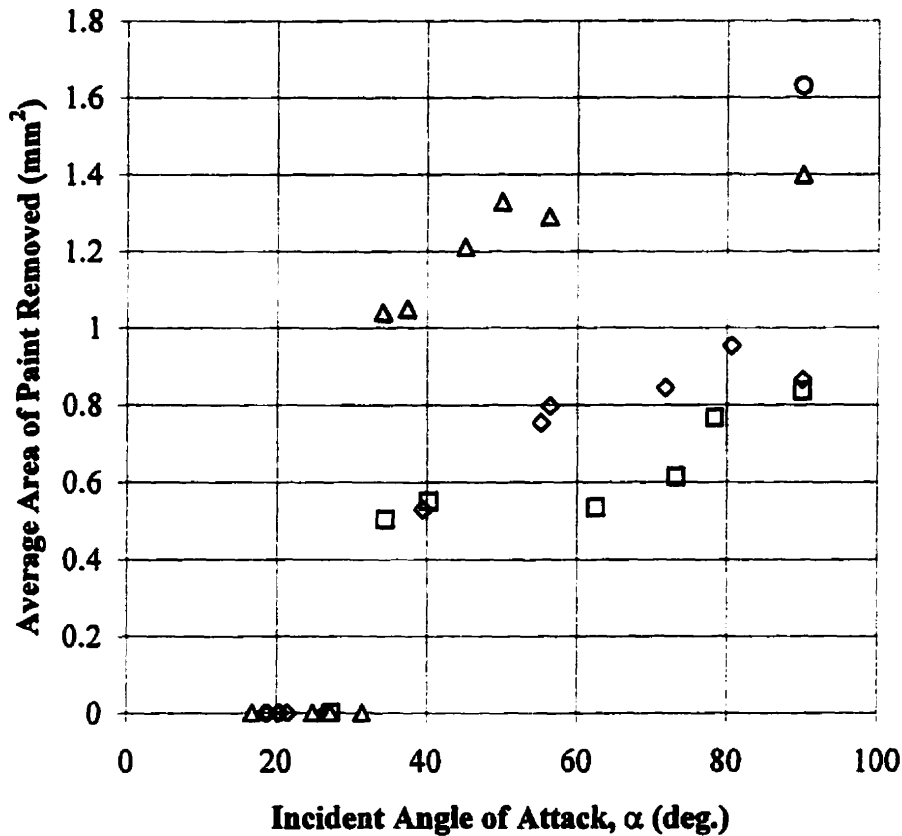


Figure 3.8: Average area of coating removed as a function of incident angle of attack for different ranges of incident total velocity and coating thickness. Data points represent averages of area removal measurements at each angle. □ - 55-62 m/s, 40 μm, ◇ - 81-90 m/s, 40 μm, △ - 78-81 m/s, 50 μm, ○ - 102-108 m/s, 50 μm.

3.3.3 Role of tangential effects

The onset of coating removal was, as demonstrated above, independent of tangential effects. However, the role of tangential effects in the magnitude of coating removal has not yet been discussed. Figure 3.6 shows that the area of coating removed increases as the normal component of incident velocity increases. These data, however, are for a large number of different impact conditions (i.e. angle of attack, incident velocity).

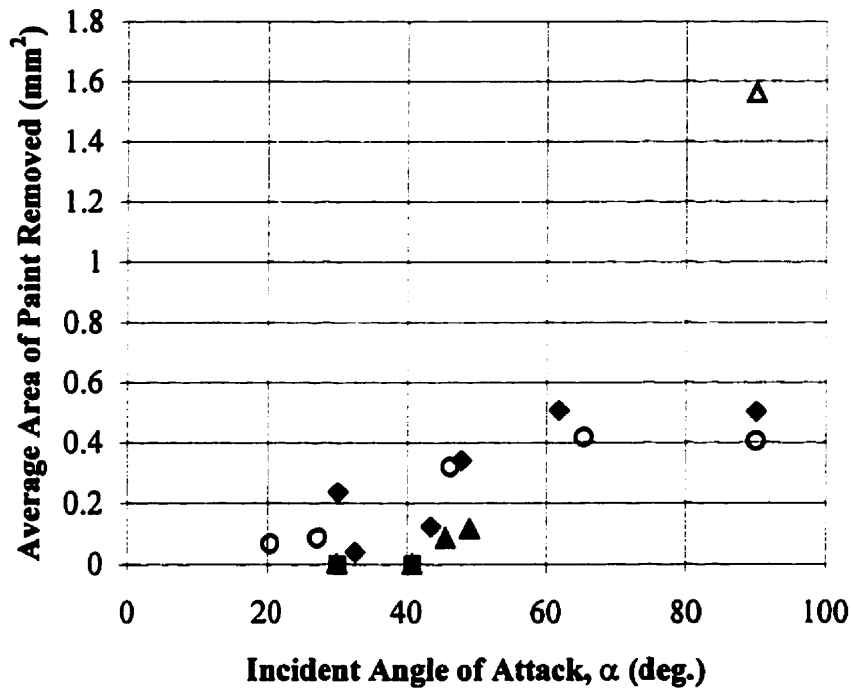


Figure 3.9: Area of paint removed as a function of incident angle of attack for different ranges of incident total velocity and coating thickness. Data points represent averages of area removal measurements at each angle. ● - 38-44 m/s, 25 μm , ■ - 25-27 m/s, 25 μm , △ - 102-110 m/s, 25 μm , ○ - 54-62 m/s, 20 μm , ▲ - 25-30 m/s, 20 μm .

In order to fully understand the role of tangential effects on the area of coating removed, a series of experiments was performed in which the incident angle and total incident velocity were varied so as to always give the same normal component of incident velocity. The average and standard deviation of the area removed was calculated for a number of experiments performed at each condition, and the results are shown in Table 3.1.

The area removed for each coating thickness is virtually independent of tangential effects (the scatter in the data is approximately constant). This result is somewhat counterintuitive, as one might expect that an increase in tangential velocity should have some effect on the amount of coating removed. As mentioned in Section 3.3.1, the only tangential effect was that, at lower impact angles (tangential component of incident velocity high), the coating removal area

changed from being axisymmetric to being slightly oval shaped, even though the total area removed was not affected by this change in shape.

Coating thickness (μm)	Incident Angle (deg)	Normal component of incident velocity (m/s)	Tangential component of incident velocity (m/s)	No. of data points	Average coating area removed (mm^2)	Standard deviation of coating area removed (mm^2)
20	90	31	0	10	0.273	0.036
20	38	31	40	11	0.261	0.030
40	90	59	0	12	0.577	0.059
40	46	59	57	12	0.545	0.060
40	33	59	91	9	0.559	0.101

Table 3.1: Comparison of coating area removed keeping normal component of velocity constant, while varying tangential component of velocity.

The above arguments lead to the conclusion that, for this particular system, normal effects dominate the onset of coating removal (i.e. the threshold value of normal incoming velocity and energy loss required to remove the coating), and that tangential effects have little or no influence on the magnitude of coating removed. Thus, for the purposes of investigating the onset of coating removal, and for simplification of analytical models, the tangential effects could be ignored.

3.4 Evaluation of possible mechanisms of coating removal

3.4.1 Dynamic versus quasi-static effects

In order to determine whether the mechanism of coating removal was dominated by dynamic (stress wave propagation) effects or quasi-static effects, a series of experimental observations was made. It was initially suspected that removal was the result of a spalling mechanism, in which the collision of the particle with the coating caused a compressive spherical stress wave to propagate through the coating. Most of the wave would then be

reflected at the coating/substrate interface (because the substrate has a much higher acoustic impedance) as a compressive wave, then reflect at the top surface of the coating, and back down towards the coating/substrate interface as a tensile wave which would delaminate the coating. It was also possible that the portion of the compressive wave that was transferred to the steel substrate could travel to the back surface of the substrate and reflect as a tensile wave which would then travel to the interface and delaminate the coating. In order to investigate the hypothesis that paint removal was due to a type of spalling, a series of experiments was performed.

A 12.5 mm thick piece of steel was clamped to the back of the painted (40 μm thick coating) steel sheet with three different coupling layers: an ultrasonic coupling fluid, honey, and a thin layer of epoxy, so that the clamped interface would transfer all waves without much attenuation. If a wave reflected from the backside of the 12.5 mm plate as a tensile wave and caused a delamination as explained above, the size of the delamination should be decreased relative to the steel sheet alone because the spherical wave would have been dispersed and attenuated by the much thicker substrate (approximately 19 times as thick as the original sample). The paint areas removed using the coupling gel, honey, and epoxy, were, respectively, 0.659, 0.643, and 0.613 mm^2 . The area removed from the painted steel sheet alone (without the 12.5 mm plate coupled to it) was 0.690 mm^2 . The differences between these values are small, and certainly well within experimental error, which is approximately $\pm 30\%$ as shown in Figure 3.4. This meant that the compressive waves reflecting as tensile waves from the back of the substrate could be eliminated as a mechanism of coating removal. Nevertheless, a spalling-type mechanism could still possibly result if compressive waves reflected at the substrate/paint interface and back down from the free surface at the top of the paint layer towards the interface as tensile waves. The other conclusion that can be drawn from this experiment is that the 0.66 mm thick steel substrate can be modelled effectively as semi-infinite.

Further insights into the mechanism of removal may be gained from Figure 3.6, a plot of the paint area removed versus the incident normal velocity component for all experiments

performed on this coating/substrate system. An interesting feature is that the area removed tends to reach a plateau at higher incoming normal velocities. Although this observation is intuitively correct, it is contrary to the spalling hypothesis, where one would expect the area removed to continue to increase, as the intensity and energy of the wave increases with the incident normal velocity.

An additional assessment of whether quasi-static or inertial (wave) effects dominate can be obtained by calculating the amount of time it takes for stress waves to traverse the coating thickness, and comparing this to the amount of time that the sphere is in contact with the coating during the collision. The longitudinal wave speed for this coating from ultrasonic tests in Section 3.2 was $\cong 2000$ m/s . For a $50 \mu\text{m}$ coating, it takes $0.025 \mu\text{s}$ for the wave to traverse the coating. Experimental observations have shown that the contact time is on the order of $50 \mu\text{s}$. Because the stress waves will traverse the thickness of the coating approximately 2000 times during the contact time, the stress field will be dominated by static, rather than inertial effects.

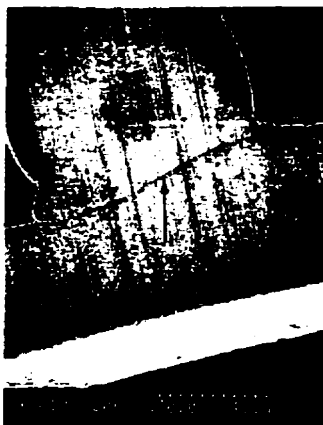


Figure 3.10: Impact near a free edge for a $40 \mu\text{m}$ thick coating. Note the attached paint in the shape of the original free edge.

The other possible mechanism for coating removal is the attainment of a quasi-static critical delamination shear stress. In this model, the collision is treated as a quasi-static

indentation problem, under the assumption that the coating will delaminate once a critical shear stress is reached. An experimental observation that appears to support this mechanism is seen in Figure 3.10, which shows an impact site very close to the cut edge of the paint layer (though relatively far away from the edge of the steel substrate). Here, a 0.64 mm glass sphere was launched at the edge of a 40 μm thick paint layer sample to investigate the effect of a free surface in the vicinity of an impact site. The coating was delaminated in the usual manner, except that in the vicinity of the free surface at the edge, a small ridge of paint (shown by arrow in Figure 3.10) remained intact in exactly the shape of the original edge of the paint layer. Because the shear stress on a free boundary must be zero, equilibrium considerations imply that the shear stress along the paint/substrate interface must also fall to zero very quickly at the edge, thereby explaining why a narrow strip of paint remains attached in the immediate vicinity of the free surface of the edge. Under the spalling hypothesis, one would expect the free surface of the edge to have little effect on the reflected tensile wave, and for all of the paint to be removed. The above experimental and analytical observations led to the conclusion that the coating removal was due to quasi-static, rather than wave effects, normal effects dominated the collision for this system, and that interfacial shear effects played a role in the delamination.

3.4.2 Analysis of incident kinematics

A realistic model of the kinematics of the incident portion of the collision assumed that the coating behaved locally in a fully plastic manner during the impact, resisting indentation with a constant dynamic flow pressure (or dynamic hardness, for a sphere, the resisting force divided by the projected contact area) [15, 24-31]. For a sphere, an estimate of the dynamic hardness can be obtained by setting the incoming kinetic energy equal to the work done indenting the coating,

$$\frac{1}{2}mv_i^2 = \int_0^{d_{max}} F d(d) \quad (3.4)$$

where F is the indentation force, which is equal to the dynamic hardness multiplied by the projection of the contact area (i.e. $F = p_d \pi c^2$).

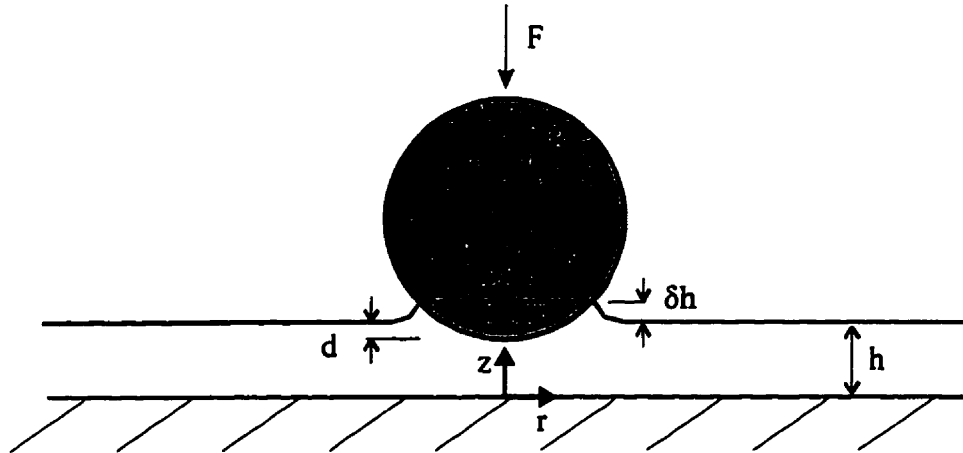


Figure 3.11: Geometry of indentation of coating (thickness h) on rigid substrate by a sphere of radius R .

By assuming a relationship between the penetration depth, d , and the contact radius, c , (Figure 3.11), of the form (neglecting the pile-up δh),

$$d = \frac{c^2}{2R} + \frac{c^4}{8R^3} \quad (3.5)$$

equation (3.4) becomes [1],

$$\frac{1}{2} m v_i^2 = p_d \pi \left[\frac{c_{\max}^4}{4R} + \frac{c_{\max}^6}{12R^3} \right] \quad (3.6)$$

where p_d is the dynamic hardness, c_{\max} is the maximum contact radius reached during the indentation, and m , R , and v_i are, respectively, the mass, radius and incident velocity of the particle.

Adjusting the dynamic hardness in the plastic model so that penetration to the bare substrate occurred for the experimental penetration velocities shown in Table 3.2 resulted in a relatively consistent dynamic hardness (also shown in Table 3.2). It should be noted that Table

3.2 includes normal incidence experiments performed with 0.72 mm diameter steel spheres, which were used to test the dependence of p_d on particle material.

Coating Thickness (μm)	Impacting Particle	Velocity required to initiate coating removal (i.e. penetrate to steel substrate) (m/s)	Kinetic Energy required to just penetrate coating to steel (mJ)	Dynamic Hardness, p_d (MPa)
20	glass	20	0.073	190
40	steel	20	0.297	170
40	glass	40	0.291	190
50	glass	45	0.369	155

Table 3.2: Experimentally determined incident velocity and kinetic energy required to remove coating, and resulting dynamic hardness for different impacting particles and coating thickness.

The dependence of the dynamic hardness on the indentation depth is quite small. One would expect that the dynamic hardness should increase with decreasing coating thickness since the influence of the substrate will be a maximum when the coating is thin. This was found to be the case for organic coatings in studies by other authors [35, 36], and is evident when comparing the 40 and 50 μm thick coatings, but not for coating thicknesses of 20 and 40 μm . The reason for this was not clear, but it is possible that, for very thin coatings, the influence of the substrate became relatively consistent. It should also be noted that the instantaneous dynamic hardness will change slightly as the particle penetrates the coating. Thus, the dynamic hardnesses in Table 3.2 should be viewed as values averaged for the whole impact.

The fact that the required kinetic energy to penetrate the coating to the substrate (to just start to remove the coating) is almost the same for the steel and glass spheres on the same 40 μm thick coating is also expected, given the fact that the particles are of similar size, and do not deform while penetrating the coating in both cases.

As an interesting side note, the dependence of dynamic hardness on the substrate material was used to explain differences in coating removal rates in a multiparticle blast cleaning application. When identical coatings were applied to aluminum and composite substrates, it

was found that the coating removal rate was much higher for the composite substrate. In addition, a 'selective stripping window' which is a period of time where, upon blasting, a coating can be removed without removing the epoxy primer, existed for the aluminum substrate panels, but not for the composite panels [36]. Because the composite matrix will be of approximately the same dynamic hardness as the coating (and the epoxy primer), whereas the aluminum will be of higher dynamic hardness, the coating should be effectively softer on the composite panels. This explains the differences in coating removal rates between the two systems. Also, for the same reason, the composite system will appear to the impacting particle as essentially a very thick panel of material of dynamic hardness approximately equal to that of the coating, whereas when the epoxy primer is reached in the case of the aluminum system, the presence of the hard aluminum substrate will be felt more by the impacting particle. Thus, one would expect the selective stripping window to appear in the case of the aluminum system, but not the composite system.

In order to further test the validity of the fully-plastic indentation model at a range of incident velocities, single glass spheres were launched against a 40 μm thick coating at normal incidence, and the diameter of the permanent indentation of the coating was measured using image analysis software, and compared to that predicted by the analysis using a constant value of $p_d = 190 \text{ MPa}$. The results are presented in Table 3.3.

Incident Velocity, V_{in} (m/s)	Plastic-flow model coating contact diameter, $2c_p$ (mm)	Measured coating contact diameter, $2c_m$ (mm)	Percent Difference $2(c_p - c_m)/(c_m + c_p) \times 100$
27	0.252	0.233	7.8
37	0.299	0.313	-4.6
20	0.220	0.231	-4.9
29	0.263	0.256	2.7
24	0.242	0.228	5.9

Table 3.3: Comparison of predicted and measured contact diameters for 40 μm thick coating impacted by glass sphere ($R=0.32 \text{ mm}$, $m=0.364 \text{ mg}$) using plastic flow model with dynamic harness, $p_d=190 \text{ MPa}$

The agreement is very good, and thus it can be concluded that this analysis, which neglects any elastic effects during the incident portion of the collision, describes the kinematics of the indentation adequately.

Table 3.4 shows a comparison of predicted penetration velocities using $p_d = 190$ MPa and the experimental observations of the normal velocity component required to begin coating removal (from Figure 3.6). There is a good correlation between the predicted coating penetration velocity and the measured velocity at which the coating begins to be removed for four different coating thicknesses. In other words, coating removal begins only when the coating is fully penetrated for this coating/substrate/particle system. The reason for this may be that the onset of delamination required the creation of a free edge that was formed when the particle reaches the substrate.

Coating thickness (μm)	Predicted normal component of velocity to penetrate coating (m/s)	Experimental normal component of velocity at which coating begins to be removed (Fig. 6) (m/s)	Difference (%)
20	20	20	1
25	25	22	13
40	39	40	4
50	50	45	11

Table 3.4: Comparison of predicted velocity ($p_d = 190$ MPa) to cause penetration of coating to steel substrate, and measured velocity at onset of coating removal.

According to Johnson [15], the dynamic hardness, p_d , is between 1.1 and 3 times the yield stress of the coating, though this relationship is for infinitely thick materials (whereas there is some dependence of the dynamic hardness on coating thickness as shown above). Thus, for this coating, the yield stress is in the range 60-170 MPa, which compares well to the values obtained by Diah and Williams [23] for other types of paints.

A certain amount of energy was lost in penetrating the coating, and then the collision proceeded as if the remaining energy (incident energy minus energy to penetrate the coating to

the substrate) was incident on a bare substrate. This is demonstrated in Figure 3.12, which shows that for all coating thicknesses, e tended to reach an approximately constant value of 0.35 when the coating began to be removed, meaning that the collision proceeded in a similar manner for all the coating thicknesses from this point. This is further illustrated in Figure 3.13, which shows that the coefficient of restitution tended to reach the value measured on bare steel at higher incoming energies.

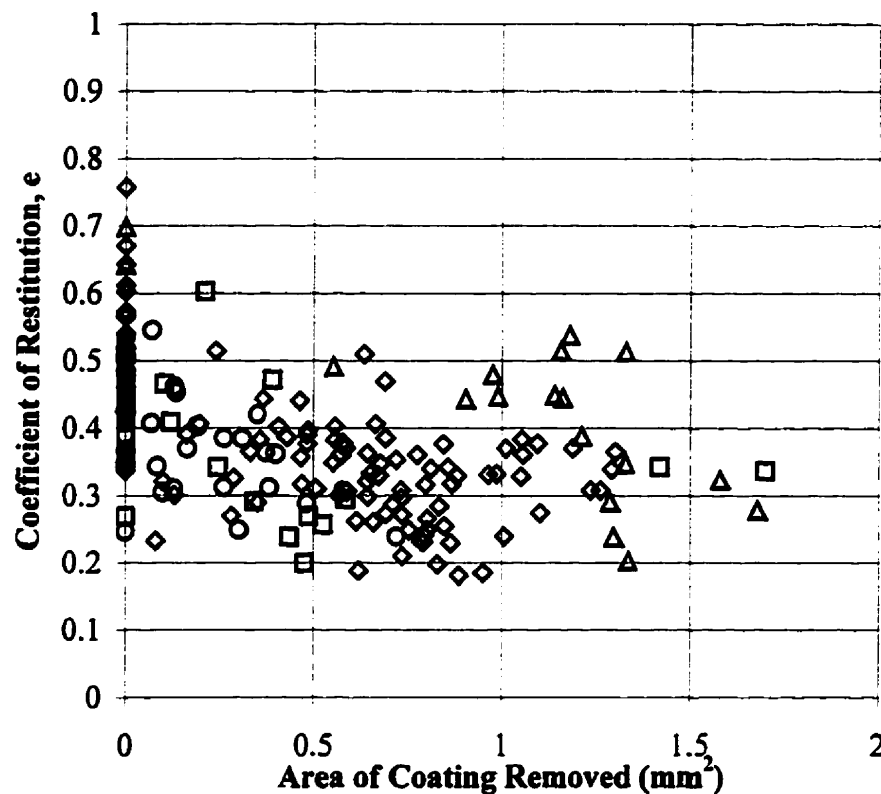


Figure 3.12: Variation of coefficient of restitution, e , with area of coating removed for coating thickness: Δ - 50 μm , \diamond - 40 μm , \square - 25 μm , \circ - 20 μm .

The coefficient of restitution can be estimated by using the fully-plastic indentation model (equation (3.6)) to describe the incident portion of the impact, and an elastic analysis to describe the elastic rebound of the particle. Johnson [15] used a similar approach with bare substrates. The elastic analysis used is similar to that developed by Matthewson [20], with a

modification by the author [1] to the expression for the indenter profile which gives more accurate results. The model is presented in Appendix B, and its application in a MathCad 7.0 (Mathsoft Inc) sheet can be found in Appendix D. This model shall be referred to as the 'modified Matthewson analysis'. Application of this procedure for incident kinetic energies less than or equal to that for penetration to the substrate (range for which the elastic model is valid), yielded predicted values of e (solid line in Figure 3.14 is linear best fit of predicted e) that agreed reasonably well with the experimental data (dashed line in Figure 3.14 is linear best fit of experimental e), given the scatter inherent to measurements of e . This further illustrates the validity of the present model, and shows that the value of Young's modulus of the coating obtained ultrasonically is a reasonable estimate of the true value under impact conditions.

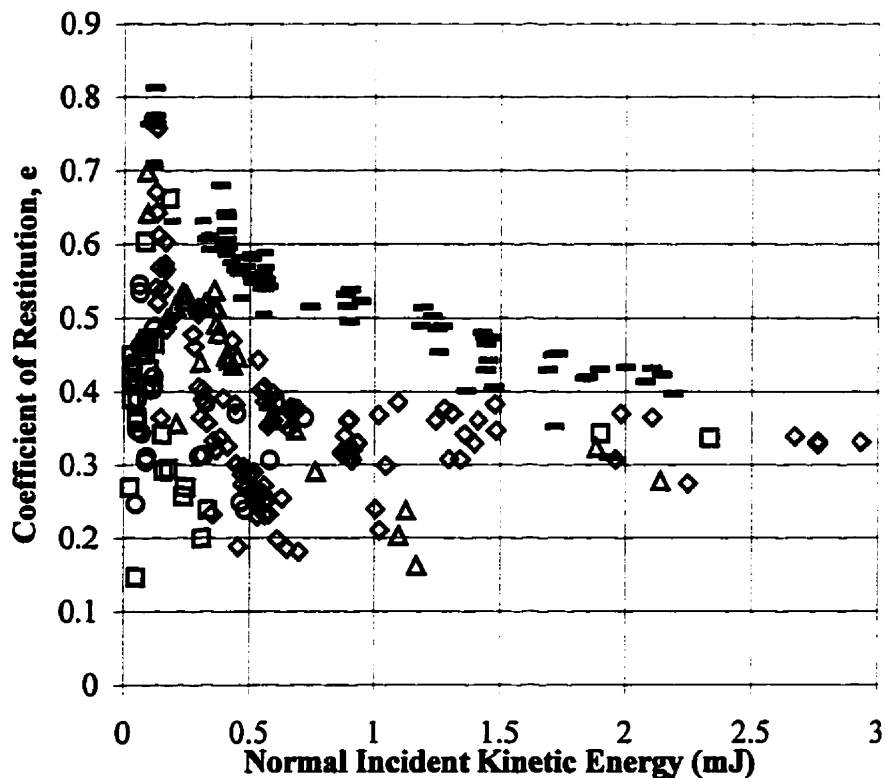


Figure 3.13: Variation of coefficient of restitution, e , with incident kinetic energy in normal direction for coating thickness: \triangle - 50 μm , \diamond - 40 μm , \square - 25 μm , \circ - 20 μm , $---$ - bare steel.

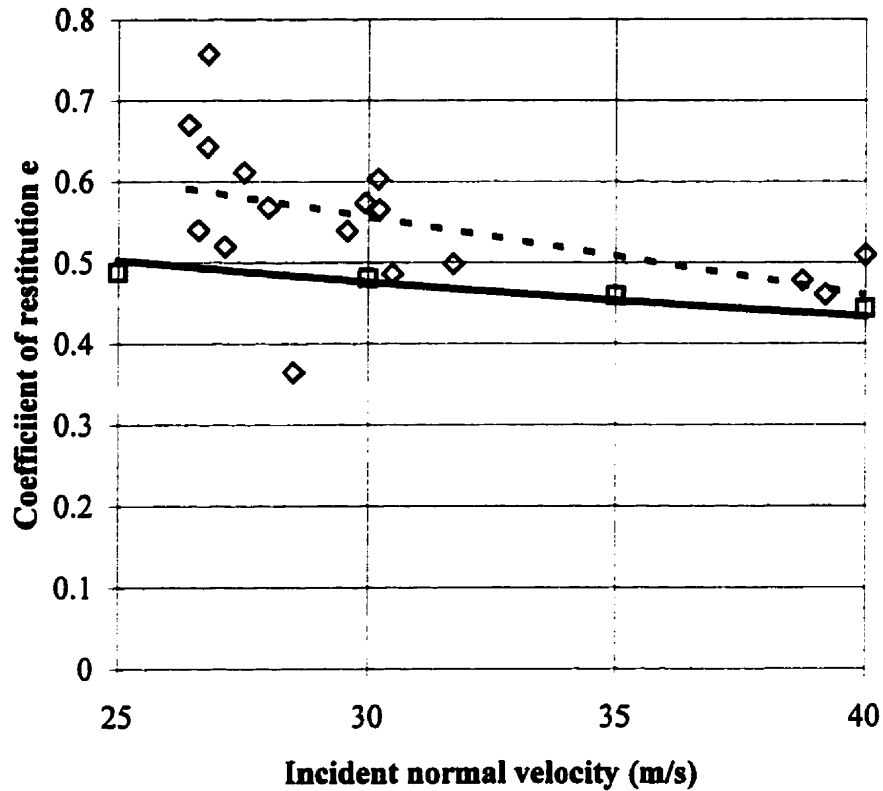


Figure 3.14: Coefficient of restitution as a function of incident normal velocity for 40 μm thick coating. \diamond -experimental data, \square - predicted using plastic analysis for incident portion and elastic analysis for rebound portion.

Figure 3.4 and Figure 3.5 show energy losses for the coated system as a whole, including energy losses due to local plastic deformation in the bare steel substrate directly below the impact site. An estimate of the amount of energy lost to the coating alone can be obtained using the normal direction energy loss for experiments performed on both coated and bare substrates, as a function of incident normal direction energy (Figure 3.15).

The following steps demonstrate how to use these plots for estimating energy losses to the coating due to normal effects at high incident normal velocities [1]. All energies and energy losses in the following steps are due to normal effects.

Let I_d be the incident kinetic energy for the particular data point of interest, and let I_p equal the incident kinetic energy of a sphere that just penetrates the coating to the substrate.

- Use the fully-plastic model (equation (3.20)) to calculate I_p , the incident kinetic energy to penetrate the coating, corresponding to the onset of coating removal.
- Subtract I_p from I_d to estimate the incident kinetic energy that is available to deform the steel substrate. As illustrated in Figure 3.12, once the coating has been penetrated, impact proceeds as if the substrate were bare.

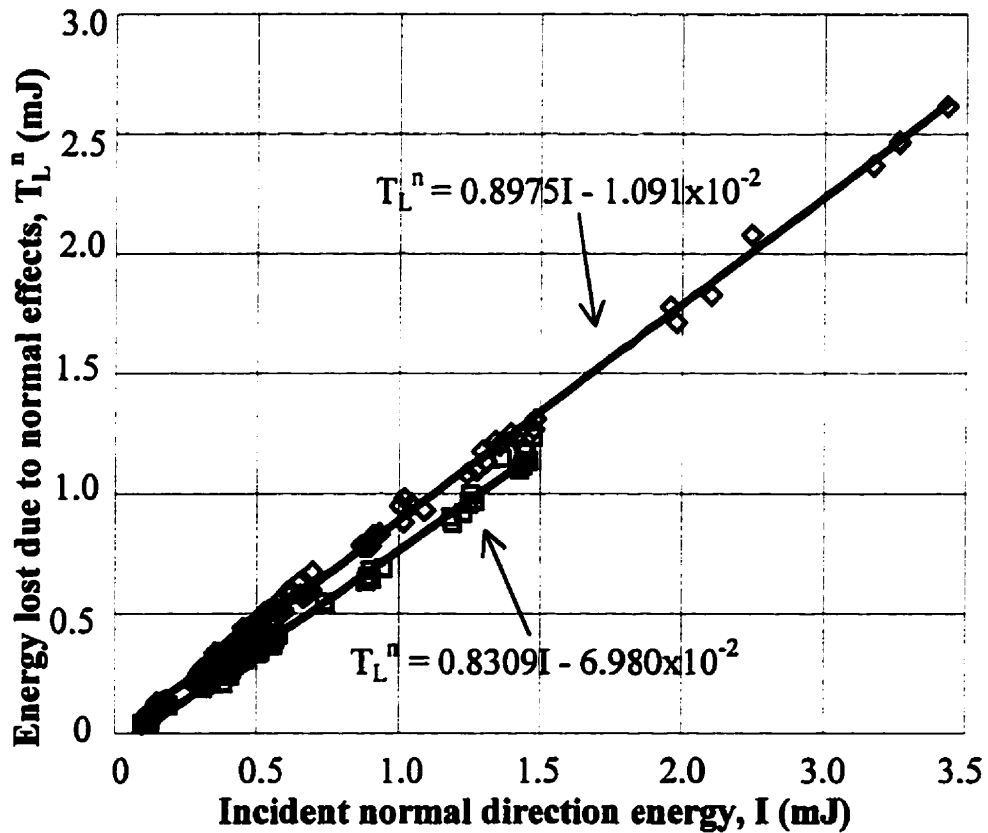


Figure 3.15: Energy loss due to normal direction effects vs. normal incident kinetic energy. Equations shown are linear regression curve fits. \diamond - 40 μ m coating, \square - bare steel.

- Use the linear curve fit of the energy loss vs. incoming energy for bare steel (bottom curve of Figure 3.15) with the result of (b) to estimate the energy loss to the steel substrate.

- (d) Use the top curve of Figure 3.15 with I_d to find the energy loss for the coated system (which is made up of energy loss to the coating and energy loss to the substrate). Subtract the energy loss to the steel substrate obtained in (c) from this energy loss. This is an estimate of the amount of the energy lost to the coating.

Figures similar to Figure 3.15 were obtained for all coating thicknesses, and the above steps were performed on all data obtained in this study. The resulting estimates of energy loss to the coating due to normal effects can be found in Figure 3.16. The lines are best- linear curve fits for each coating thickness using only the nonzero data points.

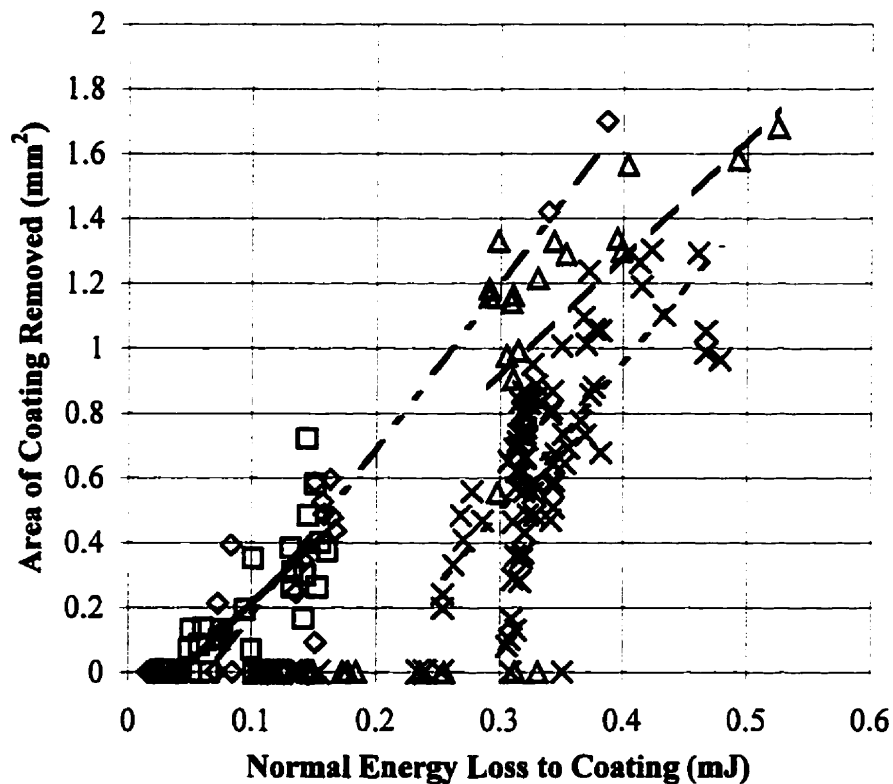


Figure 3.16: Area of coating removed vs. energy lost to coating for coating thickness: \triangle 50 μm , \times 40 μm , \diamond 25 μm , \square 20 μm . Best linear fit lines: - - - 50 μm , - - - 40 μm , - - - 25 μm , - - - 20 μm .

Though there is significant scatter, there is, as seen before in Figure 3.4, Figure 3.8, and Figure 3.9, a threshold value of the normal energy loss corresponding to the onset of coating removal. The threshold increases with coating thickness, and beyond it, the area removed

increases rapidly with energy loss (approaching a step increase). The energy losses due to tangential effects for coated substrates (Figure 3.5) are approximately equal to the energy losses due to tangential effects to the coating itself. This is because the energy losses due to tangential effects were found to be very low for impacts on bare substrates when the impact angle was varied from 17 to 90° for incident total velocities of 50 and 90 m/s (less than 10% of total energy lost in most cases).

As the incident normal kinetic energy is increased beyond that required to penetrate the coating to the substrate, the area of coating removed increases. It is hypothesised that this may be due to the deformation of the particle after it contacts the steel substrate. Because the steel's Young's Modulus was approximately three times that of the glass, it is possible that, upon contacting the steel, the glass particles experienced significant lateral deformation which resulted in increased shear stresses at the coating/substrate interface. An estimate of the extent of this deformation can be obtained by using a Hertzian analysis [37].

Although the substrate will deform plastically at higher impact velocities, it is noted that coating removal did occur for a range of velocities that do not cause plastic deformation of the steel (Figure 3.2). Hence, the use of an elastic (Hertzian) analysis was expected to yield realistic results, at least for intermediate velocities. For example, according to Table 3.4, a 39 m/s incident normal velocity was required to just penetrate a 40 µm coating, corresponding to 0.27 mJ total incident energy (particle velocity is zero at substrate contact). Now, assume that a second particle is incident at 50 m/s normal velocity, corresponding to 0.46 mJ of incident normal energy. The particle would again use 0.27 mJ of incident energy in penetrating the coating and the remaining incident energy would be 0.19 mJ. Assuming all of the remaining incident energy is available to deform the substrate and particle, the Hertzian analysis gives a maximum deflection of the steel substrate of approximately 3 µm, and the particle diameter at the point of impact decreases approximately 8 µm. The additional volume of coating displaced by this particle deformation was approximately 40% of the original coating volume displaced by the penetration to the substrate. Therefore, significant amounts of lateral deformation of the coating are expected to occur as the particle deforms (flattens), even at the relatively low

velocity of 50 m/s. This additional deformation of the coating may account for the continuing increase in the area removed.

As noted above, an interesting result in the context of coating removal using blast cleaning is that it may be possible to remove the coating without causing visible permanent damage to the substrate. An examination of the impact sites for all experiments (optical microscope at 160X) showed the existence of a range of incident normal velocities, beginning at the coating penetration velocity, where coating removal occurred with no visible damage to the substrate. For the 50 μm coating, this range was about 50-80 m/s, for the 40 μm coating about 40-65 m/s, and about 21-36 m/s for the 25 μm coating (no conclusions could be drawn from the 20 m/s experiments due to a lack of data in the proper range). The lack of damage to the substrate in these cases is thought to be due to the coating protecting the substrate. At higher velocities, the particle does not lose enough energy penetrating the coating, and sufficient incident energy remains to deform the substrate. It is important to note that this result, although interesting, is not applicable to streams of particles such as in blast cleaning, because, after removing the coating, subsequent impacts on the bare steel would damage the substrate.

3.5 Delamination mechanism: Impact-Induced Buckling

Examination of the impact sites in Figure 3.1 revealed delamination that was approximately circular, with a raised (buckled) portion of coating in the centre. This behaviour is consistent with coating delamination due to the buckling of the coating. Similar patterns of behaviour have been observed by others in the context of the quasi-static buckling of precompressed thin films [38,39,40,41,42], and in particular by Evans and Hutchinson [40], who studied the static indentation-induced buckling of thin films.

3.5.1 Theory and analysis: Buckling analysis of clamped ring constrained from deflecting at an arbitrary inner radius

In the analysis of Evans and Hutchinson [40], the delaminated coating was modelled as a clamped circular plate, and an asymptotic post-buckling solution developed by Thompson and Hunt [43] was modified and used to determine the post-buckled response of the coating. Strain energy arguments were then used to estimate the strain energy release rate and mode mix of the interface delamination crack.

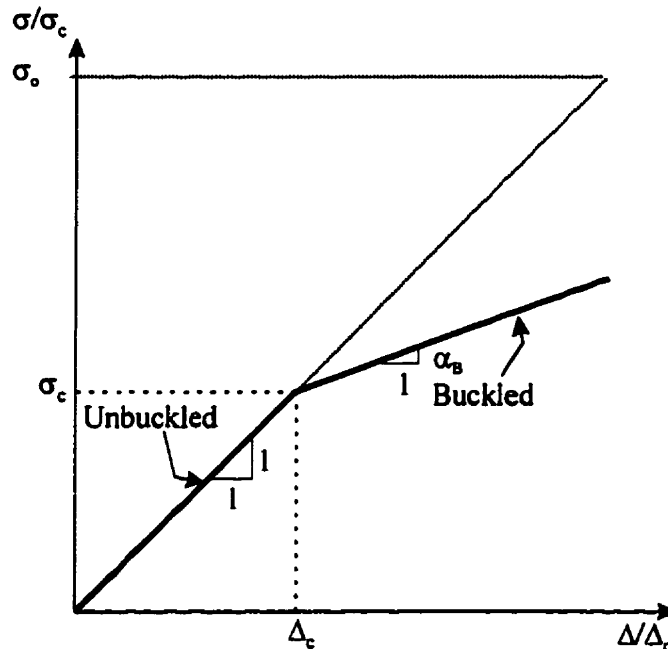


Figure 3.17: Possible equilibrium paths for an axially compressed flat plate.

Figure 3.17 depicts two possible paths that might be taken by an edge stress, σ , vs. edge displacement, Δ , curve when a flat plate is subject to an applied compressive edge force. If the edge stress is less than a critical buckling stress, σ_c , then the path taken is the one marked 'unbuckled' in Figure 3.17. Otherwise, the path taken is the one marked 'buckled'. The analysis of Evans and Hutchinson [40] relies on the calculation of the initial slope of the post-buckled path (Figure 3.17) and the calculation of the critical force at the edge of the delamination required for buckling to occur, which is expressed as a buckling parameter, C_1 defined as,

$$C_1 = \frac{P^C a^2}{D} \quad (3.7)$$

where a is the radius of delamination, P^C is the critical buckling force and D is the plane-strain flexural rigidity per unit length defined as,

$$D = \frac{Eh^3}{12(1-\nu^2)} \quad (3.8)$$

where E and h are, respectively, the Young's modulus and the thickness of the coating. The value of C_1 calculated by Evans and Hutchinson and others is 14.68 [40, 43, 44]. The analysis of Evans and Hutchinson was based on a coating free to deflect anywhere within the delamination radius. Figure 3.1, however, shows that this is not the case for the present system. The imprint of the particle is visible in the coating at the impact site and a small dot of crushed paint remains attached to the substrate, indicating that the presence of the particle may limit the buckling over a finite area. Evans and Hutchinson acknowledged this, and used a numerical analysis to calculate a buckling parameter, C_1 , of 42.68 for a buckled coating which is prevented from deflecting at a single point in the centre of the indentation; no attempt was made to calculate the initial post-buckling slope for this case [40]. Their analysis, however, is not applicable to cases, such as the present, where a finite area (i.e. more than just a single point) is prevented from deflecting. In the present work, a new post-buckling analysis developed by the author [9,10], also based on the method of Thompson and Hunt [43], was performed for cases where the coating is prevented from buckling at some radius from the centre of impact, due to the presence of the particle. This was then used to calculate the strain energy release rate and mode mix at the outer edge of the delaminating coating using an existing strain energy release rate/mode-mix analysis [38, 45].

The buckled coating is modelled as a flat plate subject to an external uniform force per unit length (circumference) P at the outer radius of delamination, $r = a$ (Figure 3.18). The outer

boundary ($r = a$) is clamped (but allowed to translate in plane), and at some radius, b , the plate is pinned (i.e. prevented from deflecting out of plane, but allowed to translate in plane) due to the presence of the impacting particle.

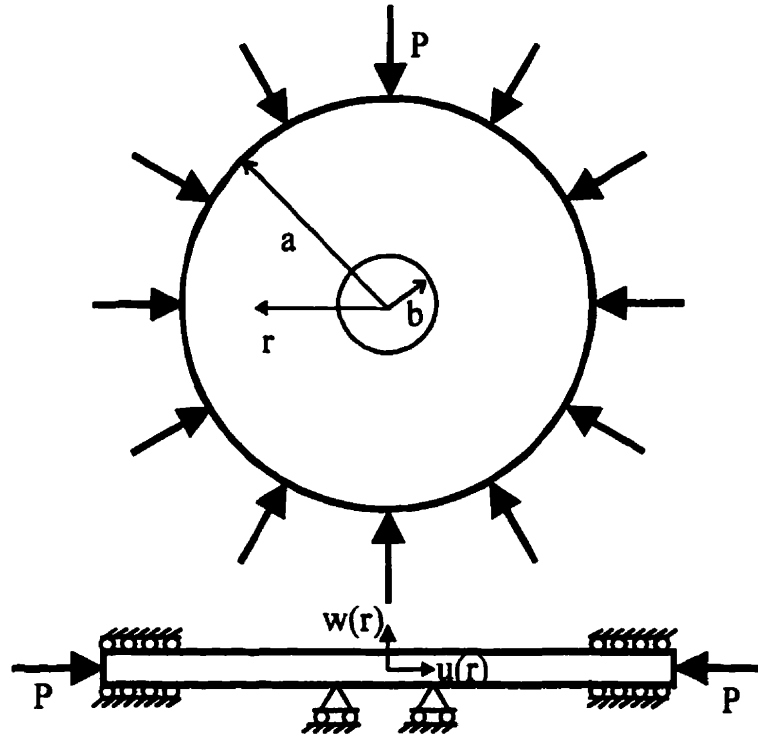


Figure 3.18: Clamped-pinned annular plate configuration used in buckling analysis.

In the absence of buckling, the “fundamental” response is,

$$\left. \begin{aligned} u^F(r) &= \frac{-P(1-\nu)}{Eh} r \\ w^F(r) &= 0 \end{aligned} \right\} \quad (3.9)$$

where $u^F(r)$ and $w^F(r)$ are the in-plane and out-of-plane displacements, respectively, of the unbuckled coating. The problem can also be interpreted as an annular ring subject to equal compressive forces per unit length, P , on the inner ($r = b$) and outer ($r = a$) boundaries.

The potential energy, V , of this system is

$$V = J_E + J_L + J_B \quad (3.10)$$

where J_E is the elastic stretching energy of the system, J_L is the work done by the force P , and J_B is the strain energy of bending which are given by,

$$J_E = \frac{Eh}{2(1-\nu^2)} \int_b^a (\epsilon_r^2 + 2\nu\epsilon_r\epsilon_\theta + \epsilon_\theta^2) 2\pi r dr \quad (3.11)$$

$$J_L = Pu(a)2\pi a - Pu(b)2\pi b \quad (3.12)$$

and

$$J_B = \pi D \int_b^a \left[w''^2 + 2\nu w'' \frac{w'}{r} + \left(\frac{w'}{r} \right)^2 \right] r dr \quad (3.13)$$

where E is the Young's modulus, h is the thickness, and ν is the Poisson's ratio of the coating, respectively, and ϵ_r and ϵ_θ are the strains in the radial and circumferential directions, respectively. The primes indicate differentiation with respect to r .

The middle surface strains, according to Von Karman non-linear plate theory, can be written as,

$$\left. \begin{aligned} \epsilon_r &= \frac{du}{dr} + \frac{1}{2} \left(\frac{dw}{dr} \right)^2 = u' + \frac{1}{2} w'^2 \\ \epsilon_\theta &= \frac{u}{r} \end{aligned} \right\} \quad (3.14)$$

Substituting equations (3.11)-(3.13) into (3.10) yields

$$\begin{aligned}
 V = \pi D \int_b^a \left[w''^2 + 2vw'' \frac{w'}{r} + \left(\frac{w'}{r} \right)^2 \right] r dr + 2\pi P (au(a) - bu(b)) + \\
 + \frac{\pi Eh}{1-\nu^2} \int_b^a \left[\left(u' + \frac{1}{2} w'^2 \right)^2 + 2v \left(u' + \frac{1}{2} w'^2 \right) \frac{u}{r} + \left(\frac{u}{r} \right)^2 \right] r dr
 \end{aligned} \quad (3.15)$$

Following the approach of Thompson and Hunt [43], the changes in displacement, due to buckling, from the fundamental (unbuckled) state are defined as,

$$\left. \begin{aligned} w(r) &= w(r) \\ u(r) &= u^F(r) + v(r) \end{aligned} \right\} \quad (3.16)$$

Substituting this into the expression for the potential energy, equation (3.15), the potential energy becomes, in terms of the incremental buckling displacements, $w(r)$ and $v(r)$,

$$\begin{aligned}
 V = \pi D \int_b^a \left[w''^2 + 2vw'' \frac{w'}{r} + \left(\frac{w'}{r} \right)^2 \right] r dr + 2\pi P \left[\begin{array}{l} a(u^F(a) + v(a)) - \\ b(u^F(b) + v(b)) \end{array} \right] \\
 + \frac{\pi Eh}{1-\nu^2} \int_b^a \left[\left(u'^F + v' + \frac{1}{2} w'^2 \right)^2 + 2v \left(u'^F + v' + \frac{1}{2} w'^2 \right) \frac{u^F + v}{r} + \left(\frac{u^F + v}{r} \right)^2 \right] r dr
 \end{aligned} \quad (3.17)$$

Substitution of the fundamental response, equation (3.9) into equation (3.17) yields,

$$\begin{aligned}
V(v, w, P) = & \pi D \int_b^a \left[w''^2 + 2vw'' \frac{w'}{r} + \left(\frac{w'}{r} \right)^2 \right] r dr - \pi P \int_b^a w'^2 r dr + \\
& + \frac{\pi E h}{1 - \nu^2} \int_b^a \left[\left(v' + \frac{1}{2} w'^2 \right)^2 + 2v \left(v' + \frac{1}{2} w'^2 \right) \frac{v}{r} + \left(\frac{v}{r} \right)^2 \right] r dr
\end{aligned} \quad (3.18)$$

where the linear terms have disappeared because the fundamental (unbuckled) state is one of equilibrium, (δV of the fundamental response equals zero). Equation (3.18) has exactly the same form as equation (3.15) except that there is a quadratic load term instead of a linear one, and can be rewritten as

$$V(v, w, P) = \int_a^b [H(w'', w', v, v')] dr \quad (3.19)$$

Taking the first variation of V ,

$$\delta V = \int_b^a \left[\frac{\partial H}{\partial w''} \delta w'' + \frac{\partial H}{\partial w'} \delta w' + \frac{\partial H}{\partial v} \delta v + \frac{\partial H}{\partial v'} \delta v' \right] dr \quad (3.20)$$

Using integration by parts, and knowing that $\delta V = 0$ must be satisfied for all δw , the resulting two differential equations are,

$$2rw'''' + 4w'''' - \frac{2w''}{r} + 2\frac{w'}{r^2} + \frac{12}{h^2} \left(\begin{array}{l} -2v'rw'' - 2w'rv'' - 3rw'^2w'' \\ -w'^3 - 2v'vw'' - 2vv'w' \end{array} \right) + \frac{P}{Eh^3} 12(1-v^2)(2w' + 2rw'') = 0 \quad (3.21)$$

for the out-of-plane response, and

$$v'' + \frac{v'}{r} - \frac{v}{r^2} + w'w'' + \frac{(1-v)w'^2}{2r} = 0 \quad (3.22)$$

for the in-plane response, with the boundary requirements given by,

$$\left. \begin{array}{l} 2rw''\delta w' - 2rw'''\delta w - 2w''\delta w + 2vw'\delta w' + \frac{2w'}{r}\delta w - \frac{12P(1-v^2)}{Eh^3}(2w'r\delta w) + \\ \quad + \frac{12}{h^2}(2rv'w'\delta w + rw'^3\delta w + 2v'vw'\delta w) \Big|_b^a = 0 \\ 2rv'\delta v + rw'^2\delta v + 2vv\delta v \Big|_b^a = 0 \end{array} \right\} \quad (3.23)$$

By integrating once, the out-of-plane equation, (3.21), can be simplified to

$$w'''' + \frac{w''}{r} - \frac{w'}{r^2} - \frac{12}{h^2} \left(v' + \frac{w'^2}{2} + v\frac{v}{r} \right) w' + \frac{12P(1-v^2)}{Eh^3} w' = \frac{k}{r} \quad (3.24)$$

where k is an integration constant to be determined from the boundary conditions:
at $r = a$ (clamped),

$$\left. \begin{array}{l} \delta w(a) = w(a) = 0 \\ \delta w'(a) = w'(a) = 0 \end{array} \right\} \quad (3.25)$$

and at $r = b$ (pinned at the inner radius due to the presence of the particle),

$$\delta w(b) = w(b) = 0 \quad (3.26)$$

After inserting equations (3.25) and (3.26) into equation (3.23), the remaining boundary conditions to be satisfied are,

$$\left. \begin{aligned} w'' + \frac{\nu}{r} w' \Big|_b &= 0 \\ \nu' + \frac{w'^2}{2} + \frac{\nu}{r} \nu \Big|_b &= 0 \end{aligned} \right\} \quad (3.27)$$

The first of equation (3.27) shows that the bending moment must be zero at the pin at b , and the second that the change in radial edge stress due to buckling is zero at both a and b . Thus, the variational procedure has provided the proper boundary conditions for the problem. The out-of-plane differential equation (3.21), and the in-plane differential equation (3.22), must be solved using the boundary conditions given by equations (3.25)-(3.27). An exact solution can be obtained numerically, but an asymptotic one [9] is sufficient for the purposes of this study, and can be obtained by the series expansion of the displacements and forces. This is explained in Appendix C.

3.5.2 Theory and analysis: Calculation of arrest strain energy release rate and mode mix for interfacial cracks

The calculation of the strain energy release rate and mode mix for interfacial cracks is, in general, complicated by the elastic mismatch between the coating and substrate, and thus some modification to the usual framework of linear elastic fracture mechanics is required [38]. Dundurs described the elastic mismatch in terms of two nondimensional parameters [46],

$$\alpha_D = \frac{\mu_S(\kappa_C + 1) - \mu_C(\kappa_S + 1)}{\mu_C(\kappa_C + 1) + \mu_S(\kappa_S + 1)} \quad \text{and} \quad \beta_D = \frac{\mu_S(\kappa_C - 1) - \mu_C(\kappa_S - 1)}{\mu_C(\kappa_S + 1) + \mu_S(\kappa_C + 1)} \quad (3.28)$$

where the subscripts C and S refer to, respectively, the coating and the substrate. In plane strain,

$$\kappa_C = 3 - 4\nu_C \quad \text{and} \quad \kappa_S = 3 - 4\nu_S \quad (3.29)$$

and μ_C and μ_S are the shear modulus of the coating and substrate, respectively. Combinations of materials that give rise to $\beta_D = 0$ give crack tip fields that are simple, and thus it is usual to assume that $\beta_D = 0$. However, in the present case, the coating is much more compliant than the substrate, and thus $\beta_D \neq 0$. In this case, the tractions on the interface at a distance r directly ahead of the crack can be written as [38],

$$\sigma_{22} + i\sigma_{12} = \frac{(K^{[1]} + iK^{[2]})}{(2\pi r)^{\frac{1}{2}}} r^{i\varepsilon} \quad (3.30)$$

where

$$\varepsilon = \frac{1}{2\pi} \ln \left(\frac{1 - \beta_D}{1 + \beta_D} \right) \quad (3.31)$$

The complex stress intensity factor $K = K^{[1]} + iK^{[2]}$ has real and imaginary parts which are similar to the conventional mode I and mode II stress intensity factors in linear elastic fracture mechanics. However, the $r^{i\varepsilon}$ term in equation (3.30) introduces an oscillating singularity which complicates matters for $\beta_D \neq 0$. In this case, the idea of mode I and mode II stress fields must be modified. Hutchinson and Suo suggested, in this case, a definition of mode mix in terms of a characteristic length, l , as follows [38],

$$\psi = \tan^{-1} \left[\frac{\text{Im}(Kl^{i\epsilon})}{\text{Re}(Kl^{i\epsilon})} \right] \quad (3.32)$$

where K is the complex stress intensity factor. A mode I crack then becomes one that has zero shear traction at a distance l ahead of the crack tip, and a mode II crack one that has zero normal traction at that point [38]. The choice of the reference length, l , is arbitrary, and Suo and Hutchinson suggest the use of the film thickness in the thin film case [38]. Comparisons of data obtained at different coating thicknesses can then be compared using the transformation law,

$$\psi_2 = \psi_1 + \epsilon \ln \left(\frac{h_2}{h_1} \right) \quad (3.33)$$

where h_1 and h_2 are the two coating thicknesses being compared. The shift is negligible for small ϵ .

Another important feature of the oscillating singularity is that the crack faces are predicted to interpenetrate at a small distance ahead of the crack tip. This further complicates matters, but, fortunately, in most cases, the size of the region in which the crack faces are in contact is very small compared to the process zone (plastic zone), and thus the usual argument of linear elastic fracture mechanics (LEFM) can be invoked (i.e. the behaviour of the material in the process zone is assumed to be characterised by the state at some distance from the crack tip where the stress state, as given by equation (3.30), is well-behaved) [47]. For the present system, the demonstrated independence of the critical interfacial strain energy release rate on geometry (i.e. coating thickness), together with the good agreement in predicted and experimentally determined delamination size (see Section 3.6.2) is used to justify the use of an LEFM approach.

Hutchinson and Suo give an estimate of the range of ψ over which the crack faces are expected to be open as a function of two parameters, l , (which characterises the size of the process zone), and L , (which characterises an in-plane length of the geometry being considered). For $\epsilon > 0$, the condition for which the crack is open is [38],

$$-\frac{\pi}{2} + 2\epsilon < \psi < \frac{\pi}{2} + 2\epsilon - \epsilon \ln\left(\frac{1}{10} \frac{L}{l}\right) \quad (3.34)$$

For a coated system, typical values of l and L are, respectively, the coating thickness, and the crack length. It will be shown in Section 3.6 that, for the present case, this range is very large. For a more detailed discussion of bimaterial interfaces under conditions of nonzero β , the reader is referred to reference [38].

Expressions for the strain energy release rate and mode mix, as defined above, for the case of a thin coating on a substrate are [38]:

$$G = \frac{6(1-\nu^2)}{Eh^3} \left(M(a)^2 + \frac{h^2 P^2}{12} \right) \quad (3.35)$$

$$\tan \psi = \frac{\text{Im}(Kh^{i\omega})}{\text{Re}(Kh^{i\omega})} = \frac{\sqrt{12}M(a) \cos \omega - hP \sin \omega}{-\sqrt{12}M(a) \sin \omega - hP \cos \omega} \quad (3.36)$$

where K is the complex stress intensity factor, G is the strain energy release rate, ψ is the phase angle (which is a measure of the relative amounts of mode I and mode II at the interface, i.e. the mode mix) and $M(a)$ and P are the bending moment per unit circumference and force per unit circumference, respectively, at the delaminated edge ($r = a$), as shown in Figure 3.19. The value of ω depends on the elastic mismatch at the interface between the coating and substrate and can be found from the tables in reference [45].

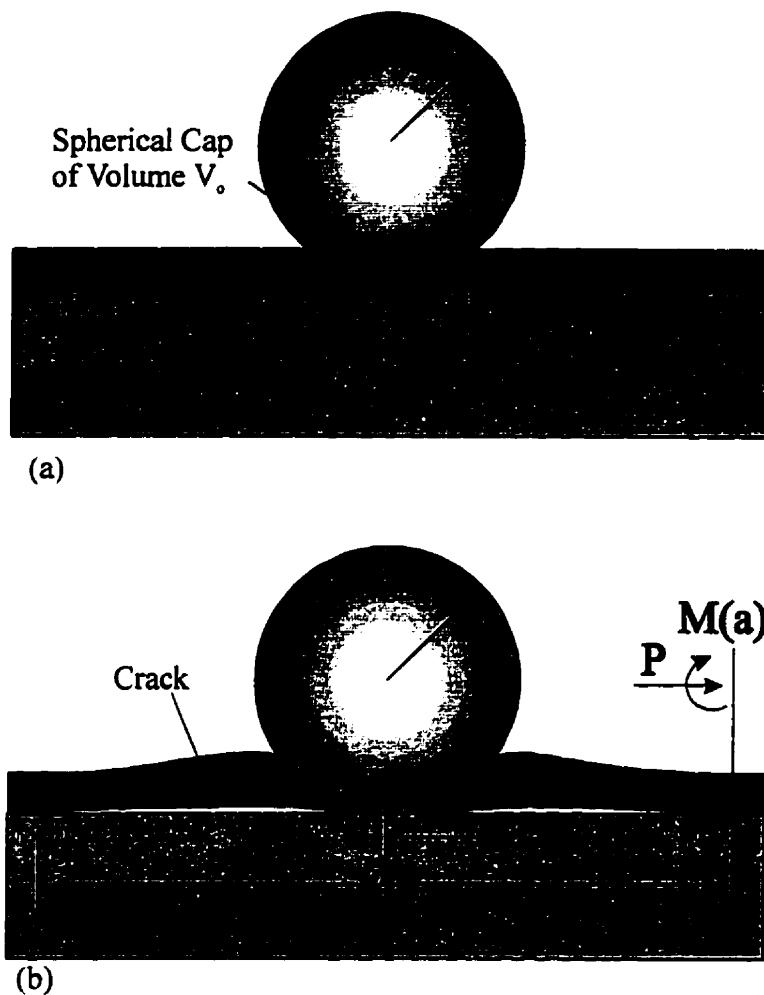


Figure 3.19: Configuration of impact site, (a) unbuckled, (b) buckled. Force, P , and moment, M , reactions in coating at edge of delamination ($r = a$).

In order to find the strain energy release rate and phase angle as defined in equations (3.35) and (3.36), the reactions $M(a)$ and P are required. The above buckling analysis can be used to find these as follows [9]. Figure 3.17 illustrates the post-buckled path. Assuming an indentation of volume V_0 , as shown in Figure 3.19, a displacement of Δ must be applied at the edge of the clamped ring ($r = a$) in the unbuckled configuration in order to offset the dilatation of the coating due to the indentation, which is given by [40],

$$\Delta = \frac{V_o}{2\pi ah} \quad (3.37)$$

This induces a compressive biaxial stress in the disk, in the unbuckled state, of

$$\sigma_o = \frac{EV_o}{2\pi(1-\nu)ha^2} \quad (3.38)$$

The initial slope of the buckled path (Figure 3.17) can be found by applying the results of the post-buckling analysis. Let Δ be the in-plane displacement at $r = a$ in the buckled configuration, and let

$$\Delta_c = u_c^F(a) = -\frac{P^c(1-\nu)a}{Eh} \quad (3.39)$$

be the critical displacement at the outer edge of the delamination ($r = a$) necessary for buckling to occur. The critical compressive stress to initiate buckling, σ_c , using equation (3.7), can then be written as,

$$\sigma_c = \frac{C_1 Eh^2}{12(1-\nu^2)a^2} \quad (3.40)$$

and, using equation (3.38), the buckling condition is expressed as a critical indentation volume, V_c ,

$$V_c = \frac{C_1 \pi h^3}{6(1 + \nu)} \quad (3.41)$$

The slope of the unbuckled portion of Figure 3.17 is 1. The equation for the buckled portion of Figure 3.17 can be written as:

$$\frac{\sigma}{\sigma_c} = \alpha_B \frac{\Delta}{\Delta_c} + (1 - \alpha_B) \quad (3.42)$$

where α_B is the initial slope of the post-buckled portion of the curve. When the coating buckles, the displacement at the outer edge ($r = a$) is, using equation (3.16),

$$u(a) = u^F(a) + v(a) = \Delta \quad (3.43)$$

where $v(a)$ is the additional in-plane displacement due to buckling. The initial post-buckled slope is written, using Figure 3.17, as,

$$\alpha_B = \frac{\frac{P}{P^c} - 1}{\frac{\Delta}{\Delta_c} - 1} \quad (3.44)$$

Manipulating equations (C.1), (C.14), (C.25), (3.40), (3.43) and (3.44), the slope becomes,

$$\alpha_B = \frac{1}{1 - \frac{av_2(a)24(1+\nu)}{C_2}} \quad (3.45)$$

which, although not obvious, is independent of a for fixed $p = b/a$. Equation (3.45) is the initial post-buckled slope, and its dependence on p is shown in Figure C.2 in Appendix C.

Rewriting equation (C.25),

$$\frac{s}{h} = \left[\left(\frac{P}{P^c} - 1 \right) \frac{2C_1}{C_2} \right]^5 \quad (3.46)$$

and using equation (3.44), and the fact that (Figure 3.17),

$$\frac{\Delta}{\Delta_c} = \frac{\sigma_o}{\sigma_c} = \frac{V_o}{V_c} \quad (3.47)$$

gives,

$$\frac{s}{h} = \left[\alpha_B \left(\frac{V_o}{V_c} - 1 \right) \frac{2C_1}{C_2} \right]^5 \quad (3.48)$$

Noting that,

$$M(r) = -D \left(w''(r) + \frac{\nu}{r} w'(r) \right) \quad (3.49)$$

where $M(r)$ is the bending moment per unit length, equations (C.11), (C.25), (3.48) and (3.49) can be used to find the force, P , and the bending moment $M(a)$ at the edge of the delamination

(Figure 3.19) for subsequent substitution into equations (3.35) and (3.36) to find the arrest value of the strain energy release rate and mode mix for cracks due to indentation-induced buckling.

3.5.3 Estimation of critical interfacial shear stress required to initiate delamination

The above analysis works well for estimating the arrest values of the strain energy release rate and phase angle of cracks in thin buckled coatings, but makes no mention of how the cracks initiated. Equation (3.38) shows that the biaxial stress induced by the indentation of the coating, and thus the strain energy release rate, increases sharply as the delamination radius decreases. It is difficult to determine the magnitude of the strain energy release rate under these conditions, because the initial location and size of the interfacial crack cannot be determined accurately, and because of the difficulty in obtaining the stress state in this area.

If one assumes a completely plastic zone directly below the indenting sphere, roughly the shape of a cylinder with radius c (contact radius), and height h (coating thickness), and the further assumption is made that the crack initiates from the edge of this zone, Matthewson [48] has developed a model for determining the interfacial shear stress required to initiate an indentation-induced delamination. This analysis shall be referred to as the 'plastic hole Matthewson analysis'. Conceptually, the analysis involves removing the cylinder of plastically deformed material, and replacing it by a radial compressive pressure equal to $2/3$ times (determined using Tresca criterion) the mean contact pressure required to create the plastic zone. This radial compressive pressure is then used as a boundary condition in the approximate elastic stress analysis presented in Appendix B, and the resulting expression for interfacial shear stress at the edge of the hole ($r = c$) is [48],

$$\tau = \frac{-\left(\frac{2}{3}\right)p_d}{\frac{K_1'\left(\frac{\chi c}{h}\right)}{K_1\left(\frac{\chi c}{h}\right)} + \frac{\nu h}{\chi^2 c}} \quad (3.50)$$

where p_d is the mean pressure (dynamic hardness), $K_1'(x) = dK_1(x)/dx$, $K_1(x)$ is the first-order modified Bessel function of the second kind, ν is Poisson's ratio of the coating, c is the contact radius, h is the coating thickness, and

$$\chi = \left[\frac{6(1-\nu)}{4+\nu} \right]^{\frac{1}{2}} \quad (3.51)$$

The normal stress across the interface is predicted to be zero. It should be noted that this approximate analysis is based on normal stresses and strains which are averaged through the thickness of the coating (as in the case in Appendix B), and thus, the resulting interfacial shear stress is not suitable for the calculation of the energy release rate and phase angle. Nevertheless, this nominal value of the interfacial shear stress at initiation is useful in describing the conditions under which initiation of a debond will occur (this will be demonstrated below).

3.6 Experimental verification of impact-induced buckling mechanism

The aim of this section is to verify the theory presented in Section 3.5 through experiment. In order to test the analysis, individual glass spheres (the same used in Section 3.3, 0.64 mm diameter, $m=0.364$ mg, $E=70$ GPa) and steel spheres (0.73 mm diameter, $m=1.49$ mg, $E=210$ GPa) were launched against alkyd coated steel panels (same as described in Section 3.2) of varying paint film thickness (20 - 50 μm), and the incident and rebound velocities were measured photographically, in the manner outlined in Chapter 2.

The coating always delaminated at the interface between the coating and the steel substrate, leaving a raised blister of coating as shown in Figure 3.1. This blister was thought to be due to the coating buckling, hence motivating the analysis of Section 3.5. In order to perform the buckling analysis, the indentation volume, V_o , the radius at which vertical deflection is prevented from occurring due to the presence of the particle, b , and the radius of delamination, a , were determined as described below [10].

3.6.1 Determination of indentation volume, V_o and radius at which buckling is prevented from occurring due to presence of particle, b

In Section 3.4.2, it was found that the kinematics of a single particle as it penetrates into the coated substrate (under conditions of impact) could be described well by a simple plastic-flow model. The coating was assumed to behave locally in a fully plastic manner during the impact, resisting indentation with a constant dynamic flow pressure (or dynamic hardness). The dynamic flow pressure is similar to the hardness in static indentation tests, and is defined as the force divided by the area over which the force is being applied by the indenting particle. Once p_d has been determined, the indentation depth, d , can be easily obtained via equations (3.5) and (3.6), and calculation of the indentation volume, V_o , for use in the buckling and strain energy release rate, becomes a simple matter of geometry.

In the cases where the incident velocity is just sufficient to cause penetration of the particle to the substrate (Figure 3.20 (a)), the calculation of V_o is simply the volume of the spherical cap portion of the sphere bounded by the coating thickness, h . The radius at which the coating is prevented from deflecting, b , is taken to be the contact radius between the particle and substrate ($b = 0$ in this case). In cases where the incident velocity is greater than that required to just penetrate the coating to the substrate (Figure 3.20 (b)), the calculation of V_o and b are more complicated, because the deformation of the particle as it collides with the hard steel substrate after penetration will displace additional coating. It is believed that this is the principle mechanism responsible for the growth in delamination area as the incident kinetic energy increases.

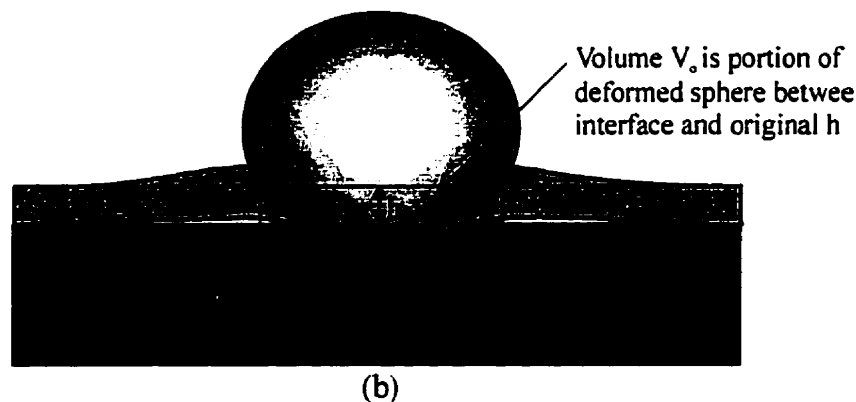
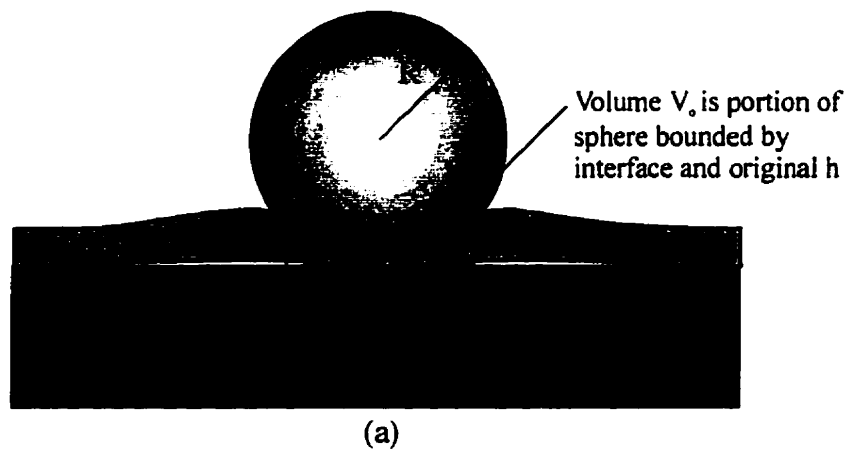


Figure 3.20: Calculation of indentation volume, V_o , and radius, b , at which coating is prevented from buckling due to presence of indenting particle: (a) penetration of particle to coating/substrate interface. (b) penetration of particle into substrate.

A complete analysis of the kinematics of the indenting particle would take into account the elastic-plastic behaviour of the coating, particle and the substrate, as it penetrates the coating. Because such an elastic-plastic compliance relationship is difficult to obtain, a Hertzian analysis [15] was used to model the deformation of the particle and substrate after penetration into the bare steel substrate. The resistance to indentation provided by the coating after the particle had reached the substrate was ignored, as was the deformation of the particle due to the coating. The indentation volume, V_o , in this case, was taken as the portion of the deformed

sphere bounded by the original interface between the coating and substrate, and the original coating thickness. After the particle penetrated to the bare substrate, the collision proceeded as if the particle were incident on a bare substrate, as explained in Section 3.4.2. The deformation of the particle after penetration to the steel substrate was thus modelled as quasi-static Hertzian, with incident kinetic energy equal to the difference between the total incident kinetic energy and the incident kinetic energy required to penetrate the coating to the bare steel substrate (Table 3.2). The radius at which the coating is prevented from deflecting due to the presence of the impacting sphere, b , is approximated as the contact radius between the particle and the substrate in this Hertzian analysis, as shown in Figure 3.20(b). The deflected profile obtained from the Hertzian analysis was then used to calculate the indentation volume, V_0 , and b , for use in the buckling analysis of Section 3.5.2.

It should be noted that after penetration to the bare substrate, there would, in some cases, be enough kinetic energy left over to plastically deform the substrate. In these cases, the Hertzian analysis must be regarded as approximate. Nevertheless, two experimental observations suggest that this approximation is valid: (1) There was a range of incident kinetic energies where the coating was removed (i.e. the particle penetrated to the bare substrate), but no visible permanent deformation was evident in the substrate; and (2) No damage or permanent deformation was seen in the impacting particles.

The choice of the Hertzian contact radius between the particle and steel substrate as b , the radius to which the coating is prevented from buckling due to the presence of the particle, is motivated, in part, by the fact that a small dot of crushed paint was left attached to the substrate after the buckled paint chip delaminated (Figure 3.2(a)). This was paint that was trapped between the particle and the substrate, and was roughly the size of the Hertzian contact radius for a sphere impacting on a bare steel substrate at the appropriate kinetic energy, as explained above (i.e. the total energy minus the portion required to penetrate the coating to the bare substrate).

3.6.2 Calculation of reactions, arrest strain energy release rate, and phase angle at edge of delamination

The delamination radius, a , for collisions between glass and steel spheres and alkyd coated panels at various incident velocities was obtained using image analysis in the manner explained in Section 3.3.1. The indentation volume, V_o , and radius at which coating deflection was prevented from occurring, b , (due to the presence of the impacting particle) was calculated, for both the case of complete indentation of the coating (where coating removal just begins to occur), and for penetrations beyond the coating thickness.

h (μm)	N	Particle	V_n (m/s)	α (deg.)	Ave. a (μm)	b (μm)	V_o ($\text{m}^3 \times 10^{-12}$)	V_c ($\text{m}^3 \times 10^{-12}$)	Arrest G_c (J/m^2)	ψ (deg.)
20	15	glass	20	90	208	0	0.394	0.131	222	2.2
40	16	glass	40	90	375	0	1.54	1.05	229	12.7
40	5	steel	20	90	402	0	1.77	1.05	219	9.0
24	3	glass	59	90	330	71	1.15	0.214	222	-8.8
24	10	glass	31	90	293	47	0.838	0.177	203	-4.0
40	18	glass	58	90	440	64	2.35	0.921	250	-0.6
40	5	steel	25	90	416	52	2.34	0.915	298	1.1
40	3	steel	87	90	561	103	3.92	0.950	210	-6.0
40	6	steel	45	90	489	80	3.10	0.932	252	-3.7
40	5	steel	57	90	504	86	3.28	0.937	246	-4.4
50	12	glass	50	90	513	49	2.99	1.80	197	9.0
24	11	glass	31	38	284	47	0.838	0.202	233	-4.5
40	12	glass	58	46	421	64	2.35	0.924	303	-1.1
40	8	glass	58	33	418	64	2.35	0.925	313	-1.2

Table 3.5: Experimentally determined arrest strain energy release rates (G_c) and phase angles (ψ) for glass and steel spheres impacting alkyd coatings of varying thickness. h = coating thickness, N = number of experiments performed, V_n = normal component of incident velocity, α = incident angle of attack, Average a = average delamination radius, b = radius at which coating is prevented from deflecting due to presence of particle, V_c = critical indentation volume to cause buckling, V_o = calculated indentation volume.

The buckling analysis (Section 3.5.1) was then used to find the bending moment, $M(a)$, and compressive force, P , per unit circumference at the edge of the delaminated coating. These

reactions were used, together with the delamination radius, a , to calculate the arrest value of the strain energy release rate, G , and the phase angle, ψ , for the impact sites, as explained in Sections 3.5.1 and 3.5.2. The phase angle calculation requires the calculation of a parameter ω , which depends on the Dundur's parameters. This value was extrapolated from the tables in Reference [45] as 52.5° . To facilitate calculations, the plastic and Hertzian analyses required for calculation of V_0 and b , the buckling analysis required for calculation of $M(a)$ and P , and the strain energy release rate/phase angle analysis were all set up in a MathCad Plus 6.0 (Mathsoft Inc.) worksheet, and the results are shown in Table 3.5. The MathCad implementation can be found in Appendix D.

In Section 3.5.2, it was noted that some coating/substrate combinations give rise to interfacial crack stress fields that are more complicated than the usual ones of linear elastic fracture mechanics. The present alkyd/steel system is one such system. The parameters that describe the elastic mismatch at the bimaterial interface are the Dundur's parameters α_D and β_D (see [38,45]). For the present system, $\alpha_D = -0.975$, and $\beta_D = -0.153$. The fact that $\beta_D \neq 0$ introduces an oscillating singularity in the stress field directly ahead of the interfacial crack, which can be described by a parameter ε (equal to 0.049 for the present system). A result of this complication is that the crack faces are predicted to interpenetrate at some distance behind the crack under certain conditions. Hutchinson and Suo [38] give an estimate of the range of phase angles, ψ , over which this is not expected to occur as a function of l , which characterises the size of the process zone (plastic zone at crack tip), and L , which characterises an in-plane length of the geometry being considered. If l is taken as a typical coating thickness, h , and L is taken as a typical radius of delamination, a , then, for the present system, the range is found to be on the order of $-84^\circ < \psi < 90^\circ$. The phase angles obtained with the present system (Table 3.5) are well within this range, so it is expected that the crack faces will not interpenetrate in any of the present cases.

For nonzero β , the phase angle must be defined in terms of a characteristic length, l . A mode I crack then becomes one that has zero shear traction at a distance l ahead of the crack tip, and a mode II crack one that has zero normal traction at that point [38]. For coatings, l is

usually taken as the coating thickness, h , which creates a problem if comparisons of G and ψ are made between different coating thicknesses. Fortunately, the ψ transformation given in equation (3.33) (which is a function of only the thicknesses involved and ϵ), and discussed in Section 3.5.2, can be used to convert between coating thicknesses. For the present system, taking the largest and smallest coating thickness (20 and 50 μm) gives a conversion factor of approximately 2.5° which must be added to the phase angle of the smaller thickness. Because this change is well within the experimental scatter of the data, it was ignored. For a detailed discussion of bimaterial interface cracks, the reader is referred to reference [38].

Each one of the entries in Table 3.5 represents the average of measurements for multiple experiments performed at each coating thickness. It was necessary to perform multiple experiments due to the relatively large scatter in coating removal radius experienced in these types of experiments [see Figure 3.6, for example]. It should be noted that the last three rows of Table 3.5 represent experiments performed at angles of attack different than 90° (i.e. not at normal incidence). In these cases, the collision was treated using only the normal component of incident velocity, and the delamination radii are average values (since for an angle of attack different from 90° , the delaminations are slightly skewed into ovals).

The first three rows in Table 3.5 represent particle velocities to just penetrate the coating to the steel substrate (Table 3.2), and the arrest strain energy release rates, G_c , should be very close to each other. This is because the strain energy release rate should be a property of the interface, and the dependence on coating thickness should thus be very weak (assuming also a weak dependence of critical strain energy release rate on phase angle over the relatively small range of phase angles in Table 3.5). The remaining entries in Table 3.5 are for velocities where the particle penetrates through the coating and into the steel substrate. Overall, the arrest strain energy release rates do not change much (average = 243 J/m^2 , standard deviation = 37 J/m^2) which is again to be expected because of the assumed weak dependence of strain energy release rate on phase angle over the range of phase angles considered. The differences are probably due more to experimental scatter than any phase angle dependence.

If the average of the first three values of G_c (Table 3.5, onset of delamination) are taken as a material property of the system, and again, assuming that G_c does not change significantly over the range of phase angles considered, predictions can be made of the delamination radii for cases in which the incident kinetic energy is such that the particle penetrates through the coating and into the substrate. The incident energy required to penetrate the coating to the substrate was subtracted from the total incident energy, and this remaining energy was used as the incident kinetic energy on a bare substrate in the Hertzian analysis giving b and V_o , as explained above. The delamination radius was then adjusted in the buckling analysis until the arrest strain energy release rate equalled G_c , the average of the first three values in Table 3.5 (223 J/m^2). This value of delamination radius was taken as the predicted delamination radius, and is compared to the measured delamination radius in Table 3.6.

Coating Thickness, h (μm)	Angle of Attack (deg.)	Incident Normal Velocity, V_n (m/s)	Measured Delamination Radius, a_m (μm)	Predicted Delamination Radius, a_p (μm)	Percent Difference $2(a_p - a_m)/(a_m + a_p) \times 100$
24	90	59	330	330	0
24	90	31	293	287	-3
40	90	58	440	452	3
40	90	25	416	445	7
40	90	87	561	554	-1
40	90	45	489	503	3
40	90	57	504	515	2
50	90	50	513	498	-3
24	38	31	284	287	1
40	46	58	421	452	7
40	33	58	418	452	8

Table 3.6: Comparison of measured and predicted delamination radii for last eleven data points of Table 3.5.

The entries in Table 3.6 correspond to the last eleven entries of Table 3.5. The agreement between measured and predicted delamination radii is good, particularly given the scatter

inherent to fracture phenomenon of this type, and the fact that the variation in critical strain energy release with respect to phase angle was ignored.

3.6.3 Estimation of critical interfacial shear stress required to initiate delamination

Initiation values of strain energy release rate and mode mix (phase angle) are not easily obtained. However, a method to estimate the critical interfacial shear stress required to initiate delamination has been developed [48] and discussed in Section 3.5.3 (plastic hole Matthewson analysis). Conceptually, the model involves removing a cylinder of radius c (the coating contact radius) and height h (coating thickness), which is assumed to be the size of the plastic zone under the indentation, and replacing it with radial compressive stress equal to $2/3$ times (due to the Tresca criterion) the dynamic hardness, p_d . A nominal value of the interfacial shear stress at the edge of this hole (where a delamination crack is assumed to initiate) was calculated using the simple stress analysis [48]. The MathCad Plus 7.0 (Mathsoft Inc) sheet constructed to perform this analysis can be found in Appendix D. The parameters that are required are the dynamic hardness, p_d (Table 3.2), and the contact radius, c . The model is only valid for indentations which are less than or equal to the thickness of the coating (i.e. it is not valid for cases in which the particle penetrates to the substrate causing particle and substrate deformation), and was originally developed for static indentations. It can easily be extended to collisions using the ideally-plastic collision model used in Section 3.4.2.

Coating Thickness h (μm)	Particle	Incident Velocity (m/s)	Coating Contact Radius, c (μm)	Penetration depth, d (μm)	Dynamic Hardness (MPa)	Interfacial Shear Stress, τ (MPa)
20	glass	20	111	20	190	110
40	steel	20	166	40	170	96
40	glass	40	155	40	190	108
50	glass	45	173	50	155	88

Table 3.7: Nominal interfacial shear stress at the edge of the 'plastic hole' using analysis explained in Section 3.5.3 and Reference [48]

Taking the values of dynamic hardness shown in Table 3.2, and calculating the contact radius at incident velocities required to just penetrate the coating results in the nominal interfacial shear stress values (at the edge of the plastic zone) shown in Table 3.7. The values are relatively constant (maximum difference between two values is about 20 %). This, together with the fact that the coating does not delaminate until the values of incident velocity in Table 3.7 are reached, indicates that the delaminations initiate under similar conditions regardless of coating thickness and particle size.

3.7 Angular Particles

The preceding analysis for spherical particles showed that the extent of buckling was largely dependent on the volume of coating displaced by the impacting particle. The analysis and experiments were simplified by the fact that the problem was axi-symmetric and that tangential effects could be ignored. For angular particles, problems arise in both an experimental and a theoretical study. The extent of buckling should still depend on the volume of coating displaced, but in order to calculate this, the particle size and shape, as well as the exact orientation of the particle at the moment of impact, would have to be known. One would have to characterise the incident particles in terms of their size and shape, and then ensure that they arrive at the target in a known orientation. In the literature, the only investigator to study angular impacts was Hutchings, who filmed impacts of square plates with metal targets using high-speed photography [7]. The particles in that study were essentially two dimensional, with the impact occurring with the plane of the plate normal to the target surface. Unfortunately, the experimental apparatus described in Chapter 2 was not suited to such experiments.

Even if an experimental study were possible, the difficulties associated with the analysis would be formidable. A numerical analysis of the type presented in Chapter 5 would have to be performed in order to calculate the trajectory of the particle as it cut/ploughed through the coating in order to calculate the volume of coating displaced. This having been done, a post-buckled analysis would have to be performed without the convenience of the problem being axi-symmetric. Even in the simple case of a two-dimensional square particle of the type Hutchings used [7], impacting at normal incidence, the compressive stresses induced in the

coating would be difficult to analyse because the simplification of equi-biaxial stress would not exist. Such an analysis would be impossible in closed-form and could only be performed numerically using finite element analysis (FEA).

In order to qualitatively assess the behaviour of the alkyd/steel system when impacted by angular particles, a series of simple experiments was performed. Irregular glass media was sorted by hand, and characterised using image analysis software. The parameters used to describe the size and shape were roundness ratio (ratio of the perimeter to 4π times the projected area of the particle), aspect ratio (ratio of longest to shortest length measured), and maximum length. The particles were measured individually in 5 random orientations, and the results were averaged. Only particles that met the following criteria were used in the experiments: roundness ratio = 1.2 to 1.4, aspect ratio = 1.2 to 1.4, maximum length = 0.8 to 1.0 mm. The average mass (0.442 mg) was found by measuring the total mass of 85 such particles, and dividing by 85. Single particles of the type meeting the above criteria were then launched at various incident velocities and angles of attack against 40 μm coating thickness specimens, and the impact sites were photographed.

It was hoped that by calculating the radius of a sphere of equivalent mass (0.34 mm) of the irregular particles, it might be possible to use the methods of this chapter to predict delamination behaviour. This, however, proved not to be the case. Examination of the impact sites revealed that none of the trends with respect to dependence of area removed on incident angle, velocity, etc. that were observed for spherical particles occurred with angular particles. In fact, it was found that, even under identical incident angle and velocity, some impacts caused buckling, and some did not. In the cases where buckling did not occur, there were simply depressions in the coating at the impact site, with no material removal. In addition, it was noted that the particles sometimes fractured upon impact, a phenomenon not observed in the impact of glass spheres.

An example of a site where buckling did occur is shown in Figure 3.21. Even at normal incidence, the loss of symmetry discussed above is evident. The buckled material is all on one side of the impact site. Removal of the buckled portion via the tape method discussed in

Section 3.3.1 revealed extensive damage to the substrate in the form of a dent in the steel. Other impacts performed at the same incident conditions revealed no buckling, but with dents left in the steel substrate below the impact site. It was found that the delamination area was always less for angular particles than that found for spherical particles of equal mass.



Figure 3.21: Impact site for irregular glass particle launched at 42 m/s and normal incidence.

The fact that such unpredictable behaviour occurs is most likely due to the fact that the orientation of the particle upon impact is variable and highly significant. In some experiments, a blunt portion of the particle probably contacted the coating, causing a large volume of coating to be displaced, and buckling to occur as in Figure 3.21. In other cases, a sharp point might have contacted, causing the particle to penetrate through the coating to the substrate, but, in the process, not displacing enough coating volume to cause buckling. In this case, the coating does not delaminate, but there is still damage to the substrate due to the particle hitting the substrate, a very undesirable effect in many blast cleaning applications.

The analysis of Chapter 5 reveals that, in angular particle impacts, a significant amount of incident kinetic energy can be converted to rotational energy upon impact. This energy is, for coating removal purposes, wasted, because the rotational energy is better used displacing the volume necessary to cause buckling to occur. In addition, with angular particles, energy is also wasted in fracturing the particle.

The above arguments and observations lead to the conclusion that spherical particles are most effective in removing coatings that buckle delaminate because of the low rebound

rotational energy, low probability of particle fracture, and the possibility of coating delamination without substrate damage. For this reason, further investigation of angular impacts for this coating system was not pursued.

3.8 Summary

For this alkyd/steel/glass bead system, both the onset and magnitude of coating delamination was controlled by normal impact effects, and a maximum in coating removal occurred at normal incidence with spherical particles. A quasi-static deformation analysis was sufficient to predict the critical amount of normal energy required to penetrate a coating of given thickness. This critical normal kinetic energy was found to correlate with the onset of coating removal, and was independent of total incident energy and angle of attack. A range of incident normal kinetic energies was found where the coating was removed without damaging the steel substrate.

The initiation of removal of the coating was consistent with the generation of a quasi-static critical interfacial shear stress. The critical shear stress appeared to be reached after the coating was completely penetrated. Thereafter, it was assumed that the particle continued the collision with the bare substrate, causing significant lateral deformation as the particle flattened, leading to a further increase in interfacial shear stress.

Analytical techniques have been developed to determine the arrest value of the strain energy release rate and the phase angle for impact-induced buckling of thin coatings on rigid substrates. The theoretical model [9] for indentation-induced buckling of thin coatings on stiff substrates has been verified experimentally using data for individual glass and steel spheres impacting against a painted steel substrate. It was found that the kinematics of particle penetration through the coating to the substrate could be accurately described using an ideally-plastic indentation model. Subsequent deformation of the substrate and particle were adequately described by a quasi-static Hertzian analysis. The coupling of a novel buckling analysis and an existing strain energy release/mode-mix analysis [38] resulted in accurate predictions of the coating delamination radius for a variety of impact conditions.

Chapter 4

Urethane Coating/Epoxy Primer/Aluminum Substrate System

In Chapter 3, single glass beads were launched against substrates coated with an alkyd paint, for the purpose of understanding the fundamental mechanisms which govern the removal of organic coatings in blast cleaning. The examination of impact sites from these experiments revealed behaviour consistent with coating delamination due to the buckling of the coating. Further experiments with an automotive topcoat have indicated that this delamination behaviour may be typical of a class of coatings having relatively weak interfacial bond strength [8]. In this chapter, a second class of coatings that cannot be made to delaminate, regardless of impact conditions due to their relatively high hardness and interfacial strength, is examined. These coatings must be removed by mechanical erosion. The rigid-plastic theory of Section 3.4.2 and a novel elastic-plastic theory are used to predict the crater size, shape, and rebound parameters as a function of incident velocity and angle for collisions between both spherical and angular particles and a thin organic coating on an aluminum substrate. Most of the material in this chapter will soon be published by the author [49].

4.1 Experiments

Impact experiments were carried out on a model system consisting of a typical aerospace coating system: MIL-P-23377 epoxy polyamide primer (nominal 25 μm thick) with MIL-C-83286 polyurethane topcoat (nominal 75 μm thick) on 0.66 mm thick AA2024-T3 clad aluminum panels (pretreated with a chemical conversion coating). All painted panels were prepared by the Canadian Department of National Defence.

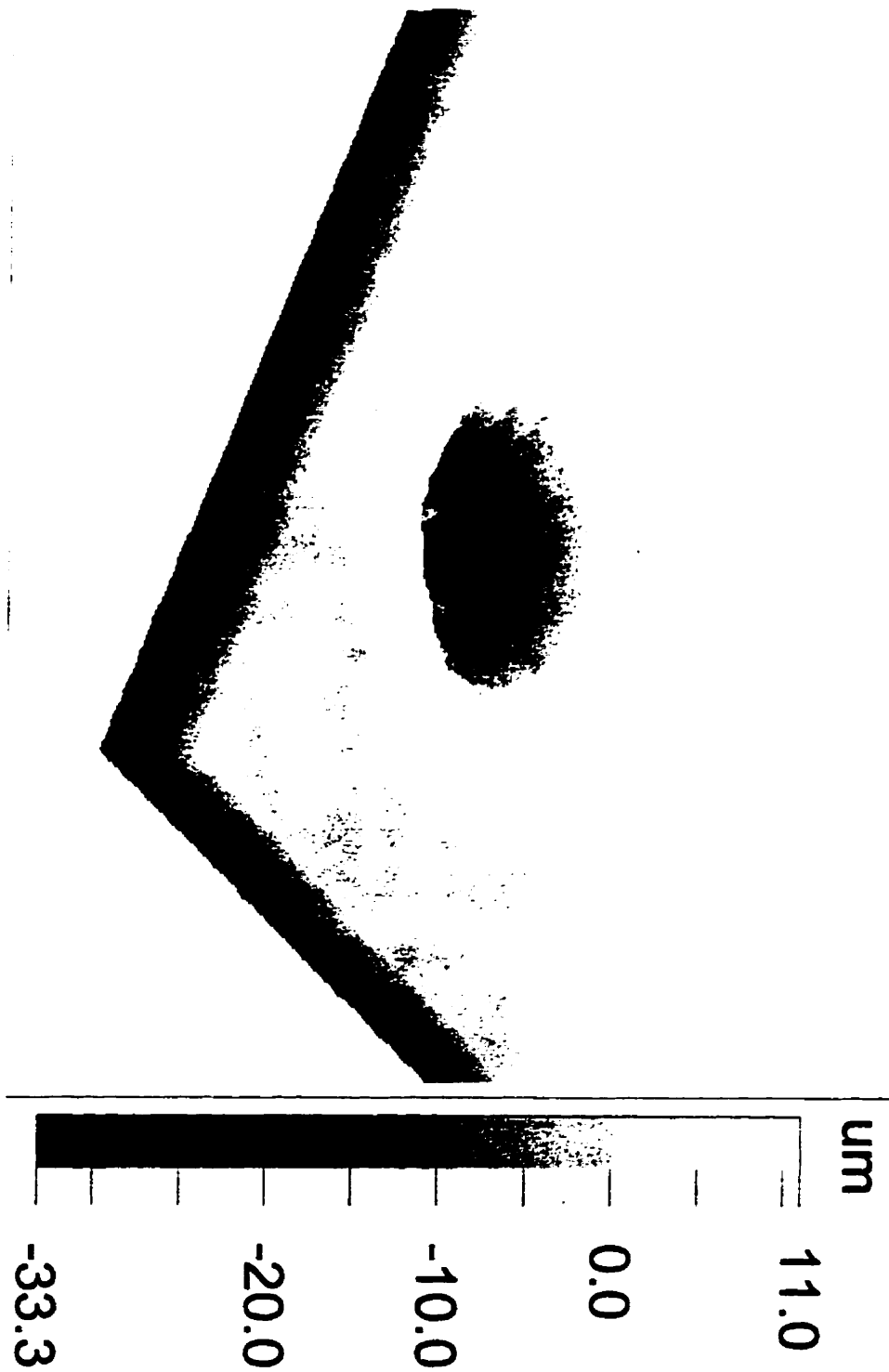


Figure 4.1: WYKO three-dimensional profile of impact site for normal incidence and 55 m/s incident velocity.

Using an ultrasonic time-of-flight method (same used in Section 3.2), the Young's Modulus and Poisson's Ratio of the coating were found to be, respectively, 4.57 GPa, and 0.376. Using the setup of Chapter 2, steel spheres (diameter = 0.89 ± 0.01 mm, mass = 2.92 ± 0.2 mg) were launched at these coated panels at different velocities and angles of attack, keeping the total incident velocity constant at 55 m/s.

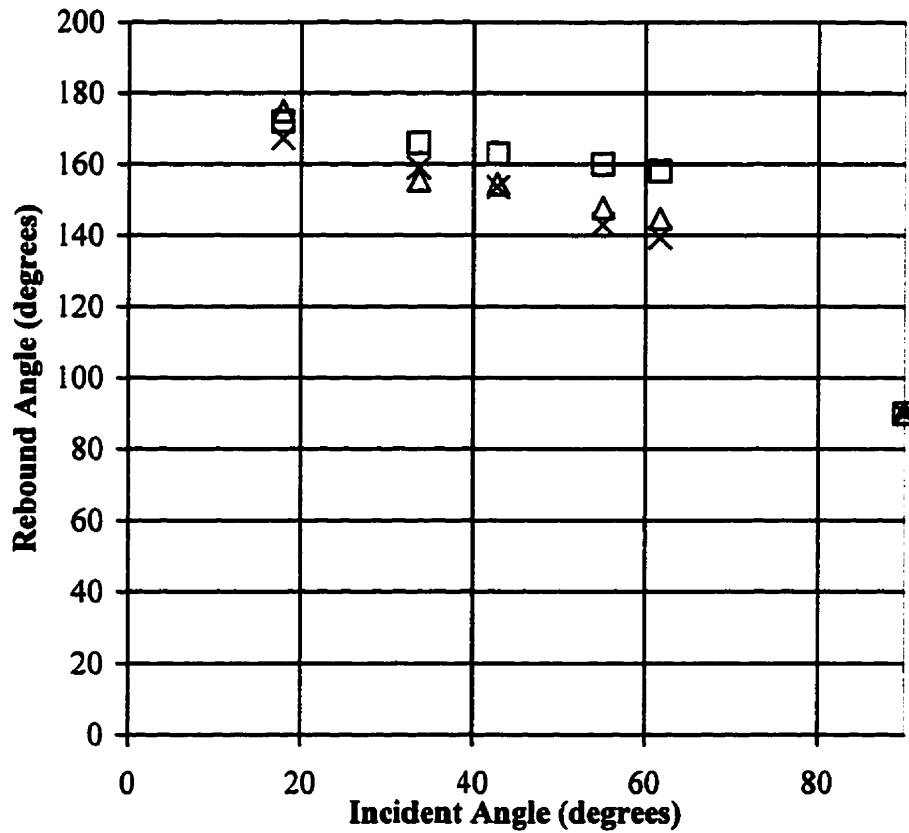


Figure 4.2: Rebound angle versus incident angle. Total incident velocity = 55m/s. X - measured values, Δ - predicted values using present elastic-plastic analysis, □ - predicted values using fully-plastic model [24]. Error bars representing ● 1 standard deviation in the five trials for each data point, are so close that they are overlaid by the data symbols, and thus are omitted here. All three symbols overlie each other at 90° incident angle.

Incident and rebound velocities and angles were measured using a video camera and strobe lights as described in Chapter 2. The three-dimensional profiles of the impact craters were also obtained with an optical surface profilometer (WYKO), with a resolution on the

order of the wavelength of white light. An example of a three-dimensional profilometer scan can be found in Figure 4.1. The raised material at the edges of the crater is thought to be available for knock-off by subsequent impacts.

The measured rebound angles and velocities are plotted versus the angle of attack in Figure 4.2 and Figure 4.3, respectively. Each experimental data point represents the average of five measurements. The incident and rebound angles were measured from the same origin on the surface of the paint (i.e. 90° corresponds to normal impact). As expected, the rebound velocity and angle decrease as the incident angle increases.

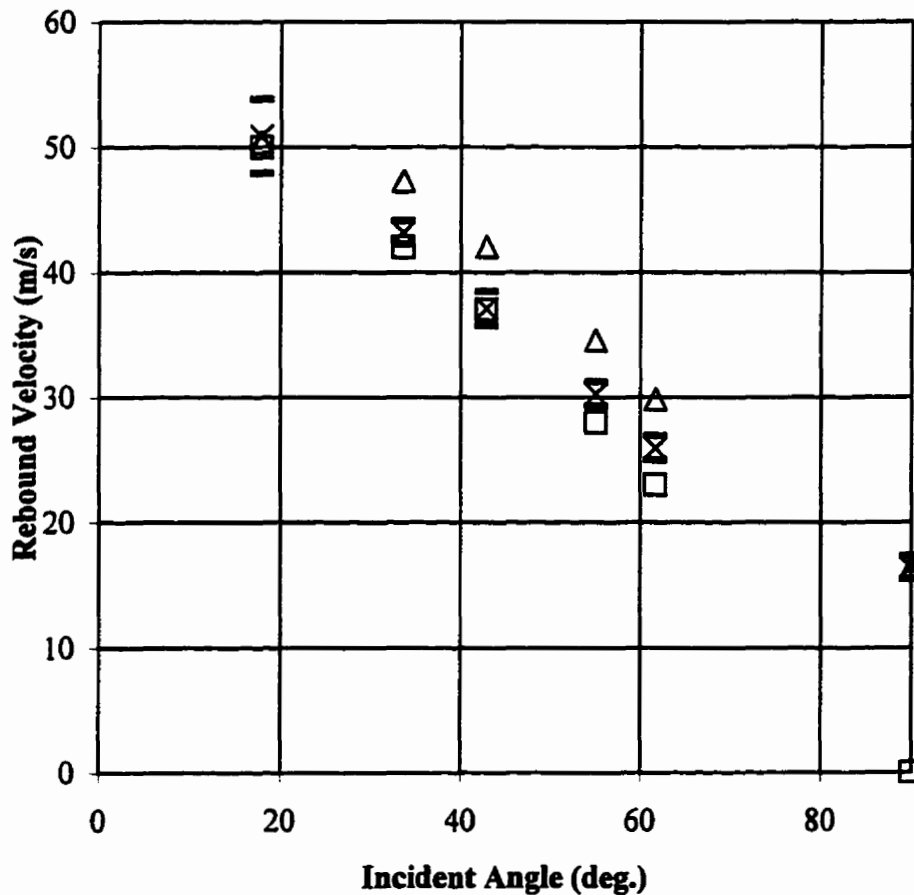


Figure 4.3: Rebound velocity versus incident angle. Total incident velocity = 55 m/s. \times -measured values, Δ - predicted values using present elastic-plastic analysis, \square - predicted values using fully-plastic model [24]. Error bars represent ± 1 standard deviation in the five trials for each experimental data point.

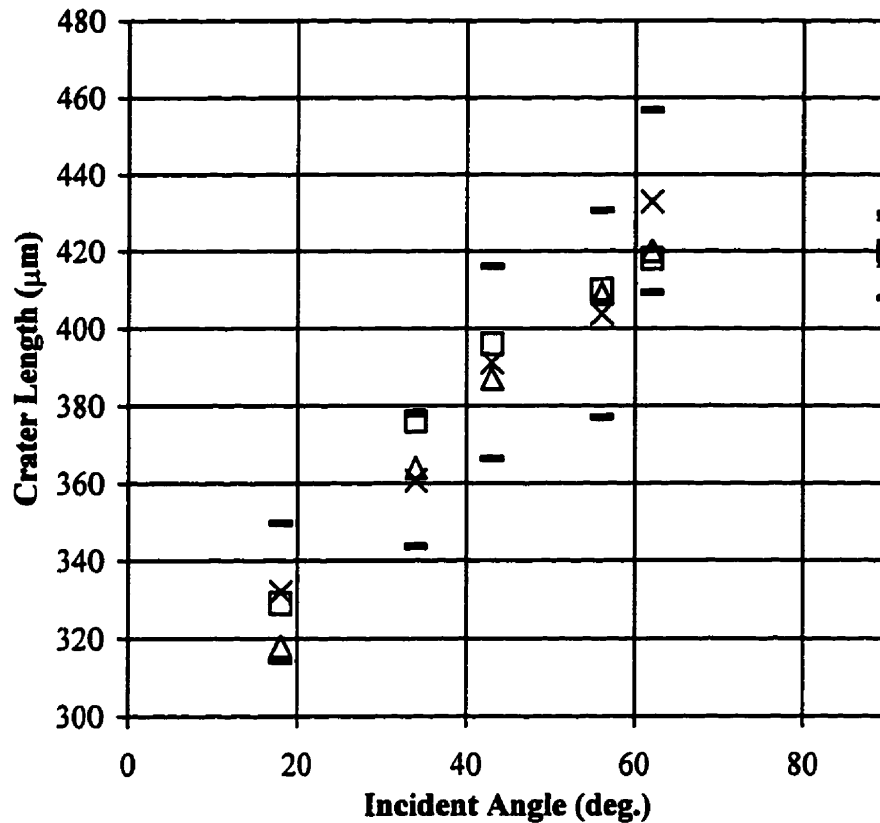


Figure 4.4: Maximum length of impact crater versus incident angle. Total incident velocity = 55 m/s. × - measured values, Δ - predicted values using present elastic-plastic analysis, □ - predicted values using fully-plastic model [24]. Error bars represent ± 1 standard deviation in the five trials for each experimental data point.

The maximum measured length, depth, and volume of each impact crater are presented in Figure 4.4, Figure 4.5, and Figure 4.6, respectively. Each data point represents the average of 5 measurements. An interesting feature is the plateau in crater length, depth and volume at high incident angles (between 70° and 90°) seen in Figure 4.4, Figure 4.5, and Figure 4.6. This plateau corresponds to the region of minimum rebound velocity seen in Figure 4.3 between approximately 70° and 90°.

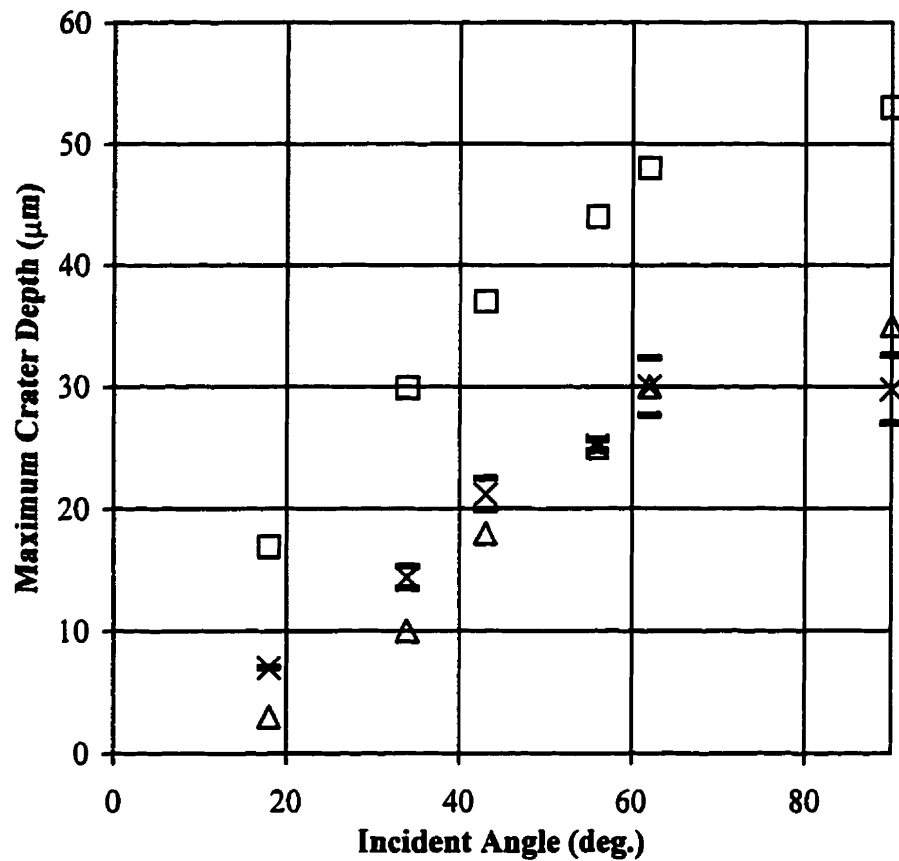


Figure 4.5: Maximum depth of impact crater versus incident angle. Total incident velocity = 55 m/s. \times - measured values, Δ - predicted values using present elastic-plastic analysis, \square - predicted values using fully-plastic model [24]. Error bars represent ± 1 standard deviation in the five trials for each experimental data point.

Because there was pileup at the edge of the crater (Figure 4.7), there was some question as to how the crater length should be defined. In Figure 4.4, the length of the crater was taken to be the distance from the inside leading edge of the crater (on the side of the pileup closer to the centre of impact) to the inside trailing edge of the crater, at a height equal to the undisturbed coating surface, as shown in Figure 4.7.

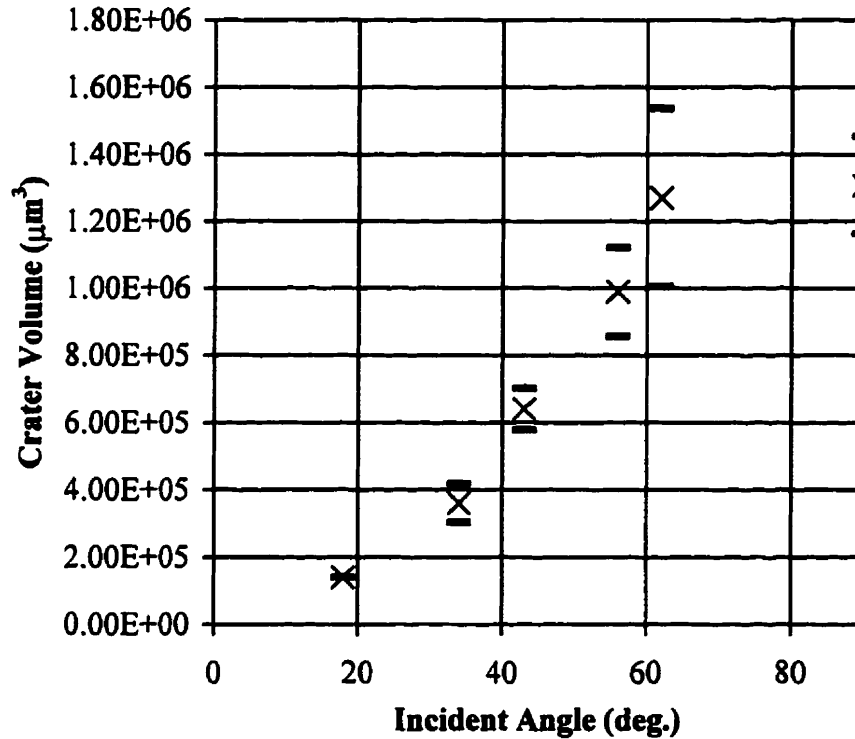


Figure 4.6: Measured crater volume versus incident angle. Error bars represent ± 1 standard deviation in the five trials for each data point.

Figure 4.8 shows the WYKO optical profilometer two-dimensional cross section (plane perpendicular to the surface, at the centre of the impact site) used to measure the length of the crater shown in Figure 4.1. In cases such as those shown in Figure 4.1, where the impact is at normal incidence and the crater is approximately symmetric, the average between the longest and shortest length (i.e. using two cross sections of the type shown in Figure 4.8) was taken as the length of the crater. In cases where the impact occurred at incidence different than normal, the length of the crater was taken as the maximum length (i.e. using the cross-section that gave a maximum length of crater).

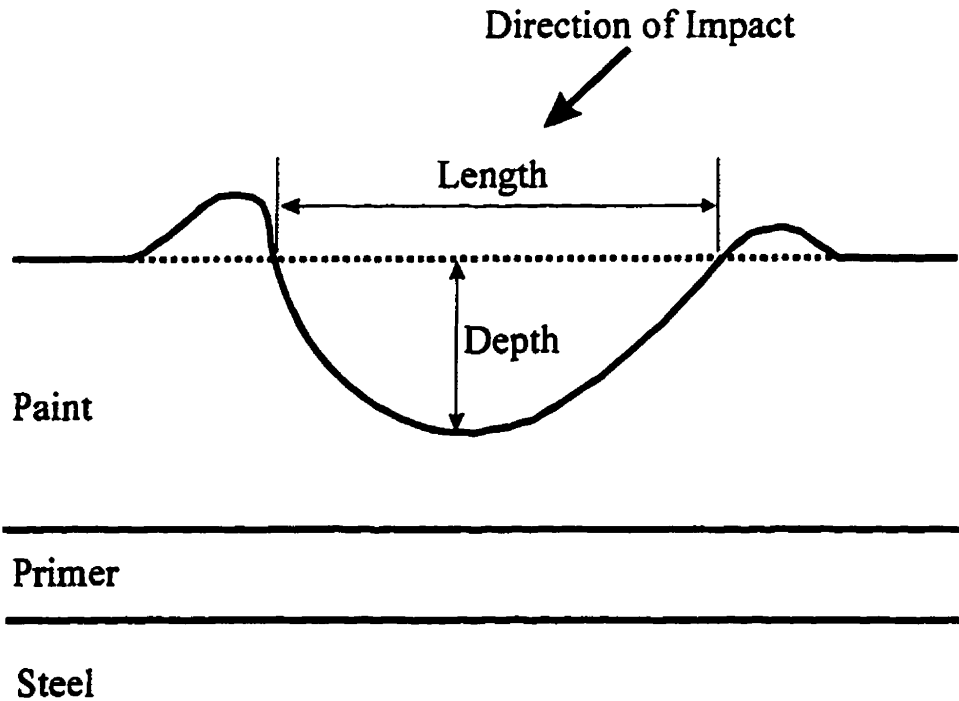


Figure 4.7: Crater definition (not to scale).

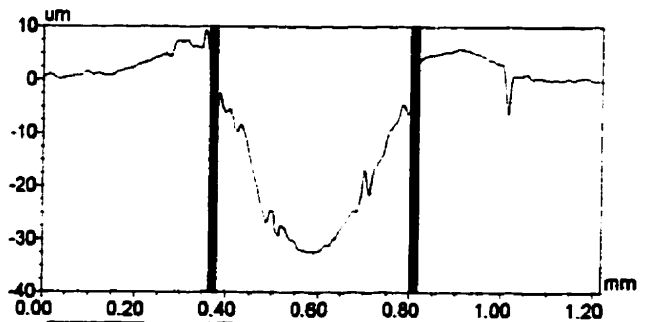
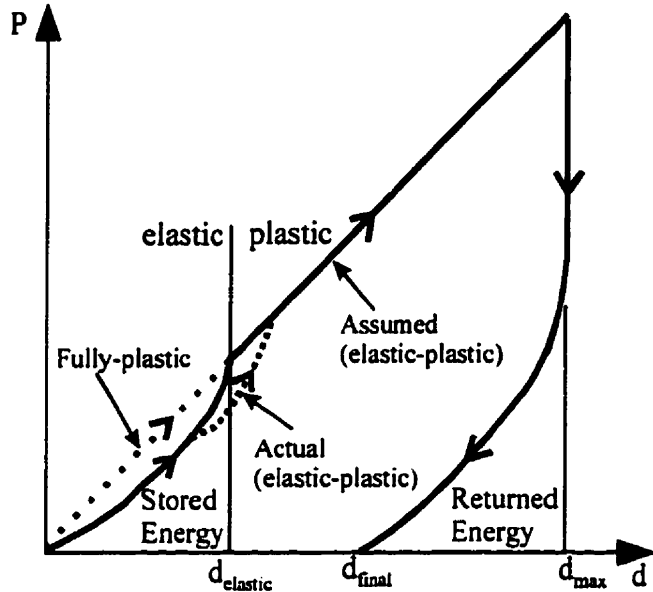


Figure 4.8: Two-dimensional cross section of profile shown in Figure 4.1 taken at centre of impact site. Vertical bars indicate where crater length was measured.

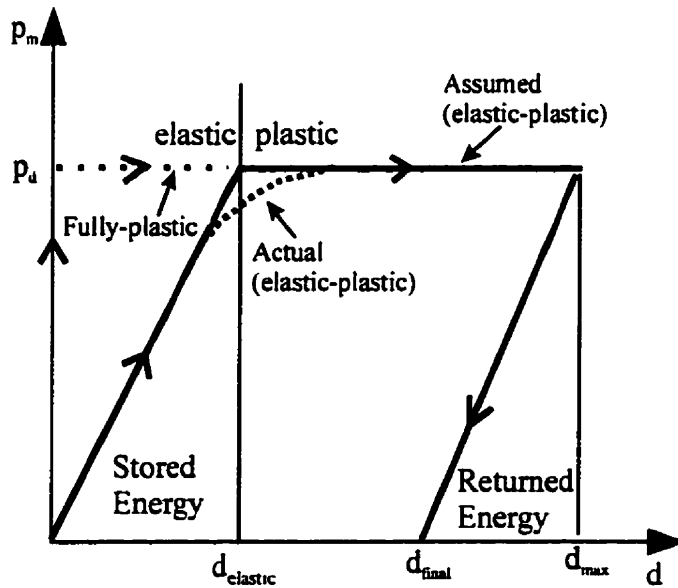
4.2 Collision kinematics

In Chapter 3, it was shown that, for particle impact against coated substrates at moderate speeds, such as those used in blast cleaning (50-150 m/s [49]), dynamic effects were found to

be negligible, and the collision could be treated as quasi-static. In order to analyse such quasi-static impacts, a relationship must be obtained between P , the instantaneous force on the particle, and d , the penetration of the particle into the coating.



(a)



(b)

Figure 4.9: Assumed (elastic-plastic), actual (elastic-plastic), and fully plastic curves of: (a) force-deflection, and (b) mean pressure-deflection.

A typical P-d curve for the collision of a sphere with a substrate at normal incidence is shown in Figure 4.9(a). If the instantaneous contact force P , is divided by the instantaneous contact area, then the mean contact pressure, p_m , can be also plotted as a function of the penetration depth, d (Figure 4.9(b)).

The amount of elastic energy stored and returned to the system can be calculated by integrating the P-d curve using the appropriate limits. When the coating has fully yielded, the contact pressure reaches a constant value, p_d , called the dynamic hardness or plastic flow pressure.

The elastic-plastic transition portion of the contact is not well defined [51], so it is usual, in the analysis of collisions with semi-infinite substrates, to assume rigid-plastic behaviour. This approach has been used with good success in the impact of hard steel spheres against soft target materials [5,24-31]. It is assumed that the particle is undeformable (and thus much harder than the substrate), and that a fully-plastic condition is reached very quickly in the impact process. In this case, the elastic and elastic-plastic transition portions of Figure 4.9 are assumed negligible. The main drawback of this approach is that, because elastic effects are ignored and the sphere itself is considered rigid, in a normal incidence impact all of the energy is consumed in plastic deformation, leading to a prediction of zero springback in the crater and thus zero rebound velocity. This is clearly not the case in realistic collisions.

Johnson obtained good predictions for the coefficient of restitution and elastic springback for normal direction collisions involving hard spheres against ductile semi-infinite metal targets by assuming rigid-plastic behaviour for the incident portion of the impact, and fully elastic behaviour for the rebound portion [15]. He assumed that after rebound, the crater would relax to some radius of curvature ρ that was less than the particle radius R . The strain energy associated with the rebound portion of the impact, being fully elastic and thus reversible, could be modelled as the reverse of an indentation of a crater of radius of curvature ρ to radius of curvature R . By assuming that the depth of indentation is relatively small, he was able to calculate rebound parameters for normal direction impacts using a Hertzian analysis [15].

For semi-infinite substrates, when yield is first exceeded, the plastic zone is small and fully contained by the surrounding elastic material, so that plastic strains are of the same order as surrounding elastic strains. The material displaced by the indenter is accommodated largely by an elastic expansion of the surrounding solid. As the indentation becomes deeper, an increasing pressure is required beneath the indenter to produce the necessary expansion (this is the elastic-plastic transition range in Figure 4.9). Eventually (in the fully plastic range), the plastic zone breaks out and the displaced material escapes by plastic flow to the sides of the indenter (plastic range with $p_m = p_d$) [15]. In the case of coated substrates, because most organic coatings (i.e. paints) are elastomeric, yielding will begin only when the indentation depth is a significant fraction of the distance to the substrate. As the force, P , on the sphere continues to increase (i.e. an increasing indentation depth), the material displaced by the indenter cannot be as readily accommodated by the elastic expansion of the surrounding coating due to the presence of the substrate, and thus the transition to fully plastic behaviour occurs rapidly. For this reason, the elastic-plastic transition portion of the impact was assumed very small, and was ignored in the present analysis.

4.3 Analysis of impacts

4.3.1 Rigid-plastic (fully plastic) analysis

It is possible that, if the impacting particle does not completely penetrate the coating to the substrate, the plastic analysis due to Hutchings et al. [24] for semi-infinite substrates can also be used for coatings. This will be shown to be the case in the present study. In the literature, this approach is usually referred to as 'rigid-plastic', implying that the particle is assumed rigid, and the target material fully plastic. Because the particle is assumed to be rigid in all analyses presented, the Hutchings et al. [24] approach shall be referred to as 'fully-plastic' in this study. As mentioned above, if fully-plastic behaviour is assumed, the elastic and elastic-plastic transition portions of Figure 4.9 are ignored. In this case, the force P , that resists indentation, is assumed to be proportional to a constant flow pressure (or dynamic hardness)

multiplied by the instantaneous contact area, and acts along a radial line, as shown in Figure 4.10.

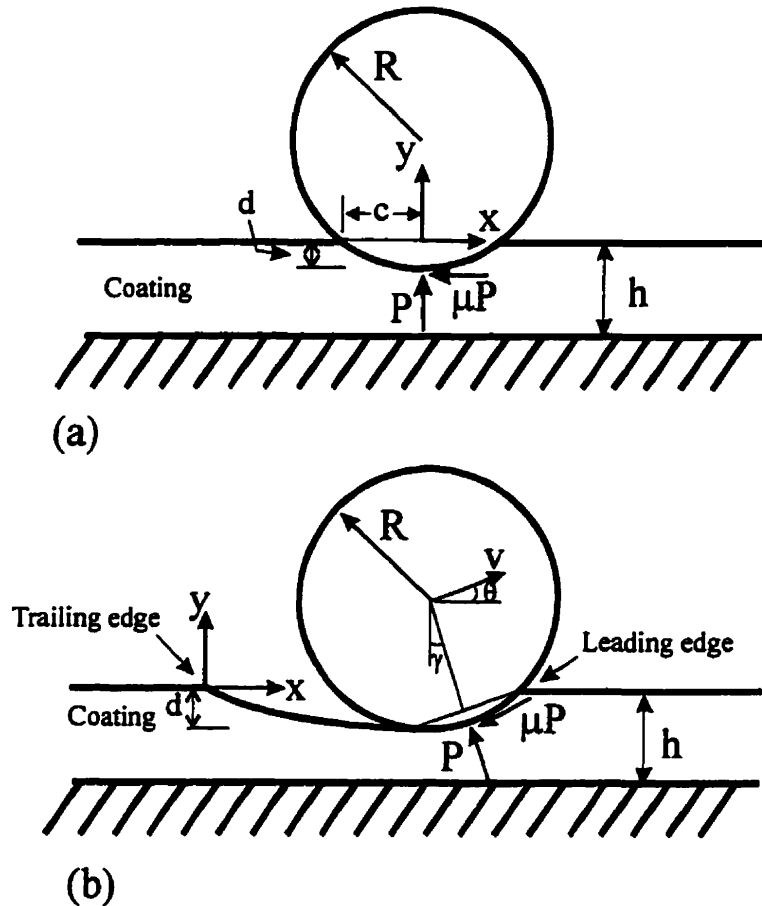


Figure 4.10: Fully-plastic analysis of impacting spheres: (a) when crater is in full contact with sphere, and (b) when crater loses full contact with sphere

In addition, a friction force is assumed, which is proportional to P (coefficient of friction, μ) and acts normal to it. The material below the indenter has yielded in compression with normal stress σ_y and flows at a constant shear stress τ_y . According to the Tresca criterion,

$$2\tau_y = \sigma_y = |\sigma_1 - \sigma_3| \quad (4.1)$$

where τ_y is the yield shear stress, and σ_1 and σ_3 are the maximum and minimum elastic principal stresses at the onset of yield.

Two different cases must be considered: the case of the spherical particle fully filling the crater (Figure 4.10a), and the case when the sphere no longer fills the crater (Figure 4.10b). For completeness, the differential equations governing the motion of the sphere through the coating are presented; the details can be found in [24, 27, 28].

For the case where the sphere fully fills the crater (Figure 4.10(a)), the equations are [27]:

$$\ddot{y} = \frac{\pi p_d}{m} (R^2 - y^2) \quad (4.2)$$

$$\ddot{x} = -\frac{\mu \pi p_d}{m} (R^2 - y^2) \quad (4.3)$$

where \ddot{y} and \ddot{x} are the y and x components of the acceleration of the centre of the sphere, p_d is the dynamic hardness of the coating defined as the indentation force required to reach fully plastic conditions divided by the contact area at that point, μ is a friction coefficient, and R and m are, respectively, the radius and mass of the sphere shown in Figure 4.10. Note that the origin of the co-ordinate system in Figure 4.10(a) is at the point of initial contact between the sphere and coating.

For the case of the sphere which no longer fills the crater (Figure 4.10(b)), the relevant equations were first developed by Hutchings et al. [24], then modified by Rickersby and MacMillan [27], and are given here in the form suggested by Sundararajan et al. [28],

$$\ddot{x} = -\frac{p_d}{m} A \sin(\gamma) - \mu \frac{p_d}{m} A \cos(\gamma) \quad (4.4)$$

$$\ddot{y} = \frac{p_d}{m} A \cos(\gamma) - \mu \frac{p_d}{m} A \sin(\gamma) \quad (4.5)$$

where p_d and m are as above, A is the instantaneous contact area, and γ is the angle defined in Figure 4.10(b). Expressions for A and γ can be found in [28]. All collisions begin with full contact, but at a certain point during the impact, the sphere will lose full contact. Equations (4.2) and (4.3) must thus be solved until the point where full contact between the sphere and the coating is lost, and equations (4.4) and (4.5) hold from that point until the end of the collision.

Knowing the incident velocity and angle of attack, the trajectory of the sphere, and thus the rebound velocity, rebound angle, and crater dimensions can be determined by non-linear differential equations (4.2)-(4.5). In practice, these equations must be solved using numerical methods, and the authors have found that the Runge-Kutta function in MathCad 7.0 (Mathsoft Inc.) is particularly useful.

The dynamic hardness, p_d , and the friction coefficient, μ , are required for this analysis. It is usual to adjust these parameters until a best fit of experimental data is achieved [7, 24-28]. In the present study, a method similar to that of Tirupataiah et. al. [30], and introduced in Section 3.4.2 was used: If the size of impact craters at a particular velocity and normal incidence are known, then the dynamic hardness can be estimated by setting the incident kinetic energy equal to the work done in plastically deforming the coating,

$$\frac{1}{2}mv_i^2 = \int_0^{d_{max}} P(d) d(d) \quad (4.6)$$

where v_i is the incident velocity, m is the mass of the incident particle, and $P(d)$ is the load as a function of the indentation depth. If the pileup of material adjacent to the crater edges is neglected, the indentation depth, d , and hence the force-depth relationship, $P(d)$, can be expressed in terms of the contact radius, c . Making the appropriate substitutions and rearranging equation (4.6) results in the following expression for the dynamic hardness,

$$P_d = \frac{mv_i^2}{2\pi \left[\sqrt{R^2 - c_{\max}^2} \left(\frac{1}{3} c_{\max}^2 + \frac{2}{3} R^2 \right) - \frac{2}{3} R^3 \right]} \quad (4.7)$$

where R is the particle radius, and c_{\max} is the maximum contact radius reached at deepest penetration. When a particle strikes, the coating below the particle will experience compressive plastic deformation in the direction of the impact, and plastic radial expansion. On rebound, some of the compression in the direction of impact will be recovered due to elastic effects, but much less radial expansion will be recovered. The material surrounding the crater will thus be left in a state of residual biaxial compressive stress, which will inhibit radial recovery within the crater. Furthermore, the elastic deformations up to the point of yield will be much greater in the direction of impact than in the radial direction [20, 52], and thus, the elastic recovery will also be greater. For these reasons, it can be assumed that the final crater radius measured after an impact (i.e. after elastic recovery) will be approximately equal to the maximum contact radius reached during the impact, c_{\max} in equation (4.7). This was found to be the case by Tirupataiah et al. for impacts on semi-infinite metal substrates [30]. In this manner, measurements of crater diameter can be used to estimate the dynamic hardness. For the present coating system, c_{\max} was measured as 0.420 mm for a 55 m/s normal direction impact of a 0.89 mm steel sphere, and hence the dynamic hardness was found to be $p_d=1120$ MPa.

The friction coefficient, in the case of impacts, is best thought of as the impulse ratio, μ , which is the ratio of the normal to tangential impulse in the impact and will, in general, be a function of the incident impact angle [19]. Hutchings et al. have found that the value of the impulse ratio has little effect on the predictions of the fully-plastic model, and as such, may be assigned an arbitrary value which best fits the experimental data [26]. The best fit was found with $\mu=0.001$ for the present data (i.e. minimal effect of friction).

The preceding fully-plastic analysis was implemented in a MathCad 7.0 (Mathsoft Inc.) spreadsheet, and predictions of rebound velocity, rebound angle, crater depth, and crater length

are plotted in Figure 4.3, Figure 4.4, and Figure 4.5, along with the experimentally determined values. The MathCad implementation of this plastic analysis can be found in Appendix D.

4.3.2 Elastic-plastic analysis of impact

The main drawback to using the fully-plastic analysis, as mentioned before, is the neglect of elastic springback. In real collisions, there will be a certain amount of springback at all angles of attack. This is most evident at normal incidence, where the rebound velocity and springback are predicted to be zero according to fully-plastic theory (Figure 4.5). This is clearly not the case in real collisions; there will be components of normal rebound velocity and springback in collisions at any angle. For this reason, an elastic-plastic model of collision was developed [49].

For normal incidence collisions, according to Figure 4.9, the particle first encounters an elastic retarding force, then an elastic-plastic transition retarding force, and finally a plastic retarding force. In order to correctly model the incident portion of the collision, the appropriate force-deflection (P-d) relationships must be known for the elastic, elastic-plastic, and fully plastic conditions. The elastic-plastic transition portion of the curve is difficult to obtain, so the collision is assumed to follow the elastic incident path until fully plastic conditions have been reached, as shown in Figure 4.9. The fully plastic condition is then used until the point of maximum penetration, where it is assumed that the particle normal (y direction) velocity is zero. At this point, an elastic rebound contact force causes the sphere to accelerate away from the coating.

The elastic portion of the impact can be modelled using the analysis of Matthewson [20], presented in its modified form in Appendix B in which the coating is assumed to be thin enough so that the stresses and strains can be described adequately by their averages through the thickness of the coating. This analysis is used to obtain the elastic P-d relationship describing the incident and rebound elastic portions of Figure 4.9. An estimate of the point of transition between elastic and fully plastic behaviour can be made using the modified Matthewson analysis by assuming that the state of stress below the indenting particle, at first

yield, is described by the Tresca criterion, equation (4.1), at a stress equal to the flow pressure (i.e. $\sigma_y = p_d$). At this point, the fully plastic analysis of Hutchings et al., described in Section 4.3.1, was used to the point where the particle velocity drops to zero (i.e. d_{max}).

The elastic rebound P-d relationship will be different from that of incidence. It can be modelled as the reverse of an elastic indentation of the final (relaxed) crater to the point where the rebound begins (d_{max}). If the final crater shape after springback is relatively flat, the rebound P-d relationship can be obtained by using the modified Matthewson analysis (Appendix B) with an equivalent coating of thickness h^* , equal to the original coating thickness, h , minus the final relaxed indentation depth, d_{final} (Figure 4.11), i.e. [49],

$$d_{final} = d_{max} - d_{elastic} = h - h^* \tag{4.8}$$

where $d_{elastic}$ is the elastic deformation for a coating of thickness h^* (equal to the final thickness at the bottom of the crater) pressed to a depth of d_{max} .

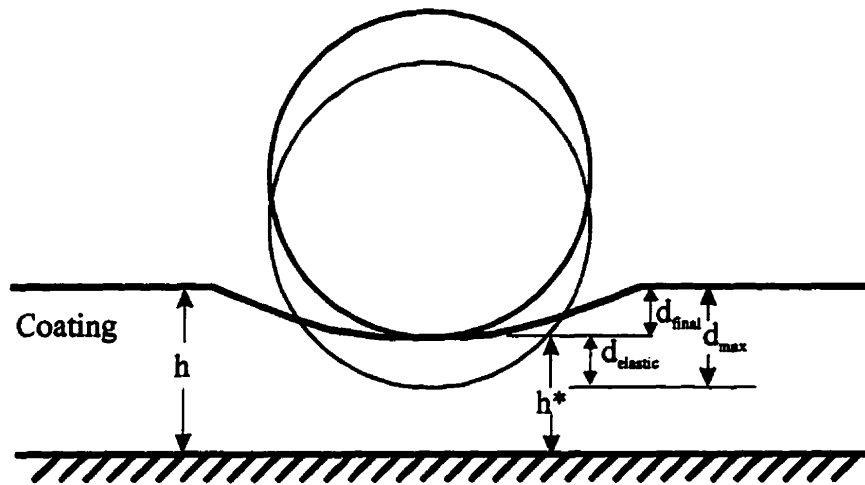


Figure 4.11: Geometry of assumed reversible rebound process.

A second condition existing at the onset of rebound is,

$$p_d = |\sigma_1 - \sigma_3| \quad (4.9)$$

corresponding to the fully plastic state. The final thickness h^* is adjusted in the modified Matthewson model until the conditions given by equations (4.8) and (4.9) are met at the point of maximum indentation. The proper P-d relationship is then extracted for use in determining the kinematics of rebound. It should be noted that the stress condition is evaluated at a point directly below the indentation, since this is the point of maximum stress where full plasticity will be reached first. This is a slightly different approach than that used by Johnson, who assumed, for semi-infinite targets, that the reversible elastic indentation would occur on the relaxed crater starting at the relaxed crater depth and ending at a Hertzian mean pressure (calculated by taking the Hertzian force and dividing it by the contact area) equal to the dynamic hardness [51].

For impacts at an arbitrary angle, the sphere does not, in general, make full contact with the whole crater (Figure 4.10b), and it is more difficult to determine the effect of elastic springback on the trajectory of the particle as it ploughs through the coating. An assumption must be made as to when the elastic rebound force takes effect. In this study, it was assumed that the elastic rebound contact force is applied to the particle from the point of deepest penetration, d_{max} (where the y velocity of the particle reaches zero), to the point where the particle leaves the coating, at d_{final} . The elastic springback of the trailing regions of the crater, prior to the maximum depth being reached, is assumed to occur after the particle has passed, and hence does not affect the trajectory. Once the particle has stopped moving in the y-direction, the coating is assumed to spring back around the particle, and the appropriate P-d relationship, as described above, is used to describe the rebound. The rebound force is assumed to always act in the y-direction.

The determination of the kinematics of indentation and rebound according to the elastic-plastic model can thus be summarised in three steps as follows [49]:

- (1) An elastic analysis such as the modified Matthewson [Appendix B] analysis is used to determine the incident P-d relationship for impact upon a coating of thickness h . This

relationship gives the kinematics of indentation to the transition point between elastic and fully plastic behaviour, i.e. to the point where equation (4.1) is satisfied with the flow pressure, p_m , equal to the dynamic hardness, p_d .

- (2) The fully plastic analysis described in Section 4.3.1 is used from the elastic-plastic transition point until the sphere has penetrated to the maximum depth, d_{max} , where the y-direction velocity is zero.
- (3) Assuming that the springback begins at d_{max} , the rebound P-d relationship is determined using an iterative procedure with equations (4.8) and (4.9). The elastic force, P, that causes the particle to rebound, is assumed to always act vertically (i.e. in the y direction). Furthermore, the elastic rebound is assumed to not affect the crater length (i.e. even though the rebound takes place from the point where the y-direction velocity is zero, and the particle may still have a significant x-direction velocity, it is assumed that the remaining x-direction velocity does not cause further permanent deformation of the coating) The crater length is thus fully defined at the point of maximum penetration.

The preceding elastic-plastic analysis was used to calculate rebound velocity, rebound angle, and the final shape of the crater. The results are presented in Figure 4.2, Figure 4.3, Figure 4.4, and Figure 4.5.

4.4 Comparison of Experimental and Analytical Results

Figure 4.2 shows that the elastic-plastic analysis fits the measured rebound angles better than the fully-plastic theory, thereby supporting the assumption that the rebound elastic effects occur only from the point of maximum indentation (where the y-direction velocity is zero). Both the fully-plastic and elastic-plastic models do not consider the effect that the lip of ploughed material at the edge of the crater will have on the trajectory of the particle. It had been speculated in the literature [29] that this might contribute to the fully-plastic model's overestimate in rebound angle, because the lip at the leading edge of the crater would increase the effective contact area, leading to a lower rebound angle. However, Figure 4.2 shows that

consideration of elastic rebound effects alone is enough to yield good agreement with experimental rebound angles.

Figure 4.3 shows that the fully-plastic theory fits the experimental data for measured rebound velocities slightly better than the elastic-plastic analysis at all angles except for normal incidence. This is most likely because the elastic-plastic analysis does not take into account any retarding force in the x-direction after the maximum depth has been reached. The elastic-plastic theory will therefore predict slightly higher x-component rebound velocities than is realistic. This is reinforced by the fact that very accurate predictions of rebound velocity are made at 90 °, where the effect of the x-component of velocity is non-existent. As expected, the fully-plastic theory cannot predict the rebound velocity at 90° incidence.

Figure 4.4 demonstrates that the elastic-plastic and fully-plastic theories are both quite good at predicting the final crater length. The elastic-plastic analysis is slightly better at intermediate incident angles, and the fully-plastic analysis is slightly better at very high and very low incident angles. The fact that the fully-plastic analysis works well at very high angles is not surprising, given that the y-component of incident velocity will be highest there, and thus fully plastic conditions will be reached relatively quickly.

Figure 4.5 shows that the elastic-plastic analysis accurately predicts the final depth of the crater after springback. This is important for calculations of material removal in blast cleaning applications, since the material that is displaced to form the lip of the crater (pile-up, shown in Figure 4.7) is in a position to be knocked off by subsequent impacts. Because the fully-plastic theory neglects springback, it is not surprising that it over-estimates the crater depth. Organic coatings are, in general, more elastomeric than metals and will thus experience more elastic recovery of crater depth upon rebound. For this reason, it can be concluded that the elastic-plastic model is a more accurate representation of organic coating behaviour, whereas, for metals, the fully-plastic model is sufficient. The assumption of a small elastic-plastic transition region (Figure 4.9) is supported by the good agreement between the predictions of the elastic-plastic model and experimental values (Figure 4.2-Figure 4.5).

In Figure 4.3, Figure 4.4, Figure 4.5, and Figure 4.6, a plateau is reached in the measured quantities for high angles of attack. There are two possible explanations for this. The first is a simple consequence of how the data are presented. The trends in Figure 4.3-Figure 4.6 look like sinusoidal curves, indicating that there is a strong correlation between the plotted data and the normal component of the incident velocity, i.e. $v_{\text{normal}}=55 \text{ m/s} \sin(\alpha)$. This implies that the plateau reached at high angles of attack is due to the relatively small change in incident normal velocity between 60° and 90° (approximately 6 m/s). Another possible reason for the plateaus is the variation in dynamic hardness. As mentioned in Section 3.4.2, in general, the dynamic hardness is not a constant for a given coating system because it can be a function both of coating thickness and indentation depth. For example, as a particle penetrates deeper, the presence of a harder substrate will increase the effective hardness of the coating; i.e. a coating becomes effectively harder the thinner it is, or the deeper the indentation, as others [35, 36] have found, and as was shown in Section 3.4.2. At high angles of attack where the penetration is greatest, it is possible that the presence of the substrate begins to strongly affect the effective hardness of the coating, resulting in the plateaus in experimental data seen in Figure 4.3-Figure 4.6. Nevertheless, because the plateaus are also seen in the predicted values in Figure 4.3-Figure 4.6, and a constant dynamic hardness is assumed for all predictions, it is likely that any dynamic hardness effects are negligible. It is concluded, therefore, that the plateaus are a result of the strong correlation between normal direction effects and the quantities plotted in Figure 4.3-Figure 4.6.

The penetration depths reached in the present experiments ranged from 50% of the coating thickness to approximately 17% of the coating thickness. Therefore, for the present models, the dynamic hardness is considered an average value, capable of adequately describing the overall behaviour of the coating system over this range of penetration depths. However, this analysis should be valid for penetrations approaching the coating thickness if the dynamic hardness is properly adjusted. For particles that penetrate the coating and strike the substrate, it might be possible to modify the model by using the present analysis until the particle reaches the substrate, and by then repeating the analysis assuming that the remaining kinetic energy is

incident on the bare substrate. The dynamic hardness and elastic P-d curve of the bare substrate would have to be determined, and the particle might no longer be considered rigid compared to the substrate.

The reason that the fully-plastic analysis works reasonably well in all but the prediction of crater depth and rebound angle is that, as the particle penetrates, a core of plastically deformed material quickly develops directly below the indenting particle, as was discussed by Johnson [51] for semi-infinite substrates. For thin coatings, the fully plastic state will be reached quickly because of the constraint of the substrate, and thus the analysis will work well in describing the incident portion of the impact, where the effect of springback is minimal. However, superimposed on this plastic stress, there will be an elastic stress that is recovered upon rebound. The elastic rebound force increases with the volume of elastically stressed coating, which in turn increases with the penetration depth. The effect of the elastic rebound force will be more pronounced at higher angles of impact where the penetration depth is greater, and thus the elastic-plastic model will be more accurate in this range.

4.5 Summary

In this chapter, it was found that a fully-plastic theory of indentation [24] gave good predictions of crater length and rebound velocity for the coating system studied. The predictions of rebound angle and crater depth, however, did not agree well with experimental observations. A new elastic-plastic analysis [49] was found to predict all of these quantities well, and can be used to calculate the amount of plastically deformed material appearing at the edges of the impact crater. It is thought that this raised coating material is prone to being knocked off by other impacting particles in a blast cleaning application.

Chapter 5

Analytical Investigation of Erosion by Angular Particles

In this chapter, the erosion of substrates of arbitrary dynamic hardness and friction coefficient, due to the impact of individual angular particles, is analysed with the purpose of predicting crater size, shape, and rebound parameters as a function of incident particle velocity, angle, orientation, and shape. A rigid-plastic theory due to Hutchings et. al. [7], developed for square plates impacting frictionless surfaces, is generalised for arbitrarily shaped particles impacting surfaces having nonzero friction. The specific case of symmetric angular particles of arbitrary angularity is studied in detail. Because of time restrictions, confirming angular particle experiments were not conducted; however, the model is shown to match Hutchings' experimental data for square steel plates on smooth steel surfaces [7]. A parametric study of the effect of the input parameters on the crater volume (and thus the amount of material appearing as pileup at the edge of the crater) is presented. It is believed that this piled-up material is available to be knocked off by subsequent collisions, and that this model can be used to predict coating removal behaviour in blast cleaning operations. Most of the material in this chapter will soon be published by the author [53, 54]

5.1 Background

In earlier papers, Hutchings [7, 24-26] showed that crater size, crater shape and rebound parameters can be successfully predicted for collisions between both spherical and square

particles and various target materials, if fully plastic behaviour was assumed for the target, and the particle was assumed rigid. These models approximated the resisting force to indentation as the dynamic hardness of the material multiplied by the instantaneous contact area. Because the contact area changes as the particle travels through the target material, the governing differential equations are non-linear, and the problem must be solved numerically. Other successful applications of this theory on semi-infinite target materials include the work of Sundararajan et. al. [28-31]. It has been demonstrated in Chapter 4 that this method can also be used successfully to predict the crater size and shape, and rebound parameters for impacts between spherical particles and certain types of organic coatings provided that the particle does not penetrate to the substrate.

In the present study, the work of Hutchings with regards to square particles [7] is extended to arbitrarily-shaped particles impacting targets at arbitrary orientations. The method is applicable to both semi-infinite and coated systems (assuming that the assumptions of rigid-plastic theory hold). The specific case of angular particles having equal length sides, but of arbitrary angularity is discussed in detail. The present model [53, 54] also accounts for the effects of friction, and is used to predict the crater volume and rebound parameters (velocity, angle, and angular velocity) for rigid, symmetric, angular particles of any size, angularity and initial orientation, impacting target materials of arbitrary dynamic hardness and friction coefficient at various angles of attack and incident velocities.

5.2 Formulation of problem for general case

Referring to Figure 5.1, the position of the centre of mass and orientation of an arbitrarily shaped 3-dimensional particle can be described at time, t , by an inertial co-ordinate system located at the first point of contact of the particle with the target (X, Y, Z), and a body-fixed co-ordinate system attached at the centre of mass (x, y, z). The target surface is defined by $Z = 0$. The co-ordinate system (x', y', z') is attached to the centre of mass of the particle but remains parallel to the inertial frame. The orientation of the particle can therefore be described by the Euler angles (θ, ϕ, ψ) depicted in Figure 5.1, and the position of the centre of mass of the

particle will be described by the co-ordinates (X_o, Y_o, Z_o) . The external contact force acting on the particle, F , can be resolved into its inertial frame components $F_x, F_y,$ and F_z . The problem has 6 degrees of freedom: three position co-ordinates, and three orientation co-ordinates.

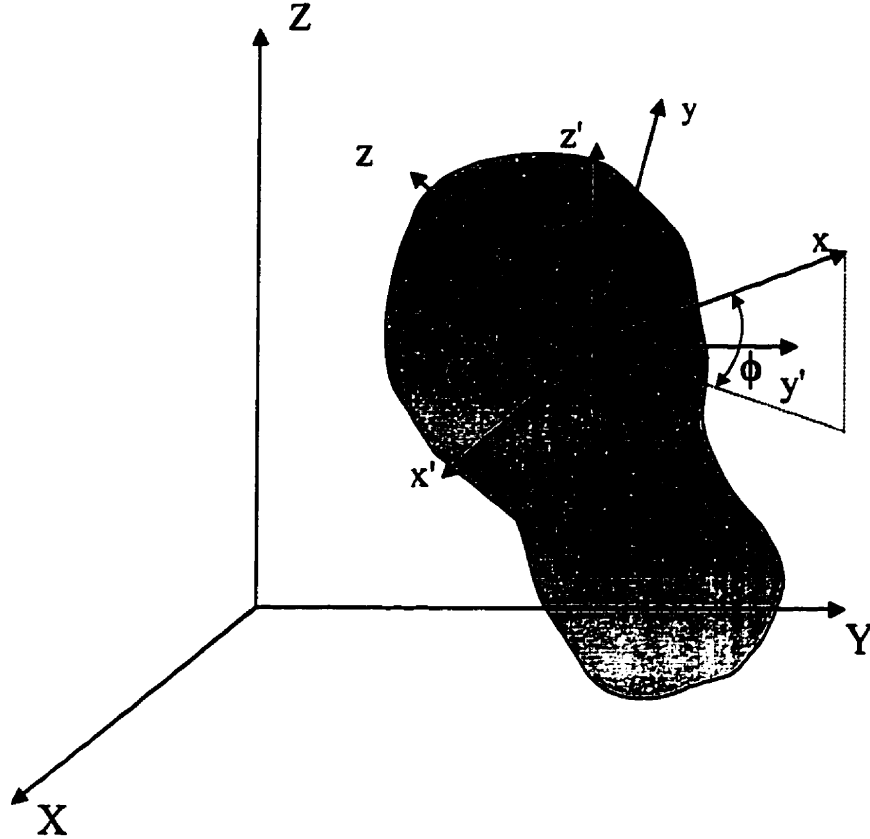


Figure 5.1: Definition of Euler Angles, θ, ψ, ϕ , inertial (X, Y, Z) , and body fixed (x, y, z) co-ordinates systems used in general analysis. Co-ordinate system (x', y', z') is attached to the centre of mass (CM), and remains parallel to the (X, Y, Z) axis.

The kinetic energy, E , of the particle at any given time is,

$$E = \frac{1}{2} m (\dot{X}_o^2 + \dot{Y}_o^2 + \dot{Z}_o^2) + \frac{1}{2} (I_x^p \omega_x^2 + I_y^p \omega_y^2 + I_z^p \omega_z^2) \quad (5.1)$$

where I_x^p , I_y^p , and I_z^p are the mass moments of inertia about the principal axes, and ω_x , ω_y , and ω_z are the components of the angular velocity of the particle relative to the inertial space resolved along the instantaneous directions of the body-fixed axes (x, y, z):

$$\begin{aligned}\omega_x &= \dot{\psi} \sin \theta \sin \phi + \dot{\theta} \cos \phi \\ \omega_y &= \dot{\psi} \sin \theta \cos \phi - \dot{\theta} \sin \phi \\ \omega_z &= \dot{\phi} + \dot{\psi} \cos \theta\end{aligned}\tag{5.2}$$

A dot above a variable represents differentiation with respect to time. Insertion of equation (5.2) into equation (5.1) results in a general expression for the kinetic energy of the particle, and using the Lagrangian formulation assuming gravitational effects negligible, the equations of motion are,

$$\frac{d}{dt} \left(\frac{\partial E}{\partial \dot{q}_i} \right) - \frac{\partial E}{\partial q_i} = Q_i\tag{5.3}$$

where q_i represents each of the six generalised co-ordinates, t is time, and Q_i is the generalised external force in the direction of the generalised co-ordinate. It is seen that, in the case of a free particle, there will be six coupled differential equations describing the motion.

According to rigid-plastic theory, the instantaneous contact force, $d\bar{P}$, acting normal to an infinitesimal element of the surface of the particle, is the dynamic hardness, multiplied by the instantaneous element of contact surface area, dA (with unit vector outward normal to the contact surface),

$$d\bar{P} = p_d \bar{n} dA\tag{5.4}$$

The surface of an arbitrarily shaped particle can be described, in body-fixed co-ordinates, by,

$$z = f(x, y) \quad (5.5)$$

and this can be expressed in terms of inertial co-ordinates using the appropriate direction cosine transformations (see, for example, [55]) to obtain $Z = g(X, Y)$.

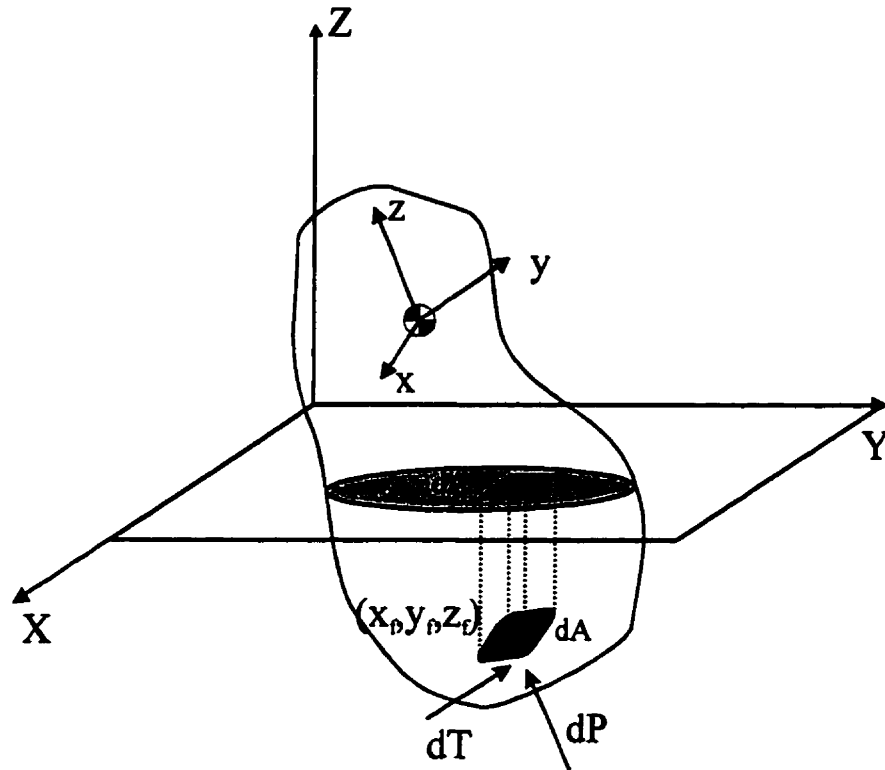


Figure 5.2: Surface area element dA , and projected surface area element dA_p . $Z = 0$ represents the surface of the target.

In the inertial frame of reference, using equation (5.4), the total contact force acting on the particle becomes,

$$\bar{P} = \int_A p_d \bar{n} dA \quad (5.6)$$

where dA is the surface area differential given by,

$$dA = \sqrt{1 + \left[\frac{\partial g(X, Y)}{\partial X} \right]^2 + \left[\frac{\partial g(X, Y)}{\partial Y} \right]^2} dA_p \quad (5.7)$$

\bar{n} is a unit vector normal to the contact surface area element dA pointing towards the inside of the particle (Figure 5.2). The area element, dA_p , over which the integration takes place is the projection of the contact area on the X-Y plane (Figure 5.2).

The components of the resisting force, \bar{P} , in each of the X, Y, and Z directions (P_x , P_y , and P_z) can be obtained by forming the dot product of equation (5.7) with each of the unit vectors in the directions of the inertial axes. The friction force, \bar{T} , can be obtained by multiplying the normal force of equation (5.6) by the friction coefficient, μ , and will be along the contacting particle surface in the direction opposite to the local direction of motion. The components of \bar{T} in the inertial frame of reference (T_x , T_y , and T_z) are obtained by forming the dot product of \bar{T} (whose direction depends on the direction of motion) with the unit vectors in the inertial frame. The resultant forces acting on the particle along each of the inertial axes are:

$$\begin{aligned} F_x &= P_x + T_x \\ F_y &= P_y + T_y \\ F_z &= P_z + T_z \end{aligned} \quad (5.8)$$

The generalised forces, Q_i , in the direction of the θ , ϕ , ψ axes in equation (5.3) are moments and must be expressed as appropriate components in each of these directions. For example, if the co-ordinates of the point of application of an element of force relative to the body-fixed co-ordinate system are (x_ξ, y_ξ, z_ξ) (Figure 5.2), then the components of the differential moments are:

$$\begin{aligned}
 dQ_{\theta} &= dM_x \cos \phi - dM_y \sin \phi \\
 dQ_{\phi} &= dM_z \\
 dQ_{\psi} &= dM_x \sin \theta \sin \phi + dM_y \sin \theta \cos \phi + dM_z \cos \theta
 \end{aligned}
 \tag{5.9}$$

where the moments dM_x , dM_y , and dM_z are in the direction of the body-fixed co-ordinates (i.e. $dM_x = dF_z y_f - dF_y z_f$, etc. with dF_x , dF_y , dF_z being expressed along the directions of the body-fixed axes (x,y,z) [55]).

The moments of equation (5.9) can be found by integrating equation (5.9) over the contact area, which is initially the intersection of the surface $g(X, Y)$ with the $Z = 0$ plane (if the target is flat). It should be noted that the contact area will change during the impact, and thus should be considered a function of time (i.e. it is the instantaneous contact area). Since the total force depends on the contact area, it too will change in both direction and magnitude with time.

5.3 Symmetric particles

5.3.1 Formulation of equations of motion

The erosion behaviour typical of angular particles can be obtained by studying the simplified case of symmetric particles of uniform thickness (two-dimensional) [53, 54]. Figure 5.3 shows a particle of this type at some time, t , during impact on a flat surface ($Z = 0$). The notation for the body-fixed and inertial co-ordinate systems is the same as the general case described above. The problem is essentially two dimensional, and ψ , ϕ , ω_y , ω_z , X_0 , F_x , M_y , and M_z all equal zero, thereby reducing equations (5.1) and (5.9) to,

$$E = \frac{1}{2} m (\dot{Y}_0^2 + \dot{Z}_0^2) + \frac{1}{2} (I_x^p \omega_x^2)
 \tag{5.10}$$

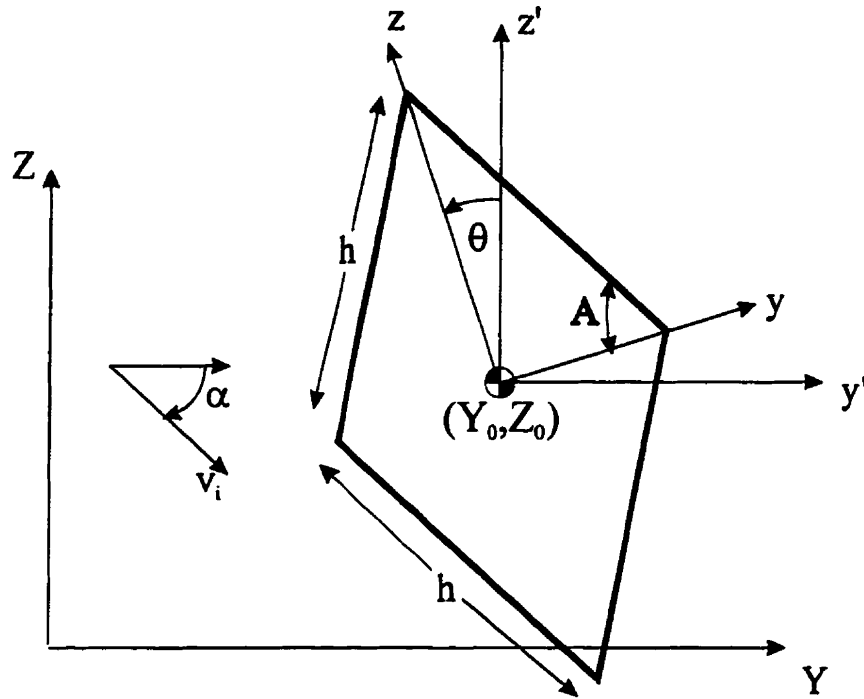


Figure 5.3: Co-ordinate system definitions used for specific case of symmetric particles of side length h .

$$\begin{aligned}
 dQ_{\theta} &= dM_x = dM_x \\
 dQ_{\psi} &= 0 \\
 dQ_{\psi} &= 0
 \end{aligned}
 \tag{5.11}$$

and the differential equations describing the motion, equation (5.3), reduce to

$$\begin{aligned}
 m\ddot{Y}_0 &= F_Y \\
 m\ddot{Z}_0 &= F_Z \\
 I_x\ddot{\theta} &= M_x
 \end{aligned}
 \tag{5.12}$$

Because the particle was assumed to impact with the Y - Z plane perpendicular to the surface (i.e. the x' direction was always parallel to the X direction in Figure 5.3), the problem remains two dimensional at all times, and thus the mass, m , moment of inertia, I_x , and applied

forces are expressed per unit thickness in the x direction. For the particle in Figure 5.3, the moment of inertia is,

$$I_x = \frac{1}{6} mh^2 \quad (5.13)$$

Referring to Figure 5.3, the particle shape can be described in body-fixed co-ordinates by the following function,

$$\begin{aligned} z(y) &= \pm y \tan(A) \pm h \sin(A) & -h \cos(A) \leq y \leq 0 \\ z(y) &= \mp y \tan(A) \pm h \sin(A) & 0 \leq y \leq h \cos(A) \end{aligned} \quad (5.14)$$

where A is the particle angularity, and h is the length of one side of the particle (Figure 5.3). The \pm in the above equations refers to the fact that there are two values of z for each y (the upper sign in each \pm pair refers to the surface of the particle above the $z = 0$ plane in Figure 5.3, and shall be referred to as the 'top' of the particle, while the lower sign refers to the surface of the particle below the $z = 0$ plane and shall be referred to as the 'bottom' of the particle). Equation (5.14), in the inertial frame co-ordinates, becomes,

$$\begin{aligned} Z(X, Y) &= Z_0 + (Y - Y_0) \tan(\theta \pm A) \pm \frac{h \sin(2A)}{2 \cos(\theta \pm A)} \\ \text{for } Y_0 - h \cos(A) \cos(\theta) &\leq Y \leq Y_0 \mp h \sin(A) \sin(\theta) \end{aligned} \quad (5.15)$$

$$\begin{aligned} Z(X, Y) &= Z_0 + (Y - Y_0) \tan(\theta \mp A) \pm \frac{h \sin(2A)}{2 \cos(\theta \mp A)} \\ \text{for } Y_0 \mp h \sin(A) \sin(\theta) &\leq Y \leq Y_0 + h \cos(A) \cos(\theta) \end{aligned}$$

The instantaneous contact force (equation (5.6)) is, in this case

$$\bar{P} = p_d \int_{Y_c} (-\tan(\theta \mp A) \bar{j} + \bar{k}) dY \quad (5.16)$$

where, the \pm sign now indicates whether the force in question is on the left (-) or right (+) side, of the bottom part of the particle (the portion of the particle above the y axis is assumed not to contact the substrate at any time). The unit vectors, \bar{j} and \bar{k} , in equation (5.16) are in the Y and Z directions, respectively. The integration takes place over the region Y_c , which is the projection of the contact area on the Y axis. It must be noted that the contact area may be broken up into distinct intervals on each side of the particle if the particle makes simultaneous contact over more than one contiguous area. At any instant in time, from equation (5.15), $dZ = \tan(\theta \mp A) dY$, so that equation (5.16) can be rewritten as,

$$\begin{aligned} P_Y &= -p_d \int_{Z_c} dZ \\ P_Z &= p_d \int_{Y_c} dY \end{aligned} \quad (5.17)$$

which is valid for both the left and right sides of the bottom of the particle. The regions of integration in equation (5.17), Z_c and Y_c , are the projections of the instantaneous contact area on the Z and Y axes, respectively.

The magnitude of the friction forces acting on the contacting surfaces will be the magnitude of the force in equation (5.16) multiplied by the coefficient of friction and will act along the contact surface. Unit vectors along the surface of the particle are,

$$\begin{aligned} \bar{t}_L &= \pm \cos(\theta - A) \bar{j} \pm \sin(\theta - A) \bar{k} \\ \bar{t}_R &= \mp \cos(\theta + A) \bar{j} \mp \sin(\theta + A) \bar{k} \end{aligned} \quad (5.18)$$

where the upper sign in each \pm pair indicates that the friction force acts towards the vertex of the particle, and the lower sign away from the vertex, and the subscripts L and R, represent the left and right contact faces, respectively. Multiplication of the magnitude of the force in equation (5.17) by the friction coefficient, μ , and the vectors in equation (5.18) results in the friction forces acting over the instantaneous contact area. The expressions for the friction forces acting on the left and right sides of the particle in the Y and Z directions, T_{LY} , T_{LZ} , T_{RY} , and T_{RZ} are,

$$\begin{aligned}
 T_{Y_L} &= \pm \mu p_d \int_{Y_c} dY \\
 T_{Z_L} &= \pm \mu p_d \int_{Z_c} dZ \\
 T_{Y_R} &= \mp \mu p_d \int_{Y_c} dY \\
 T_{Z_R} &= \mp \mu p_d \int_{Z_c} dZ
 \end{aligned}
 \tag{5.19}$$

where, as before, the upper sign indicates friction towards the vertex of the particle, and the lower one, friction away from the vertex. The total instantaneous forces acting on the left and right side of the particle in the Y and Z directions become,

$$\begin{aligned}
 F_{Y_L} &= -p_d \int_{Z_c} dZ \pm \mu p_d \int_{Y_c} dY \\
 F_{Z_L} &= p_d \int_{Y_c} dY \pm \mu p_d \int_{Z_c} dZ \\
 F_{Y_R} &= -p_d \int_{Z_c} dZ \mp \mu p_d \int_{Y_c} dY \\
 F_{Z_R} &= p_d \int_{Y_c} dY \mp \mu p_d \int_{Z_c} dZ
 \end{aligned}
 \tag{5.20}$$

where, again the upper sign on the \pm denotes friction towards the particle vertex, and the lower sign is for friction away from the particle vertex.

Because there is no ϕ and ψ dependence in this problem, the body-fixed x-axis will always remain parallel to the inertial X axis, and $M_x = M_X = M_\theta$; therefore it is convenient to work in inertial co-ordinates. The instantaneous moments in the X direction acting on the left and right sides of the bottom portion of the particle are found by multiplying the differentials of the forces in equation (5.20) by the appropriate moment arms expressed in inertial co-ordinates, ($Z_0 - Z$ for forces in the Y direction, and $Y - Y_0$ for forces in the Z direction) and integrating over the contact area, i.e.,

$$\begin{aligned}
 M_{x_l} = M_{\theta_l} &= -p_d \int_{z_c} (Z_0 - Z) dZ \pm \mu p_d \int_{z_c} \frac{(Z_0 - Z)}{\tan(\theta - A)} dZ + \\
 &\quad + p_d \int_{y_c} (Y - Y_0) dY \pm \mu p_d \int_{y_c} (Y - Y_0) \tan(\theta - A) dY \\
 M_{x_r} = M_{\theta_r} &= -p_d \int_{z_c} (Z_0 - Z) dZ \mp \mu p_d \int_{z_c} \frac{(Z_0 - Z)}{\tan(\theta + A)} dZ \\
 &\quad + p_d \int_{y_c} (Y - Y_0) dY \mp \mu p_d \int_{y_c} (Y - Y_0) \tan(\theta + A) dY
 \end{aligned} \tag{5.21}$$

with the usual \pm sign convention for the direction of friction, and Y_0 and Z_0 are the co-ordinates of the centre of mass of the particle expressed in the inertial frame of reference. Substitution of equations (5.20) and (5.21) into equation (5.12) results in a system of three coupled differential equations describing the motion of the centre of mass of the particle (Y_0, Z_0) and the orientation of the particle, θ , at any time during the impact.

5.3.2 Numerical solution of the differential equations

The forces and moments acting on the particle, equations (5.20) and (5.21) were derived for a fixed instant in time. The area of integration (i.e. the contact area) for these forces and moments, however, will change with time as the particle travels through the target material. As

long as the particle is in full contact with the target material, the limits of integration in equations (5.20) and (5.21) are defined by the vertex of the particle contacting the target, and the intersection of the left and right sides of the particle with the Y axis. However, at some point during the impact the particle will probably lose full contact with the target material, and may be in contact only over segments of each of the left and right side of the particle (Figure 5.4). It is thus very difficult to obtain general expressions for the limits of integration in equations (5.20) and (5.21) at any instant in time. The equations are best solved numerically in time steps, with the above forces and moments assumed constant over each time interval.

The system of second order differential equations describing the particle dynamics, equation (5.12), can be reduced to the following set of six first-order differential equations,

$$\begin{aligned} m \frac{d\dot{Y}_0}{dt} &= F_Y \\ m \frac{d\dot{Z}_0}{dt} &= F_Z \\ I_x \frac{d\dot{\theta}}{dt} &= M_\theta \\ \frac{dY_0}{dt} &= \dot{Y}_0 \\ \frac{dZ_0}{dt} &= \dot{Z}_0 \\ \frac{d\theta}{dt} &= \dot{\theta} \end{aligned} \tag{5.22}$$

where all parameters are functions of time. Equations (5.22) can be solved by using the fourth-order Runge-Kutta method over each time step as follows [53]:

- (1) Specify the input variables: incident velocity, V_i , angle of attack, α , and particle orientation, θ_i , friction coefficient, μ , dynamic hardness of the target, p_d , length of a side of

the particle, h , angularity of the particle, A , and density of the particle material, ρ . The initial rotational velocity is assumed to be zero.

- (2) The initial contact areas, and thus the limits of integration for equations (5.20) and (5.21), are determined by assuming the particle is initially in full contact with the target material. Equations (5.22) are then solved to obtain the position and orientation at the end of the first time step. The co-ordinates of the vertex of the particle, and the left and right intersection of the particle profile with the Y axis, are stored as the crater profile at the end of the first step.
- (3) The position, orientation, linear and angular velocities of the particle obtained from the previous time step (step (2)) are used as the initial conditions in solving equation (5.22) to obtain the current particle position, velocities and orientation, again assuming full contact. By using the algorithm outlined below, the current crater profile, as well as the contact area for use in equations (5.20) and (5.21) (to calculate the force and moment for the next time step) can be determined based on this current particle position. The contact area may only be over portions of the particle at this point, so that the integrals of equations (5.20) and (5.21) may have to be carried out over different contact intervals on each of the left and right side of the particle.

Step (3) is repeated using the position, orientation, linear and angular velocities of the particle at the end of each time step, as the initial conditions for the next time step. At the end of each time step, the intersection between the current particle profile and the previous crater profile is used to update the crater profile, and to determine the contact area, and thus the force, for the next time step. The direction of friction is determined by comparing the contact areas in subsequent time steps. If the contact area over a given contact interval on either the left or right side, in a given time step, decreases in the subsequent time step, the friction is assumed to act towards the particle vertex for the subsequent interval, otherwise it is assumed to act away from the particle vertex. The procedure is repeated until the particle vertex Z-co-ordinate reaches $Z = 0$, indicating that the collision has ended.

5.3.3 Algorithm for determining crater profile and contact area at end of each step

The most difficult part of the above procedure is the determination of the crater profile and contact area at the end of each time step. Figure 5.4 depicts a certain time step with the current position of the particle shown, and the current and previous crater profiles. The 'nodes' marked by the numbers without primes in Figure 5.4 define line segments making up the crater profile determined in the previous time step, and are assumed stored in an array, and the nodes marked by numbers with primes define the current crater profile. The distance between nodes has been exaggerated for clarity. The Roman numerals I, II, and III, defining the co-ordinates of the left vertex, middle vertex, and right vertex of the particle in the current position are assumed known, obtained from the co-ordinates of the centre of mass (Y_0, Z_0) by application of equation (5.15).

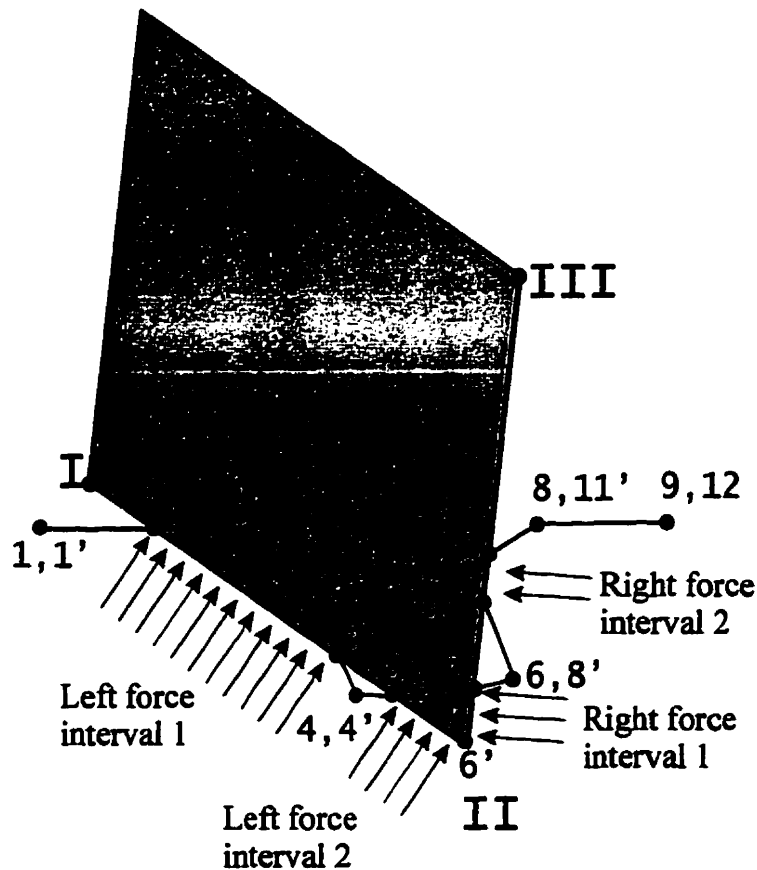


Figure 5.4: Previous crater profile (1,2,3...), current crater profile (1',2',3'...) and force application intervals for the next time step.

In order to determine the current crater profile, it is necessary to determine the intersection of the current particle surface with the previous crater profile. This can be done by finding the intersection of previous crater segments (the lines formed by connecting two consecutive unprimed nodes, Figure 5.4) with the particle surface. Because the left and right side of the bottom part of the particle surface are described by different equations, it is necessary to locate the transition from checking the intersection of previous crater segments with the left side of the current particle surface to checking the intersection of previous crater segments with the right side of the current particle surface. It is thus assumed that the previous crater segment at which this transition occurs is known at the beginning of each time step (determination of this crater segment is explained below). In general, there can be multiple intersection points (and thus multiple force segments) of the current particle surface with the previous crater profile on either of the left and right side of the particle. In practice, however, the author has found that no more than two force segments appear on either the left or right sides of the particle.

The tasks are: (a) to determine if the previous crater nodes will be part of the current crater profile (b) find the intersection of the current particle position with the previous crater profile, and (c) determine the interval of Y over which contact occurs for use in equations (5.20) and (5.21) to determine the forces for the next time step.

The detailed procedure is as follows [53]:

- (1) Determine the equations defining the current left and right sides of the particle by using points I, II, and III (Figure 5.4). The equations will have the form,

$$\begin{aligned} Z_p^L &= m_p^L Y + b_p^L \\ Z_p^R &= m_p^R Y + b_p^R \end{aligned} \tag{5.23}$$

where m and b are the slope and Z intercept of the current particle profile, respectively, the superscripts L and R refer to the left and right side of the particle, and the subscript P indicates that the equations refer to the particle.

- (2) Determine the equation of the first segment of the previous crater profile using points 1 and 2 in Figure 5.4, which will have the form,

$$Z_c = m_c Y + b_c \quad (5.24)$$

where m_c and b_c are the slope and Z intercept of the crater profile.

- (3) Find the intersection of the current particle surface with the previous crater segment in question using equations (5.23) and (5.24). Determine whether this intersection actually occurs on the previous crater segment in question. If it does not, determine whether the two crater nodes forming the crater segment in question are on the inside or outside of the particle surface. For example, to determine if a specific crater node on the left side of vertex II is inside or outside of the particle surface, the points (Y_L^N, Z_L^N) and (Y_L^*, Z_L^*) (Figure 5.5) are formed by projecting the node (Y_L^N, Z_L^N) onto the particle surface. A similar procedure holds for crater nodes on the right side of vertex II. The criteria for a node being inside or outside of the particle surface is different depending on whether nodes are being checked against the left or right side of the particle, and Figure 5.5 shows an example of each case:

Left side :

$$m_L = \frac{Z_{II} - Z_I}{Y_{II} - Y_I}$$

$$b_L = Z_{II} - m_L Y_{II}$$

$$Y_L^* = \frac{Z_L^N - b}{m_L}$$

$$\text{inside : } Y_L^* - Y_L^N \leq 0$$

$$\text{outside : } Y_L^* - Y_L^N > 0$$

Right side :

$$m_R = \frac{Z_{III} - Z_{II}}{Y_{III} - Y_{II}}$$

$$b_R = Z_{III} - m_R Y_{III}$$

$$Y_R^* = \frac{Z_R^N - b}{m_R}$$

$$\text{inside : } Y_R^* - Y_R^N \geq 0$$

$$\text{outside : } Y_R^* - Y_R^N < 0$$

(5.25)

If the node is on the outside of the particle, then it becomes a node in the current crater, otherwise it is not a node on the current crater.

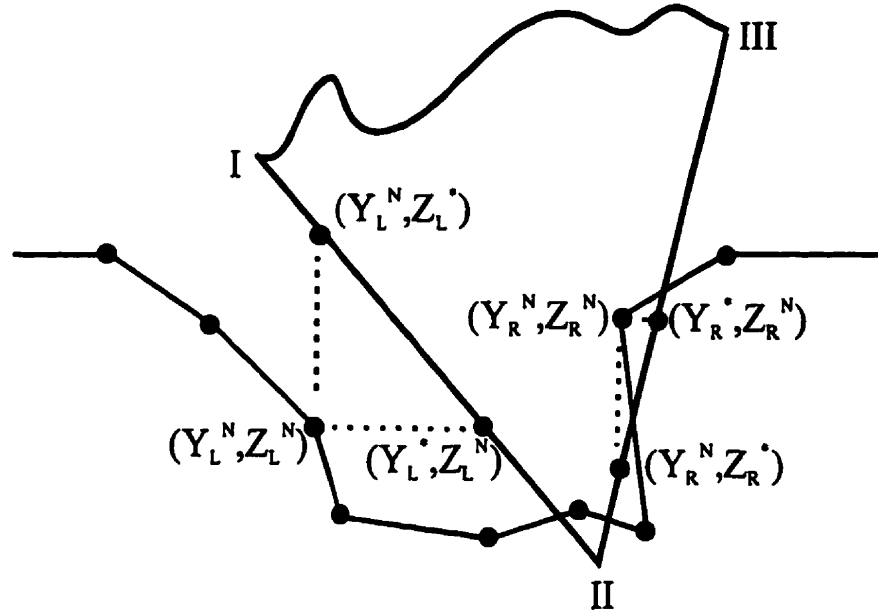


Figure 5.5: Points (Y_L^N, Z_L^*) , (Y_L^*, Z_L^N) , (Y_R^N, Z_R^*) , and (Y_R^*, Z_R^N) used to determine whether given nodes (Y_L^N, Z_L^N) and (Y_R^N, Z_R^N) are inside or outside of particle surface.

Step (3) is repeated on subsequent nodal segments until an intersection between the particle and the previous crater profile is obtained. The intersection point becomes a node on the current crater profile, and the first of the limits of integration for the forces and moments of equations (5.20) and (5.21). Step (3) is then repeated on subsequent segments until another intersection point is reached, which then becomes the second limit of integration.

In this manner, all nodal segments for the previous crater profile are checked for intersection with the left side of the particle, nodes are checked to see whether they belong in the current crater profile or not, and integration limits are assigned for forces and moments on the left side of the particle.

When the transition crater segment (at which the transition between checking the left and right side of the particles against the previous crater profile) is reached, the vertex of the particle is checked as a possible node on the current crater profile. This is done by determining

whether the vertex is inside or outside of the crater, using the method of equation (5.25), but with the transition crater segment (e.g. segment 4-5 in Figure 5.4) used in place of the particle profile (I-II), and the particle vertex co-ordinates (Y_{II}, Z_{II}) used in place of the crater node (Y_n, Z_n). If the vertex is found to be on the outside of the crater profile, then the vertex is assigned as a current crater profile node and the subsequent nodes on the previous crater profile are checked against the right side of the particle. The crater segment (current) containing the vertex is stored as the transition segment for the next time step. If the vertex is found to be inside of the crater profile, then it is not part of the current crater profile, and the transition segment does not change.

5.3.4 Limitations of model

It would be useful at this point to list the limitations of the model, as applied to the symmetric particles of Figure 5.3. The limitations on the model can be summarised as follows:

- (a) Rigid-plastic theory is assumed. The particles must be non-deforming, and the target material must behave fully plastic, and is thus described by a constant dynamic hardness defined as the normal force resisting the indentation divided by the instantaneous contact area. The direction of a force differential is assumed perpendicular to the instantaneous contact area differential. No elastic effects are accommodated by the model.
- (b) Particles are symmetric, with side length h , as shown in Figure 5.3. The thickness of the particle is constant, and impact is assumed to occur with the y - z plane of the particle perpendicular to the surface of the target material. The problem is thus essentially two-dimensional, with particle mass, moment of inertia, and the volume of the crater all expressed on a per-unit-thickness basis.
- (c) The model will sometimes predict that the particle rotates forward (i.e. it tumbles) to the point that a secondary impact occurs. The model is valid only to the start of the secondary impact, and thus predictions of crater area will not include the secondary

- impact. This is not a limitation of the fundamental theory, but a limitation of the computer program written to implement the model (as explained in Section 5.5).
- (d) Though the model can accommodate nonzero initial rotational velocity, to reduce the number of variables, the initial rotational velocity was assumed zero in this study.
 - (e) At any point during the impact, only the bottom part of the particle (the material below the y axis in Figure 5.3) is assumed to contact the target. Note that this does not necessarily mean that the vertices at $y = h \cos(A)$ cannot be below the Y axis. If one of the edges on the top part of the particle above the y axis becomes a trailing edge (as a result of backward rotation), it will not come into contact with the target material, and thus the model is still valid. However, if the particle rotates forwards, the top part of the particle will become a leading edge and thus contact the material, and the model is not valid. This is not a limitation of the model, but the computer implementation.
 - (f) The model does not consider the destination of the plowed target material (i.e. the model does not predict the formation of 'lips' of plowed target material above $Z = 0$).
 - (g) The model assumes constant friction coefficient, μ .

5.4 Comparison with experimental data

In the case of square particles (i.e. $A = 45$ deg.), the model can be compared with experimental data involving the collision of $8 \times 8 \times 1.5$ mm thick steel plates with steel targets obtained by Hutchings [7]. The measured crater volume, energy loss, and rebound rotational energy obtained by Hutchings, together with the results of the present model are presented in Figure 5.6, Figure 5.7, and Figure 5.8. It should be noted that the data are a combination of the data at $\theta_i = 0^\circ, 10^\circ, \text{ and } 25^\circ$ plotted together. The initial rake angle defined by Hutchings is equal to 45° minus the present initial orientation angle, θ_i . The dynamic hardness, p_d , used in these figures was the same as used by Hutchings (4 GPa), and, to facilitate comparison with the results of Hutchings' analysis, the friction coefficient, μ , was chosen to be zero. It will be shown in the next section that friction has a very small effect on the results of the model, if μ is small (approx. < 0.1).

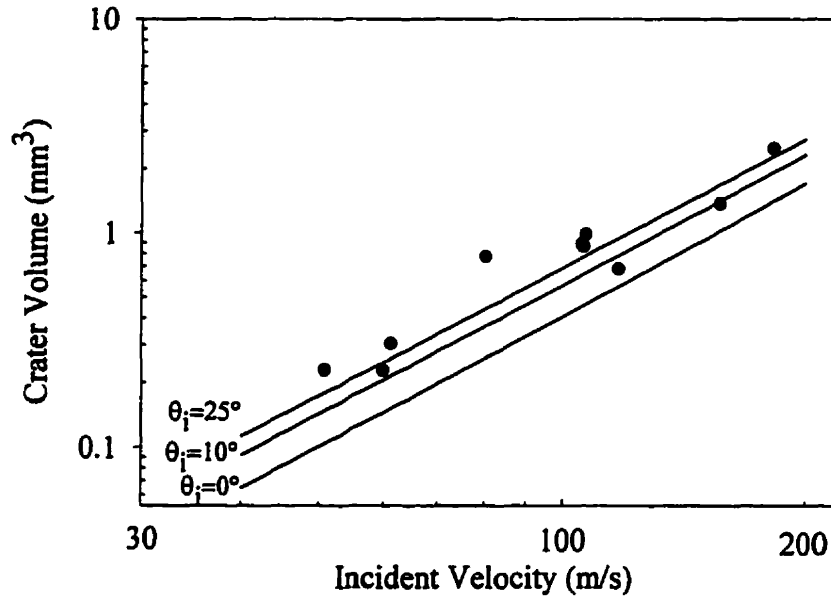


Figure 5.6: Crater Volume vs. Incident Velocity for different initial particle orientations, θ_i (Figure 5.3). Predictions of model with angle of attack $\alpha = 30^\circ$, angularity, $A = 45^\circ$, dynamic hardness $p_d = 4$ GPa, friction coefficient, $\mu = 0$ shown as solid lines. Experimental data of Hutchings [7] for $8 \times 8 \times 1.5$ mm thick steel plates impacting steel targets for $\theta_i = 0^\circ, 10^\circ, 25^\circ$ shown as dots.

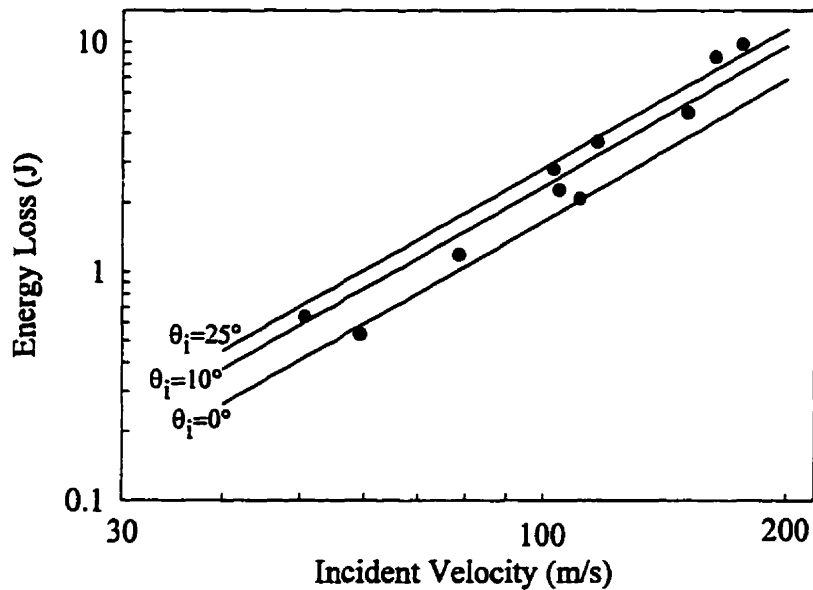


Figure 5.7: Energy Loss vs. Incident Velocity for different initial particle orientations, θ_i (Figure 5.3). Predictions of model with angle of attack $\alpha = 30^\circ$, angularity $A = 45^\circ$, dynamic hardness $p_d = 4$ GPa, friction coefficient $\mu = 0$ shown as solid lines. Experimental data of Hutchings [7] for $8 \times 8 \times 1.5$ mm thick steel plates impacting steel targets for $\theta_i = 0^\circ, 10^\circ, 25^\circ$ shown as dots.

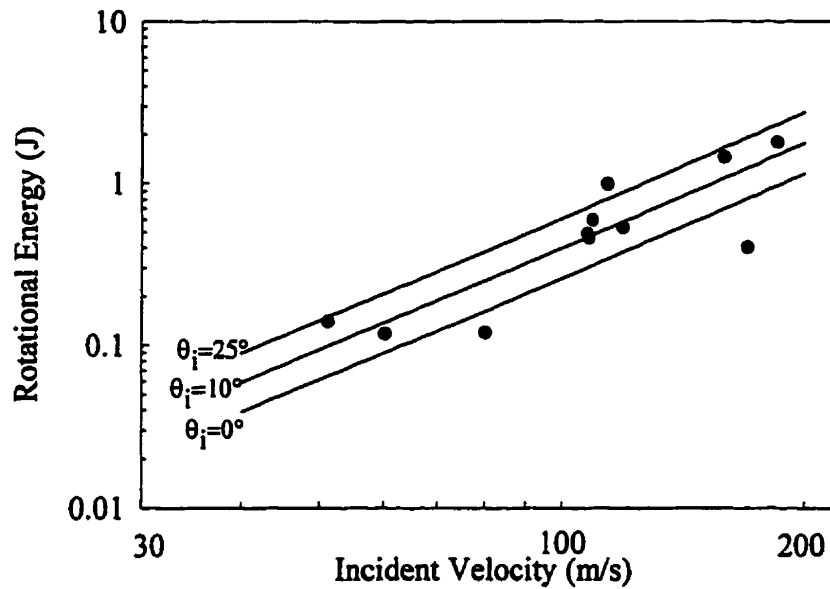


Figure 5.8: Rotational Energy vs. Incident Velocity for different initial particle orientations, θ_i (Figure 5.3). Predictions of model with angle of attack $\alpha = 30^\circ$, angularity $A = 45^\circ$, dynamic hardness $p_d = 4$ GPa, friction coefficient $\mu = 0$ shown as solid lines. Experimental data of Hutchings [7] for $8 \times 8 \times 1.5$ mm thick steel plates impacting steel targets for $\theta_i = 0^\circ, 10^\circ, 25^\circ$ shown as dots.

There is good agreement with the experimental results in all cases. No systematic variation in the measured quantities with rake angle was observed in the experiments of Hutchings [7]. Although the present model predicts a small variation with initial orientation, if such a variation actually exists in the experimental data, the inherent data scatter would most likely hide it.

It should be noted that all predictions obtained by the present model shown in Figure 5.6, Figure 5.7, and Figure 5.8 are within 1% of the predictions made by the Hutchings model (not shown) [7]. This, together with the agreement with the experimental data lends support to the validity of the present model.

5.5 Parametric study of impact of symmetric angular particles

In Section 5.3, a rigid-plastic theory for the impact of symmetric particles with plastic targets was developed. It was found that the resulting differential equations cannot be solved in closed-form, and the problem is best solved in time steps via a computer. In this section, the crater size, A_c , is examined as a function of particle size, h , angularity, A , initial particle orientation, θ_i , initial angle of attack, α , initial velocity, v_i , target dynamic hardness, p_d , and friction coefficient, μ . The purpose is to predict the conditions under which maximum material removal occurs.

5.5.1 Implementation of model

A computer program to implement the analysis of the symmetric particle of Section 5.3 was written using the MathCad 7.0 Plus programming language. This program can be found in Appendix D, with a brief description of each function written also being given. The program allowed for all of the inputs discussed at the end of the previous paragraph, along with the chosen time step, and calculated the trajectory of the particle as it ploughed through the target, the final crater profile, rebound angle, rebound linear velocity, rebound rotational velocity, and rebound orientation. In each time step, the differential equations were solved using the fourth order Runge-Kutta function in MathCad. The time step required for model convergence was determined by decreasing it until the difference between successive runs of the model was less than 1%. Depending on the input parameters used, the required time steps varied between 0.01 μs and 0.2 μs , which corresponds to approximately 0.5 % of the impact duration.

5.5.2 Dimensional analysis

The following eight input parameters can be varied: incident velocity, v_i , length of a side of the particle, h , angle of attack, α , initial particle orientation, θ_i , angularity of the particle, A , target dynamic hardness, p_d , particle density, ρ , and friction coefficient, μ . The output of current interest is the crater volume per unit width, or, equivalently, the crater cross-sectional

area, A_c in the Y-Z plane (the rebound velocity and rebound angle can also be predicted by the model, but these are of secondary interest). A simple dimensional analysis reveals that the number of parameters can be reduced by use of the following two dimensionless groups [54]:

$$\pi_1 = \frac{p_d}{\rho v_i^2} \quad (5.26)$$

$$\pi_2 = \frac{A_c}{2h^2 \cos A \sin A} \quad (5.27)$$

The denominator of equation (5.27) is the area of the particle in the Y-Z plane so that π_2 gives the ratio of the crater volume to the particle volume (both per unit thickness). If the numerator and denominator of π_1 are multiplied by the particle volume, it is seen that (see equation (5.30)) π_1 is ratio of the plastic work required to create a crater having the size of the incident particle to the incident kinetic energy of the particle. In order to verify that the model results scaled, different values of p_d and v_i were used, each giving $\pi_1=12.8$, and the model was run for different values of θ , A , and α . It was found that corresponding π_2 values (model output in this case) were within 2% of each other, provided that the time steps were adjusted for convergence, and that the conditions outlined in Section 5.3.4 were met. The number of parameters to be varied is thus reduced to π_1 , α , θ , μ , and A , and the only output parameter is π_2 .

5.5.3 Model systems

Two model systems were chosen for a parametric study of the effects of varying input parameters on crater area. The first was chosen to facilitate comparison between the present model and the work of Hutchings [7], who studied the impact of square steel plates with steel targets. The relevant parameters are: dynamic hardness, $p_d = 4$ GPa, density of steel, $\rho=7813$ kg/m³, and a typical value of $v_i = 200$ m/s. This results in a π_1 value of 12.8. The time step

used for this system was $0.2 \mu\text{s}$, which is the same value used by Hutchings [7] for the special case of $A = 45^\circ$.

The second system was meant to emulate erosion of an organic coating by wheat starch particles [36]. As discussed in Section 3.4.2, the dynamic hardness, p_d , of such a coating is dependant on the substrate material on which the coating is applied and on the thickness of the coating [35, 36]. For the coating of Chapter 4, the dynamic hardness is approximately 1120 MPa, and the density, ρ , of wheat starch is approximately 1450 kg/m^3 . Measurements of particle velocities in blast cleaning applications have shown that a typical value of particle incident velocity is 188 m/s [36]. This results in a π_1 value of 21.9, and the time step used for this system was $0.02 \mu\text{s}$.

5.5.4 Results and Discussion

Figure 5.9 and Figure 5.10 show some typical particle trajectories (plotted every $4 \mu\text{s}$ from left to right) obtained with the computer implementation of the model for particles of various sizes and shapes and input conditions. Figure 5.9 shows the results of the model for low to mid angularity, and Figure 5.10 shows the results for high angularity. In each of Figure 5.9 and Figure 5.10, (a) and (c) illustrate backwards rotation of the particle, and (b) and (d) illustrate forward rotation of the particle. Hutchings also observed this type of behavior in his study of the impact of square particles [7].

Figure 5.11 and Figure 5.12 show the final calculated crater profiles corresponding to the conditions in in Figure 5.9 and Figure 5.10. In general, collisions in which backward rotation occurs ((a) and (c)) result in long shallow craters, while collisions with forward rotation ((b) and (d)) result in shorter, but deeper craters.

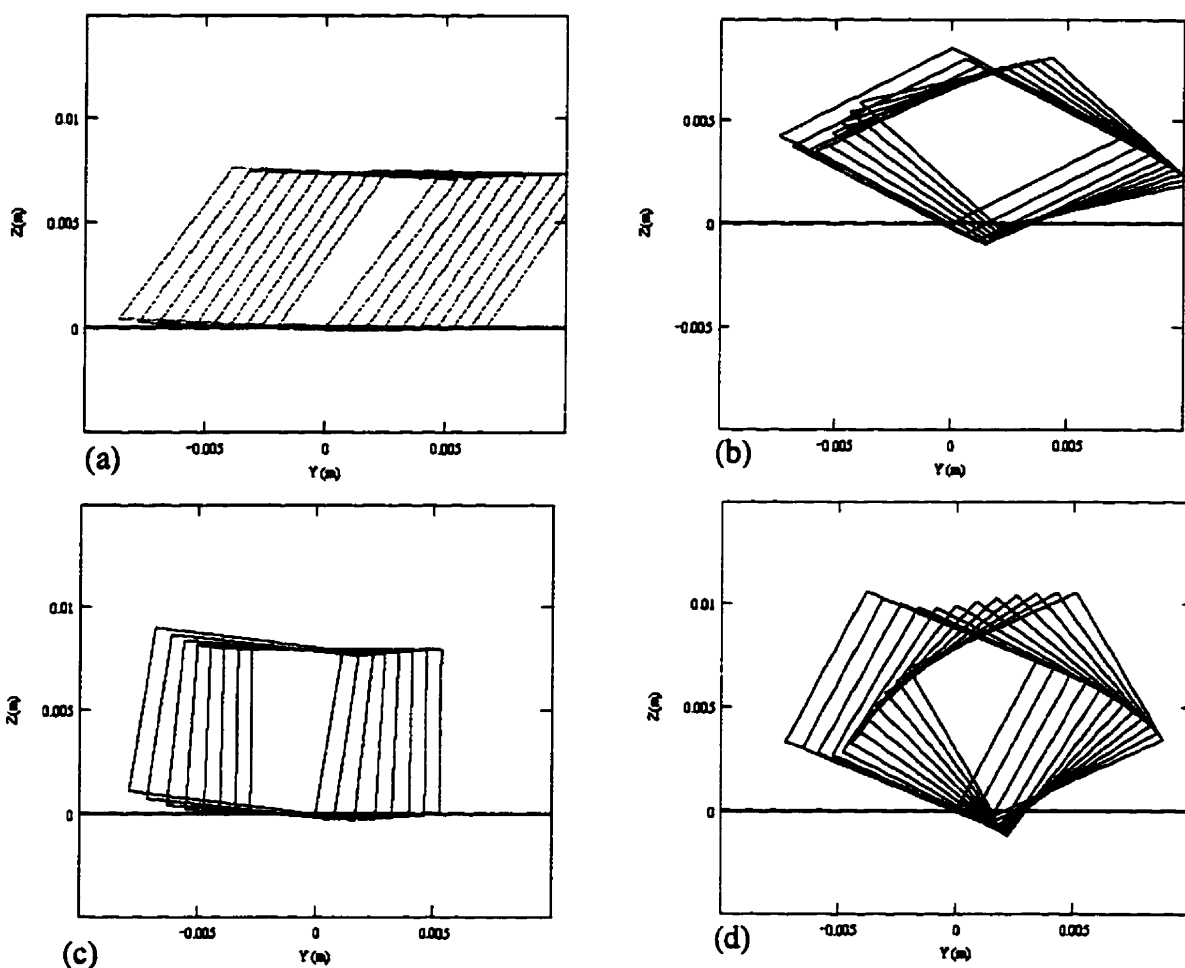


Figure 5.9: Particle trajectories at $4 \mu\text{s}$ intervals, obtained with model for $\pi_1 = 12.8$, and angularity, A , incident angle, α , initial orientation, θ_i , and particle side length, h , of: (a) 30° , 15° , 27° , 8.6 mm (b) 30° , 45° , 0° , 8.6 mm (c) 45° , 25° , 37° , 8.0 mm (d) 45° , 25° , 20° , 8.0 mm . A solution time step of $0.2 \mu\text{s}$ was used in all cases.

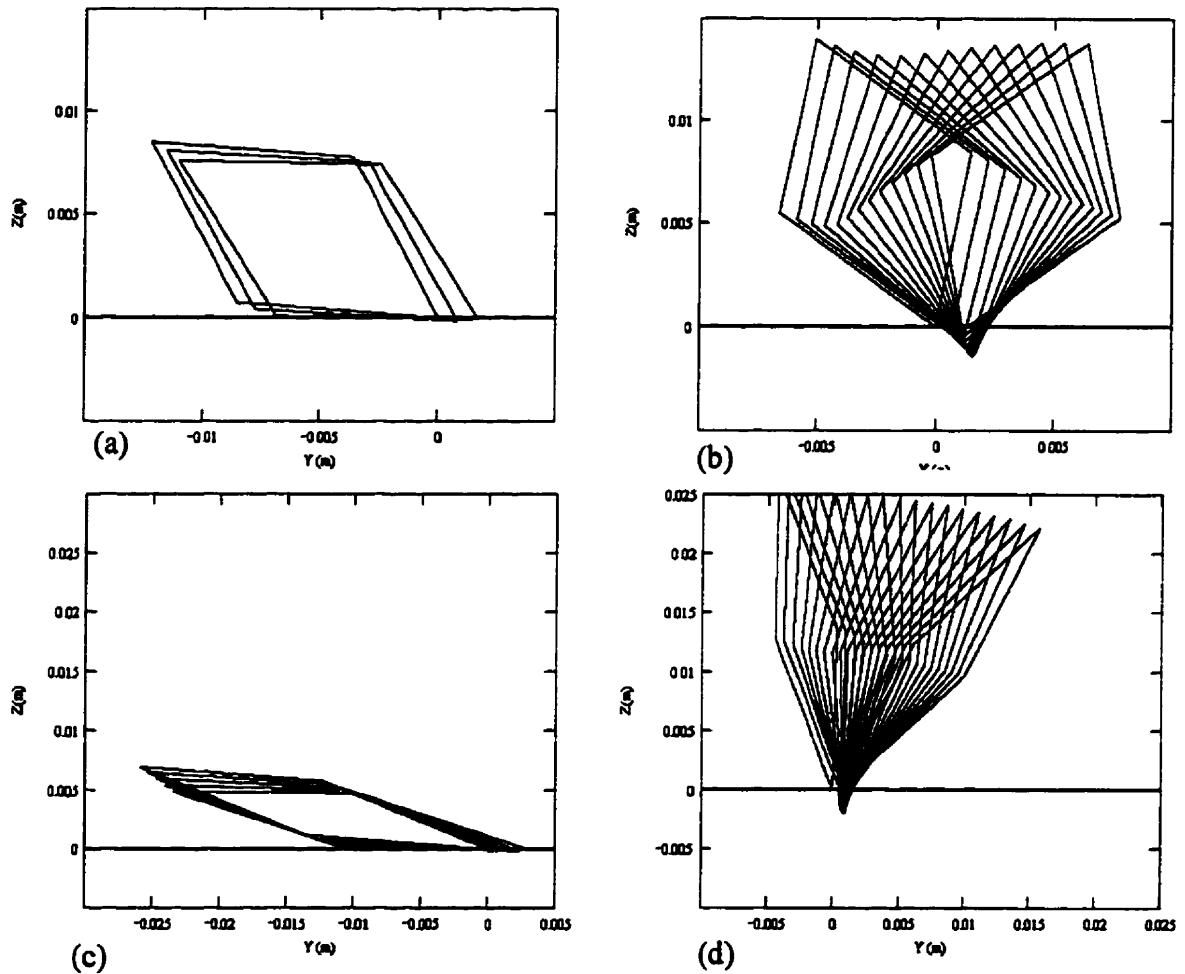


Figure 5.10: Particle trajectories at $4 \mu\text{s}$ intervals, obtained with model for $\pi_1 = 12.8$, and angularity, A , incident angle, α , initial orientation, θ_0 , and particle side length, h , of: (a) $60^\circ, 25^\circ, 55^\circ, 8.6 \text{ mm}$ (b) $60^\circ, 25^\circ, 20^\circ, 8.6 \text{ mm}$ (c) $80^\circ, 25^\circ, 75^\circ, 13.7 \text{ mm}$ (d) $80^\circ, 25^\circ, 9^\circ, 13.7 \text{ mm}$. A solution time step of $0.2 \mu\text{s}$ was used in all cases.

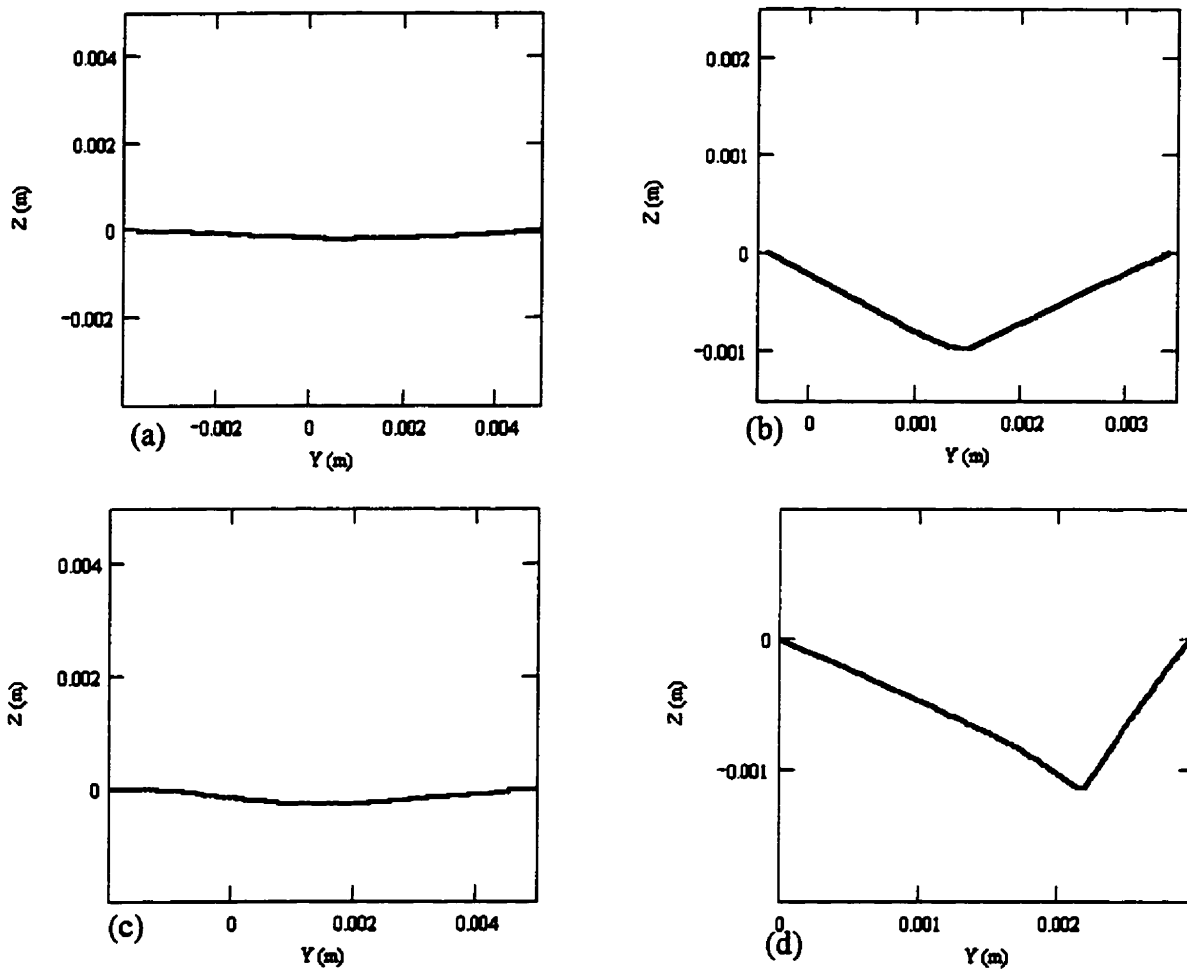


Figure 5.11: Crater profiles obtained with model corresponding to impacts shown in Figure 5.9.

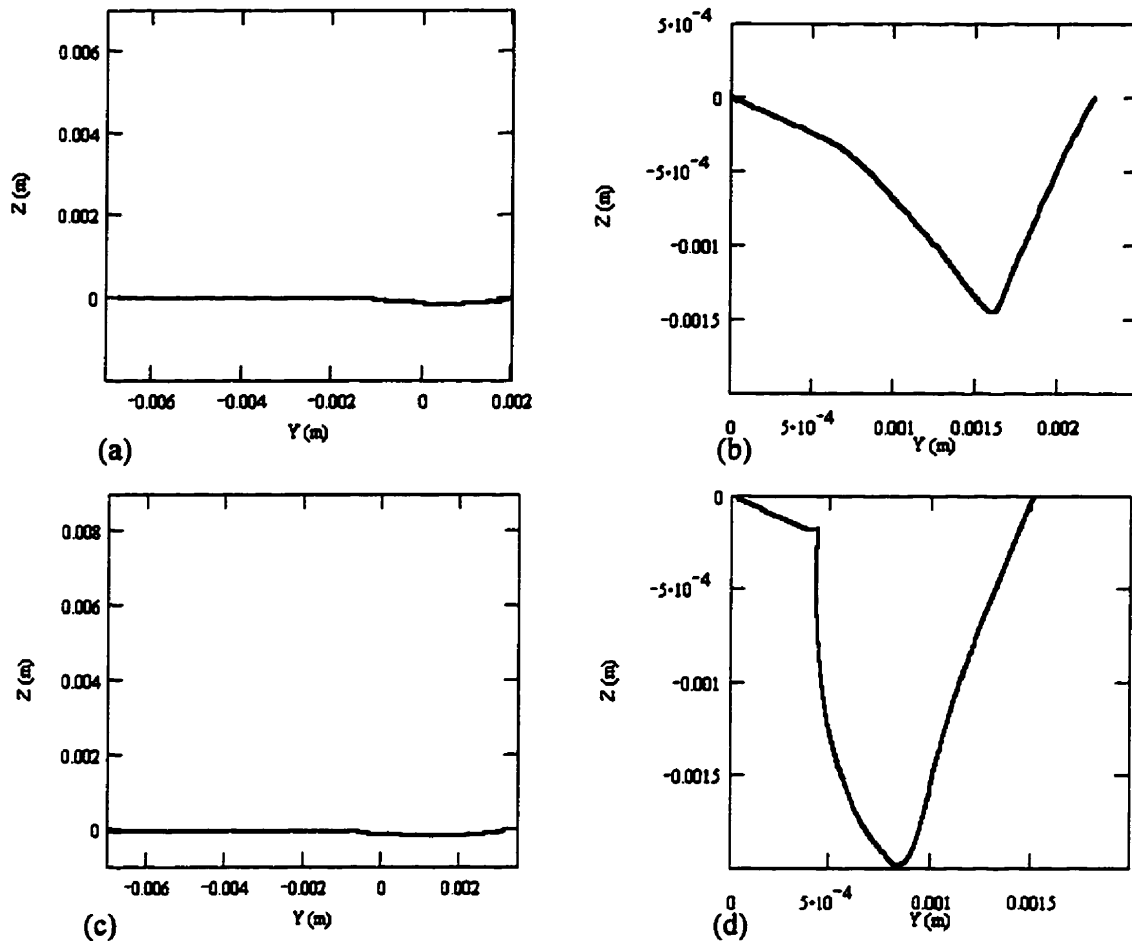


Figure 5.12: Crater profiles obtained with model corresponding to impacts shown in Figure 5.10.

Figure 5.13-Figure 5.15 demonstrate how the dimensionless crater volume, π_2 , varies with π_1 for square particles ($A = 45^\circ$) at three different angles of attack, $\alpha = 25^\circ, 45^\circ$, and 85° in the frictionless case. It is seen that the dimensionless crater volume, π_2 , decreases with increasing π_1 (increased p_d or smaller kinetic energy), that the general shape of the curve is maintained for all π_1 , and that the peak value of π_2 occurs at the same value of θ_i regardless of π_1 . The implication is that, for a given particle, and fixed target material (i.e. fixed h , ρ , and p_d), increasing the incident velocity does not significantly change the impact behaviour, but does create proportionally bigger craters.

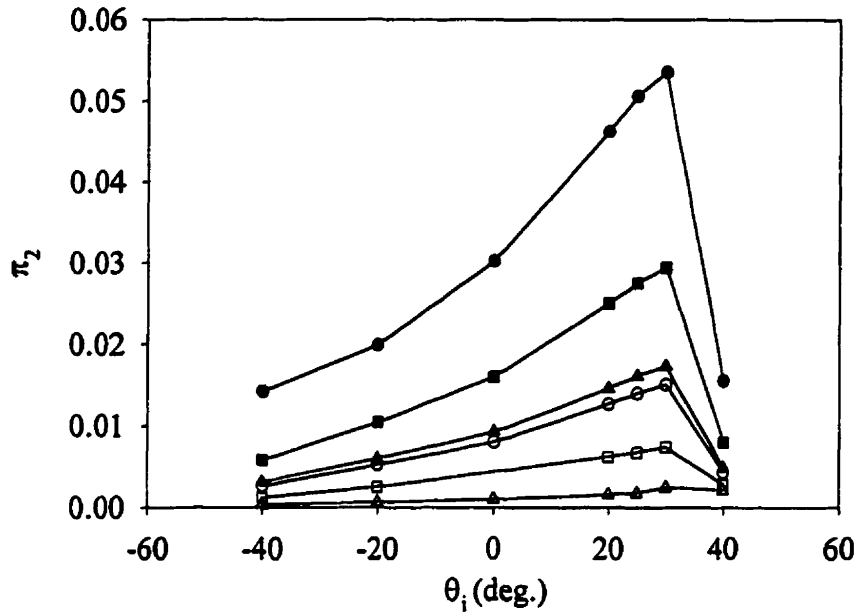


Figure 5.13: Dimensionless crater volume, π_2 , as a function of initial orientation, θ_i , for square particles impacting a frictionless target at angle of attack, $\alpha = 25^\circ$ and π_1 equal to: ● 7, ■ 12.8, ▲ 21.4, ○ 25, □ 51, △ 205.

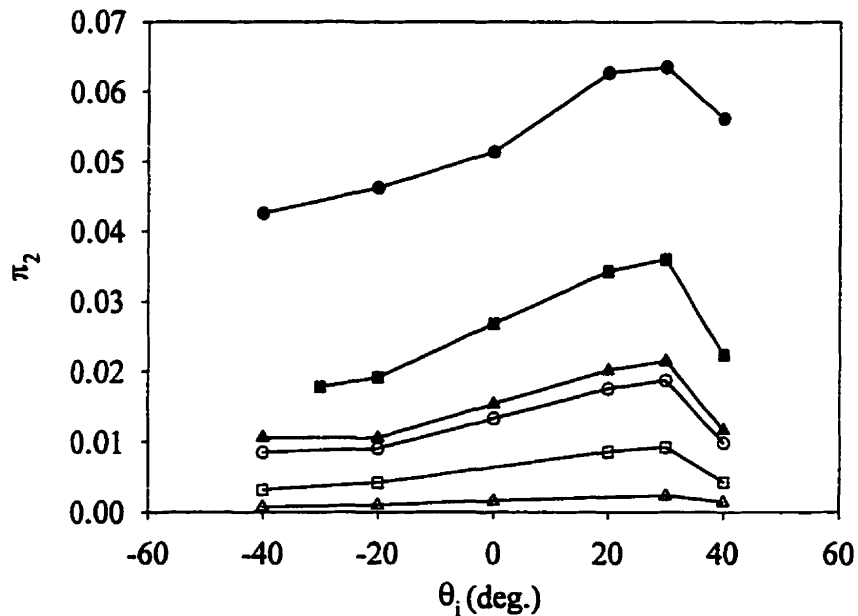


Figure 5.14: Dimensionless crater volume, π_2 , as a function of initial orientation, θ_i , for square particles impacting a frictionless target at angle of attack, $\alpha = 45^\circ$ and π_1 equal to: ● 7, ■ 12.8, ▲ 21.4, ○ 25, □ 51, △ 205.

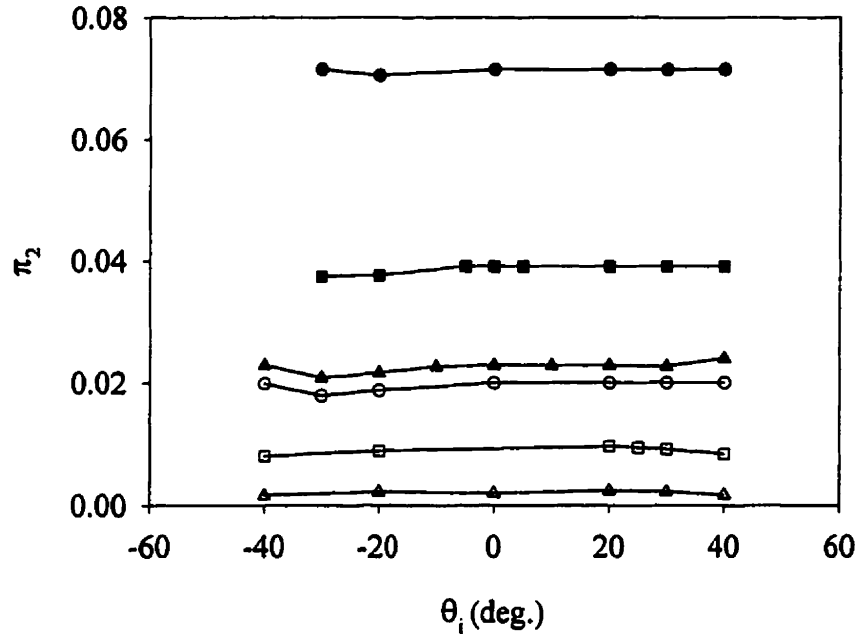


Figure 5.15: Dimensionless crater volume, π_2 , as a function of initial orientation, θ_i , for square particles impacting a frictionless target at angle of attack, $\alpha = 85^\circ$ and π_1 equal to: \bullet 7, \blacksquare 12.8, \blacktriangle 21.4, \circ 25, \square 51, \triangle 205.

The relative difference between the peak and minimum π_2 values becomes smaller with increasing π_1 , meaning that the effect of initial particle orientation, θ_i , becomes less pronounced as π_1 increases. Similar trends are observed at all angles of attack, α . Finally, comparison of Figure 5.15 with Figure 5.13 and Figure 5.14 shows that the effect of initial orientation diminishes at high angles of attack. This point will be further addressed later.

It should be noted that the initial orientation, θ_i , is only varied from $-A$ to A . Behaviour for values of θ_i outside this range can be predicted by noting that the initial conditions in this case are the same as for an impact of a particle with complementary angularity, A^* occurring at an initial orientation, θ_i^* described by the following relationship:

$$\begin{aligned} \theta_i^* &= \theta_i - 90^\circ & \text{for } \theta_i > 0 \\ \theta_i^* &= \theta_i + 90^\circ & \text{for } \theta_i < 0 \end{aligned} \quad (5.28)$$

where the relationship between the angularity, A , and its complement, A^* , is,

$$A = 90^\circ - A^* \quad (5.29)$$

For example, a particle with $A = 30^\circ$ impacting with $\theta_i = 35^\circ$ can equivalently be described by a particle with angularity, $A^* = 60^\circ$ impacting with $\theta_i = -55^\circ$.

It also should be noted that, especially at high angles of attack, a particle might lose all of its kinetic energy at some point during the impact, and remain embedded in the target material (because the model neglects elastic spring-back). An estimate of the conditions under which this will occur can be obtained by noting that the dynamic hardness, p_d , multiplied by the final crater volume (cross-sectional A_c times l), is approximately equal to the work done in creating the crater, in the absence of friction. Assuming that all of the kinetic energy is consumed in work done creating the crater, the following relationship holds (per unit width):

$$p_d A_c = \frac{1}{2} m v_i^2 \quad (5.30)$$

The mass per unit width of the particle, m , is

$$m = 2\rho h^2 \cos(A) \sin(A) \quad (5.31)$$

where ρ is the density of the particle, and A is the angularity (Figure 5.3). Using equations (5.26), (5.27), (5.30), and (5.31), the condition for the particle embedding becomes,

$$\pi_1 \hat{\pi}_2 = 0.5 \quad (5.32)$$

where $\hat{\pi}_2$ is the maximum possible dimensionless crater area corresponding to particle embedding. For the square particle cases ($A = 45^\circ$) shown in Figure 5.13- Figure 5.15, for $\pi_1 = 7.0, 12.8, 21.9, 25, 51,$ and $205,$ $\hat{\pi}_2 = 0.071, 0.039, 0.023, 0.020, 0.010,$ and $0.0024,$ respectively. Comparison of the peak values of π_2 with $\hat{\pi}_2$ in Figure 5.13 and Figure 5.14 shows that the particles do not embed in these cases. The flatness of the curves in Figure 5.15 near or at $\hat{\pi}_2$ indicates that particles are very likely to embed at high angles of attack, regardless of orientation. The fact that particles are more likely to embed at steep angles of attack is to be expected, given that particles will rotate less impacting at close to normal incidence (and thus less of the incident kinetic energy will be converted to rotational energy). This point is further supported by noting that the peaks in material removal occur at the transition between forward and backward rotation (see discussion of Figure 5.16-Figure 5.20 below) where particle rotation through the impact is minimized.

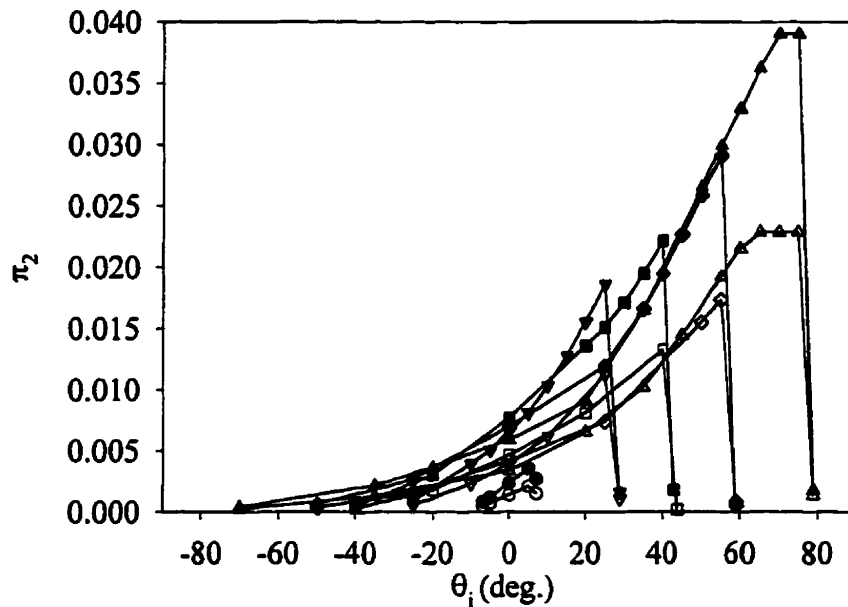


Figure 5.16: Dimensionless crater volume, π_2 , as a function of initial orientation, θ_i , for particles impacting a frictionless target at angle of attack, $\alpha = 5^\circ$ and π_1 fixed at two values: $\pi_1 = 12.8$ and A values: $\blacktriangle 80^\circ, \bullet 60^\circ, \blacksquare 45^\circ, \blacktriangledown 30^\circ, \bullet 10^\circ$. $\pi_1 = 21.9,$ A values: $\triangle 80^\circ, \diamond 60^\circ, \square 45^\circ, \triangledown 30^\circ, \circ 10^\circ$.

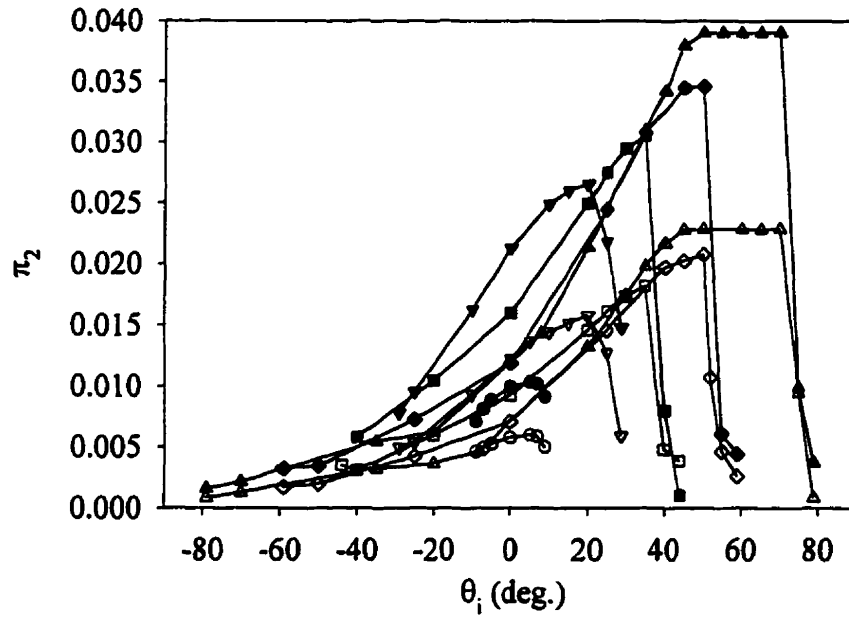


Figure 5.17: Dimensionless crater volume, π_2 , as a function of initial orientation, θ_i , for particles impacting a frictionless target at angle of attack, $\alpha = 25^\circ$ and π_1 fixed at two values: $\pi_1 = 12.8$ and $\pi_1 = 21.9$, A values: \blacktriangle 80° , \bullet 60° , \blacksquare 45° , \blacktriangledown 30° , \bullet 10° . $\pi_1 = 12.8$, A values: \triangle 80° , \diamond 60° , \square 45° , \triangledown 30° , \circ 10° .

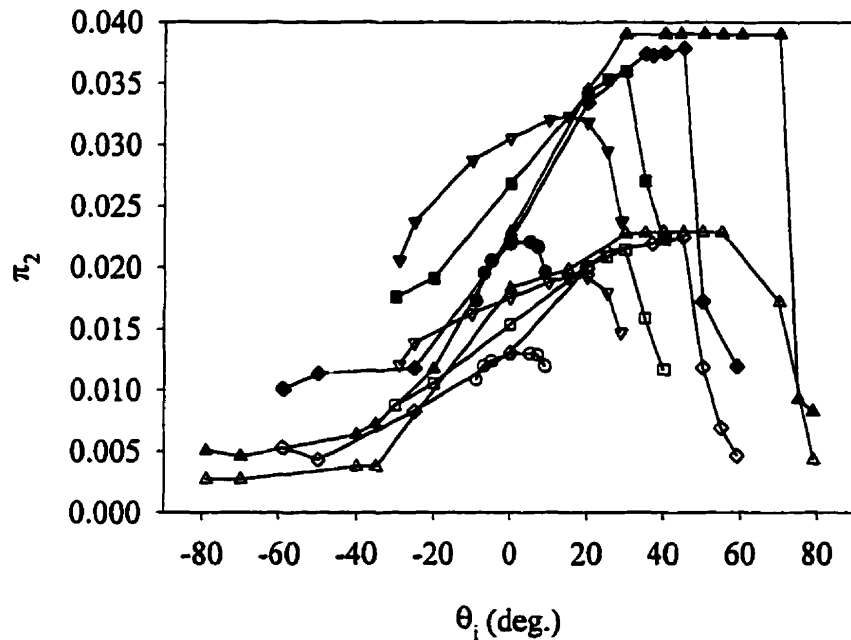


Figure 5.18: Dimensionless crater volume, π_2 , as a function of initial orientation, θ_i , for particles impacting a frictionless target at angle of attack, $\alpha = 45^\circ$ and π_1 fixed at two values: $\pi_1 = 12.8$ and $\pi_1 = 21.9$, A values: \blacktriangle 80° , \bullet 60° , \blacksquare 45° , \blacktriangledown 30° , \bullet 10° . $\pi_1 = 12.8$, A values: \triangle 80° , \diamond 60° , \square 45° , \triangledown 30° , \circ 10° .

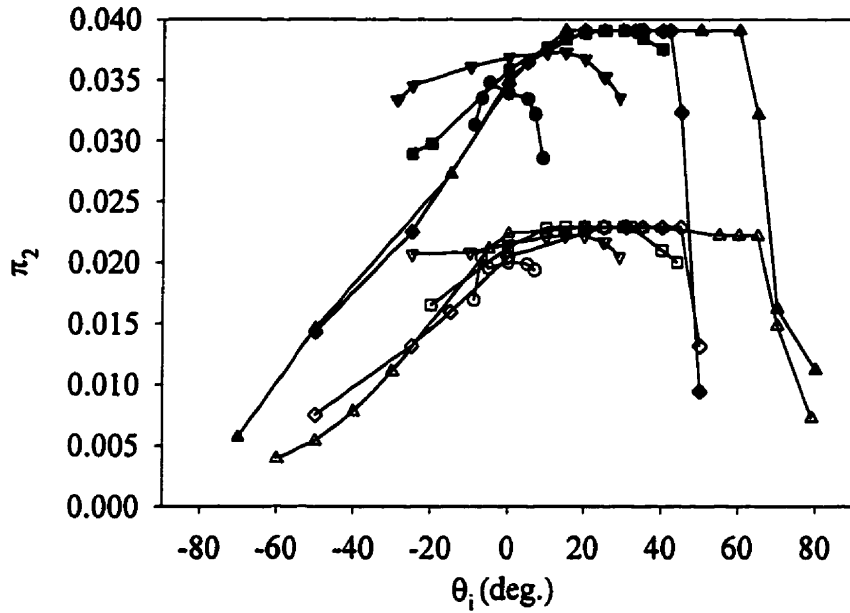


Figure 5.19: Dimensionless crater volume, π_2 , as a function of initial orientation, θ_i , for particles impacting a frictionless target at angle of attack, $\alpha = 65^\circ$ and π_1 fixed at two values: $\pi_1 = 12.8$ and A values: \blacktriangle 80° , \bullet 60° , \blacksquare 45° , \blacktriangledown 30° , \bullet 10° . $\pi_1 = 21.9$, A values: \triangle 80° , \diamond 60° , \square 45° , \triangledown 30° , \circ 10° .

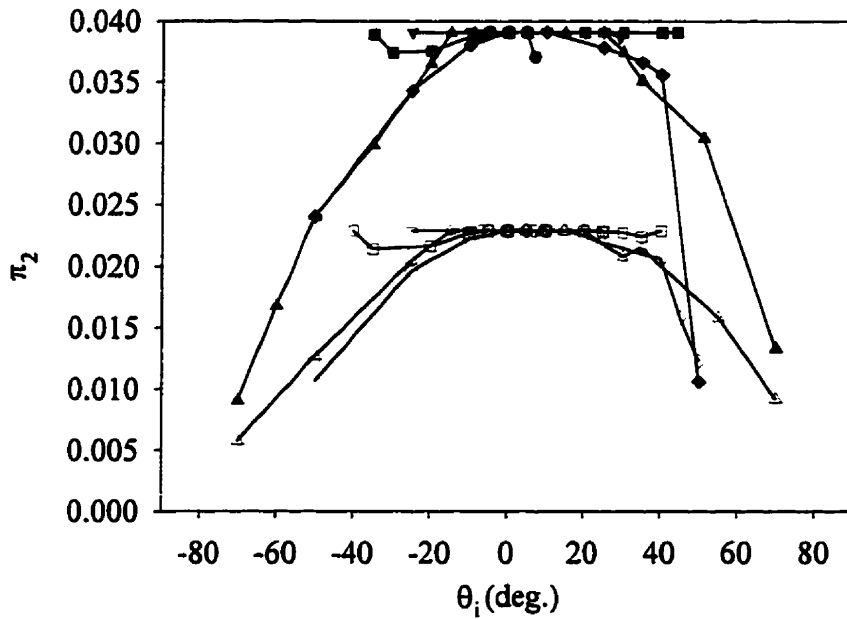


Figure 5.20: Dimensionless crater volume, π_2 , as a function of initial orientation, θ_i , for particles impacting a frictionless target at angle of attack, $\alpha = 85^\circ$ and π_1 fixed at two values: $\pi_1 = 12.8$ and A values: \blacktriangle 80° , \blacklozenge 60° , \blacksquare 45° , \blacktriangledown 30° , \bullet 10° . $\pi_1 = 21.9$, A values: \triangle 80° , \diamond 60° , \square 45° , \triangledown 30° , \circ 10° .

Figure 5.16-Figure 5.20 show the effect of varying the initial orientation angle, θ_i , on π_2 for the two model systems described in Section 5.5.3. Similarly shaped curves result for the two systems, with the material removal being higher for the lower π_1 value, as expected from Figure 5.13-Figure 5.15.

Noting that π_2/ρ gives the crater volume per unit particle mass, since the particle density, ρ , is fixed in each of the two model systems, direct comparisons of the effect of angularity on material removal can be made using Figure 5.16-Figure 5.20 (i.e. each set of π_2 curves at a constant π_1 effectively describes particles having the same mass, regardless of A). For example, in Figure 5.16, one can say that a particle of fixed mass and fixed incident velocity having angularity $A = 80^\circ$ will remove the most material from a prescribed target (i.e. fixed p_d), or equivalently, it can be said that particles having $A = 80^\circ$ make the most efficient use of particle mass.

The rapid decrease in material removal after the peaks seen in Figure 5.16-Figure 5.20 is due to the transition between forward rotation (ploughing) and backward rotation (cutting) of the particle (see Figure 5.9 and Figure 5.10). This implies that material removal is a maximum at the orientation at which the transition between forward and backward rotation occurs. It is interesting to note that this transition does not occur for $A = 30^\circ$ and $A = 45^\circ$ at $\alpha=85^\circ$ (Figure 5.20). This is because the energy is all consumed in plastic deformation of the target material before significant rotation can occur. There is no transition point for $A = 10^\circ$ (an extremely flat particle) at all angles of attack because the vertical contact force moment arm tending to rotate the particle (the distance from the centre of mass to the vertical contact force) backwards is too small.

The values of $\hat{\pi}_2$ corresponding to total loss of kinetic energy (particle remains embedded and does not rebound) for the two values of π_1 plotted in Figure 5.16-Figure 5.20 (12.8 and 21.9) are 0.039 and 0.023, respectively. The curves for $A = 80^\circ$ in Figure 5.16 (for $\alpha = 5^\circ$) flatten at the $\hat{\pi}_2$ values, indicating that particle embedding occurs even at very shallow angles of attack for very angular particles. Embedding occurs with sharp (high A) particles over

greater intervals of initial orientation as the angle of attack increases (i.e. the impact becomes closer to normal), and particles of lower angularity (i.e. 45°) also begin to embed at $\alpha = 65^\circ$. At close to normal incidence (Figure 5.20), particles embed regardless of angularity over some range of initial orientations. It is interesting to note that at normal incidence, $\alpha = 90^\circ$, even though the model neglects elastic spring back, the higher angularity particles will not embed over the whole range of incident orientations; this model will still predict both a rebound rotational and translational velocity. This is because, for high angularity particles at very high and very low initial orientations, there will be Y-direction (Figure 5.3) movement of the centre of mass of the particle induced by the Y-component of the contact force.

The curves in Figure 5.16-Figure 5.20 display increasingly large, flattened peaks as the angle of attack increases, indicating that there is less dependence of material removal on initial orientation for higher angles of attack (i.e. closer to normal incidence). In a blast cleaning application, the particles are likely to be of different angularity, and to impinge with random orientation. This, together with the fact that the material removal is highest for a specific orientation at higher angles of attack, implies that, one would expect maximum removal at normal incidence (i.e. $\alpha = 90^\circ$) for blast cleaning, neglecting any multiparticle interference (i.e. collisions between inbound and rebounding particles).

The greatest values of π_2 in Figure 5.16-Figure 5.20 occur for the $A = 80^\circ$ particles, implying that on a per unit particle mass basis, the most material can be removed by highly angular particles, if they impact at the proper orientation angle. Highly angular particles are not, however, the most efficient at every initial orientation angle, as can be seen from Figure 5.16-Figure 5.20 (at lower θ_i). As mentioned above, it is likely that particles in a blast stream would arrive at the target surface in random orientations, and it would thus be desirable to make some overall assessment of the effectiveness of a particle of a given angularity over the full range of initial orientations. As shown in equations (5.28) and (5.29), particles of complementary angularity (e.g. $A = 10^\circ$ and $A = 80^\circ$) are actually the same particle, impacting with either the sharper vertex leading (as in the $A = 80^\circ$ case) or the blunter vertex leading (as in the $A = 10^\circ$ case) depending on the initial orientation. Thus, particles with complementary

angularity can be paired, and the average volume removed for a specific particle (i.e. $A = 80^\circ/10^\circ$, $A = 30^\circ/60^\circ$, $A = 45^\circ/45^\circ$) calculated in each of the cases in Figure 5.16-Figure 5.20. To do this, the area under the π_2 curves for each of these three paired particle sets was calculated, and the result divided by 180° (which is the full range of orientation angles spanned by any particle). The results are shown in Table 5.1 for all cases plotted in Figure 5.16-Figure 5.20.

α (deg)	$\pi_1 = 12.8$			$\pi_1 = 21.9$		
	10/80	30/60	45/45	10/80	30/60	45/45
5	0.0103	0.00827	0.00848	0.00632	0.00502	0.00504
25	0.0151	0.0161	0.0156	0.00933	0.00937	0.00917
45	0.0212	0.0238	0.0254	0.0131	0.0140	0.0142
65	0.0272	0.0297	0.0341	0.0158	0.0175	0.0188
85	0.0289	0.0335	0.0383	0.0170	0.0196	0.0220

Table 5.1: Average value of π_2 for all cases in Figure 5.16-Figure 5.20.

If one assumes that particles of a particular angularity set are blasted at a surface, and that particles are no more likely to arrive in one orientation than any other, the values in Table 5.1 represent the per particle expected value of π_2 . At very low angles of attack ($\alpha = 5^\circ$), highly elongated particles are most effective; at a shallow angle of attack ($\alpha = 25^\circ$), all particles are equally effective; and at intermediate and high angles of attack ($\alpha = 45^\circ$ to 85°), square particles are most effective. The effect of particle shape on material removal is more pronounced as the angle of attack becomes steeper (e.g. for $\pi_1=12.8$, the difference between the maximum and minimum π_2 in Table 5.1 increases from 6 % at $\alpha = 25^\circ$ to 28 % at $\alpha = 85^\circ$). The effect of particle shape on material removal, is, however, relatively insensitive to variations in π_1 (e.g. at $\alpha = 85^\circ$ the difference in maximum and minimum π_2 in Table 5.1 changes from 25% for $\pi_1 = 21.9$ to 28% for $\pi_1 = 12.8$). It should be emphasized that the results in Table 5.1 are averages over the whole range of incident orientations, and that higher π_2

values can be obtained if the orientation angles are fixed at the values corresponding to the peaks in Figure 5.16-Figure 5.20 (recall that $\hat{\pi}_2 = 0.039$ for $\pi_1 = 12.8$, and $\hat{\pi}_2 = 0.023$ for $\pi_1 = 21.9$).

In Figure 5.16-Figure 5.20, towards the left side of the figures, there are some missing points inside the range $\theta_i > -A$. These points represent cases where point (e) of Section 5.3.4 is violated, and the model cannot properly predict the total crater area. This only occurs at higher angles of attack ($>45^\circ$), and over a very limited range of θ_i .

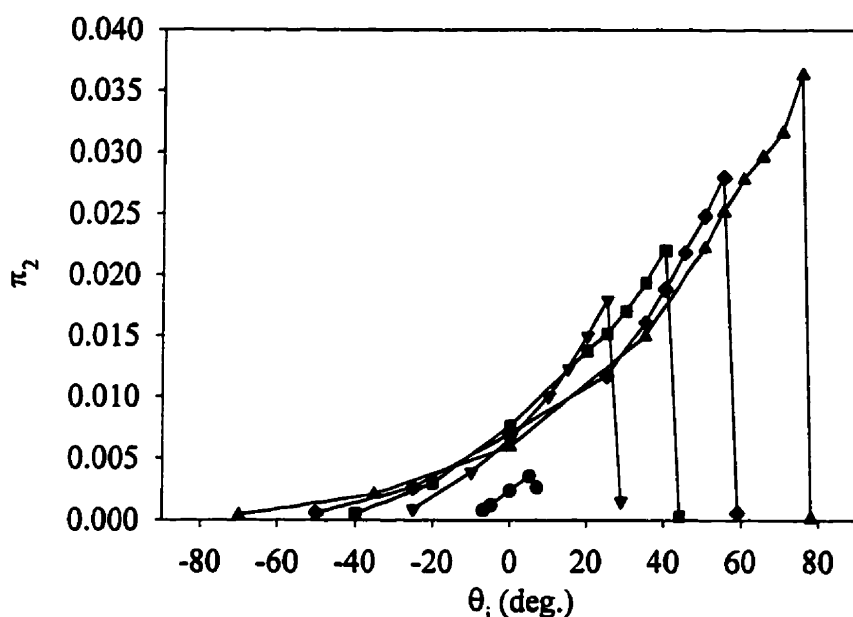


Figure 5.21: Dimensionless crater volume, π_2 , as a function of initial orientation, θ_i , for particles impacting a target having friction coefficient, $\mu = 0.1$ at an angle of attack, $\alpha = 5^\circ$ and $\pi_1 = 12.8$. Angularity, A values: \blacktriangle 80° , \blacklozenge 60° , \blacksquare 45° , \blacktriangledown 30° , \bullet 10° .

For very low values of coefficient of friction (such as the 0.001 value used in the analysis of rigid-plastic collisions of steel spheres on the urethane coating discussed Chapter 4), the effect of friction on collisions involving the angular particles in the present study was found to be negligible. However, for collisions between steel spheres and various metal targets, Sundararajan [31] found that the coefficient of friction can be significantly larger, on the order of 0.1. To illustrate the effect of friction for angular particles, Figure 5.21, Figure 5.22, and Figure 5.23 were constructed, assuming collision between steel spheres and a steel target at 200

m/s ($\pi_1 = 12.8$) with a constant coefficient of friction of $\mu = 0.1$ at three different angles of attack.

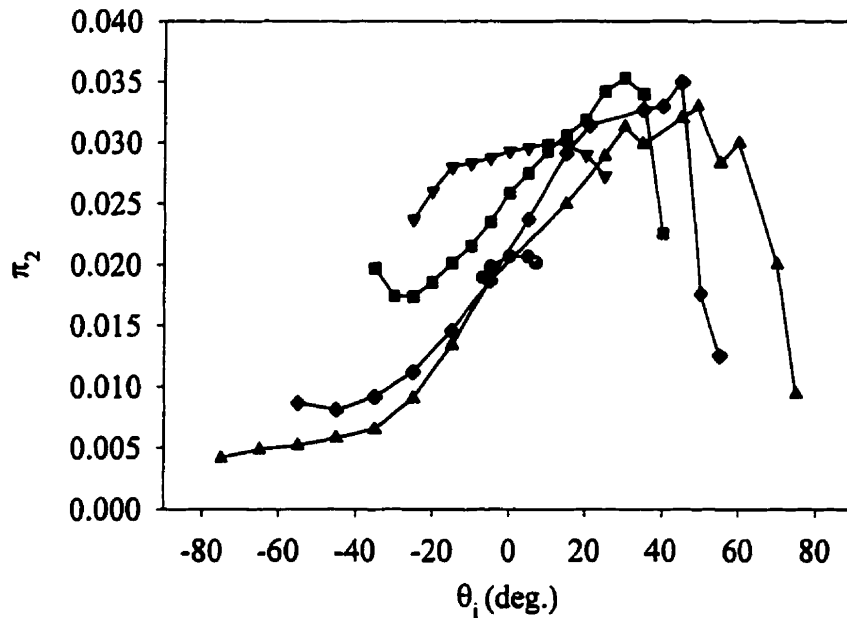


Figure 5.22: Dimensionless crater volume, π_2 , as a function of initial orientation, θ_1 , for particles impacting a target having friction coefficient, $\mu = 0.1$ at an angle of attack, $\alpha = 45^\circ$ and $\pi_1 = 12.8$. Angularity, A values: \blacktriangle 80° , \blacklozenge 60° , \blacksquare 45° , \blacktriangledown 30° , \bullet 10° .

Comparing Figure 5.16 and Figure 5.21, it is evident that the effect of friction is minimal at very shallow angles of attack ($\alpha = 5^\circ$), which is not surprising, given that the contact area, and thus the area over which the friction is assumed to act, is relatively small. The π_2 values are slightly lower in the constant friction case (Figure 5.21) than in the frictionless case (Figure 5.16). This is expected because some of the kinetic energy that is available to deform the target in the frictionless case will be consumed in the constant friction case. In Figure 5.21, the peak of the $A = 80^\circ$ curve represents approximately 94% energy loss, whereas in the frictionless case, Figure 5.16, the peak is at 100% energy loss (i.e. $\hat{\pi}_2$), implying that particle embedding is less likely to occur for higher friction materials than for lower friction ones at very shallow angles of attack. The transition from forward to backward rotation occurs at approximately the

same initial orientation regardless of the presence of friction for collisions at very shallow angle of attack.

Comparison of Figure 5.18 and Figure 5.22 for collisions at $\alpha = 45^\circ$ reveals a more pronounced effect of friction than was seen at very shallow angles of attack. The basic trends are the same in both figures, with the values of π_2 being lower in the constant friction case, as expected. It is important to note that for the case of nonzero friction, equation (5.32) no longer holds, and there thus will not be a well defined cut-off value of $\hat{\pi}_2$ for particle embedding. The portions of the curves for $A = 80^\circ$ and $A = 60^\circ$ in Figure 5.22 falling between approximately $30^\circ < \theta_i < 70^\circ$ and $35^\circ < \theta_i < 45^\circ$, respectively, were found to represent full energy loss and thus particle embedding. The range of values over which particle embedding takes place is approximately equal in Figure 5.18 and Figure 5.22, indicating that the presence of friction has little effect on whether the particles are likely to embed at intermediate angles of attack. The π_2 values over these particle embedding ranges are somewhat sensitive to the initial orientation of the particle, resulting in the irregular shape of the curves, but the variation of π_2 is not very large over this range. The transition from forward to backward rotation of the particle (onset of sharp decrease in π_2) also occurs at approximately the same incident orientation, regardless of the presence of friction. It is interesting to note that, in the case of constant friction, the overall maximum in π_2 occurs for square ($A = 45^\circ$) particles, whereas it occurs in the $A = 80^\circ$ case for frictionless surfaces. This is probably because the square particles will produce friction forces on the two contact surfaces that are closer to each other in magnitude than the ones produced by sharper particles. This results in a minimisation of the effects of the frictional force on the rotation of the particle, in turn resulting in less energy being consumed in rotational energy in the square particle case.

Comparison of Figure 5.20 and Figure 5.23 for collisions at $\alpha = 85^\circ$ shows the effect of friction at a high angle of attack. The overall trends of the curves in Figure 5.20 and Figure 5.23 are the same, with the π_2 values being lower in the constant friction case, as expected. Particle embedding for the constant friction case of Figure 5.23 was found to occur over the range $-20^\circ < \theta_i < 20^\circ$ for $A = 80^\circ$, $-5^\circ < \theta_i < 5^\circ$ for $A = 60^\circ$ and over the whole range of valid

θ_i for $A = 45^\circ, 30^\circ$ and 10° . These ranges are approximately the same as those found in the frictionless case. A striking difference between Figure 5.20 and Figure 5.23 is that the maximum in π_2 is a function of particle angularity in Figure 5.23, whereas in Figure 5.20 it is a constant value, $\hat{\pi}_2$. This is probably because the more angular particles penetrate the target deeper than the less angular particles, and thus have larger contact areas, resulting in more of the incident kinetic energy being consumed by friction. In Figure 5.23, the highest π_2 values occur for the least angular particles, as expected, because the friction forces will act more in the direction of vertical motion for the more angular particles, and thus the retarding force caused by friction will be maximised in this case.

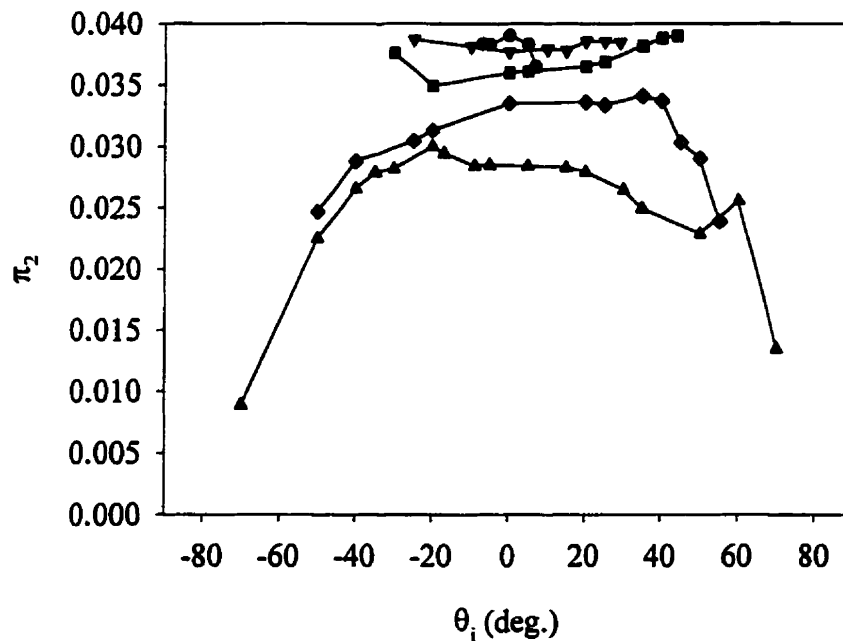


Figure 5.23: Dimensionless crater volume, π_2 , as a function of initial orientation, θ_i , for particles impacting a target having friction coefficient, $\mu = 0.1$ at an angle of attack, $\alpha = 85^\circ$ and $\pi_1 = 12.8$. Angularity, A values: \blacktriangle 80° , \bullet 60° , \blacksquare 45° , \blacktriangledown 30° , \bullet 10° .

Similar trends in the effect of friction were found for higher friction coefficients, with the resulting π_2 values decreasing as the coefficient of friction increased. For example, for $\mu = 0.3$,

$\alpha = 45^\circ$, and $A = 80^\circ$, particle embedding (peak π_2) was found to occur over an interval of $30^\circ < \theta_i < 70^\circ$ (the same as the for $\mu = 0.1$ and frictionless cases), at a value that oscillated between approximately 0.017 and 0.022 (as opposed to between 0.028 and 0.033 in the $\mu = 0.1$ case).

One limitation of the model is the assumption of constant friction. In reality, the friction coefficient can be a function of the local sliding velocity; for example, Sundararajan [31] found that for brass and copper targets, the coefficient of friction can vary as much as 100% as the sliding velocity changes from 20-160 m/s. Including this effect in the model might result in significantly different results for some materials. Nevertheless, there are target materials such as steel where the coefficient of friction is approximately constant [31], and the results of the present constant friction model can be used. A modification of the present model for non-constant coefficient of friction is a subject for future study.

5.6 Summary

A method to analyse collisions between arbitrarily shaped rigid particles and flat target materials has been presented under the assumption of fully plastic behaviour of the target material. The general formulation of the model can be applied to rigid particles of arbitrary shape, size and density colliding with targets of specified dynamic hardness (under the assumption of fully plastic behaviour) at arbitrary incident velocity, orientation, and angle of attack.

The special case of symmetric particles of the type shown in Figure 5.3 was discussed in detail, and a further subset, the case of square particles, was compared to experimental data obtained by Hutchings [7]. The excellent agreement obtained with the experimental data and an earlier model by Hutchings provides an initial confirmation of the validity of the present model.

The effect of varying input parameters on the amount of target material removed was then studied with the main conclusions summarised as follows:

- (a) A dimensional analysis resulted in dimensionless parameters that greatly simplify the problem of impact of a rigid, symmetric particle of arbitrary angularity with a plastically behaving target having arbitrary friction coefficient at any angle of attack, initial particle orientation, and initial velocity.
- (b) An upper limit to crater volume occurs when the particles embed. The limit is well defined and independent of particle angularity in the frictionless case, and dependant on initial particle orientation and angularity in the constant friction case.
- (c) Low angularity (blunter) particles are generally more likely to embed at high angles of attack regardless of orientation for both the constant friction and frictionless case. Embedding occurs for sharp (high angularity) particles over greater intervals of initial orientation, as the angle of attack increases.
- (d) Changing the dimensionless parameter π_1 resulted in similar trends with respect to the variation of π_2 with initial orientation angle. Overall, however, the π_2 values decreased with increasing π_1 .
- (e) The crater volume was maximum at the transition between forward and backward rotation of the particle.
- (f) The crater volume was maximum at normal incidence in the frictionless case.
- (g) On a per unit particle mass basis, highly angular particles created the largest craters, provided that they arrived at the proper incident orientation in the frictionless case. For constant friction, this was true only at very shallow to intermediate angles of attack.
- (h) When averaged over all possible initial particle orientations, elongated particles are most effective at removing target material at very shallow angles of attack, all particles are equally effective at shallow angles of attack, and square particles are most effective at intermediate and high angles of attack.
- (i) Very low friction coefficients produce negligible changes in crater volume as compared to the frictionless case at all angles of attack. Higher friction coefficients result in negligible changes in crater volume at shallow angles of attack, with the effects increasing as the

angle of attack becomes steeper. In all cases, the initial orientation for transition from forward to backward rotation is unaffected by friction.

Chapter 6

Discussion of mechanical properties and blasting parameters affecting coating removal

The two coating systems described in Chapters 3 and 4 have completely different removal mechanisms associated with them. This chapter considers the differences between these systems, as well as the implications of these differences for blast cleaning and for coating manufacturers.

6.1 Coating system and particle properties

The coating removal mechanism of the alkyd coating system discussed in Chapter 3 was found to be impact-induced buckling delamination, whereas, the urethane system of Chapter 4 was found to erode, rather than delaminate. It is important to identify the properties of the coating systems and the blasting parameters that determine the removal mechanism, and the extent of removal. In other words, how can coating removal be maximised (or conversely, how can coating systems be designed to maximise removal resistance) for a given type of particle impact? It is clear that the properties of the coating/substrate system are as important as those of the coating itself. Moreover, the coating/substrate system can exhibit different behaviour depending on the characteristics of the particle and its incident conditions.

6.1.1 Hardness

Clearly, the single most important material property of the coating is the dynamic hardness. For the alkyd coating system, the onset of removal is governed by the volume of coating displaced by the impacting particle, which is strongly dependant on the coating dynamic

hardness, and for the urethane system, the amount of coating pushed into lips at the edge of the crater also depends strongly on the coating dynamic hardness. In both cases, a coating should be made as hard as possible if it is not to be removed by impacting particles.

It has become clear that the dynamic hardness, p_d , of a coating is, to some extent, a function of the thickness of the coating (see Chapters 3 and 4). The thicker the coating, in general, the easier it is to indent because p_d is effectively decreased. This is not a material effect but rather one of constraint of the plastic field below the indenter by the substrate. In fact, p_d has also been found to depend on substrate properties, with coatings applied to harder substrates having higher effective hardness [36]. Thinner coatings will resist indentation more than thick ones, as the presence of the harder substrate is felt more by the impacting particle. An impacting particle at a given velocity will thus leave a bigger dimple on a thicker coating than a thin one. But, at the same time, it takes more incident kinetic energy to delaminate a thicker coating, assuming that, as in Chapter 3, the particle must penetrate the coating to the bare substrate to initiate delamination. Because large dimples are not pleasing from an aesthetic point of view, and coating delamination is obviously not desirable, the paint thickness should be chosen such that the trade-off between improving appearance after impact (use thin coating) and prevention of delamination (use thick coating) is optimised.

The hardness of the particle is also important. If the particle is softer than the coating, then it will lose all of its incident kinetic energy in its own deformation and essentially leave the coating untouched. For both coating systems studied, the impacting particle must be harder than the target coating if any damage is to be done to the coating. A test of this hypothesis was made by launching 0.96 mm cellulose acetate spheres ($m = 0.602$ mg) at a 40 μm thick alkyd/steel specimen at 100 m/s. The incident energy corresponding to the incident conditions is approximately 3 mJ, which, according to Figure 3.8, is comparable with the incident energies of the glass spheres used in Chapter 3. The original purpose of the experiment was to see if a polymer particle would remove more material than a glass particle, given that it would surely deform more (and thus displace more paint) upon penetration to the substrate. The result of the experiments was that the cellulose acetate spheres did not damage the coating at all, and, upon

examination of the spheres after impact, it was found that they were permanently flattened. The reason for the lack of damage to the coating was because the cellulose acetate spheres were not hard enough to indent the coating, and thus all of the kinetic energy was lost deforming the particles themselves.

In the case of the alkyd/steel system, it would be desirable, from a maximal coating removal perspective, for the particle to be softer than the substrate material below the coating. This would encourage greater flattening of the particle as it hit the substrate, thereby displacing more coating volume, and thus increasing the amount of coating removed (Figure 3.20). The optimum particle would be one (launched at a kinetic energy sufficient to penetrate the coating fully to the substrate) that is hard enough to penetrate the coating, but is compliant enough to flatten significantly when it reaches the harder substrate. A hollow particle, or one with a foam core would meet these criteria. It would be hard enough on the outside to penetrate the coating, but being hollow would allow it to deform (flatten) more when it hits the substrate, thus minimising damage to the substrate while maximising coating removal.

6.1.2 Young's Modulus

The Young's modulus, E , of the coating is also very important. For the alkyd/steel system, the critical buckling volume did not depend on Young's modulus (the volume was dependent on dynamic hardness, as discussed above), but the strain energy release rate was inversely proportional to E (equation (3.35)). However, competing with this was the fact that bending moments induced by buckling were directly proportional to E (equation (3.49)), and since the bending moment is squared in the strain energy release expression, the net effect is that the strain energy release rate increases with increasing E . Thus, if two coatings had the same interfacial fracture strength (G_c), and dynamic hardness, p_d , then the one with the higher Young's modulus, E , would delaminate more upon impact. Coating manufacturers should thus lower the Young's modulus of coatings to enhance buckling delamination resistance (assuming other properties constant).

For coatings that erode, plastic effects largely dominate the process and thus Young's modulus is not very important. For the same yield strength however, a low E will promote more springback (and hence less material pushed into lips at the edge of the impact crater), because the amount of recoverable elastic deformation will be increased. The conclusion is again that a lower E coating is more erosion resistant.

The Young's modulus of the particle is also important in buckle-driven delamination systems. It was found in Chapter 3 that, for particles penetrating through the coating to the bare substrate, significant amounts of additional coating volume were displaced by the particle flattening as it hit the substrate (Figure 3.20). A low particle modulus would encourage this behaviour, as discussed above.

In the case of eroding coating systems, the more rigid the particle the better from the perspective of maximising coating removal. The Young's modulus should be as high as possible to minimise incident kinetic energy being wasted in elastic deformation of the particle.

6.1.3 Poisson's ratio

There was also, according to the plastic hole Matthewson analysis, a dependence of the interfacial shear stress on Poisson's ratio. Equation (3.50) predicts a 30% decrease in maximum interfacial shear stress when Poisson's ratio is increased from 0.1 to 0.5. Incompressible materials (such as rubber-like coatings) are thus less likely to delaminate.

As in the case of Young's modulus, Poisson ratio effects for coatings that erode such as the urethane of Chapter 4 are minimum, because the erosion is dominated by plastic effects characterised by the dynamic hardness alone.

As the Poisson's ratio of the particle increases, there should be increasing lateral deformation (or flattening) a particle that is colliding with a bare substrate. By the arguments presented in Section 6.1.2, this would mean that more coating would be displaced by the impacting particle (if it reaches the substrate). Thus, it would be desirable for a particle to be as close to incompressible as possible, for maximum coating removal, and hence the 'ideal' hollow particle discussed in Section 6.1.1 should be made of incompressible material.

6.1.4 Yield strength

The coating yield strength was an important parameter in both coating systems examined. In the case of the urethane coating, which was found to fail by erosion, plastic effects controlled the entire process. A coating with low yield strength would exhibit much less elastic springback (see Figure 4.9) in such a system, and thus more material would be pushed into lips at the edge of the impact crater, available for removal by subsequent impacts.

In the case of coatings that are removed by buckle-driven delamination, the lower the yield strength (for constant E), the quicker full plasticity will be reached, and the greater will be the extent of volume displaced by the indenting particle. There will thus be higher biaxial compressive stresses induced in the delaminated coating adjacent to the contact zone, and thus a larger extent of buckling.

If the coating is an elastomer (i.e. a material that has a very high elongation to yield), then most of the incident kinetic energy will be returned to the particle on rebound, with very little damage to the coating. In this case, a very small amount of the energy is available to either delaminate or erode the coating, and the coating would prove difficult to remove in either manner.

In both coating systems, a high particle yield strength would ensure that no incident energy is wasted in plastic deformation of the particle, and blast cleaning particles should thus be very high strength.

6.1.5 Interfacial strength

In both coating systems tested, the use of a fully plastic analysis to describe the incident kinematics proved adequate. This raises the important question of why the two coating systems exhibit such different removal mechanisms given that the incident kinematics are essentially the same.

The answer may lie in the last of the important material properties of the coating system: the interfacial bond strength. It is hypothesised that coatings with very high interfacial strength will not delaminate, no matter how high the incident kinetic energy. In this case, the material

displaced by the presence of the indenting particle does not induce high enough interfacial stress to delaminate the coating. For these types of coatings, one should see a crater where the particle impacted, as there will be significant local plastic flow, but there will not be any delamination. The only way to remove such a coating is by erosion, as was the case for the urethane coating system of Chapter 4.

Recent experiments performed on an automotive urethane topcoat/steel substrate system have led to the conclusion that removal is governed by a buckle-driven delamination mechanism similar to that experienced by the alkyd system in Chapter 3 [8]. The Young's modulus, Poisson's ratio and dynamic hardness are of the same order as the eroding urethane system of Chapter 4, and yet the coating delaminates rather than erodes. In addition, the coating of Reference [8] delaminated to a much lesser extent than the system of Chapter 3. This cannot be due to the differences in Young's modulus, because the arguments of Section 6.1.2 imply that the higher E would cause higher reactions at the crack tip and thus a larger delamination. The only explanation for this behaviour is differences in interfacial strength: the alkyd system of Chapter 3 has the lowest interfacial strength, followed by the coating of Reference [8], and finally, the coating of Chapter 4, whose interfacial strength is so high as to not allow delamination to occur.

6.2 Effect of incident parameters on coating removal mechanism

The fact that the incident kinematics of both coatings could be described by the same model implies that it may be possible to force a coating to erode simply by altering the incident parameters. For example, it might be possible to erode the alkyd system of Chapter 3 by launching angular particles at low velocity (to maximise cutting erosion behaviour, and minimise displaced coating volume). This was found to be the case, as explained in Section 3.6, where it was found that angular particles sometimes caused buckling, and sometimes did not. In the cases where buckling did not occur, examination of the impact sites revealed behaviour consistent with ploughing or cutting erosion. In addition, Figure 3.1 (a) shows that, if the incident normal velocity is below that required for penetration to the bare substrate (and

thus delamination) to occur in the alkyd system of Chapter 3, a crater similar to that observed in the urethane system of Chapter 4 results. Thus, the alkyd system can be made to exhibit both erosion and buckle-delamination behaviour depending on incident parameters.

The reverse of the above behaviour (i.e. forcing a coating to buckle-delaminate by changing the incident parameters) is, however, not thought to be possible. Striking the urethane system of Chapter 4 with steel spheres at a velocity necessary to cause penetration did not induce any buckling or delamination. As explained above, because of the high interfacial strength, it is not possible to raise interfacial stresses high enough to cause delamination.

Chapter 7

Conclusions and Recommendations

7.1 Conclusions

7.1.1 Experimental setup

A gas gun capable of launching single particles at speeds of up to 120 m/s was designed and constructed. A CCD camera/frame grabber/high-speed flash setup capable of measuring incident and rebound angles and velocities of single particles launched using the gas gun was also designed and constructed.

7.1.2 Alkyd paint/steel substrate model system

The impact behaviour of an alkyd paint/steel substrate model coating system was examined by performing impact experiments using glass and steel spheres. It was found that:

- (1) The stress response of the system could be modelled effectively using quasi-static methods. Dynamic effects such as wave reflection at the interface and spalling were eliminated as possible coating removal mechanisms. The coating delaminated along the interface between the coating and the steel substrate.
- (2) Tangential velocity effects were found to be negligible in both the initiation and magnitude of coating removed, and could be ignored for modelling purposes. Thus, only normal effects needed to be considered.
- (3) The initiation of coating removal correlated well with the normal component of incident velocity required to just penetrate the coating to the bare steel substrate. This velocity

could be calculated using a quasi-static fully plastic indentation model. The coating was not removed unless this critical incident velocity to penetrate the coating to the bare substrate was achieved.

- (4) After penetration to the bare substrate, the collisions proceeded as if the particles were incident on a bare steel substrate. At higher speeds, the magnitude of coating removal increased beyond that at penetration to the bare steel substrate due to the subsequent deformation of the particle, which displaced more of the coating.
- (5) A range of incident kinetic energies was found where the coating was removed, but the substrate was not damaged.

The mechanism of coating removal was found to be impact-induced buckling delamination, in which the impacting particle kinematics were described by a fully-plastic analysis, giving the volume of coating displaced by the impacting particle. This displaced volume caused equi-biaxial compressive elastic stresses in the coating at some distance from the impact site, which, in turn, caused the coating to buckle and delaminate in approximately circular blisters (when impacted by single spheres). A method coupling a novel post-buckled analysis of a compressed disk with an existing strain energy release analysis was developed and found to predict the size of delaminations accurately.

In addition, an approximate elastic stress analysis in which the local plastically deformed material was replaced by a hole with a compressive stress (obtained via the Tresca criterion) applied to it, was used to calculate the elastic interfacial stress to initiate a debond. It was found that the debond stress obtained in this manner was not suitable for calculating initiation strain energy release rates, but matched experimentally obtained debond conditions well.

7.1.3 Urethane/epoxy/aluminum model system

The impact behaviour of a urethane/epoxy/aluminum model coating system was examined by performing impact experiments using steel spheres. It was found that:

- (1) The coating did not delaminate, no matter the incident kinetic energy of the particle.
- (2) Tangential effects were important in the removal process.
- (3) The coating was removed by ploughing erosion, in which plastically deformed material is pushed into lips at the edge of the impact crater, where it is available for knock-off by subsequent impacts.
- (4) A fully-plastic analysis adequately predicted the rebound velocity and crater length, but was unable to predict crater depth and the rebound angle accurately, owing to its neglect of elastic effects.

The fully-plastic analysis of (4) was modified to account for elastic effects (using an approximate elastic stress analysis), and it was found that the rebound angle and crater depth could be predicted accurately.

7.1.4 Analytical investigation of erosion by angular particles

A method to analyse collisions between arbitrarily shaped rigid particles and flat target materials was presented under the assumption of fully plastic behaviour of the target material. The general formulation of the model could be applied to rigid particles of arbitrary shape, size and density colliding with targets of specified dynamic hardness (under the assumption of fully plastic behaviour) at arbitrary incident velocity, orientation, and angle of attack.

The special case of symmetric particles of the type shown in Figure 5.3 was discussed in detail, and a further subset, the case of square particles, was compared to experimental data obtained by Hutchings [7]. The good agreement obtained with the experimental data provided an initial confirmation of the validity of the present, more general, model.

The effect of varying input parameters on the amount of target material removed was then studied with the main conclusions summarised as follows:

- (1) A dimensionless analysis resulted in dimensionless parameters that greatly simplify the problem of impact of a rigid, symmetric particle of arbitrary angularity with a plastically

behaving target having arbitrary friction coefficient at any angle of attack, initial orientation, and initial velocity.

- (2) An upper limit to crater volume existed when the particles embed. The limit was well defined and constant in the frictionless case, and dependant on initial orientation and particle angularity in the constant friction case.
- (3) Low angularity particles were generally more likely to embed at high angles of attack regardless of orientation for both the constant friction and frictionless case. Embedding occurred for sharp (high angularity) particles over greater intervals of initial orientation, as the angle of attack increased.
- (4) Changing the dimensionless parameter π_1 resulted in similar trends with respect to the variation of π_2 with initial orientation angle. Overall, however, the π_2 values decreased with increasing π_1 .
- (5) The maximum crater volume occurred at the transition between forward and backward rotation of the particle.
- (6) The maximum crater volume occurred at normal incidence in the frictionless case.
- (7) On a per unit particle mass basis, highly angular particles created the largest craters, provided that they arrived at the proper incident orientation in the frictionless case. For constant friction, this was true only at very shallow to intermediate angles of attack.
- (8) High aspect ratio particles were most effective at removing target material at very shallow angles of attack, all particles were equally effective at shallow angles of attack, and square particles were most effective at intermediate and high angles of attack.
- (9) Very low friction coefficients produced negligible changes in crater volume as compared to the frictionless case at all angles of attack. Higher friction coefficients resulted in negligible changes in crater volume at shallow angles of attack, with the effects increasing as the angle of attack became steeper. In all cases, the initial orientation for transition from forward to backward rotation was unaffected by friction.

7.1.5 Mechanical properties affecting coating system behaviour

The mechanical properties affecting coating system behaviour were discussed in Chapter 6. The conclusions can be summarised as follows:

- (1) The most important material property of the coating is the dynamic hardness. From the perspective of making erosion resistant coatings, it was found that for both coating systems examined, a coating should be made as hard as possible.
- (2) Because large dimples are not pleasing from an aesthetic point of view, and coating delamination is obviously undesirable, the paint thickness should be chosen such that the trade-off between aesthetics and prevention of delamination is optimised.
- (3) The hardness of particles was found also to be very important. The optimum particle for coating removal of systems that buckle-delaminate would be one that is hard enough to penetrate the coating, but is compliant enough to flatten significantly when it reaches the harder substrate (launched at a kinetic energy sufficient to penetrate the coating fully to the substrate).
- (4) The Young's modulus, E , of the coating is an important property in the case of buckle-delaminating coatings. Coatings with a low E are resistant to buckling delamination. For coatings that erode, plastic effects largely dominate the process and E is not very important. For the same yield strength, however, a low E will promote more springback (and thus less material pushed into lips at the edge of the impact crater), because the amount of recoverable elastic deformation will be increased. The conclusion is again that a coating with a low E is more erosion resistant.
- (5) The Young's modulus of the particle is also important in buckle-driven delamination systems. A low particle modulus encourages flattening upon impact with the bare substrate, thus increasing the extent of buckling. Particle manufacturers should keep this in mind when choosing blast cleaning media material. In the case of coating systems that erode, the more rigid the particle, the better. The Young's modulus should be as high as possible to minimise incident kinetic energy being wasted in elastic deformation of the particle.

- (6) Incompressible materials are less likely to delaminate, due to the lower interfacial stresses associated with them, and thus a high Poisson's ratio of the coating would be desirable in the case of buckle-delaminating coating systems. As in the case of Young's modulus, Poisson ratio effects for coatings that erode such as the one of Chapter 4 are negligible, because the erosion is dominated by plastic effects characterised by the dynamic hardness alone.
- (7) As the Poisson's ratio of the particle increases, there will be increasing lateral deformation (or flattening) during collision with a bare substrate. By the same arguments as in (3), it would be desirable for a particle to be as close to incompressible as possible, for maximum coating removal.
- (8) The coating yield strength is an important parameter in both coating systems examined. In the case of the eroding coating system, the entire process is controlled by plastic effects. A coating with low yield strength will exhibit much less elastic springback in such a system, and thus more material will be pushed into lips at the edge of the impact crater, available for removal by subsequent impacts. In the case of coatings that are removed by buckle-driven delamination, the lower the yield strength (for constant E), the quicker full plasticity will be reached, and the greater will be the extent of volume displaced by the indenting particle. There will thus be higher biaxial compressive stresses induced, and thus a larger extent of buckling.
- (9) In both coating systems, a high yield strength would ensure that no incident energy is wasted in plastic deformation of the particle, and particles should thus be very high strength.
- (10) It was concluded that the interfacial strength was the factor controlling whether a coating delaminates or erodes. Coatings with very high interfacial strength cannot be made to delaminate, no matter how high the incident kinetic energy may be. However, coatings with lower interfacial strength can be made to either delaminate or erode by varying the properties of the incident particles.

7.2 Contribution

This thesis represents the first quantitative analysis of the blast cleaning process, and the mechanisms of coating removal associated with it. Though only single impacts are considered, it constitutes a significant first step to a complete understanding of the blast cleaning process. In addition, several contributions to the fields of solid particle erosion and coating analysis were made, specifically:

- (1) A novel post-buckling/strain energy release rate analysis to predict delamination size for coatings impacted by spherical particles. The post-buckling analysis is the first to include the constraint of buckling prevented at a certain radius due to the presence of the impacting particle [9].
- (2) A modification of the existing approximate Matthewson [20] elastic coating stress analysis for the more accurate representation of a spherical indenter profile.
- (3) The experimental verification that the rigid-plastic erosion model of Hutchings [24] can be successfully applied to coatings.
- (4) The modification of the rigid-plastic erosion theory to account for elastic rebound effects [49].
- (5) The generalisation of the rigid-plastic erosion model for square particles of Hutchings [7] to include arbitrarily-shaped particles [53]. The study of the effect of incident particle parameters on crater volume for symmetric angular particles is also novel [54].

7.3 Recommendations

This thesis, as mentioned previously, constitutes a first step to understanding the blast-cleaning process. There are several areas that need to be explored further:

- (1) The application of the theories and analyses presented in this thesis should be adapted for multiparticle streams. For example, a statistical model that predicts, as a function of incident angle, the likelihood of rebounding particles interfering with incident particles

for a given particle stream size should be possible. This would aid in the application of the analyses of this thesis to real blast cleaning applications.

- (2) This thesis identified two fundamental removal mechanisms: impact-induced buckling delamination and erosion. It is thought that these are typical mechanisms for a large variety of coating systems used in industry. Recent work on an automotive urethane topcoat system [8] has shown that the methods of Chapter 3 can be used to predict buckle-delamination behaviour for that system as well. More experiments on a wider variety of coatings would be desirable, in the hopes of identifying exactly what distinguishes the two classes of coating systems, and perhaps identify new coating removal mechanisms.
- (3) Due to time limitations and the difficulty associated with performing angular particle experiments, it was only possible to compare the angular particle erosion model with published data for square plates. It would be interesting if the analytical trends of Chapter 5 could be verified experimentally for other conditions. This, together with the conclusions of Chapter 6 regarding important particle material properties might result in the design of an optimum particle for blast cleaning. The effects of particle orientation being very important, it might be possible to combine the analysis of Chapter 5 with an aerodynamic drag analysis to design a particle that is guaranteed to arrive at the target surface in the orientation that removes the most amount of material.
- (4) The symmetric angular particle analysis of Chapter 5 could be fairly simply modified to account for the effect of varying moment of inertia, without changing the shape of the contacting portion of the particle. This would be accomplished by essentially splitting the particle into a top and bottom part, with the bottom part staying a symmetric wedge of side length h , and the top part having an arbitrary shape, chosen at will to represent any moment of inertia. The moment of inertia is an important parameter because it contributes to the determination of how much incident kinetic energy is converted into (wasted) rebound rotational kinetic energy.

- (5) The symmetric angular particle analysis of Chapter 5, in its present form, can account for an incident rotational kinetic energy, though this was not studied due to time constraints.
- (6) The coating stress analysis of Chapter 3 is approximate, with the stresses and strains being represented by an average through the thickness of the coating. It would be desirable for a more accurate stress analysis to be developed in order that interfacial stresses for the initiation of delamination be investigated more rigorously. The ultimate aim would be to determine initiation critical strain energy release rates. A number of more accurate stress analyses exist in the literature, though they are quite complicated (see, for example, Reference [47]). FEA techniques might be used as an alternative.
- (7) As discussed in Chapters 3 and 4, the dynamic hardness of a coating is a function of its thickness. This implies that in a real blast cleaning process, as a coating is eroded, the resistance to indentation will increase. When the coating is eroded to the point of being very thin, the dynamic hardness might be several orders of magnitude higher, because the influence of the substrate will be large. Furthermore, as the coating is completely removed, the bare substrate will be left exposed, and thus prone to damage from impacting particles. Methods of accounting for this behaviour must be investigated.
- (8) The conclusions of Chapter 6 should be tested. For example, the effect of Young's modulus of the coating could be tested in the following manner: Because the coatings are visco-elastic, there is a strain rate/temperature equivalence. It would be interesting to cool the urethane system of Chapter 4 (thus raising its Young's modulus and making it more prone to buckle-driven delamination) and then perform experiments to determine if it is possible to delaminate the coating. The converse could be attempted as well – the alkyd coating system of Chapter 3 might be made to erode at higher velocities if it was heated up (and thus the Young's modulus decreased). Though other particle properties might also change with temperature, the results of such experiments would, nevertheless, be interesting.

Appendix A

Computer Program for Experimental Setup

The following computer program was written in Turbo C to control the flashes, OPTO 22 I/O board, and frame grabber in the experimental setup of Figure 2.1. The resulting images are stored in a TIFF file named 'test.tif'.

```
#include <dos.h>
#include <odx.h>      /* Definition of each ODX function */
#include <opr.h>      /* Symbol definition for each OPR */
#include <stdio.h>
#include <stdlib.h>
#include <math.h>
#include <conio.h>
#include <cmp.h>      /* Compiler Dependent function mapping */

#include <string.h>
#include <dos.h>
#include <process.h>

/* global variable declarations */
int first, expt, stop;
char line[100];
char myname[100];
char answer;
char sav;
unsigned base;
/* function prototypes */

void menu(void);
void grab( void);

void store(void);
void initio (void);

void initio (void)
/* THIS PROCEDURE INITIALIZES THE IO OPTO22 BOARD WITH CHANNEL
O AS AN INPUT*/
```

```

{
base=0x220; /*base address for opto 22 is 220 hex*/
outp(base+1,0);
outp(base,0xFE); /* configures all channels as inputs */
outp(base+1, 0x34);

}

void menu (void)
{
char line[100];
expt=0;
if (first ==1) {

printf("\fn\n\n");

printf("\nt*****");
printf("\nt*");
printf("\nt*");
printf("\nt*   ***  \"High speed grab\"  ***   *");
printf("\nt*");
printf("\nt*   Version 1.0 (1995)   *");
printf("\nt*");
printf("\nt*   by   *");
printf("\nt*   Marcello Papini   *");
printf("\nt*");
printf("\nt*");
printf("\nt*****\n\n");

printf("\nt  Press Return to continue");
fgets(line, sizeof(line), stdin);
}

printf("\fn\n\nMENU:\n\n");
printf("\t1. Setup cameras\n");
printf("\t2. Shoot particle/get images\n");
printf("\t3. Exit\n");
printf("\n");
printf("\tSelect (1-3):");

first = 0;
}

/* VGA Modes */
#define VGA_640x480_16 0x12

```

```

/* Keying Modes */
#define FrameBufferOnly 4

int VgaMode( int Mode)
{
    static union _REGS regs;

    if( Mode == -1)
    {
        regs.h.ah = 0xf; /* Get Current Display Mode */
        _int86( 0x10, &regs, &regs);
        return( (int)regs.h.al);
    }
    else
    {
        regs.h.ah = 0; /* Mode Select */
        regs.h.al = Mode; /* Mode Number */
        _int86( 0x10, &regs, &regs);
        return(0);
    }
}

void grab(void)
{

    int OldVgaMode;
    unsigned mw, mh;
    int keying;

    /* Bind to the Oculus Driver */
    if( odxbind() < 1)
    {
        printf("Cannot Access any ODx Driver\n");
        exit(1);
    }
    setdmajor( 0); /* Bind to first device */
    reset(); /* Reset Board */
    OldVgaMode = VgaMode(-1);

    /* Set the VGA card in Graphic Mode 640x480 16 colors */
    keying = opr_inq( KEYING);
    VgaMode( VGA_640x480_16);
    select( 0); /* Select Frame Buffer Minor Device */
    format( 11); /* Set Memory Format to 1024x512 */
    mw = opr_inq( MW);
    mh = opr_inq( MH);
    opr_set( FZOOMOUT, opr_inq( FZOOMOUTSIZ)); /* Maximum Acquisition Zooming */
    vidin( 3, 5, 1, 0, 0); /* Select Acquisition 640x480 NTSC */
    fwin( 0, 0, mw, mh); /* Set fwin to maximum */
    vidout( 5, 1, 1, 0, 0); /*Select Display 640x480 VGA */
    dwin( 0, 0, mw, mh); /* Set dwin to maximum */
}

```

```

/* Display Frame Buffer Only */

if (expt==0) /* Only setup*/
{
printf("%i",inp(base));
getch();
opr_set( KEYING, FrameBufferOnly);
fbgrab(-1); /* Continuous Acquisition */
_getch();
fbgrab(0); /* Stop Acquisition */
}
else /* perform experiment*/
{opr_set( KEYING, FrameBufferOnly);
fbgrab(-1);
while(inp(base)==0); /*while not triggered */

fbgrab(0);
getch();
/* Restore Old Keying Mode */
opr_set( KEYING, keying);
/* Return to Old Display Mode */
VgaMode( OldVgaMode);

printf("\tSave frame? (y,n)\n");
fgets(line, sizeof(line), stdin);
sscanf(line, "%c", &sav);
if (sav=='y')
{printf("%i",execl("tiffsave.exe",0));
printf("done");
}
getch();
}

/* Restore Old Keying Mode */
opr_set( KEYING, keying);
/* Return to Old Display Mode */
VgaMode( OldVgaMode);
return;
}

void main(void)
{
first=1;
initio();
while (1)
{
menu();
fgets(line, sizeof(line), stdin);
sscanf(line, "%c", &answer);
}
}

```

```
switch (answer)
{
  case '1': /* want to see live images */
    expt=0;
    grab();
    break;
  case '2': /* want to perform experiment */
    expt=1;
    grab();
    break;
  case '3':
    stop=1;
    break;
  default:
    printf("\n");
    printf("*** INVALID SELECTION ***\n");
}
if (stop==1)
break;
}
```

Appendix B

Approximate Elastic Stress/Strain Model (Modified Matthewson Analysis)

The derivation proceeds in the same manner as the original Matthewson [20] paper, and was presented, in part, by the author in Reference [1]. Assuming the displacements in the r and z directions, $u_M(r,z)$ and $v_M(r,z)$, respectively, can be approximated by a power series as,

$$\begin{aligned}u_M(r,z) &= A(r) + B(r)z + C(r)z^2 \\v_M(r,z) &= D(r) + E(r)z\end{aligned}\tag{B.1}$$

the strains become

$$\begin{aligned}\varepsilon_r &= \frac{\partial u_M}{\partial r} = \frac{d}{dr}(B(r)z) + \frac{d}{dr}(C(r)z^2) \\ \varepsilon_\theta &= \frac{u_M}{r} = \frac{B(r)z}{r} + \frac{C(r)z^2}{r} \\ \varepsilon_z &= \frac{\partial v_M}{\partial z} = E(r)\end{aligned}\tag{B.2}$$

where $A(r)$ and $D(r)$ disappear due to the fact that $u_M(r,0) = v_M(r,0) = 0$. The coating was assumed very thin and the stress and strains were assumed to be described adequately by averaging through the thickness of the coating. The average strains were thus,

$$\begin{aligned}
\bar{\varepsilon}_r &= \frac{1}{h} \int_0^h \varepsilon_r dz = \frac{1}{2} \frac{d}{dr} B(r) + \frac{1}{3} h^2 \frac{d}{dr} C(r) \\
\bar{\varepsilon}_\theta &= \frac{1}{h} \int_0^h \varepsilon_\theta dz = \frac{\bar{u}_M}{r} = \frac{1}{2} h \frac{B(r)}{r} + \frac{1}{3} h^2 \frac{C(r)}{r} \\
\bar{\varepsilon}_z &= \frac{1}{h} \int_0^h \varepsilon_z dz = \frac{v_M(r, h)}{h} = E(r)
\end{aligned} \tag{B.3}$$

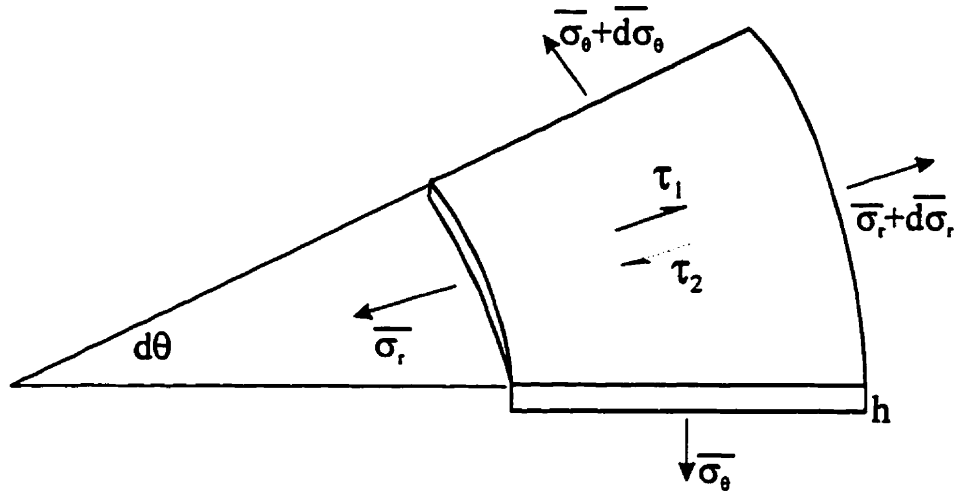


Figure B.1: Stresses acting on an element of the coating

The equilibrium of the stresses acting on a small element of the coating (Figure B.1), in the radial direction, gives,

$$\frac{d\bar{\sigma}_r}{dr} + \frac{\bar{\sigma}_r - \bar{\sigma}_\theta}{r} = \frac{\tau_0 - \tau_1}{h} \tag{B.4}$$

The engineering strain is

$$\gamma_{rz} = \frac{\partial u_M}{\partial z} + \frac{\partial v_M}{\partial r} = B(r) + 2C(r)z + \frac{\partial v_M(r, z)}{\partial r} \tag{B.5}$$

which results in

$$\tau_0 = G^* \gamma_{rz}(z=0) = G^* B(r) \quad (\text{B.6})$$

where G^* is the shear modulus of the coating. Because the friction between the indenter and the coating is ignored, $\tau_t = 0$, which gives the relationship between $B(r)$ and $C(r)$.

By using Hooke's law, the average stresses can be written as

$$\left. \begin{aligned} \bar{\sigma}_r(r) &= \frac{2\nu G^*}{1-2\nu} \left(\bar{\varepsilon}_r + \bar{\varepsilon}_\theta + \bar{\varepsilon}_z \right) + 2G^* \bar{\varepsilon}_r \\ \bar{\sigma}_\theta(r) &= \frac{2\nu G^*}{1-2\nu} \left(\bar{\varepsilon}_r + \bar{\varepsilon}_\theta + \bar{\varepsilon}_z \right) + 2G^* \bar{\varepsilon}_\theta \\ \bar{\sigma}_z(r) &= \frac{2\nu G^*}{1-2\nu} \left(\bar{\varepsilon}_r + \bar{\varepsilon}_\theta + \bar{\varepsilon}_z \right) + 2G^* \bar{\varepsilon}_z \\ \tau_0(r) &= G^* B(r) \end{aligned} \right\} \quad (\text{B.7})$$

where $\bar{\sigma}_r$, $\bar{\sigma}_\theta$, $\bar{\sigma}_z$ are the average normal stresses in the r , θ , and z directions as shown in Figure B.1, τ_0 is the interfacial shear stress, $\bar{\varepsilon}_r$, $\bar{\varepsilon}_\theta$, and $\bar{\varepsilon}_z$ are the corresponding strains averaged through the thickness of the coating layer, h is the coating thickness, ν and G^* are the Poisson's ratio and shear modulus of the coating, respectively.

By manipulating the above equation, Matthewson [20] was able derive differential equations in $B(r)$ and $f(r)$, for both inside and outside the contact radius, c ,

$$\left. \begin{aligned} D^* \left\{ B(r) - \frac{1}{2} \frac{df}{dr} \right\} - \frac{3}{2h^2} \frac{1-2\nu}{1-\nu} B(r) + \frac{3\nu}{h^2(1-\nu)} \frac{df}{dr} &= 0 \quad 0 \leq r \leq c \\ D^* \{ B(r) \} - \frac{6(1-\nu)}{4+\nu} \frac{B(r)}{h^2} &= 0 \quad r > c \end{aligned} \right\} \quad (\text{B.8})$$

where $D^* \{ x(r) \} = \frac{d^2x}{dr^2} + \frac{1}{r} \frac{dx}{dr} - \frac{x}{r^2}$

which could be solved for any indenter profile. The profile of the indenter, $f(r)$, in Matthewson's paper, was approximated by the first term of a parabolic series expansion as,

$$f(r) = \frac{r^2 - c^2}{2R} \quad (\text{B.9})$$

where c is the contact radius, and R is the radius of the indenting sphere. This expression was used to calculate the average strain in the z direction, and it assumes that the ratio $c/R \leq 0.2$. Assuming that the profile given in equation (B.9) is used, expressions for $B(r)$ and $C(r)$ can be found in Reference [20]. By a simple modification of the model, the author has found that the restriction of small c/R can be relaxed somewhat for deeper indentations by adding a term to the indenter (particle) profile, equation (B.9), as,

$$f_m(r) = \frac{r^2 - c^2}{2R} + \frac{r^4 - c^4}{8R^3} \quad (\text{B.10})$$

This improved approximation to the actual spherical indenter profile, for $c/R=0.5$, has a maximum error of 2 %, whereas equation (B.9) has a maximum error of almost 14%. Substitution of the improved indenter profile, equation (B.10), into equation (B.8) gave,

$$\left. \begin{aligned} B(r) &= \frac{-\nu r^3}{(2\nu-1)R^3} - \left[\frac{4(6\nu-1)(\nu-1)h^2}{3R^3(2\nu-1)^2} + \frac{2\nu}{R(2\nu-1)} \right] r + \\ &\quad + \beta_m I_1 \left(\sqrt{\frac{1-2\nu}{2(1-\nu)}} \frac{r}{h} \right) \quad (0 \leq r \leq c) \\ B(r) &= \alpha_m^* K_1 \left(\sqrt{\frac{6(1-\nu)}{4+\nu}} \frac{r}{h} \right) \quad (r \geq c) \end{aligned} \right\} \quad (\text{B.11})$$

and

$$\left. \begin{aligned} C(r) &= -\frac{1}{2h} \left(B(r) + \frac{df_m(r)}{dr} \right) & (0 \leq r \leq c) \\ C(r) &= -\frac{2-\nu}{4h} B(r) & (r \geq c) \end{aligned} \right\} \quad (\text{B.12})$$

These expressions can be used to find the stresses and strains in the coating, and the shear stress along the interface with,

$$\alpha_m^* = -\frac{1}{h(4+\nu)(K'I - KI)} \left\{ \frac{hI}{3cI'} \left[\frac{4(6\nu-1)(\nu-1)}{3(2\nu-1)^2 R^3} h^2 + \frac{I(3c^2 + 2R^2)(6\nu-1)}{4R^3(2\nu-1)} \right] - \frac{4(6\nu-1)(\nu-1)h^3}{9(2\nu-1)^2 R^3} - \frac{(6\nu-1)(2R^2 + c^2)h}{12(2\nu-1)R^3} \right\} \quad (\text{B.13})$$

and

$$\beta_m = \frac{4h^2(-7\nu + 6\nu^2 + 1)}{3(2\nu-1)^2 R^3 I'} + \alpha_m^* (4+\nu) \frac{K'}{4I'} + \frac{(3c^2 + 2R^2)(6\nu-1)}{4(2\nu-1)R^3 I'} \quad (\text{B.14})$$

where $I_1(x)$ and $K_1(x)$ are the first-order modified Bessel functions with,

$$I = I_1 \left(\sqrt{3 \frac{(1-2\nu)c}{2(1-\nu)h}} \right) \quad (\text{B.15})$$

$$K = K_1 \left(\sqrt{6 \frac{(1-\nu)c}{4+\nu h}} \right) \quad (\text{B.16})$$

$$\Gamma' = \frac{dI}{dc} \quad (\text{B.17})$$

$$K' = \frac{dK}{dc} \quad (\text{B.18})$$

An expression for the indentation force, F , can be obtained by integrating the average stress in the z direction over the contact area,

$$F(c) = \int_0^c \bar{\sigma}_z \cdot 2\pi r \cdot dr \quad (\text{B.19})$$

resulting in,

$$\begin{aligned} F_m(c) = & \frac{G^* \pi h \nu (4 + \nu) c \alpha_m^*}{6(2\nu - 1)} \frac{d}{dc} (cK) - \\ & \frac{G^* \pi (\nu - 1) c^6}{3hR^3(2\nu - 1)} + \left[\frac{\nu G^* \pi h (6\nu - 1)}{3(2\nu - 1)^2 R^3} - \frac{G^* \pi (\nu - 1)}{2(2\nu - 1)Rh} \right] c^4 + \\ & \left[\frac{16G^* \pi \nu h^3 (6\nu - 1)(\nu - 1)}{9(2\nu - 1)^3 R^3} + \frac{2G^* \pi \nu h (6\nu - 1)}{3(2\nu - 1)^2 R} \right] c^2 + \frac{4G^* \pi \nu h \beta_m I_c}{3(2\nu - 1)} \end{aligned} \quad (\text{B.20})$$

This can be compared with the indentation force that results from Matthewson's original analysis [20]:

$$F(c) = \frac{1}{6} \frac{G^* \pi h \nu (4 + \nu) c \alpha^*}{2\nu - 1} \frac{d}{dc} (cK) - \frac{1}{2} G^* \frac{(1 - \nu) \pi c^4}{1 - 2\nu hR} \quad (\text{B.21})$$

where

$$\alpha^* = \frac{-4(1 - 6\nu)}{2R(4 + \nu)(1 - 2\nu)K'} \left\{ 1 + \frac{\Gamma' \frac{d}{dc} (cK)}{(KI' - IK')} \right\} \quad (\text{B.22})$$

The pile-up of coating at the edge of the indentation (Figure 3.11), δh , is the same as the one derived by Matthewson [20], and is given by,

$$\delta h = -\frac{\nu}{1-\nu} \frac{(4+\nu)}{12} \frac{h^2}{c} \alpha' (K'c + K) \quad (\text{B.23})$$

For the range of c/R ratios for the glass bead/alkyd paint system of Chapter 3, the modified analysis based on the indenter profile of equation (B.9), yielded forces that were 20-25% higher than the original Matthewson analysis [20].

Appendix C

Asymptotic solution of the buckling problem

The following asymptotic solution to the buckling problem of Section 3.5.1 has been published by the author in Reference [9].

To obtain the post-buckling solution to equations (3.21) and (3.22), the displacements and forces can be expanded in a series as follows,

$$\left. \begin{aligned} w(r) &= sw_1(r) + s^2w_2(r) + s^3w_3(r) + \dots \\ v(r) &= sv_1(r) + s^2v_2(r) + s^3v_3(r) + \dots \\ P &= P^C + sP^{(1)} + \frac{s^2P^{(2)}}{2} + \dots \end{aligned} \right\} \quad (C.1)$$

where s is a perturbation parameter that defines progress along the equilibrium path corresponding to buckling, and $P^{(i)}$ signifies the i 'th derivative of P with respect to s . If equation (C.1) is substituted into the differential equations (3.21) and (3.22), and the boundary conditions (equations (3.23), (3.25)-(3.27)) and the coefficients of the powers of s are set to zero, then a set of differential equations and boundary conditions can be constructed. The first three sets of resulting equations are,

$$\left. \begin{aligned} \zeta_1'' + \frac{\zeta_1'}{r} - \frac{\zeta_1}{r^2} + \frac{12P^c(1-\nu^2)}{Eh^3} \zeta_1 &= \frac{k_1}{r} \\ v_1'' + \frac{v_1'}{r} - \frac{v_1}{r^2} &= 0 \end{aligned} \right\} \quad (C.2)$$

$$\left. \begin{aligned} \zeta_2'' + \frac{\zeta_2'}{r} - \frac{\zeta_2}{r^2} - \frac{12}{h^2} \left(\zeta_1 v_1' + \frac{\nu \zeta_1 v_1}{r} \right) + \frac{12P^c(1-\nu^2)}{Eh^3} \zeta_2 + \frac{12P^{(1)}(1-\nu^2)}{Eh^3} \zeta_1 &= \frac{k_3}{r} \\ v_2'' + \frac{v_2'}{r} - \frac{v_2}{r^2} + w_1' w_1'' + \frac{(1-\nu)w_1'^2}{2r} &= 0 \end{aligned} \right\} \quad (C.3)$$

$$\left. \begin{aligned} \zeta_3'' + \frac{\zeta_3'}{r} - \frac{\zeta_3}{r^2} - \frac{12}{h^2} \left(\zeta_1 v_2' + \frac{\zeta_1^3}{2} + \nu \zeta_1 \frac{v_2}{r} + \zeta_2 v_1' + \nu \frac{\zeta_2 v_1}{r} \right) + \\ \frac{12(1-\nu^2)}{Eh^3} \left[P^c \zeta_3 + P^{(1)} \zeta_2 + \frac{P^{(2)}}{2} \zeta_1 \right] &= \frac{k_4}{r} \\ v_3'' + \frac{v_3'}{r} - \frac{v_3}{r^2} + \zeta_1 \zeta_2' + \zeta_2 \zeta_1' + (1-\nu) \frac{\zeta_1 \zeta_2}{r} &= 0 \end{aligned} \right\} \quad (C.4)$$

where

$$\zeta_i = \frac{dw_i}{dr} \quad (C.5)$$

The first equation in each set of equations (C.2)-(C.4) describes the out-of-plane behaviour of the buckled plate, and the second describes the in-plane behaviour. These equations are the same as those obtained by Thompson and Hunt [43], with the exception of the extra constants k_i , which are to be determined by the boundary conditions given by,

$$\left. \begin{aligned} w_i(a) = \zeta_i(a) = 0 \\ w_i(b) = 0 \\ w_i' + \frac{vw_i'}{r} \Big|_b = 0 \end{aligned} \right\} \quad (C.6)$$

for all i , and

$$\left. \begin{aligned} v_1' + \frac{v}{r} v_1 \Big|_b = 0 \\ v_2' + \frac{w_1'^2}{2} + \frac{v}{r} v_2 \Big|_b = 0 \\ v_3' + \frac{w_1' w_2'}{r} + \frac{v v_3}{r} \Big|_b = 0 \end{aligned} \right\} \quad (C.7)$$

The sets of equations (C.2)-(C.4) are solved individually using the boundary conditions, equations (C.6) and (C.7). Considering the first of equation (C.2), the homogeneous part is Bessel's equation, and the particular solution can be found as,

$$\zeta_i^p(r) = \frac{Eh^3 k_1}{12P^c(1-\nu^2)r} = \frac{k_1 D}{P^c r} = \frac{k_1}{\gamma^2 r} \quad (C.8)$$

where γ is given by,

$$\gamma = \sqrt{\frac{P^c}{D}} \quad (C.9)$$

and the general solution can thus be written as,

$$\zeta_1 = A_1 J_1(\gamma r) + B_1 Y_1(\gamma r) + \frac{k_1}{\gamma^2 r} \quad (C.10)$$

where $J_1(x)$ and $Y_1(x)$ are the first order Bessel functions, and A_1 , B_1 , and k_1 are constants to be determined by the boundary conditions. Integration of equation (C.10) gives,

$$w_1 = -\frac{A_1}{\gamma} J_0(\gamma r) - \frac{B_1}{\gamma} Y_0(\gamma r) + \frac{k_1 \ln(r)}{\gamma^2} + k_2 \quad (C.11)$$

where k_2 is another integration constant. Applying the boundary conditions results in the following homogeneous system of equations,

$$\left. \begin{aligned} A_1 J_1(\gamma a) + B_1 Y_1(\gamma a) + \frac{k_1}{a\gamma^2} &= 0 \\ A_1 \left(\gamma J_0(\gamma b) + \frac{J_1(\gamma b)}{b} (\nu - 1) \right) + B_1 \left(\gamma Y_0(\gamma b) + \frac{Y_1(\gamma b)}{b} (\nu - 1) \right) + \frac{k_1}{b^2 \gamma^2} (\nu - 1) &= 0 \\ -\frac{A_1}{\gamma} J_0(\gamma b) - \frac{B_1}{\gamma} Y_0(\gamma b) + \frac{k_1}{\gamma^2} \ln b + k_2 &= 0 \\ -\frac{A_1}{\gamma} J_0(\gamma a) - \frac{B_1}{\gamma} Y_0(\gamma a) + \frac{k_1}{\gamma^2} \ln a + k_2 &= 0 \end{aligned} \right\} \quad (C.12)$$

This is an eigenvalue problem and the characteristic equation can be found by setting the determinant of the matrix of coefficients of equation (C.12) to zero. The resulting characteristic equation can be rewritten in terms of

$$\left. \begin{aligned} \Psi &= \gamma b \\ p &= \frac{b}{a} \end{aligned} \right\} \quad (C.13)$$

and the solution for the smallest nonzero value of P^C satisfying the homogenous equation is found as,

$$P^C = \frac{C_1 D}{a^2} \quad \text{with} \quad C_1 = (\gamma a)^2 = \left(\frac{\Psi}{p} \right)^2 \quad (\text{C.14})$$

The particular value of Ψ depends on p , while the buckling parameter, C_1 varies with p as in Figure C.1, shown to facilitate calculations. The buckling parameter for very small holes ($p \rightarrow 0$) is 44.2, based on $\nu = 0.406$ (which is the Poisson's ratio for the coating in this study), which compares well to the value of 42.68 obtained numerically by Evans and Hutchinson for $\nu = 0.3$ (for deflection prevented at a single point, i.e. $b \rightarrow 0$) [40].

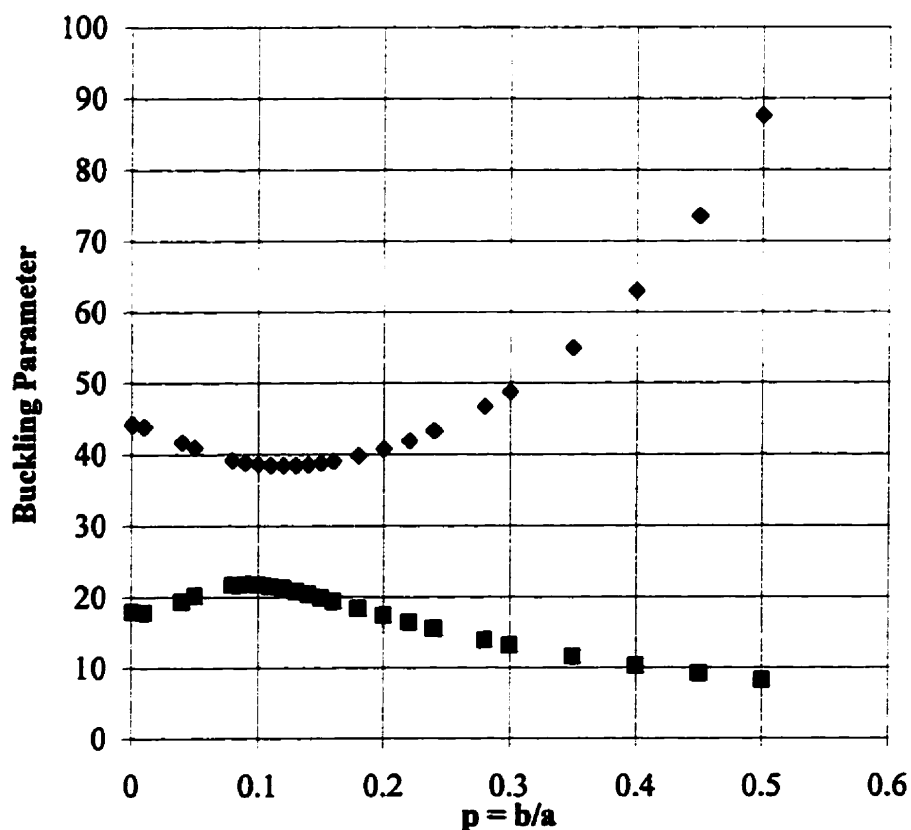


Figure C.1: Buckling parameters C_1 -●, and C_2 -■ as a function of $p = b/a$.

Because this is an eigenvalue problem, the complete solution cannot be found without a normalising condition. Following Thompson and Hunt [43], the perturbation parameter s is defined as the displacement at the midpoint of the deflected coating. All calculated quantities will then be in terms of the midpoint deflection:

$$w\left(\frac{a+b}{2}\right) = s, \quad \text{and thus,} \tag{C.15}$$

$$w_i\left(\frac{a+b}{2}\right) = 1, \quad w_i\left(\frac{a+b}{2}\right) = 0 \quad \text{for } i > 1$$

This normalising condition, together with equation (C.12) and the boundary conditions, gives the constants A_1 , B_1 , k_1 , and k_2 , as,

$$A_1 = \gamma \left\{ \begin{aligned} & \left[-Y_0\left(\gamma \frac{a+b}{2}\right) + Y_0(\gamma a) - a\gamma Y_1(\gamma a) \ln\left(\frac{2a}{b+a}\right) \right] \\ & \cdot \left[\frac{(\nu-1)J_1(\gamma a) - \frac{b}{a}(\nu-1)J_1(\gamma b) - \frac{b^2\gamma}{a}J_0(\gamma b)}{(\nu-1)Y_1(\gamma a) - \frac{b}{a}(\nu-1)Y_1(\gamma b) - \frac{b^2\gamma}{a}J_0(\gamma b)} \right] + \\ & + J_0(\gamma a) - J_0\left(\frac{a+b}{2}\gamma\right) + a\gamma \ln\left(\frac{2a}{b+a}\right) J_1(\gamma a) \end{aligned} \right\}^{-1}$$

$$B_1 = -A_1 \frac{\gamma a J_1(\gamma a) \ln \frac{b}{a} + \frac{b}{a} [J_0(\gamma b) - J_0(\gamma a)]}{\gamma a Y_1(\gamma a) \ln \frac{b}{a} + \frac{b}{a} [Y_0(\gamma b) - Y_0(\gamma a)]}$$

$$k_1 = -\gamma A_1 \frac{J_0(\gamma b) - J_0(\gamma a)}{\ln\left(\frac{a}{b}\right)} - \gamma B_1 \frac{Y_0(\gamma b) - Y_0(\gamma a)}{\ln\left(\frac{a}{b}\right)}$$

$$k_2 = A_1 \frac{\ln b J_0(\gamma a) - \ln a J_0(\gamma b)}{\gamma \ln\left(\frac{b}{a}\right)} + B_1 \frac{\ln b Y_0(\gamma a) - \ln a Y_0(\gamma b)}{\gamma \ln\left(\frac{b}{a}\right)} \tag{C.16}$$

which gives the full first mode buckling solution. The second of equations (C.2), together with the first of equations (C.7) gives that $v_1=0$.

Proceeding to the second set of equations, the first of equations (C.3) is rewritten in the following manner,

$$\left[\frac{1}{r} (rw_2')' \right]' + \frac{12P^c(1-\nu^2)}{Eh^3} w_2' - \frac{k_3}{r} = -\frac{12P^{(1)}(1-\nu^2)}{Eh^3} w_1' \quad (C.17)$$

and multiplying equation (C.17) by rw_1' then integrating the result from b to a (using integration by parts), the unknown left-hand side will disappear due to the boundary conditions. This procedure is originally due to Croll [56], and was used by Thompson and Hunt [43] in their analysis of a clamped buckled plate. Thus, $P^{(1)} = 0$, and equation (C.17) is the same as the first out-of-plane equation (C.2), and using the last of equation (C.15), $w_2 = 0$. The second of equations (C.3) can be rewritten as,

$$(v_2')' + \left(\frac{v_2}{r} \right)' + \left(\frac{w_1'^2}{2} \right)' + \frac{(1-\nu)}{2r} w_1'^2 = 0 \quad (C.18)$$

and integrating twice, equation (C.18) can be put in the following form,

$$v_2 + \frac{(1-\nu)}{4r} \int r w_1'^2 dr + \frac{1}{4} (1-\nu) r \int \frac{w_1'^2}{r} dr + \frac{c_1 r}{2} + \frac{c_2}{r} = 0 \quad (C.19)$$

The first of the integrals in equation (C.19) is,

$$\int r w_i'^2 dr = I(r) = \frac{r^2}{2} Z_1^2 - \frac{r^2}{2} Z_0 Z_2 - \frac{2k_1 Z_0}{\gamma^3} + \frac{k_1^2}{\gamma^4} \ln r \quad (C.20)$$

where $Z_i = A_i J_i(\gamma r) + B_i Y_i(\gamma r)$

and the second of the integrals in equation (C.19) can be written as,

$$\int \frac{w_i'^2}{r} dr = L(r) = -\frac{1}{2} (Z_1^2 + Z_0^2) - \frac{k_1^2}{2\gamma^4 r^2} + 2 \frac{k_1}{\gamma} N(\gamma r)$$

where

$$N(\gamma r) = \int \frac{Z_1(\gamma r)}{(\gamma r)^2} d(\gamma r) = -\frac{Z_1(\gamma r)}{2(\gamma r)} + \frac{1}{2} \left(A_1 \int \frac{J_0(\gamma r)}{\gamma r} d(\gamma r) + B_1 \int \frac{Y_0(\gamma r)}{\gamma r} d(\gamma r) \right)$$

$$\int \frac{J_0(\gamma r)}{\gamma r} d(\gamma r) = \sum_{k=1}^{\infty} \frac{(-1)^k (\gamma r)^{2k}}{2^{2k} k! \Gamma(k+1) 2k} + \ln(\gamma r)$$

$$\int \frac{Y_0(\gamma r)}{\gamma r} d(\gamma r) = \frac{2}{\pi} \left[\left(\ln \left(\frac{\gamma r}{2} \right) + g \right) \int \frac{J_0(\gamma r)}{\gamma r} d(\gamma r) - \frac{[\ln(\gamma r)]^2}{2} \sum_{k=1}^{\infty} \frac{(-1)^k (\gamma r)^{2k}}{2^{2k} k! \Gamma(k+1) (2k)^2} \right] +$$

$$+ \frac{2}{\pi} \left\{ \sum_{k=1}^{\infty} \left[\frac{(\gamma r)^{2k} (-1)^{k+1}}{2k \prod_{i=1}^k (2i)^2} \sum_{j=1}^k \frac{1}{j} \right] \right\} \quad (C.21)$$

where g is Euler's constant (≈ 0.577). The series expansions are necessary because these integrals do not have exact solutions. They were derived based on series expressions found in the literature (see [57], for example).

Substituting equations (C.20) and (C.21) in equation (C.19) gives $v_2(r)$. The only unknowns are the constants c_1 and c_2 which can be found by applying the second-order boundary condition, given by the second of equation (C.15), yielding,

$$\left. \begin{aligned} c_2 &= -\frac{(1+\nu)[b^2 I(a) - a^2 I(b)]}{4(b^2 - a^2)} + \frac{(1+\nu)a^2 b^2 [L(a) - L(b)]}{4(b^2 - a^2)} \\ c_1 &= \frac{(1-\nu)}{2a^2} I(a) - \frac{(1-\nu)}{2} L(a) + \frac{2c_2(1-\nu)}{a^2(1+\nu)} \end{aligned} \right\} \quad (C.22)$$

The third out of plane equation, equation (C.4), can be written as

$$\zeta_3'' + \frac{\zeta_3'}{r} - \frac{\zeta_3}{r^2} + \frac{12(1-\nu^2)}{Eh^3} P^C \zeta_3 - \frac{k_4}{r} = \frac{12}{h^2} \left(\zeta_1 \nu_2' + \frac{\zeta_1^3}{2} + \frac{\nu \zeta_1 \nu_2}{r} \right) - \frac{12(1-\nu^2)}{Eh^3} \frac{P^{(2)}}{2} \zeta_1 \quad (C.23)$$

noting that $P^{(1)} = \nu_1 = 0$. By performing the manipulation of Croll [56] (multiplying by rw_1' and integrating from b to a), the unknown left-hand-side vanishes due to the boundary conditions, and, after simplification,

$$\left. \begin{aligned} P^{(2)} &= \frac{\frac{D}{h^2 a^2} \left[-24a^2 \int_b^a I(r) \left(-\frac{(1-\nu^2)}{2r^3} I(r) - \frac{2(1-\nu)}{r^3} c_2 \right) dr \right]}{I(a) - I(b)} \\ \text{or} \\ P^{(2)} &= \frac{D}{h^2 a^2} C_2 \\ \text{where} \\ C_2 &= \frac{-24a^2 \int_b^a I(r) \left(-\frac{(1-\nu^2)}{2r^3} I(r) - \frac{2(1-\nu)}{r^3} c_2 \right) dr}{I(a) - I(b)} \end{aligned} \right\} \quad (C.24)$$

This was integrated numerically, because an exact solution is extremely tedious. The force can then be rewritten as,

$$\frac{P}{P^C} = 1 + \frac{C_2}{2C_1} \frac{s^2}{h^2} \quad (C.25)$$

where C_2 depends on p as in Figure C.1, and the dependence of $C_2/2C_1$ is shown in Figure C.2, to facilitate calculations. One could proceed to the third in-plane equation, and then the fourth order equations, etc., however, the leading terms obtained in equation (C.25) are sufficient to obtain the initial slope of the post-buckling path necessary for strain energy release calculations.

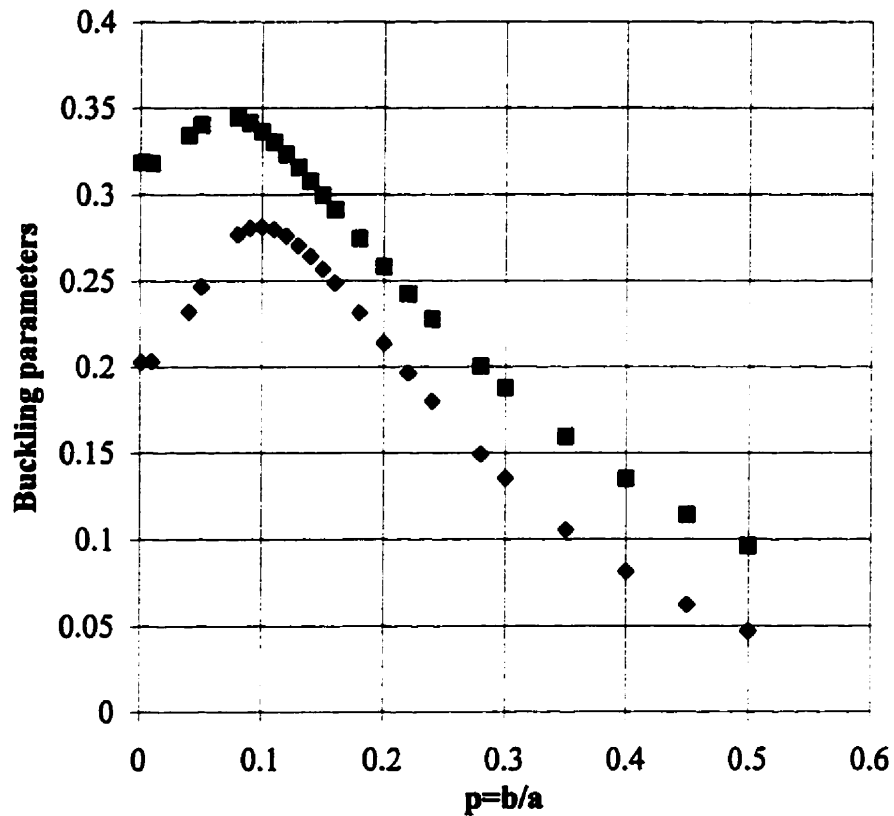


Figure C.2: Buckling parameters $C_2/2C_1$ -●, and α_B -■ as a function of $p = b/a$.

Appendix D

Excel and MathCad spreadsheets used to analyse data

D.1 Sample Microsoft Excel experimental data spreadsheet

Inputs:		BRACH'S ANALYSIS		Image Pro Incident Particle					
Delay incident (μ s)	129	inc. tang. vel (m/s)	-1.08023E-14	Impulse Ratio μ	1.58947E-16	x- centroid	y- centroid	angle α	
Delay rebound (μ s)	300	inc. norm vel (m/s)	-58.78092609	Coeff. of Rest. e	0.254123957	1	43.4298	44.79194	90
Incident α (deg)	270	reb. tang. vel.	9.15041E-16	Critical Imp. Ratio μ_c	4.1867E-17	2	43.34704	52.37423	
Rebound α (deg)	90	reb.norm. vel. (m/s)	14.93764152	Normalized Energy Loss Tangential Direction	-8.58104E-32	Image Pro Rebound Particle			
Diameter (mm)		Tang. Impulse	1.17173E-14	Normalized Energy Loss Normal Direction	0.935421015	1	43.0443	31.97131	angle α
Mass (kg)	1	Norm. Impulse	73.7185676	Total Normalized Energy Loss	0.935421015	2	42.43882	36.41151	90
Incident Velocity (m/s)	58.78092609								
	14.93764152								
λ for sphere	2.5	MEDIA	glass	TARGET	steel	SPECIMEN P (Psi)	L1		33
					paint thickness				
					40 microns				

D.2 Sample of implementation of analysis of Appendix B in a MathCad sheet

Modified Matthewson Analysis

Marcello Papini 1997

Input parameters here:

$$h := 40 \cdot 10^{-6} \quad m := 3.64286 \cdot 10^{-7}$$

$$E := 2470 \cdot 10^6$$

$$v := .406$$

$$G := \frac{E}{2 \cdot (1 + v)}$$

$$a := (.0000822) \quad \text{Contact Radius}$$

$$\frac{h}{a} = 0.487$$

$$R := .32 \cdot 10^{-3} \quad \text{Radius of Particle}$$

$$K(r) := K1 \sqrt{6} \frac{\sqrt{1-v} \cdot r}{\sqrt{4+v} \cdot h}$$

$$K(a) = 0.171$$

$$I(r) := I1 \left[\sqrt{3 \cdot \frac{1-2v}{2 \cdot (1-v)} \cdot \frac{r}{h}} \right]$$

$$I(a) = 0.901$$

$$dI(a) := \frac{d}{da}(I(a))$$

$$dI(a) = 1.604 \cdot 10^4$$

$$dK(a) := \frac{d}{da}(K(a))$$

$$A(a) := \frac{1}{12} \cdot h \cdot (4 + v) \cdot \frac{\left[\frac{d}{da}K(a) \cdot I(a) - K(a) \cdot \frac{d}{da}I(a) \right]}{a \cdot \frac{d}{da}I(a)}$$

$$B(a) := \frac{1}{3} \frac{h}{a} \left[\frac{4}{3} \frac{((6 \cdot v - 1) \cdot (v - 1))}{(-1 + 2 \cdot v)^2 \cdot R^3 \cdot \frac{d}{da} I(a)} \cdot h^2 + \frac{1}{4} \cdot 3 \cdot a^2 + 2 \cdot R^2 \cdot \frac{(6 \cdot v - 1)}{R^3 \cdot (-1 + 2 \cdot v) \cdot \frac{d}{da} I(a)} \right] \cdot I(a)$$

$$C(a) := \frac{4}{9} \cdot (6 \cdot v - 1) \cdot \frac{(v - 1)}{(-1 + 2 \cdot v)^2 \cdot R^3} \cdot h^3$$

$$D(a) := \left[\frac{-1}{12} \cdot (6 \cdot v - 1) \cdot \frac{2 \cdot R^2 + a^2}{(-1 + 2 \cdot v) \cdot R^3} \right] \cdot h$$

$$\alpha(a) := \frac{-(B(a) - C(a) + D(a))}{A(a)} \quad \alpha(a) = 0.625$$

$$\beta(a) := -3 \left[\frac{-4}{9} \frac{-7 \cdot v + 6 \cdot v^2 + 1}{(-1 + 2 \cdot v)^2 \cdot R^3 \cdot \frac{d}{da} I(a)} \right] \cdot h^2 - \frac{-1}{4} \alpha(a) \cdot (4 + v) \cdot \frac{\frac{d}{da} K(a)}{\frac{d}{da} I(a)} - \frac{1}{4} \frac{[3 \cdot a^2 + 2 \cdot R^2 \cdot (6 \cdot v - 1)]}{R^3 \cdot (-1 + 2 \cdot v) \cdot \frac{d}{da} I(a)}$$

$$\beta(a) = -1.137$$

$$\text{delta}(a) := -\frac{1}{12} \cdot v \cdot \alpha(a) \cdot h \cdot (4 + v) \cdot \frac{(K(a) + (dK(a)) \cdot a)}{((1 - v) \cdot a)}$$

$$\text{del} := \text{delta}(a) \cdot h$$

$$\text{delta}(a) = 0.019$$

$$\text{del} = 7.758 \cdot 10^{-7}$$

$$B1(r) := \left[\frac{-v}{(-1 + 2 \cdot v) \cdot R^3} r^3 + \left[\frac{-4}{3} \cdot (6 \cdot v - 1) \cdot \frac{(v - 1)}{(-1 + 2 \cdot v)^2 \cdot R^3} \cdot h^2 - 2 \cdot \frac{v}{(R \cdot (-1 + 2 \cdot v))} \right] \cdot r \right] \dots$$

$$+ \left[\beta(a) \cdot \text{II} \left[\sqrt{3 \cdot \frac{1 - 2 \cdot v}{2 \cdot (1 - v)}} \cdot \frac{r}{h} \right] \right]$$

$$C1(r) := -\frac{1}{2 \cdot h} \left[\left[\frac{-v}{(-1 + 2 \cdot v) \cdot R^3} r^3 + \left[\frac{-4}{3} \cdot (6 \cdot v - 1) \cdot \frac{(v - 1)}{(-1 + 2 \cdot v)^2 \cdot R^3} \cdot h^2 - 2 \cdot \frac{v}{(R \cdot (-1 + 2 \cdot v))} \right] \cdot r \right] \dots \right]$$

$$+ \left[\beta(a) \cdot \text{II} \left[\sqrt{3 \cdot \frac{1 - 2 \cdot v}{2 \cdot (1 - v)}} \cdot \frac{r}{h} \right] + \left[\frac{1}{2 \cdot R^3} r^3 + \frac{1}{R} r \right] \right]$$

for $r < a$

Stresses and strains

Inside contact area

$$\varepsilon_{r1}(r) := \frac{-4}{9} \cdot (6 \cdot v - 1) \cdot \frac{(v-1)}{[(-1+2 \cdot v)^2 \cdot R^3]} \cdot h^3 + \left[\frac{1}{3} \cdot \beta(a) \cdot \frac{d}{dr} I(r) - \frac{1}{6} \cdot \frac{(6 \cdot v - 1)}{(R \cdot (-1 + 2 \cdot v))} - \frac{1}{4} \cdot r^2 \cdot \frac{(6 \cdot v - 1)}{[R^3 \cdot (-1 + 2 \cdot v)]} \right] \cdot h$$

$$\varepsilon_{\theta 1}(r) := \frac{1}{3} \cdot \frac{h}{r} \cdot \beta(a) \cdot I(r) + \frac{-4 \cdot ((6 \cdot v - 1) \cdot (v - 1))}{9 \cdot [(-1 + 2 \cdot v)^2 \cdot R^3]} \cdot h^3 + \left[\frac{-1}{6} \cdot \frac{(6 \cdot v - 1)}{(R \cdot (-1 + 2 \cdot v))} - \frac{1}{12} \cdot \frac{(6 \cdot v - 1)}{(-1 + 2 \cdot v)} \cdot \frac{r^2}{R^3} \right] \cdot h$$

$$\varepsilon_{z1}(r) := \frac{r^2 - a^2}{2 \cdot R \cdot h} + \text{delta}(a) + \frac{r^4 - a^4}{8 \cdot R^3 \cdot h}$$

$$v(r, h) := \varepsilon_{z1}(r) \cdot h$$

$$\tau_1(r) := G \cdot B1(r)$$

$$\sigma_{r1}(r) := \frac{2 \cdot v \cdot G}{1 - 2 \cdot v} \cdot \varepsilon_{r1}(r) + \varepsilon_{\theta 1}(r) + \varepsilon_{z1}(r) + 2 \cdot G \cdot \varepsilon_{r1}(r)$$

$$\sigma_{\theta 1}(r) := \frac{2 \cdot v \cdot G}{1 - 2 \cdot v} \cdot \varepsilon_{r1}(r) + \varepsilon_{\theta 1}(r) + \varepsilon_{z1}(r) + 2 \cdot G \cdot \varepsilon_{\theta 1}(r)$$

$$\sigma_{z1}(r) := \frac{2 \cdot v \cdot G}{1 - 2 \cdot v} \cdot \varepsilon_{r1}(r) + \varepsilon_{\theta 1}(r) + \varepsilon_{z1}(r) + 2 \cdot G \cdot \varepsilon_{z1}(r)$$

Contact Force

$$P(a) := \frac{1}{6} \cdot (4 + v) \cdot G \cdot \pi \cdot v \cdot \alpha(a) \cdot h \cdot a \cdot \frac{K(a) + a \cdot \frac{d}{da} K(a)}{(-1 + 2 \cdot v)} - \frac{1}{3} \cdot G \cdot \pi \cdot \frac{(v-1)}{[(-1 + 2 \cdot v) \cdot R^3 \cdot h]} \cdot a^6 \dots$$

$$+ \left[\left[\frac{1}{3} \cdot v \cdot G \cdot \pi \cdot h \cdot \frac{(6 \cdot v - 1)}{[(-1 + 2 \cdot v)^2 \cdot R^3]} - \frac{1}{2} \cdot G \cdot \pi \cdot \frac{(v-1)}{((-1 + 2 \cdot v) \cdot (R \cdot h))} \right] \cdot a^4 \dots \right.$$

$$+ \left[\left[\frac{16}{9} \cdot v \cdot G \cdot \pi \cdot h^3 \cdot \frac{((6 \cdot v - 1) \cdot (v - 1))}{[(-1 + 2 \cdot v)^3 \cdot R^3]} + \frac{2}{3} \cdot v \cdot G \cdot \pi \cdot h \cdot \frac{(6 \cdot v - 1)}{[(-1 + 2 \cdot v)^2 \cdot R]} \right] \cdot a^2 \dots \right.$$

$$\left. + \left[\frac{4}{3} \cdot v \cdot \frac{G}{(1 - 2 \cdot v)} \cdot h \cdot \pi \cdot \beta(a) \cdot I(a) \cdot a \right] \right]$$

$$P(a) = -10.868$$

$$\text{delta}'(a) := \frac{1}{12} \cdot v \cdot h \cdot (4 + v) \left[\frac{d}{da} \left[\frac{\alpha(a)}{a} \cdot \frac{d}{da} (a \cdot K(a)) \right] \right]$$

$$\text{delta}'(a) = 571.348$$

Stresses and strains Outside contact area

for $r > a$

$$C2(r) := -\frac{2-v}{4 \cdot h} \cdot \alpha(a) \cdot K1 \left[\sqrt{6 \cdot \frac{1-v}{4+v} \cdot \frac{r}{h}} \right]$$

$$B2(r) := \alpha(a) \cdot K1 \left[\sqrt{6 \cdot \frac{1-v}{4+v} \cdot \frac{r}{h}} \right]$$

$$\varepsilon_{r2}(r) := \frac{1}{2} \cdot h \cdot \frac{d}{dr} B2(r) + \frac{1}{3} \cdot h^2 \cdot \frac{d}{dr} C2(r)$$

$$\varepsilon_{\theta 2}(r) := \frac{1}{2} \cdot \frac{h}{r} \cdot B2(r) + \frac{1}{3} \cdot \frac{h^2}{r} \cdot C2(r)$$

$$\varepsilon_{z2}(r) := -\frac{v}{(1-v)} \cdot \varepsilon_{r2}(r) + \varepsilon_{\theta 2}(r)$$

$$\tau_{r2}(r) := G \cdot B2(r)$$

$$\sigma_{r2}(r) := \frac{2 \cdot v \cdot G}{1 - 2 \cdot v} \cdot \varepsilon_{r2}(r) + \varepsilon_{\theta 2}(r) + \varepsilon_{z2}(r) + 2 \cdot G \cdot \varepsilon_{r2}(r)$$

$$\sigma_{\theta 2}(r) := \frac{2 \cdot v \cdot G}{1 - 2 \cdot v} \cdot \varepsilon_{r2}(r) + \varepsilon_{\theta 2}(r) + \varepsilon_{z2}(r) + 2 \cdot G \cdot \varepsilon_{\theta 2}(r)$$

$$\sigma_{z2}(r) := \frac{2 \cdot v \cdot G}{1 - 2 \cdot v} \cdot \varepsilon_{r2}(r) + \varepsilon_{\theta 2}(r) + \varepsilon_{z2}(r) + 2 \cdot G \cdot \varepsilon_{z2}(r)$$

$$r := 1 \cdot 10^{-20} \quad a = 8.22 \cdot 10^{-5}$$

Results for stresses and strains at r. If $r < a$, where a is contact radius, then solution on left, otherwise, solution on right.

For $r < a$

$$\epsilon_{r1}(r) = 0.049$$

$$\epsilon_{\theta1}(r) = 0.049$$

$$\epsilon_{z1}(r) = -0.249$$

$$\tau_1(r) = 4.631 \cdot 10^{-8}$$

$$\sigma_{r1}(r) = -4.821 \cdot 10^8$$

$$\sigma_{\theta1}(r) = -4.821 \cdot 10^8$$

$$\sigma_{z1}(r) = -1.006 \cdot 10^9$$

For $r > a$

$$\epsilon_{r2}(r) =$$

$$\epsilon_{\theta2}(r) = 4.085 \cdot 10^{-30}$$

$$\epsilon_{z2}(r) =$$

$$\tau_2(r) = 2.443 \cdot 10^{-24}$$

$$\sigma_{r2}(r) =$$

$$\sigma_{\theta2}(r) =$$

$$\sigma_{z2}(r) =$$

Contact force

$$P(a) = -10.868$$

Penetration depth

$$v(0, h) = -9.956 \cdot 10^{-6}$$

Fileup

$$\text{del} = 7.758 \cdot 10^{-7}$$

$$W(a) = \int_0^a \left[P(a) \cdot h \cdot \text{delta}'(a) - \frac{a}{R} - \frac{a^3}{R^3 \cdot 2} \right] da \quad \text{Work done on coating}$$

$$W1(a) := \int_0^a P(a) \cdot (h \cdot \text{delta}'(a)) da$$

$$W1(a) = -3.157 \cdot 10^{-6}$$

$$W2(a) := - \int_0^a \left[\frac{a}{R} + \frac{a^3}{R^3 \cdot 2} \right] \cdot P(a) da$$

$$W2(a) = 3.787 \cdot 10^{-5}$$

$$W(a) := W1(a) + W2(a)$$

$$W(a) =$$

$$V2(a) := \left[2 \cdot \frac{W2(a)}{m} \right]^{\frac{1}{2}}$$

Incident velocity required for given contact radius

$$V(a) := \left[2 \cdot \frac{W(a)}{m} \right]^{\frac{1}{2}}$$

$$V2(a) = 14.419$$

D.3 Sample of implementation of plastic hole Matthewson analysis in a MathCad sheet

Plastic Hole Shear Matthewson Analysis

Marcello Papini 1997

Input parameters here:

$$h := 50 \cdot 10^{-6} \quad m := 3.64286 \cdot 10^{-7}$$

$$E := 2470 \cdot 10^6$$

$$v := .4$$

$$G := \frac{E}{2 \cdot (1 + v)}$$

$$a := (.000173)$$

$$\frac{h}{a} = 0.289$$

$$R := .32 \cdot 10^{-3}$$

Assuming that the "crushed" area found in the impact sites is equal to the contact area, a , at full penetration (and this should be experimentally verified), then we can (Matthewson '89) assume that a cylinder of plastically deformed material of dimensions 'a' by 'h' exists. Assuming that a constant dynamic hardness or flow stress, H , acts (see dynamic hardness folder) over the cylinder's top surface, then Tresca says (see Matthewson '89) that a radial compressive pressure of $2/3 H$ exits at $r=a$.

The problem then becomes to remove the "cylinder" and replace it by the radial stress described above. The $2/3 H$ radial stress is used as the BC to a Matthewson type analysis:

The solution to this problem is in my binder and is called "plastic hole"

$$H := 190 \cdot 10^6$$

$$K(r) := K1 \cdot \sqrt{6} \cdot \frac{\sqrt{1-v} \cdot r}{\sqrt{4+v} \cdot h}$$

$$K(a) = 0.034$$

$$I(r) := I1 \left[\sqrt{3 \cdot \frac{1-2v}{2 \cdot (1-v)} \cdot \frac{r}{h}} \right]$$

$$I(a) = 2.398$$

$$dI(a) := \frac{d}{da}(I(a))$$

$$dI(a) = 3.081 \cdot 10^4$$

$$dK(a) := \frac{d}{da}(K(a))$$

$$\alpha_1(a) := -\frac{2}{3} \cdot H \cdot G \cdot \frac{1 - \nu}{G \cdot h \cdot (4 + \nu) \cdot \left(\frac{dK(a)}{da} + \nu \cdot \frac{K(a)}{a} \right)}$$

$$C2(r) := -\frac{2 - \nu}{4 \cdot h} \cdot \alpha_1(a) \cdot K(r)$$

$$B2(r) := \alpha_1(a) \cdot K(r)$$

$$B2(a) = 0.122$$

$$\alpha(a) := \left[6 \cdot \frac{1 - \nu}{h \cdot (4 + \nu)} \right]^{\frac{1}{5}}$$

Stresses and strains

$$\varepsilon_{r2}(r) := \frac{1}{2} \cdot h \cdot \frac{d}{dr} B2(r) + \frac{1}{3} \cdot h^2 \cdot \frac{d}{dr} C2(r) \quad r := a$$

$$\varepsilon_{\theta 2}(r) := \frac{1}{2} \cdot \frac{h}{r} \cdot B2(r) + \frac{1}{3} \cdot \frac{h^2}{r} \cdot C2(r)$$

$$\varepsilon_{z2}(r) := -\frac{\nu}{(1 - \nu)} \cdot (\varepsilon_{r2}(r) + \varepsilon_{\theta 2}(r))$$

$$\sigma_{r2}(r) := \frac{2 \cdot \nu \cdot G}{1 - 2 \cdot \nu} \cdot (\varepsilon_{r2}(r) + \varepsilon_{\theta 2}(r) + \varepsilon_{z2}(r)) + 2 \cdot G \cdot \varepsilon_{r2}(r)$$

$$\sigma_{\theta 2}(r) := \frac{2 \cdot \nu \cdot G}{1 - 2 \cdot \nu} \cdot (\varepsilon_{r2}(r) + \varepsilon_{\theta 2}(r) + \varepsilon_{z2}(r)) + 2 \cdot G \cdot \varepsilon_{\theta 2}(r)$$

$$\sigma_{z2}(r) := \frac{2 \cdot \nu \cdot G}{1 - 2 \cdot \nu} \cdot (\varepsilon_{r2}(r) + \varepsilon_{\theta 2}(r) + \varepsilon_{z2}(r)) + 2 \cdot G \cdot \varepsilon_{z2}(r)$$

$$\tau(r) := G \cdot B2(r)$$

$$\sigma_{r2}(r) = -1.267 \cdot 10^8 \quad \varepsilon_{r2}(r) = -0.048$$

$$\sigma_{\theta 2}(r) = -1.864 \cdot 10^7 \quad \varepsilon_{\theta 2}(r) = 0.013$$

$$\sigma_{z2}(r) = -7.451 \cdot 10^{-9} \quad \varepsilon_{z2}(r) = 0.024$$

Interfacial shear stress at $r = a$

$$\tau(r) = 1.079 \cdot 10^8$$

$$\text{(note that } \tau(a) = \frac{2}{3} \cdot 190 \cdot 10^6 \cdot \left(\frac{1}{\frac{dK(a)}{\alpha(a)^2 \cdot K(a)} + \frac{\nu}{a \cdot \alpha(a)^2}} \right)$$

D.4 Sample of implementation of buckling/strain energy release rate calculation in a MathCad sheet

Buckling analysis and strain energy calculations

Marcello Papini 1997

INPUTS

$$E := 2470 \cdot 10^6$$

$$t := .000040 \quad \text{Coating thickness}$$

$$v := .406$$

$$b := .000052 \quad \text{Radius at which buckling prevented due to presence of particle}$$

$$a := .000416 \quad \text{Contact radius}$$

$$V_0 := \frac{1}{3} \cdot \pi \cdot t^2 \cdot (3 \cdot \text{ParRad} - t)$$

$$b = 5.2 \cdot 10^{-5}$$

$$p := \frac{b}{a}$$

$$p = 0.125$$

Particle Radius

$$\text{ParRad} := .000365$$

Steel substrate properties

$$v_s := .3 \quad E_s := 210 \cdot 10^9$$

$$H := 10$$

$$V_0 = 1.768 \cdot 10^{-12}$$

$$V_0 := 2.34 \cdot 10^{-12}$$

Calculation of first buckling mode:

$$F(\Psi) := \left[\ln(p) \cdot \left[-J_0(\Psi) \cdot Y_1 \cdot \frac{\Psi}{p} + J_1 \cdot \frac{\Psi}{p} \cdot Y_0(\Psi) \right] + \ln(p) \cdot \left[-J_1(\Psi) \cdot Y_1 \cdot \frac{\Psi}{p} + J_1 \cdot \frac{\Psi}{p} \cdot Y_1(\Psi) \right] \cdot \frac{(v-1)}{\Psi} \right] \dots$$

$$+ \left[\frac{J_0 \cdot \frac{\Psi}{p} \cdot Y_0(\Psi) - J_0(\Psi) \cdot Y_0 \cdot \frac{\Psi}{p}}{\Psi} \dots \right]$$

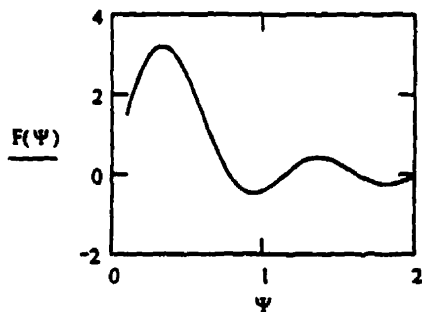
$$+ \left[\frac{J_0(\Psi) \cdot Y_1 \cdot \frac{\Psi}{p} - J_0 \cdot \frac{\Psi}{p} \cdot Y_1 \cdot \frac{\Psi}{p} + J_1 \cdot \frac{\Psi}{p} \cdot Y_0 \cdot \frac{\Psi}{p} - J_1 \cdot \frac{\Psi}{p} \cdot Y_0(\Psi) \cdot \frac{(v-1)}{\Psi^2}}{\Psi^2} \right]$$

$$+ \left[\frac{J_1(\Psi) \cdot Y_0 \cdot \frac{\Psi}{p} - J_0(\Psi) \cdot Y_1(\Psi) \cdot v - J_0 \cdot \frac{\Psi}{p} \cdot Y_1(\Psi) + J_0(\Psi) \cdot Y_1(\Psi) \dots}{\Psi^2} \right]$$

$$+ \left[\frac{J_0 \cdot \frac{\Psi}{p} \cdot Y_1(\Psi) \cdot v + J_1(\Psi) \cdot v \cdot Y_0(\Psi) - J_1(\Psi) \cdot Y_0(\Psi) - J_1(\Psi) \cdot v \cdot Y_0 \cdot \frac{\Psi}{p}}{\Psi^2} \right] \cdot p$$

$$\Psi := .1, .11..2$$

Find first root of F(Ψ)



Guess a value for root finding

$$\Psi := .7$$

$$\Psi := \text{root}(F(\Psi), \Psi)$$

$$\Psi = 0.774$$

$$p = 0.125$$

$$\gamma a := \frac{\Psi}{p} \quad \gamma a = 6.195$$

$$\gamma := \frac{\gamma a}{a} \quad \gamma = 1.489 \cdot 10^4$$

$$K1 := (\gamma \cdot a)^2$$

$$K1 = 38.379466$$

First buckling parameter

Constants needed for post-buckled analysis

(Expression for A too large to appear in printout)

$$A := \frac{\left[-Y0 \left[\frac{1}{2} \gamma \cdot (b + a) \right] + Y0(\gamma \cdot a) \right] + a \cdot \ln \left[2 \cdot \frac{a}{(b + a)} \right] \cdot Y1(\gamma \cdot a) \cdot \gamma}{\frac{(v - 1) \cdot J1(\gamma \cdot a) - \frac{b}{a} \cdot (v - 1) \cdot J1(\gamma \cdot b) - \frac{b}{a} \cdot (v - 1) \cdot Y1(\gamma \cdot b) + (1 - v) \cdot Y1(\gamma \cdot a) + \dots}{\dots}}$$

$$A = 1.182 \cdot 10^4$$

$$B := -A \cdot \frac{\left(J1 \left(\frac{\Psi}{p} \right) \cdot \Psi \cdot \ln(b) - J1 \left(\frac{\Psi}{p} \right) \cdot \Psi \cdot \ln(a) - p \cdot J0 \left(\frac{\Psi}{p} \right) + p \cdot J0(\Psi) \right)}{\left(Y1 \left(\frac{\Psi}{p} \right) \cdot \Psi \cdot \ln(b) - Y1 \left(\frac{\Psi}{p} \right) \cdot \Psi \cdot \ln(a) - p \cdot Y0 \left(\frac{\Psi}{p} \right) + p \cdot Y0(\Psi) \right)}$$

$$B = -1.453 \cdot 10^4$$

$$k := -\gamma \cdot \frac{\left(-J_0\left(\frac{\psi}{p}\right) + J_0(\psi)\right)}{(-\ln(b) + \ln(a))} \cdot A - \gamma \cdot \frac{\left(-Y_0\left(\frac{\psi}{p}\right) + Y_0(\psi)\right)}{(-\ln(b) + \ln(a))} \cdot B$$

$$k = -4.119 \cdot 10^7$$

$$k2 := \left[\frac{\left(-J_0(\psi) \cdot \ln(a) + \ln(b) \cdot J_0\left(\frac{\psi}{p}\right)\right)}{\left(\gamma \cdot (\ln(b) - \ln(a))\right)} \right] \cdot A + \left[\frac{\left(-Y_0(\psi) \cdot \ln(a) - \ln(b) \cdot Y_0\left(\frac{\psi}{p}\right)\right)}{\left(\gamma \cdot (\ln(b) - \ln(a))\right)} \right] \cdot B$$

$$k2 = -1.043$$

First out of plane equation:

$$w1(r) := -\frac{A}{\gamma} \cdot J_0(\gamma \cdot r) - \frac{B}{\gamma} \cdot Y_0(\gamma \cdot r) + \frac{k \cdot \ln(r)}{\gamma} + k2$$

$$w1(a) = 0$$

$$w1(b) = 0$$

Check to see if deflection zero at $r=a$ and $r=b$, and 1 at $r=(a+b)/2$ as it should be

$$w1\left(\frac{a+b}{2}\right) = 1$$

$$\zeta1(r) := A \cdot J1(\gamma \cdot r) + B \cdot Y1(\gamma \cdot r) + \frac{k}{\gamma} \cdot r$$

Slope

Note that $x = \gamma \cdot r$

$$Z(n, x) := A \cdot Jn(n, x) + B \cdot Yn(n, x)$$

$$I(r) := \frac{r^2}{2} \cdot Z(1, \gamma \cdot r)^2 - \frac{r^2}{2} \cdot Z(0, \gamma \cdot r) \cdot Z(2, \gamma \cdot r) - 2 \cdot \frac{k}{\gamma} \cdot Z(0, \gamma \cdot r) + \frac{k^2}{\gamma} \cdot \ln(r)$$

Bessel function and integral of Bessel function calculations:

$$\text{Sum}(x) := \frac{2}{x} \cdot \left[\sum_{k=1}^{70} \frac{x^{2k} \cdot (-1)^{k+1} \cdot \sum_{j=1}^k \frac{1}{j}}{2 \cdot k \cdot \prod_{i=1}^k (2 \cdot i)^2} \right]$$

Euler := .5772156649

Euler's constant

$$J(x) := \sum_{k=1}^{80} \frac{(-1)^k \cdot x^{2 \cdot k}}{2^{2 \cdot k} \cdot k! \cdot \Gamma(k+1) \cdot 2 \cdot k} + \ln(x)$$

$$Y(x) := \frac{2}{\pi} \left[\ln\left(\frac{x}{2}\right) \cdot J(x) - \frac{(\ln(x))^2}{2} - \sum_{k=1}^{80} \frac{(-1)^k \cdot x^{2 \cdot k}}{2^{2 \cdot k} \cdot k! \cdot \Gamma(k+1) \cdot (2 \cdot k)^2} \right] + \text{Sum}(x) + 2 \cdot \frac{\text{Euler}}{\pi} \cdot J(x)$$

$$M(x) := \frac{-Z(1, x)}{2 \cdot x} + .5 \cdot (A \cdot J(x) + B \cdot Y(x))$$

$$L(x) := \left[-.5 \cdot (Z(0, x)^2 + Z(1, x)^2) - \frac{k^2}{\gamma^2 \cdot x^2 \cdot 2} \right] + \frac{2 \cdot k}{\gamma} \cdot M(x)$$

$$I(r) := \frac{r^2}{2} \cdot Z(1, \gamma r)^2 - \frac{r^2 \cdot Z(0, \gamma r) \cdot Z(2, \gamma r)}{2} - 2 \cdot \frac{k}{\gamma^3} \cdot Z(0, \gamma r) + \frac{k^2}{\gamma^4} \cdot \ln(r)$$

$$c2 := -\frac{1+v}{4 \cdot (b^2 - a^2)} \cdot (b^2 \cdot I(a) - a^2 \cdot I(b)) + (1+v) \cdot \frac{1}{4 \cdot (b^2 - a^2)} \cdot a^2 \cdot b^2 \cdot (L(\gamma a) - L(\gamma b))$$

$$c2 = -0.093$$

$$c1 := \left[\frac{1-v}{2 \cdot a^2} \cdot I(a) - (1-v) \cdot \frac{L(\gamma a)}{2} \right] + \frac{2 \cdot c2 \cdot (1-v)}{a^2 \cdot (1+v)}$$

$$c1 = 4.679 \cdot 10^6$$

Second in-plane response:

$$v2(r) := -\frac{1+v}{4} \cdot \frac{I(r)}{r} - \frac{1}{4} \cdot (1-v) \cdot r \cdot L(\gamma r) - c1 \cdot \frac{r}{2} - \frac{c2}{r}$$

$$v2(a) = -3.207 \cdot 10^3$$

Integrals must be evaluated numerically:

$$X := -24 \cdot a^2 \cdot \int_b^a I(r) \cdot \left[-\left(\frac{1-v^2}{2 \cdot r^3} \cdot I(r) \right) - 2 \cdot \frac{1-v}{r^3} \cdot c2 \right] dr$$

$$X = 64.664$$

$$Y := I(a) - I(b)$$

$$Y = 3.086$$

$$K2 := \frac{X}{Y}$$

$$K1 = 38.379$$

$$p = 0.125$$

$$K2 = 20.952$$

$$\Psi = 0.774$$

Buckling parameters

$$\gamma \cdot a = 6.195$$

$$\frac{K2}{2 \cdot K1} = 0.27296$$

Slope of initial post-buckled path:

$$\text{slope} := \frac{1}{1 - \frac{2 \cdot a \cdot v2(s) \cdot 12 \cdot (1 + v)}{K2}}$$

$$\text{slope} = 0.3176$$

Critical Buckling volume:

$$Vc := \frac{\pi \cdot K1 \cdot t^3}{6 \cdot (1 + v)} \quad Vc = 9.147 \cdot 10^{-13}$$

Analysis of Suo and Hutchinson for mode ratios and G calcs

$$\kappa_1 := 3 - 4 \cdot v$$

$$\kappa_2 := 3 - 4 \cdot v_s$$

$$p = 0.125$$

$$\mu_1 := \frac{E}{2 \cdot (1 + v)}$$

$$\mu_2 := \frac{E_s}{2 \cdot (1 + v_s)}$$

$$p = 0.125$$

$$\beta := \frac{\mu_1 \cdot (\kappa_2 - 1) - \mu_2 \cdot (\kappa_1 - 1)}{\mu_1 \cdot (\kappa_2 + 1) + \mu_2 \cdot (\kappa_1 + 1)}$$

$$\alpha := \frac{\mu_1 \cdot (\kappa_2 + 1) - \mu_2 \cdot (\kappa_1 + 1)}{\mu_1 \cdot (\kappa_2 + 1) + \mu_2 \cdot (\kappa_1 + 1)}$$

$$\beta = -0.153$$

$$\alpha = -0.975$$

Dundurs
parameters

$$\omega := 52.5 \cdot \text{deg}$$

(This value was found using the chart of Zuo+Hutchinson (1990))

If $V_0 > V_c$, then the buckled solution is valid, otherwise, the unbuckled solution is valid

Unbuckled

$$\frac{V_0}{V_c} = 2.558$$

$$G_u := E \cdot \frac{V_0^2}{4 \cdot \pi^2 \cdot (1 - v) \cdot a^4 \cdot t}$$

$$G_u = 481.448$$

$$\psi_u := 90$$

D13

$$s := \left[2 \cdot \frac{K1}{K2} \cdot \text{slope} \cdot \left(\frac{V_o}{V_c} - 1 \right) \right]^5 \cdot t$$

$$s = 5.386 \cdot 10^{-5}$$

Reactions at crack tip:

$$M(r) := \frac{E \cdot t^3}{12 \cdot (1 - \nu^2)} \cdot \frac{d^2}{dr^2} w1(r) \cdot s$$

$$P := \frac{K1 \cdot E \cdot t^3}{12 \cdot (1 - \nu^2) \cdot a^2} + \frac{s^2 \cdot E \cdot t^3}{12 \cdot (1 - \nu^2)} \cdot \frac{K2}{t^2 \cdot a^2 \cdot 2} \quad M(a) = 0.076$$

$$P := \frac{-1}{24} \cdot E \cdot \frac{(2 \cdot K1 \cdot t^2 + s^2 \cdot K2)}{[(1 + \nu^2) \cdot a^2]} \cdot t \quad P = 5.229 \cdot 10^{-3}$$

$$G := 6 \cdot (1 - \nu^2) \cdot E^{-1} \cdot t^{-3} \cdot \left(M(a)^2 + t^2 \cdot \frac{P^2}{12} \right)$$

$$\psi := \text{atan} \left(\frac{\sqrt{12} \cdot M(a) \cdot \cos(\omega) - t \cdot P \cdot \sin(\omega)}{-\sqrt{12} \cdot M(a) \cdot \sin(\omega) - t \cdot P \cdot \cos(\omega)} \right)$$

Results are here:

$$G = 297.911$$

$$\psi = 1.025 \cdot \text{deg}$$

D.5 Sample of implementation of rigid-plastic analysis for spherical particles in a MathCad sheet

Spherical particle Hutchings analysis:

Inputs

$$\begin{aligned}
 r &:= .000445 \cdot \text{m} \\
 p_d &:= 1120 \cdot 10^6 \cdot \text{Pa} & V &:= 54.79 \frac{\text{m}}{\text{sec}} & \text{mass} &:= .000002918 \cdot \text{kg} \\
 \mu &:= .001 & \alpha &:= -61.69 \cdot \text{deg} & \text{mass} &= 2.918 \cdot 10^{-6} \cdot \text{kg} \\
 y_0 &:= r \\
 x_0 &:= 0 \\
 v_{ly0} &:= V \cdot \sin(\alpha) & v_{ly0} &= -48.237 \cdot \text{m} \cdot \text{sec}^{-1} \\
 v_{lx0} &:= V \cdot \cos(\alpha) & v_{lx0} &= 25.984 \cdot \text{m} \cdot \text{sec}^{-1}
 \end{aligned}$$

Full contact solution:

$$y_1 := \begin{bmatrix} \frac{r}{m} \\ v_{ly0} \frac{\text{sec}}{m} \\ 0 \\ v_{lx0} \frac{\text{sec}}{m} \end{bmatrix}$$

These two matrices are needed by the Runge Kutta function to calculate solution

$$D_1(t, y_1) := \begin{bmatrix} y_{1_1} \\ \frac{r^2 - (y_{1_0})^2}{\text{mass}} \\ y_{1_3} \\ \frac{r^2 - (y_{1_0})^2}{\text{mass}} \\ -\mu \cdot \frac{r \cdot p_d}{\text{mass}} \end{bmatrix}$$

$$\text{time}_{\text{full}} := 1.319 \cdot 10^{-6}$$

$$Z_1 := \text{rkfixed}(y_1, 0, \text{time}_{\text{full}}, 100, D_1) \quad \text{RungeKutta implementation}$$

$Z_1 =$	-17.1967432	$3.08322458 \cdot 10^{-5}$	25.95267221
	-16.60017761	$3.11745577 \cdot 10^{-5}$	25.95207564
	-16.00082236	$3.15168616 \cdot 10^{-5}$	25.95147629
	-15.39877963	$3.18591576 \cdot 10^{-5}$	25.95087424
	-14.79415186	$3.22014456 \cdot 10^{-5}$	25.95026961
	-14.18704179	$3.25437257 \cdot 10^{-5}$	25.9496625
	-13.57755243	$3.28859977 \cdot 10^{-5}$	25.94905302
	-12.96578704	$3.32282617 \cdot 10^{-5}$	25.94844125
	-12.35184911	$3.35705176 \cdot 10^{-5}$	25.94782731
	-11.73584239	$3.39127654 \cdot 10^{-5}$	25.94721131
	-11.11787084	$3.4255005 \cdot 10^{-5}$	25.94659333

Solution is all in Z1

$$\begin{aligned}
 x_1 &:= Z_1^{<3>} \cdot m \\
 y_1 &:= Z_1^{<1>} \cdot r \\
 v_1 &:= \sqrt{velx_1^2 + vely_1^2} \\
 velx_1 &:= Z_1^{<4>} \cdot \frac{m}{sec} \\
 vely_1 &:= Z_1^{<2>} \cdot \frac{m}{sec} \\
 \alpha_1 &:= atan\left(\frac{vely_1}{velx_1}\right) \cdot rad \\
 pen &:= r - y_1
 \end{aligned}$$

$a_{star} =$	$1.623 \cdot 10^{-4}$	$\cdot m$
	$1.625 \cdot 10^{-4}$	
	$1.626 \cdot 10^{-4}$	
	$1.627 \cdot 10^{-4}$	
	$1.628 \cdot 10^{-4}$	
	$1.629 \cdot 10^{-4}$	
	$1.63 \cdot 10^{-4}$	
	$1.63 \cdot 10^{-4}$	
	$1.631 \cdot 10^{-4}$	
	$1.631 \cdot 10^{-4}$	
	$1.631 \cdot 10^{-4}$	
	$1.63 \cdot 10^{-4}$	

Here, you need to find where 'astar' starts to decrease, because that is point of separation. Once found, then adjust the higher time limit, so that the hundredth entry is where the sphere detaches.

Sphere not fully in contact:

Enter disattached data here:

$$\begin{aligned}
 y_0 &:= Z_{100,1} \cdot \text{m} & y_0 &= 3.989 \cdot 10^{-4} \cdot \text{m} \\
 x_0 &:= a_{100,0} & x_0 &= 1.973 \cdot 10^{-4} \cdot \text{m} \\
 v_{y_0} &:= Z_{100,2} \cdot \frac{\text{m}}{\text{sec}} & v_{y_0} &= -11.118 \cdot \text{m} \cdot \text{sec}^{-1} \\
 v_{x_0} &:= Z_{100,4} \cdot \frac{\text{m}}{\text{sec}} & v_{x_0} &= 25.947 \cdot \text{m} \cdot \text{sec}^{-1} \\
 x' &= v_x \\
 y' &= v_y
 \end{aligned}$$

$$\text{atan} \left(\frac{v_{y_0}}{v_{x_0}} \right) = -23.195 \cdot \text{deg}$$

$$\text{pen} := r - y_1$$

$$y := \begin{bmatrix} \frac{y_0}{\text{m}} \\ v_{y_0} \cdot \frac{\text{sec}}{\text{m}} \\ \frac{x_0}{\text{m}} \\ v_{x_0} \cdot \frac{\text{sec}}{\text{m}} \end{bmatrix}$$

D matrix needed for runge kutta calculation is too large for printout

$$D(t,y) := \begin{bmatrix} -1 & \sqrt{2} & \frac{-\sqrt{r-y_0} \cdot \sqrt{r+y_0} \cdot \sqrt{(y_3)^2 + y_1^2} + r \cdot y_1 + \mu \cdot r \cdot y_3 - \mu \cdot y_0 \cdot \sqrt{(y_3)^2 + y_1^2}}{2 \cdot [(y_3)^2 + y_1^2]^{\frac{1}{4}}} & \dots \\ \dots & \dots & \dots & \dots \\ 1 & \sqrt{2} & \left[-r \cdot y_3 + y_0 \cdot \sqrt{(y_3)^2 + (y_1)^2} - \mu \cdot \sqrt{r-y_0} \cdot \sqrt{r+y_0} \cdot \sqrt{(y_3)^2 + (y_1)^2} + \mu \cdot r \cdot y_1 \right] & \dots \end{bmatrix}$$

D17

$$\left[\frac{1}{2} \sqrt{2} \frac{r y_3 \cdot y_0 \sqrt{y_3} \cdot y_1 + \mu \sqrt{r} y_0 \sqrt{r} \cdot y_0 \sqrt{y_3} \cdot y_1 + \mu \cdot r y_1}{\left[(y_3)^2 + (y_1)^2 \right]^{\frac{1}{4}} \left[\sqrt{r} \sqrt{r} \sqrt{(y_3)^2 + (y_1)^2} - \sqrt{r - y_0} \sqrt{r + y_0} y_1 - y_0 y_3 \right]} \right]$$

time_{part} := 2.239 · 10⁻⁶

Z := rckfixed(y, 0, time_{part}, 100, D)

Here, you need to find where Z goes imaginary (that is where the sphere loses contact and rebounds). Adjust the upper limit of time so that the hundredth element of Z is where the sphere loses contact

Z =

0	0.0003988871	-11.117870836
2.239 · 10 ⁻⁸	0.0003986496	-10.1034696149
4.478 · 10 ⁻⁸	0.0003984345	-9.1140584787
6.717 · 10 ⁻⁸	0.0003982412	-8.1544085353
8.956 · 10 ⁻⁸	0.0003980691	-7.2280229716
1.1195 · 10 ⁻⁷	0.0003979173	-6.33740528
1.3434 · 10 ⁻⁷	0.000397785	-5.4842339381
1.5673 · 10 ⁻⁷	0.0003976714	-4.6694957832
1.7912 · 10 ⁻⁷	0.0003975756	-3.8935973567
2.0151 · 10 ⁻⁷	0.0003974968	-3.1564621364
2.239 · 10 ⁻⁷	0.000397434	-2.4576170106

velx := Z^{<4>} · $\frac{m}{sec}$

vely := Z^{<2>} · $\frac{m}{sec}$

α₂ := atan $\left(\frac{vely}{velx} \right)$

v₂ := $\sqrt{velx^2 + vely^2}$

α := stack(α₁, α₂)

Rebound velocity and angle

$$\mu = 1 \cdot 10^{-3}$$

$$\text{time} := \text{time}_{\text{full}} + \text{time}_{\text{part}}$$

$$\text{time} = 3.558 \cdot 10^{-6}$$

$$\alpha_{\text{reb}} := \alpha_{200}$$

$$V_{\text{rebound}} := v_{2,100}$$

$$V_{\text{rebound}} = 23.262 \cdot \text{m} \cdot \text{sec}^{-1}$$

$$\alpha_{\text{reb}} = 22.291 \text{ -deg}$$

Now make an array of the x and y coordinates of the center of the sphere in the original (unattached) coordinate system

$$x_2 := Z^{<3>} \cdot \text{m} - (a_{1,100} - Z_{1,100,3} \cdot \text{m})$$

$$x := \text{stack}\left(\frac{x_1}{\text{m}}, \frac{x_2}{\text{m}}\right) \cdot \text{m}$$

$$y_2 := Z^{<1>} \cdot \text{m}$$

$$v := \text{stack}\left(\frac{y_1}{\text{m}}, \frac{y_2}{\text{m}}\right) \cdot \text{m}$$

$$a_2 := \sqrt{r^2 - y_2^2}$$

$$a := \text{stack}\left(\frac{a_1}{\text{m}}, \frac{a_2}{\text{m}}\right) \cdot \text{m}$$

$$\text{pen} := r - y$$

$$\text{maxpen} := \max(\text{pen})$$

$$\text{maxpen} = 4.767 \cdot 10^{-5} \cdot \text{m}$$

Below is for animating the impact

Plots a circle of specified radius at a specified origin.

Enter radius: $r := r$

Default scale for plot: $s := .0004$ $h := .00032$

$current := 0, 10.. FRAME$

$an := 0, 0.1.. 2 \cdot \pi + .1$

$x_{circle_{current, \frac{an}{I}}} := (r \cdot \cos(an) + x_{current})$

$y_{circle_{current, \frac{an}{I}}} := r \cdot \sin(an) + y_{current}$

Quick X-Y Plot of a Function



Produces a nicely formatted X-Y plot from a function definition you supply.

Enter a function $f(x)$ you want to plot:

$f(r) := 0$

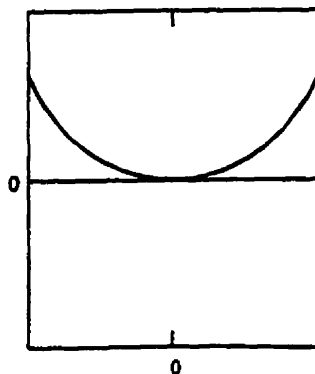


Default scales for plots: $r1 := -s$ $r2 := s$

Enter number of points to plot on x range:

$rr := -r1, -r1 + \frac{r1}{n}.. r1$

$n := 100$



Animation appears here

Crater Volume calcs

$$i := 0..100$$

$$A_{1_i} := .5 \cdot r^2 \cdot \left(2 \cdot \arccos \left(\frac{y_{2_i}}{r \cdot \cos(\alpha_{2_i})} \right) - \sin \left(2 \cdot \arccos \left(\frac{y_{2_i}}{r \cdot \cos(\alpha_{2_i})} \right) \right) \right)$$

$$i := 0..99$$

$$dA_{1_i} := \frac{A_{1_{i+1}} - A_{1_i}}{(Z_{i+1,0} - Z_{i,0}) \cdot \text{sec}}$$

$$dt_i = (Z_{i+1,0} - Z_{i,0}) \cdot \text{sec}$$

$$dv_{2_i} := \frac{(v_{2_{i+1}} - v_{2_i})}{(Z_{i+1,0} - Z_{i,0}) \cdot \text{sec}}$$

Translational component of Volume

$$i := 0..99$$

$$dV_{t_i} := \left[A_{1_i} + .5 \cdot dA_{1_i} \cdot [(Z_{i+1,0} - Z_{i,0}) \cdot \text{sec}] \right] \cdot \left[v_{2_i} + .5 \cdot dv_{2_i} \cdot [(Z_{i+1,0} - Z_{i,0}) \cdot \text{sec}] \right] \cdot [(Z_{i+1,0} - Z_{i,0}) \cdot \text{sec}]$$

$$d\alpha_{2_i} := \frac{(\alpha_{2_{i+1}} - \alpha_{2_i})}{(Z_{i+1,0} - Z_{i,0}) \cdot \text{sec}}$$

$$dV_{r_i} := \frac{2}{3} \cdot d\alpha_{2_i} \cdot [(Z_{i+1,0} - Z_{i,0}) \cdot \text{sec}] \cdot \left[(r)^2 - \frac{1}{4} \cdot \left[\frac{y_{2_i}}{\cos(\alpha_{2_i})} + \frac{(y_{2_i}) - v_{2_i} \cdot [(Z_{i+1,0} - Z_{i,0}) \cdot \text{sec}]}{\cos[\alpha_{2_i} + d\alpha_{2_i} \cdot [(Z_{i+1,0} - Z_{i,0}) \cdot \text{sec}]]} \right] \right]$$

$$V_t := \sum dV_t$$

$$V_t = 2.50332 \cdot 10^{-4} \text{ mm}^3$$

Rotational component of Volume

$$V_r := \sum dV_r - dV_{r_0}$$

$$V_r = 2.86905 \cdot 10^{-3} \text{ mm}^3$$

This is volume after disattachment

$$\text{Vol} := V_r + V_t$$

$$\text{Vol} = 3.119 \cdot 10^{-3} \text{ mm}^3$$

Crater Length calcs

$$i := 1..100$$

$$L_{0\text{to}100}_i := 2 \cdot a \cdot l_i$$

$$L_{0\text{to}100}_{100} = 3.945 \cdot 10^{-4} \text{ m}$$

$$L := a_2 + x_2 + a_{l_{100}}$$

$$L_{100\text{to}200} := a_2 + x_2 + a_{l_{100}} - x_{l_{100}}$$

$$L := \text{stack} \left(\frac{L_{0\text{to}100}}{m}, \frac{L_{100\text{to}200}}{m} \right) \cdot m$$

$$i := 1..100$$

$$i := 1..200$$

$$L_{\text{ave}_i} := .5 \cdot (L_i + L_{i-1})$$

$$L_{\text{final}} := L_{201}$$

$$L_{\text{final}} = 418.192 \text{ } \mu\text{m}$$

$$V_{\text{rebound}} = 23.262 \text{ m} \cdot \text{sec}^{-1} \quad \alpha_{\text{reb}} = 22.291 \text{ deg}$$

$$\mu\text{m} := \left(\frac{\text{mm}}{1000} \right)$$

$$\text{elasticpen} := 23 \text{ } \mu\text{m}$$

$$\text{maxpen} := \text{max}(\text{pen})$$

$$\text{maxpen} = 47.673 \text{ } \mu\text{m}$$

$$\text{Vol} = 3.119 \cdot 10^6 \text{ } \mu\text{m}^3$$

$$\text{maxpen} - \text{elasticpen} = 24.673 \text{ } \mu\text{m}$$

$$180\text{-deg} - \alpha_{\text{reb}} = 157.709\text{-deg}$$

$L_{\text{ave}} =$

0
$2.379 \cdot 10^{-5}$
$5.741 \cdot 10^{-5}$
$7.479 \cdot 10^{-5}$
$8.868 \cdot 10^{-5}$
$1.006 \cdot 10^{-4}$
$1.112 \cdot 10^{-4}$
$1.209 \cdot 10^{-4}$
$1.298 \cdot 10^{-4}$
$1.381 \cdot 10^{-4}$
$1.459 \cdot 10^{-4}$
$1.533 \cdot 10^{-4}$

$\cdot m$

D.6 Sample of implementation of rigid-plastic analysis for symmetric angular particles in a MathCad sheet

Impact of a 3D 6 sided symmetric particle with a surface of constant dynamic hardness

By Marcello Papini, University of Toronto, Dept. Mechanical and Industrial Engineering, 1998

This sheet will calculate the path take by a 6-sided angular particle having equal length sides in the cross section (length h) and depth w into the page, colliding with a surface having a dynamic hardness equal to p_d . The particle is assumed to impact with one edge parallel to the target surface to eliminate some 3 d effects. The particle can be a "diamond" of any internal angle that meets the above criteria, and can impact with any rake angle measure counterclockwise positive from the normal to the surface to the axis of symmetry of the particle. A particle with equal angles would be a square and would look like a diamond in the configuration corresponding to zero rake angle. It can impact at any angle of attack and incident velocity and can be made of any "rigid" (i.e. nondeforming) material. Note that to run this decently requires at least a Pentium 166, and 32 Megs of RAM. For accurate results and small timesteps, a Pentium II with 64 Megs of SDRAM would be adequate. Please be patient when running the model, as it can take a bit of time to complete on lower end systems. This formulation includes the particle width, but can be easily converted to a per-unit width basis (as was done in the alternate program found in the file named "Final").

Material properties and shape definition

$$\begin{aligned}
 p_d &:= 4000 \cdot 10^6 \text{ Pa} & h &:= .0136789 \text{ m} \\
 A &:= \frac{45}{180} \cdot \pi & w &:= .0015 \text{ m} \\
 \rho &:= 7813 \frac{\text{kg}}{\text{m}^3} & \mu &:= 0 \\
 \text{Volume} &:= w \cdot h^2 \cdot 2 \cdot \cos(A) \cdot \sin(A) \\
 \text{mass} &:= \rho \cdot \text{Volume} & \text{mass} &= & A &= \text{deg}
 \end{aligned}$$

Initial angle of attack, α_i , rake angle, θ_i , and velocity, V_i

$$\begin{aligned}
 \alpha_i &:= \frac{-25}{180} \cdot \pi \\
 \theta_i &:= \frac{15}{180} \cdot \pi & V_i &:= 200 \frac{\text{m}}{\text{sec}}
 \end{aligned}$$

y_0, z_0 are the coordinates of the c of mass of the particle

$$\begin{aligned} z_0 &:= h \cdot \sin(A) \cdot \cos(\theta_i) & I_x &:= \frac{1}{6} \cdot \text{mass} \cdot h^2 \\ y_0 &:= -h \cdot \sin(A) \cdot \sin(\theta_i) \\ v_{0z} &:= V_i \cdot \sin(\alpha_i) \\ v_{0y} &:= V_i \cdot \cos(\alpha_i) \end{aligned}$$

This is the initial condition vector needed for the rkfixed function. The entries are modified in the program each time step. Initially, alot of these are zero due to the trick explained below. The entries at each timestep are the instantaneous (top to bottom):

y_0 - y coordinate of center of mass

v_{0y} - y velocity of center of mass

z_0 - z coordinate of center of mass

v_{0z} - z velocity of center of mass

θ - rake angle

θ' - angular velocity

y_6 - y coordinate of first point on first left side force interval

y_7 - y coordinate of second point on first left side force interval

y_8 - y coordinate of first point on second left side force interval

y_9 - y coordinate of second point on second left side force interval

y_{10} - y coordinate of first point on first right side force interval

y_{11} - y coordinate of second point on first right side force interval

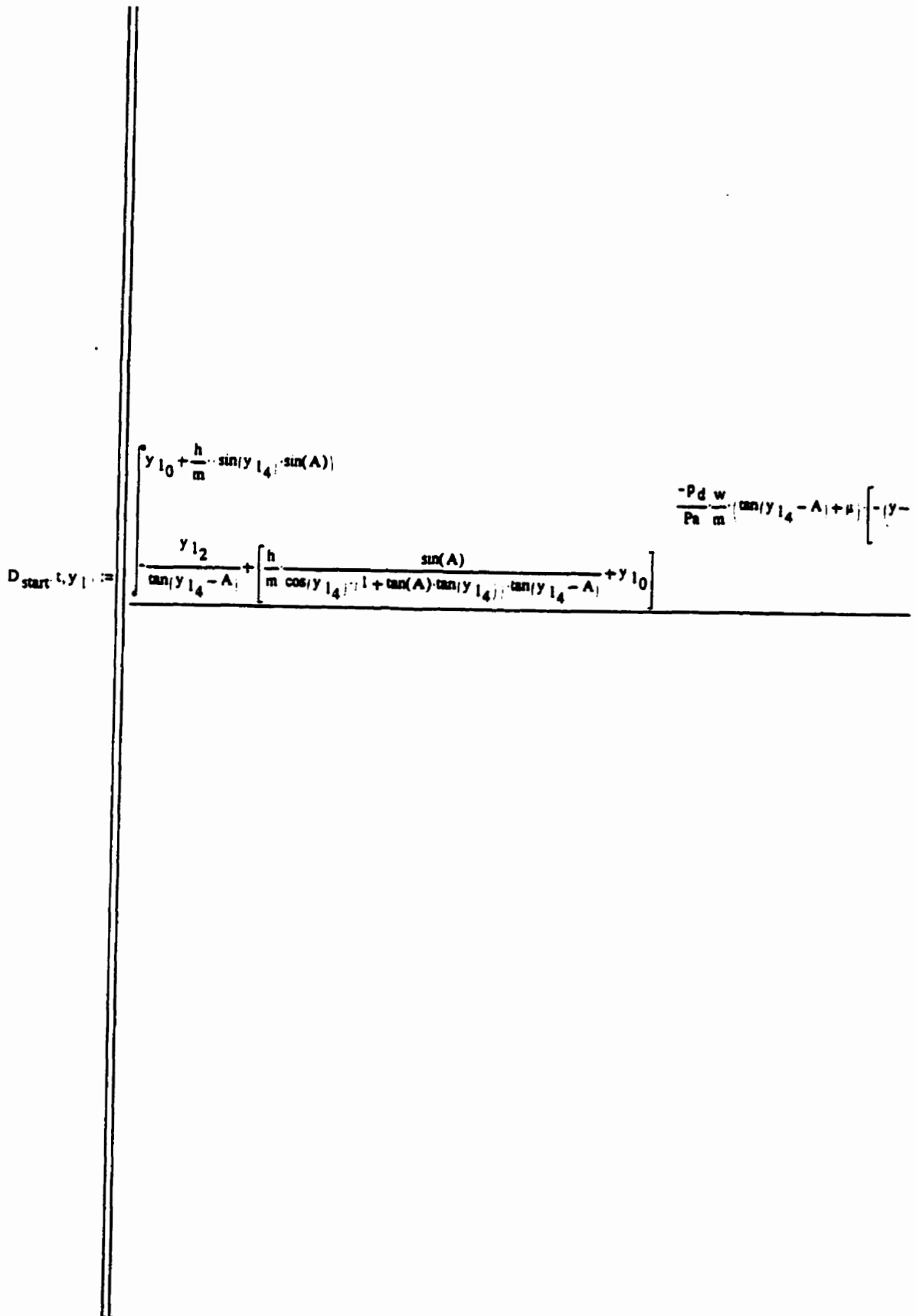
y_{12} - y coordinate of first point on second right side force interval

y_{13} - y coordinate of second point on second right side force interval

y_{14} - y_{21} positive or negative values of coefficient of friction depending on whether left or right side of particle, and towards or away from vertex

y_{22} - y_{29} z coordinates matching y_6 - y_{13}

Here I was forced to use a trick to get conditions and values (constants in each timestep such as force intervals and coefficients of friction) into the D matrix. MathCad will not accept changing values inside the D matrix, because it is a matrix of functions, so you need to perform a trick. You have to pass these to the D matrix by making them part of the system of differential equations. i.e, for example, the value of y_6 contains the a y coordinate of a force application segment, so the value is a constant for each time step. Then, inside the D matrix, have to add an element that represents the derivative of this condition (which is a constant), and thus you pass zero. Same thing goes for y_7 - y_{29} . This is a limitation of MathCad, and hopefully will be fixed sometime.



$$\frac{\text{kg}\cdot\text{m}^2}{\text{I}_x} \left[\left[\left[\frac{-\text{P d w}}{\text{Pa m}} [y_{22} (y_{223} - y_{222}) - \frac{1}{2} [(y_{223})^2 - (y_{222})^2]] \cdot \left(1 + \frac{y_{214}}{\sin(y_{24} - A)} \right) \right] + \frac{\text{P d w}}{\text{Pa m}} \left[\frac{1}{2} (y_{27}^2 - y_{26}^2) \right] \right] \right]$$

Dt.y2 :=

This function takes the coordinates of two points defining a side of the particle and the coordinates of a two crater nodes defining a crater segment, and outputs the intersection point of the two lines, and whether the intersection occurs on the particle side or not.

```

intersection(y1,zp1,yp2,zp2,yc1,zc1,yc2,zc2) :=
cond=0
par←[yp1 zp1
      yp2 zp2]
cr←[yc1 zc1
     yc2 zc2]
sortpar←sort(par,0)
sortcr←sort(cr,0)
mcrta← $\frac{\text{sortcr}1,1 - \text{sortcr}0,1}{\text{sortcr}1,0 - \text{sortcr}0,0}$ 
bcra← $\frac{\text{sortcr}0,1 - \text{mcrta} \cdot \text{sortcr}0,0}{\text{sortpar}1,0 - \text{sortpar}0,0}$ 
mpar← $\frac{\text{sortpar}1,1 - \text{sortpar}0,1}{\text{sortpar}1,0 - \text{sortpar}0,0}$ 
bpar← $\frac{\text{sortpar}0,1 - \text{mpar} \cdot \text{sortpar}0,0}{\text{bcrta} - \text{mcrta} - \text{bpar}}$ 
iny← $\frac{\text{bcrta} - \text{bpar}}{\text{mpar} - \text{mcrta}}$ 
mza←mcrta·iny + bcrta
if (intzsortcr)0,1::intzsortcr)1,1
cond=1
cond=2 if (intzsortpar)0,1::intzsortpar)1,1
if (intzsortcr)0,1::intzsortcr)1,1
if (mper<0)-(mcrta<0)
intz←iny
intz0←intz
intz1←intz
intz2←cond
intz

```

This function determines whether a given node defined by the node coordinates is inside or outside of the particle side, and is used to define the current crater profile. The yp 's and zp 's define the particle side, and $(nodey, nodez)$ define the node in question. The variable 'left' is 1 if the left side of the particle is in question, and 0 if the right side is in question. The function returns a 1 (in the variable 'cond') if the node is inside the particle, and 0 if it is outside.

```

inorout(yp1, zp1, yp2, zp2, nodey, nodez, left) :=
  conde ← 0
  mpar ←  $\frac{zp2 - zp1}{yp2 - yp1}$ 
  bpar ←  $zp2 - mpar \cdot yp2$ 
  mpare ←  $1 \cdot 10^{-50}$  if (mpar=0) · (left=1)
  mpare ←  $1 \cdot 10^{-50}$  if (mpar=0) · (left=0)
  y2 ←  $\frac{nodez - bpar}{mpar}$ 
  z2 ←  $mpar \cdot nodey + bpar$ 
  if left=1
    | conde ← 1 if (y2 - nodey) ≤ 0
    | conde ← 2 if (y2 - nodey) > 0
  if left=0
    | conde ← 1 if (y2 - nodey) ≥ 0
    | conde ← 2 if (y2 - nodey) < 0
  cond

```

This function takes the coordinates of the left, middle, and right vertices of the particle, along with the previous crater profile, and determines the current crater profile, and the intervals over which the forces must be applied in the following timestep. Calls to 'intersection' and 'inorout' functions are made when needed, of course. The variable 'mcratass' contains the transition segment from checking the left and right sides of the particle for intersections.

```

cratdet(crat, mcratass, ly, lz, ry, rz, my, mz) :=
  count ← 0
  counti ← 0
  countr ← 0
  lastpt ← 1
  for i ∈ 1..rows(crat) - 1
    if i ≤ mcratass
      | yp1 ← ly
      | zp1 ← lz
      | yp2 ← my
      | zp2 ← mz
      | left ← 1
    if i > mcratass
      | yp1 ← my
      | zp1 ← mz
      | yp2 ← ry
      | zp2 ← rz

```

```

| left=0
int← intersection(y1,zp1,y2,zp2, crati,0, crati,1, crati-1,0, crati-1,1)
inty← int
if (inorout(y1,zp1,y2,zp2, crati-1,0, crati-1,1, left)≠2 if int2=0
| if lastpt≠(i-1)
|   newcratcount,0← crati-1,0
|   newcratcount,1← crati-1,1
|   count← count + 1
newcratcount,0← crati,0
newcratcount,1← crati,1
count← count + 1
lastpt← i
if int2=2
| if (inorout(y1,zp1,y2,zp2, crati-1,0, crati-1,1, left)≠2
|   if lastpt≠(i-1)
|     newcratcount,0← crati-1,0
|     newcratcount,1← crati-1,1
|     count← count + 1
|     lastpt← i-1
newcratcount,0← int0
newcratcount,1← int1
count← count + 1
if left=1
| flimleftcount,0← int0
| flimleftcount,1← int1
| count← count + 1
if left=0
| flimrightcount,0← int0
| flimrightcount,1← int1
| count← count + 1
if (inorout(y1,zp1,y2,zp2, crati-1,0, crati-1,1, left)≠1
| newcratcount,0← int0
| newcratcount,1← int1
if left=1
| flimleftcount,0← int0
| flimleftcount,1← int1
| count← count + 1
if left=0
| flimrightcount,0← int0
| flimrightcount,1← int1
| count← count + 1
count← count + 1

```

```

newcrat
count, 0 ← crati, 0
newcrat
count, 1 ← crati, 1
count ← count + 1
lastpt ← i
if #mcratass
this ← inorout ( crati-1, 0, crati-1, 1, crati, 0, crati, 1, my, mz, 1 ) if crati, 1 < crati-1, 1
this ← inorout ( crati-1, 0, crati-1, 1, crati, 0, crati, 1, my, mz, 0 ) if crati, 1 > crati-1, 1
next ← inorout ( crati, 0, crati, 1, crati+1, 0, crati+1, 1, my, mz, 1 ) if crati+1, 1 < c
next ← inorout ( crati, 0, crati, 1, crati+1, 0, crati+1, 1, my, mz, 0 ) if crati+1, 1 > c
if ((this#2) + (next#2)) ≥ 1
newcrat
count, 0 ← my
mcratassnew ← count
newcrat
count, 1 ← mz
count ← count + 1
flimleft
count, 0 ← my
flimleft
count, 1 ← mz
count ← count + 1
flimright
count, 0 ← my
flimright
count, 1 ← mz
count ← count + 1
mcratassnew ← count if (this#2) + (next#2) < 1
int ← mcratassnew
C0 ← newcrat
if flimleft ≠ 0
flimleftfin ← flimleft if mod(rows(flimleft) - 1, 2) ≠ 0
flimleftfin ← submatrix(flimleft, 0, rows(flimleft) - 2, 0, 1) if (mod(rows(flimleft) - 1,
flimleftfin ← flimleft if flimleft = 0
flimleft ← 0 if rows(flimleft) = 1
if flimright ≠ 0
flimrightfin ← flimright if mod(rows(flimright) - 1, 2) ≠ 0
flimrightfin ← submatrix(flimright, 1, rows(flimright) - 1, 0, 1) if (mod(rows(flimright
flimrightfin ← flimright if flimright = 0
C1 ← flimleftfin
C2 ← flimrightfin
C3 ← mcratassnew
C4 ← ly
C5 ← my
C6 ← mz
C7 ← ry
C8 ← inty
C

```

In cases for which the angularity and orientation sum to 90 deg. or 0 deg., there can be problems with the tangent going to infinity or dividing by zero. These cases must be handled separately. This function determines which case is in question.

```
singularity( $\theta$ , A, toler) :=
  p ← ( $\theta + A$ )
  m ← ( $A - \theta$ )
  tol90min ←  $(1 - \text{toler}) \cdot \frac{\pi}{2}$ 
  tol90plus ←  $(1 + \text{toler}) \cdot \frac{\pi}{2}$ 
  tol0min ← -toler
  tol0plus ← toler
  if ((p > tol0min) · (p < tol0plus))
    | conde ← 4
    | return conde
    | break
  if (((p > tol90min) · (p < tol90plus)) + ((m > tol0min) · (m < tol0plus)) + ((m > tol90min) · (m < tol90plus))) ≥ 1
    | conde ← 3 if ((m > tol0min) · (m < tol0plus))
    | if ((p > tol90min) · (p < tol90plus))
    | | conde ← 1
    | | conde ← 5 if ((m > tol0min) · (m < tol0plus))
    | conde ← 2 if ((m > tol90min) · (m < tol90plus))
  conde ← 0 if (((p > tol90min) · (p < tol90plus)) + ((m > tol0min) · (m < tol0plus)) + ((m > tol90min) · (m < tol90plus)))
  return conde
```

THE TIME STEP IS ENTERED HERE

step := $2 \cdot 10^{-6}$

Here is the actual "main program" which calls all of the functions. Every time step, the Runge Kutta function is called, the current crater profile is calculated, the direction of friction is determined, and the force intervals are determined. The program loops until the z coordinate of the middle vertex of the particle goes above the Z=0 axis indicating that the collision is over. The main program returns: the y and z velocities and positions of the center of mass and the particle orientation angle at all times during the impact, along with the final crater profile carved by the particle. This data is then used to calculate the trajectory of the particle and the rebound parameters.

```

Solution(y, step) := counte-0
Z_start ← rfixed(y, 0, step, 1, D_start)
Z ← Z_start
y0 ← Z_1,1
z0 ← (Z)_1,3
θ ← (Z)_1,5
ly ←  $\left[ \frac{-z0}{\tan(\theta - A)} + \frac{h}{m} \frac{\sin(A)}{\cos(\theta) \cdot \tan(\theta - A) \cdot (1 + \tan(A) \cdot \tan(\theta))} + y0 \right]$ 
my ←  $y0 + \sin(A) \cdot \sin(\theta) \cdot \frac{h}{m}$ 
mz ←  $z0 + (my - y0) \cdot \tan(\theta - A) - \frac{h}{m} \frac{\sin(A)}{\cos(\theta) \cdot (1 + \tan(A) \cdot \tan(\theta))}$ 
ry ←  $\left[ \frac{-z0}{\tan(\theta + A)} + \frac{h}{m} \frac{\sin(A)}{\cos(\theta) \cdot \tan(\theta + A) \cdot (1 - \tan(A) \cdot \tan(\theta))} + y0 \right]$ 
y0 ← Z_start_1,1
y1 ← Z_start_1,2
y2 ← Z_start_1,3
y3 ← Z_start_1,4
y4 ← Z_start_1,5
y5 ← Z_start_1,6
crat_0,0 ← -10
crat_0,1 ← 0
crat_1,0 ← ly
crat_1,1 ← 0
crat_2,0 ← my
crat_2,1 ← mz
crat_3,0 ← ry
crat_3,1 ← 0
crat_4,0 ← -10
crat_4,1 ← 0
time ← step
time ← 2 · step
y6 ←  $\frac{-y2}{\tan(y4 - A)} + \frac{h}{m} \frac{\sin(A)}{\cos(y4) \cdot \tan(y4 - A) \cdot (1 + \tan(A) \cdot \tan(y4))} + y0$ 
y7 ←  $y0 + \sin(A) \cdot \sin(y4) \cdot \frac{h}{m}$ 
y10 ←  $y0 + \sin(A) \cdot \sin(y4) \cdot \frac{h}{m}$ 

```

```

                                m
y11 ← [  $\frac{-y_2}{\tan(y_4 + A)} + \frac{h}{m \cos(y_4) \cdot \tan(y_4 + A) \cdot (1 - \tan(A) \cdot \tan(y_4))} + y_0 ]$ 
y14 ← μ
y15 ← 0
y16 ← -μ
y17 ← 0
y18 ← -μ
y19 ← 0
y20 ← μ
y21 ← 0
Cr3 ← 2
oldleft0 ← y6
oldleft1 ← y7
oldright0 ← y10
oldright1 ← y11
oldly ← ly
oldmy ← my
for i ∈ 0..1
  oldlefti ← [  $z_0 + \text{oldleft}_i - y_0 \cdot \tan(\theta - A) - \frac{h}{m \cos(\theta) \cdot (1 + \tan(A) \cdot \tan(\theta))} \cdot \frac{\sin(A)}{\cos(\theta)}$  ]
  oldrighti ← [  $z_0 + \text{oldright}_i - y_0 \cdot \tan(\theta + A) - \frac{h}{m \cos(\theta) \cdot (1 - \tan(A) \cdot \tan(\theta))} \cdot \frac{\sin(A)}{\cos(\theta)}$  ]
while (mz < 0)
  mcratass ← Cr3
  cratold ← Cr
  Ztemp ← rfixcd(y, timel, timer, l, D)
  Z ← stack i Z, [ [ [ [ Ztemp ]T <1> ] ] ]T
  timel ← Ztemp[1,0]
  timer ← timel + step
  y0 ← Ztemp[1,1]
  z0 ← Ztemp[1,3]
  θ ← Ztemp[1,5]
  sing ← singularity(θ, A, 0.01)
  lvy ←  $\frac{-z_0}{\tan(\theta - A)} + \frac{h}{m \cdot 2} \cdot \frac{\sin(A \cdot 2)}{\sin(\theta - A)} + y_0$ 
  lvy ← y0 -  $\frac{h}{m} \cdot \cos(A) \cdot \cos(\theta)$ 
  lvz ←  $z_0 + (lvy - y_0) \cdot \tan(\theta - A) - \frac{h}{m \cdot 2} \cdot \frac{\sin(A \cdot 2)}{\cos(\theta - A)}$ 
  rvy ←  $y_0 + \frac{h}{m} \cdot \cos(A) \cdot (\cos(\theta))$ 

```

```

m
rvz= z0 + (rvy - y0) * tan(theta + A) - h * sin(A * 2) / (m * 2 * cos(theta + A))
my= y0 + sin(A) * sin(theta) * h / m
mz= z0 + (my - y0) * tan(theta - A) - h * sin(A * 2) / (m * 2 * cos(theta - A))
ry= (-z0 / tan(theta + A) + h * sin(A * 2) / (m * 2 * sin(theta + A)) + y0)
if sing=1
  rvz= mz + h / m
  Cr= cratdet(crat, mcratass, ly, 0, ry, 0, my + 1 * 10^-50, mz)
if sing=2
  rvz= z0 + (rvy - y0) * tan(theta + A) - h * sin(A * 2) / (m * 2 * cos(theta + A))
  lvz= mz + h / m
  Cr= cratdet(crat, mcratass, ly, 0, ry, 0, my - 1 * 10^-50, mz)
if sing=3
  ly= lvy
  lvz= z0 + (lvy - y0) * tan(theta - A) - h * sin(A * 2) / (m * 2 * cos(theta - A))
  Cr= cratdet(crat, mcratass, ly, 0, ry, 0, my, mz)
break if sing=4
if sing=5
  ly= y0 - h / (2 * m)
  mz= z0 - h / (2 * m)
  lvz= z0 - h / (2 * m)
  rvz= z0 + h / (2 * m)
  Cr= cratdet(crat, mcratass, ly, 0, ry, 0, my - 1 * 10^-50, mz)
Cr= cratdet(crat, mcratass, ly, 0, ry, 0, my, mz) if (lvz > 0) * (rvz > 0) * (sing = 0)
if (lvz < 0) * (rvz > 0) * (sing = 0)
  Cr= cratdet(crat, mcratass, lvy, lvz, ry, 0, my, mz)
  ly= lvy
if (lvz > 0) * (rvz < 0) * (sing = 0)
  Cr= cratdet(crat, mcratass, ly, 0, rvy, rvz, my, mz)
  ry= rvy
crat= Cr0
newleft= Cr1 <0> if Cr1 > 0
newright= Cr2 <0> if Cr2 > 0
newleft= 0 if Cr1 = 0
newright= 0 if Cr2 = 0

```

```

newleftz ← (Cr1)<1> if Cr1 ≠ 0
newrightz ← (Cr2)<1> if Cr2 ≠ 0
newleftz ← 0 if newleftz = 0
newrightz ← 0 if newrightz = 0
for i ∈ 0..29
  yi ← 0
  for s ∈ 6..rows(Cr1) - 1 + 6 if Cr1 ≠ 0
    if rows(Cr1) > 4
      return error("too much")
      break
    ys ← (Cr1)s-6,0
    ys+16 ← (Cr1)s-6,1
    t ← s
  t ← 5 if Cr1 = 0
  for s ∈ 10..rows(Cr2) - 1 + 10 if Cr2 ≠ 0
    if rows(Cr2) > 4
      return error("too much")
      break
    ys ← Cr2s-10,0
    ys+16 ← Cr2s-10,1
    t ← s
  t ← 9 if Cr2 = 0
  if rows(oldleft) = 0
    Distold0 ← 0
    Distold1 ← 0
  if rows(newleft) = 0
    Distnew0 ← 0
    Distnew1 ← 0
  if rows(newleft) = 2
    if newleft0 = y

```



```

0
|
| Distrold0 ← √((oldright1 - oldright0)2 + (oldrightz1 - oldrightz0)2
| Distrold1 ← 0
| if oldright0 ≠ oldmy
|   | Distrold0 ← 0
|   | Distrold1 ← √((oldright1 - oldright0)2 + (oldrightz1 - oldrightz0)2
| if rowa(newright)=4
|   | Distnew0 ← √((newright1 - newright0)2 + (newrightz1 - newrightz0)2
|   | Distnew1 ← √((newright3 - newright2)2 + (newrightz3 - newrightz2)2
| if rowa(oldright)=4
|   | Distrold0 ← √((oldright1 - oldright0)2 + (oldrightz1 - oldrightz0)2
|   | Distrold1 ← √((oldright3 - oldright2)2 + (oldrightz3 - oldrightz2)2
| if Distnew0 > Distrold0
|   | y14 ← μ
|   | y18 ← -μ
| if Distnew0 < Distrold0
|   | y14 ← -μ
|   | y18 ← μ
| if Distnew1 > Distrold1
|   | y15 ← μ
|   | y19 ← -μ
| if Distnew1 < Distrold1
|   | y15 ← -μ
|   | y19 ← μ
| if Distnew0 > Distrold0
|   | y16 ← -μ
|   | y20 ← μ
| if Distnew0 < Distrold0
|   | y16 ← μ
|   | y20 ← -μ
| if Distnew1 > Distrold1
|   | y17 ← -μ
|   | y21 ← μ
| if Distnew1 < Distrold1
|   | y17 ← μ

```

```

| y21 ← μ
| y0 ← Z temp1,1
| y1 ← Z temp1,2
| y2 ← Z temp1,3
| y3 ← Z temp1,4
| y4 ← Z temp1,5
| y5 ← Z temp1,6
| oldleft ← newleft
| oldright ← newright
| oldleftz ← newleftz
| oldrightz ← newrightz
| oldly ← ly
| oldmy ← my
| count ← count + 1
| End0 ← Z
| End1 ← cratold
| End

```

The call to the main program is here

```

Answ := Solution(y, step)
Ans := Answ0
rowAns := rows(Ans)
rowAns = 357

```

Here are the coordinates and velocities of the center of mass of the particle, along with orientation, and angular velocity of the particle at any time during the impact.

$$y_0 := \text{Ans}^{<1>} \cdot \text{m} \quad v_y := \text{Ans}^{<2>} \frac{\text{m}}{\text{sec}} \quad z_0 := \text{Ans}^{<3>} \cdot \text{m} \quad v_z := \text{Ans}^{<4>} \frac{\text{m}}{\text{sec}} \quad \theta := \text{Ans}^{<5>} \quad \dot{\theta} := \text{Ans}^{<6>} \frac{\text{rad}}{\text{sec}}$$

What follows below is just to plot the solution in terms of a graph of the position of the particle through the impact

```
rowX := rows(Ans) - 1
```

Plots a square

Default scale for plot:

only plot every 20th pt

```
current := 0, 20.. rowX
```

$$\overrightarrow{\text{left1}} := y_0 - (h \cdot \cos(A)) \cdot \cos(\theta)$$

$$\overrightarrow{\text{left2}} := y_0 - (h \cdot \cos(A)) \cdot \cos(\theta)$$

$$\overrightarrow{\text{right1}} := -\sin(\theta) \cdot h \cdot \sin(A) + y_0$$

$$\overrightarrow{\text{right2}} := \sin(\theta) \cdot h \cdot \sin(A) + y_0$$

$$\overrightarrow{\text{left3}} := -\sin(\theta) \cdot h \cdot \sin(A) + y_0$$

$$\overrightarrow{\text{left4}} := \sin(\theta) \cdot h \cdot \sin(A) + y_0$$

$$\overrightarrow{\text{right3}} := y_0 + h \cdot \cos(\theta) \cdot \cos(A)$$

$$\overrightarrow{\text{right4}} := y_0 + h \cdot \cos(\theta) \cdot \cos(A)$$

re defines how many points to plot defining each side of the particle

re := 100

~~As of now, the particle is defined by the following parameters:~~

range1 := for i ∈ 0..rowX

$$\left. \begin{array}{l} \text{temprange}_0 \leftarrow \text{left1}_i \\ \text{for } j \in 0..re \\ \left| \begin{array}{l} \text{temprange}_{j+1} \leftarrow \text{temprange}_j + \left(\frac{\text{right1}_i - \text{left1}_i}{re} \right) \\ \text{range}_{i,j} \leftarrow \text{temprange}_j \end{array} \right. \\ \text{range} \end{array} \right\}$$

range2 := for i ∈ 0..rowX

$$\left. \begin{array}{l} \text{temprange}_0 \leftarrow \text{left2}_i \\ \text{for } j \in 0..re \\ \left| \begin{array}{l} \text{temprange}_{j+1} \leftarrow \text{temprange}_j + \left(\frac{\text{right2}_i - \text{left2}_i}{re} \right) \\ \text{range}_{i,j} \leftarrow \text{temprange}_j \end{array} \right. \\ \text{range} \end{array} \right\}$$

range3 := for i ∈ 0..rowX

$$\left. \begin{array}{l} \text{temprange}_0 \leftarrow \text{left3}_i \\ \text{for } j \in 0..re \\ \left| \begin{array}{l} \text{temprange}_{j+1} \leftarrow \text{temprange}_j + \left(\frac{\text{right3}_i - \text{left3}_i}{re} \right) \\ \text{range}_{i,j} \leftarrow \text{temprange}_j \end{array} \right. \\ \text{range} \end{array} \right\}$$

range4 := for i ∈ 0..rowX

$$\left. \begin{array}{l} \text{temprange}_0 \leftarrow \text{left4}_i \\ \text{for } j \in 0..re \\ \left| \begin{array}{l} \text{temprange}_{j+1} \leftarrow \text{temprange}_j + \left(\frac{\text{right4}_i - \text{left4}_i}{re} \right) \\ \text{range}_{i,j} \leftarrow \text{temprange}_j \end{array} \right. \\ \text{range} \end{array} \right\}$$

j := 0..re

$$\overrightarrow{z1_{\text{current},j}} := z_{0_{\text{current}}} + (\text{range1}_{\text{current},j} - y_{0_{\text{current}}}) \cdot \tan(\theta_{\text{current}} + A) + h \cdot \frac{\sin(A)}{\cos(\theta_{\text{current}}) \cdot (1 - \tan(A) \cdot \tan(\theta_{\text{current}}))}$$

$$\overrightarrow{z2_{\text{current},j}} := \left[z_{0_{\text{current}}} + (\text{range2}_{\text{current},j} - y_{0_{\text{current}}}) \cdot \tan(\theta_{\text{current}} - A) \right] - h \cdot \frac{\sin(A)}{\cos(\theta_{\text{current}}) \cdot (1 + \tan(A) \cdot \tan(\theta_{\text{current}}))}$$

$$\overrightarrow{z3_{\text{current},j}} := z_{0_{\text{current}}} + (\text{range3}_{\text{current},j} - y_{0_{\text{current}}}) \cdot \tan(\theta_{\text{current}} - A) + h \cdot \frac{\sin(A)}{\cos(\theta_{\text{current}}) \cdot (1 + \tan(A) \cdot \tan(\theta_{\text{current}}))}$$

$$z_{\text{current},j} := \left[z_{0\text{current}} + (range_{\text{current},j} - y_{0\text{current}}) \cdot \tan(\theta_{\text{current}} + A) \right] - h \frac{\sin(A)}{\cos(\theta_{\text{current}}) \cdot (1 - \tan(A) \cdot \tan(\theta_{\text{current}}))}$$

d := 0.03-m

s := d

Default scales for plots: r1 := -s r2 := s

n := 100

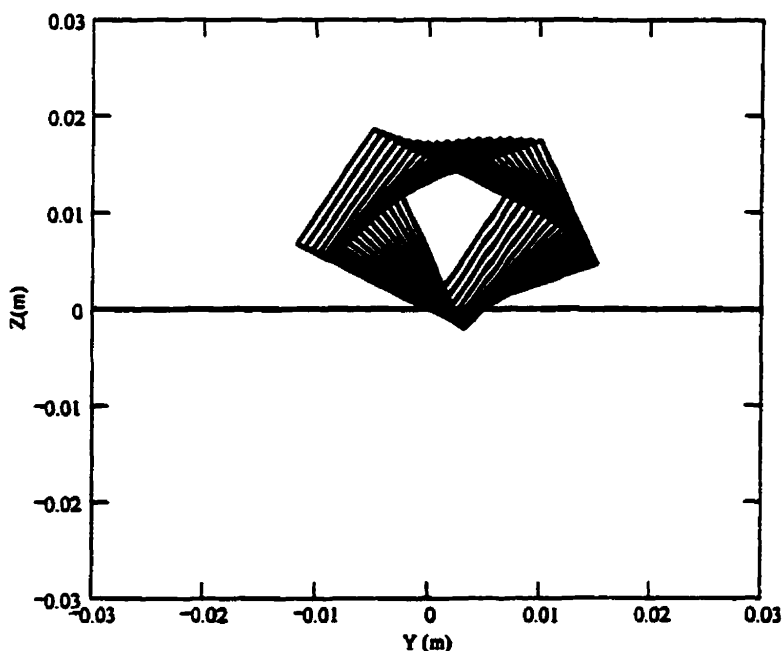
$$r := -r1, -r1 + \frac{r1}{n}, r1$$

These Frame variables are for doing animations. Just activate them by right clicking on them, and you can animate the impact.

FRAME := FRAME - 10⁸

current := 0. FRAME⁸

The solution is plotted here. Note that to maintain the correct aspect ratio, you should make the plotting area square!



CALCULATION OF REBOUND PARAMETERS AND ENERGY LOSSES:
Energy loss

$$E_{\text{loss}} := \left[0.5 \cdot \text{mass} \cdot V_i^2 - 0.5 \cdot \text{mass} \cdot \left[\left(\text{Ans}_{\text{rowX},2} \frac{\text{m}}{\text{sec}} \right)^2 + \left(\text{Ans}_{\text{rowX},4} \frac{\text{m}}{\text{sec}} \right)^2 \right] \right] - .5 \cdot I_x \cdot \frac{(\text{Ans}_{\text{rowX},6})^2}{\text{sec}^2}$$

$$E_{\text{loss}} = 24.613 \cdot \text{kg} \cdot \text{m}^2 \cdot \text{s}^{-2}$$

$$E_{\text{in}} := 0.5 \cdot \text{mass} \cdot V_i^2$$

$$\frac{E_{\text{loss}}}{E_{\text{in}}} \cdot 100 = 56.121$$

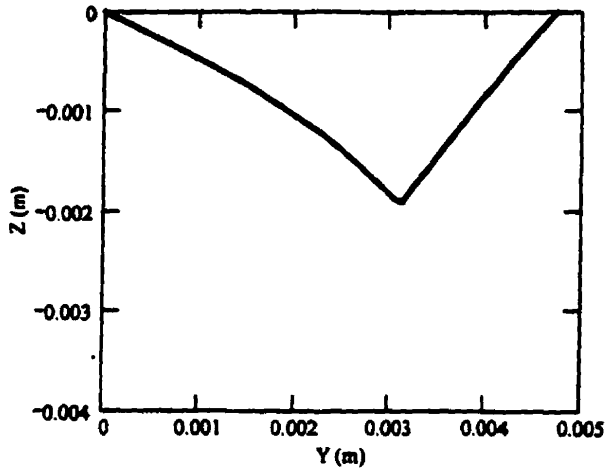
CraterFinal contains the final crater profile

$$\text{CraterFinal} := (\text{Answ}_1)_0$$

-10	0
$6.974 \cdot 10^{-6}$	0
$3.625 \cdot 10^{-5}$	$-1.69 \cdot 10^{-5}$
$7.251 \cdot 10^{-5}$	$-3.38 \cdot 10^{-5}$
$1.088 \cdot 10^{-4}$	$-5.07 \cdot 10^{-5}$
$1.45 \cdot 10^{-4}$	$-6.76 \cdot 10^{-5}$
$1.812 \cdot 10^{-4}$	$-8.45 \cdot 10^{-5}$
$2.174 \cdot 10^{-4}$	$-1.014 \cdot 10^{-4}$
$2.535 \cdot 10^{-4}$	$-1.183 \cdot 10^{-4}$
$2.897 \cdot 10^{-4}$	$-1.352 \cdot 10^{-4}$
$3.257 \cdot 10^{-4}$	$-1.521 \cdot 10^{-4}$
$3.617 \cdot 10^{-4}$	$-1.69 \cdot 10^{-4}$
$3.977 \cdot 10^{-4}$	$-1.859 \cdot 10^{-4}$
$4.336 \cdot 10^{-4}$	$-2.028 \cdot 10^{-4}$

$$\text{CraterFinalair} := \text{substr}(\text{CraterFinal}, 1, \text{rows}(\text{CraterFinal}) - 2, 0, 1)$$

Plot of crater profile:



Calculation of crater volume (or area if per/unit depth)

`CratCalc := submatrix(CraterFinal, 1, rows(CraterFinal) - 2, 0, 1)`

This function takes the crater profile, and finds the area above it; i.e. the crater area or volume depending on whether per/unit or not

```
CratVol := | Vol ← 0
           | for i ∈ 1..rows(CratCalc) - 1
           |   temp ← CratCalci,1 · (CratCalci,0 - CratCalci-1,0) - 0.5 · (CratCalci,0 - CratCalci-1,0) · (CratCalci,1 - CratCalci-1,1)
           |   Vol ← Vol + temp
           | Volume ← | Vol · m2 · w |
           | Volume
```

Crater Volume returned here

$$\text{CratVol} = 6.207056283813115 \text{ mm}^3$$

Crater Volume/unit width:

$$\text{CratArea} := \frac{\text{CratVol}}{w}$$

$$\text{CratArea} = 4.138 \cdot 10^{-6} \text{ m}^2$$

$\pi 1$ is here:

$$\frac{\text{CratArea}}{h^2 \cdot 2 \cdot \cos(A) \cdot \sin(A)} = 0.022$$

and $\pi 2$ is here:

$$\frac{P_d}{\rho \cdot v_i^2} = 12.799$$

Estimate of energy loss using dynamic hardness and crater volume. Compare this with the actual energy loss and see that they are about the same, meaning that dynamic hardness X crater volume gives energy loss.

$$P_d \cdot \text{CratArea} \cdot w = 24.828 \cdot \text{kg} \cdot \text{m}^2 \cdot \text{s}^{-2}$$

Actual energy loss

$$E_{\text{loss}} = 24.613 \cdot \text{kg} \cdot \text{m}^2 \cdot \text{s}^{-2}$$

Final Rebound parameters:

$$v_{\text{reb}} := \sqrt{(v_{y\text{rows}}(v_y) - 1)^2 + (v_{z\text{rows}}(v_z) - 1)^2}$$

$$v_{\text{reb}} = 108.981 \cdot \text{m} \cdot \text{s}^{-1}$$

$$\alpha_{\text{reb}} := \arctan\left(\frac{v_{z\text{rows}}(v_z) - 1}{v_{y\text{rows}}(v_y) - 1}\right)$$

$$\alpha_{\text{reb}} = 13.215 \cdot \text{deg}$$

$$\text{RebRoten} := 5 \cdot 1 \times (\theta_{\text{rows}}(\theta) - 1)^2$$

$$\text{RebRoten} = 6.222 \cdot \text{kg} \cdot \text{m}^2 \cdot \text{s}^{-2}$$

Numbered References

- [1] M. Papini and J.K. Spelt, Organic coating removal by particle impact, *Wear* 213 (1997), 185-199.
- [2] I. M. Hutchings and R.E. Winter, A simple small-bore laboratory gas-gun, *Journal of Physics E: Scientific Instruments*, 8, (1975), 85-86.
- [3] M.E. Graham, J.D. Carlyle, and T.L. Menna, Facility for high-speed particle impact testing, *The Review of Scientific Instruments*, 46 (9), (1975), 1221-1225 .
- [4] I.M. Hutchings, M.C. Rochester, and J.J. Camus, A rectangular bore gas gun, *Journal of Physics E: Scientific Instruments*, 10, (1977), 455-457.
- [5] G. Sundararajan and P. G. Shewmon , The oblique impact of a hard ball against ductile, semi-infinite target materials-experiment and analysis, *International Journal of Impact Engineering*, 6 (3), (1987) 3-22.
- [6] R.W. White and R. Fowles, Effect of valve opening time on gas gun performance, *The Review of Scientific Instruments*, 39 (9), (1975), 1296-1297.
- [7] I. M. Hutchings, Deformation of metal surfaces by the oblique impact of square plates, *International Journal of Mechanical Sciences*, 19, (1977), 45-52.
- [8] M. Ahmed, Experimental study of paint removal due to particle impact, M. A. Sc. Thesis, University of Toronto, Department of Mechanical and Industrial Engineering, 1998.
- [9] M. Papini and J. K. Spelt, Impact-induced buckling of organic coatings- Part I: Theory and analysis, *International Journal of Mechanical Sciences.*, 40 (10), (1998), 1043-1059.
- [10] M. Papini and J. K. Spelt, Impact-induced buckling of organic coatings-Part II: Measurements with impacting particles, *International Journal of Mechanical Sciences*, 40 (10), (1998), 1061-1068.
- [11] J. Oestreich and D.J.L. Monette, An investigation of Envirostrip starch media coating removal from 2024-T3 aluminum alloys, *Proceedings of the 1994 DOD/Industry Advanced Coatings Removal Conference*, New Orleans, Louisiana, May 17-19, 1994, 113-152.
- [12] G. Neumeister and J. Kozol, Type V plastic media blasting of monolithic graphite epoxy composites, *Proceedings of the 1994 DOD/Industry Advanced Coatings Removal Conference*, New Orleans, Louisiana, May 17-19, 1994, 409-424.
- [13] T. Mickle and J. Talia, Paint removal on composites by particle blasting, *Proceedings of the 1993 DOD/Industry Advanced Coatings Removal Conference*, Phoenix, Arizona, May 25-27, 1993, 110-129.

-
- [14] I. Finnie, Erosion of surfaces by solid particles, *Wear*, 3, (1960), 87-103.
- [15] K.L. Johnson, *Contact Mechanics*, Cambridge University Press, U.K, 1985, 351-373.
- [16] K.L. Johnson, *Contact Mechanics*, Cambridge University Press, U.K, 1985, 136-142.
- [17] A.C. Ramamurthy, W.I. Lorenzen, and S.J. Bless, Stone impact damage to automotive paint finishes: an introduction to impact physics and impact induced corrosion, *Progress in Organic Coatings*, 25, (1994), 43-71.
- [18] A.C. Ramamurthy, W.I. Lorenzen, A.M. Rajendran, and D. Grove, *Proceedings of the ACS, PMSE Division*, 67, (1992), 43-44.
- [19] R.M. Brach, Impact dynamics with applications to solid particle erosion, *International Journal of Impact Engineering*, 7 (1), (1988), 37-53.
- [20] M.J. Matthewson, Axi-symmetric contact on thin compliant coatings, *Journal of the Mechanics and Physics of Solids*, 29 (2), (1981), 89-113.
- [21] Y.A. Rossikhin and M.V. Shitikova, The impact of a rigid sphere with an elastic layer of finite thickness, *Acta Mechanica*, 112, (1995), 83-93.
- [22] M. Lu, Observations of indentation cracks in brittle coating/substrate systems, *Journal of Applied Physics*, 66 (8), (1989), 3916-3918
- [23] N.N. Diah and J.G. Williams, The impact behavior of paints, *Journal of Materials Science*, 29, (1994), 6091-6096.
- [24] I. M. Hutchings, R. E. Winter, and J. E. Field, Solid particle erosion of metals: the removal of surface material by spherical projectiles, *Proc. Roy. Soc. London.*, A348, (1976), 379.
- [25] I. M. Hutchings, Mechanisms of the erosion of metals by solid particles, *Erosion: Prevention and Useful Applications*, ASTM STP664, W. F. Adler, Ed., American Society for Testing and Materials, 1979, 59-76.
- [26] I. M. Hutchings, N. H. Macmillan, and D. R. Rickerby, Further studies of the oblique impact of a hard sphere against a ductile solid, *International Journal of Mechanical Sciences*, 23 (11), (1981), 639-646.
- [27] D. G. Rickersby and N. H. MacMillan, On the oblique impact of a rigid sphere against a rigid-plastic solid, *International Journal of Mechanical Sciences*, 22, (1980), 491-494.
- [28] G. Sundararajan and P. G. Shewmon, The oblique impact of a hard ball against ductile, semi-infinite, target materials- experiment and analysis, *International Journal of Impact Engineering*, 6 (1), (1987), 3-22.

-
- [29] Y. Tirupataiah, B. Venkataraman, and G. Sundararajan, The nature of the elastic rebound of a hard ball impacting on ductile, metallic target materials, *Materials Science and Engineering A24*, (1990), 133-140.
- [30] Y. Tirupataiah and G. Sundararajan, A dynamic indentation technique for the characterization of the high strain rate plastic flow behaviour of ductile metals and alloys, *Journal of the Mechanics and Physics of Solids*, 39 (2), (1991), 243-271.
- [31] G. Sundararajan, The energy absorbed during the oblique impact of a hard ball against ductile target materials, *International Journal of Impact Engineering*, 9, No. 3, (1990), 343-358.
- [32] P.H. Shipway and I.M. Hutchings, Measurement of coating durability by solid particle erosion, *Surface Coatings and Technology*, 71, (1995), 1-8.
- [33] ASTM D3359 -93, Standard test methods for measuring adhesion by tape test, *Annual Book of ASTM Standards*, American Society for Testing and Materials.
- [34] B. Ratner and E.E. Styller, Characteristics of impact friction and wear of polymeric materials, *Wear*, 73, (1981), 213-234.
- [35] D. J. Skrovanek and C. K. Schoff, Thermal mechanical analysis of organic coatings, *Progress in Organic Coatings* 16, (1988), 135-163.
- [36] B. Djurovic, E. Jean, M. Papini, P. Tangestanian, and J. K. Spelt, Coating removal from fiber-composites and aluminum using starch media blasting, to be published in *Wear* (1998).
- [37] K.L. Johnson, *Contact Mechanics*, Cambridge University Press, U.K, 1985, 84-106.
- [38] J. W. Hutchinson and Z. Suo, Mixed mode cracking in layered materials, *Advances in Applied Mechanics* 29 (1992), 63-191.
- [39] H. Chai, Three-dimensional fracture analysis of thin-film debonding, *International Journal of Fracture* 46 (1990), 237-256
- [40] A. G. Evans and J. W. Hutchinson, On the mechanics of delamination and spalling in compressed films, *International Journal of Solids and Structures* 20, No. 5 (1984), 455-466.
- [41] J. W. Hutchinson, M. D. Thouless, and E. G. Liniger, Growth and configurational stability of circular, buckling-driven film delaminations, *Acta Metall. Mater.* 40, No. 2 (1992), 295-308.
- [42] W. L. Yin, Axisymmetric buckling and growth of a circular delamination in a compressed laminate, *International Journal of Solids and Structures*, 21, No. 5 (1985), 503-514.

-
- [43] J. M. T. Thompson and G. W. Hunt, *A General Theory of Elastic Stability*, John Wiley and Sons, London, U.K., 1973, 161-171.
- [44] E. Meissner and E. T. H. Zurich, Ueber das knicken kreisringformiger scheiben, *Schweiss Bauz.*, Bd. 101, S.87 (1933).
- [45] Z. Suo and J. W. Hutchinson, Interface crack between two elastic layers, *International Journal of Fracture* 43 (1990), 1-18.
- [46] J. Dundurs, *ASME Journal of Applied Mechanics* 36 (1969), 650-652.
- [47] M. J. Matthewson, Adhesion measurement of thin films by indentation, *Applied Physics Letters* 49, No. 21 (1986), 1426-1428.
- [48] M. Papini and J. K. Spelt, The plowing erosion of organic coatings by spherical particles, under review, *Wear*, (1998).
- [49] B. Djurovic, Coating removal from fibre composites using wheat starch blast cleaning, M.A.Sc. Thesis, University of Toronto, 1997.
- [50] K.L. Johnson, *Contact Mechanics*, Cambridge University Press, U.K, 1985, 171-184.
- [51] R.J. Crawford, Micro hardness testing of plastics, *Polymer testing*, 3 (1982), 37-54.
- [52] M. Papini and J. K. Spelt, Erosion with angular particles: Part I – Theory and analysis, under review, *Int. J. Mech. Sci.*, (1998).
- [53] M. Papini and J. K. Spelt, Erosion with angular particles: Part II – Parametric study, under review, *Int. J. Mech. Sci.*, (1998).
- [54] D. A. Wells, *Schaum's Outline of Theory and Problems of Lagrangian Dynamics*, Schaum Publishing Company, United States, 1967, 139-167.
- [55] S. A. G. Oliveira and A. F. Bower, An analysis of fracture and delamination in thin coatings subjected to contact loading, *Wear* 198 (1996), 15-32.
- [56] J. G. A. Croll, Continuum perturbation method in the branching analysis of conservative systems, *International Journal of Mechanical Sciences* 13 (1971), 65.
- [57] I. S. Gradshteyn and I. M. Ryzhik, *Table of Integrals Series and Products*, 4th Ed., Academic Press, New York, 1965, 951-990.